Interaction of Liquid Copper With Sintered Iron Compacts

Nader Parvin

Doctor of Philosophy

Aston University

June 1989

Aston University

Interaction of Liquid Copper with Sintered Iron Compacts.

Nader Parvin Ph.D. 1989

Abstract

Interaction of liquid copper with sintered iron is important in brazing, liquid phase sintering and infiltration. In brazing, the penetration of liquid copper into the pores is to be "avoided", whereas in infiltration processes it is "encouraged", and in liquid phase sintering it should be "controlled" so that optimum mechanical properties are achieved. The main objective of the research is to model the interaction by studying the effect of the process variables on the mechanisms of copper interaction in Fe-Cu and Fe-Cu-C systems. This involves both theoretical and experimental considerations.

Dilatometric investigations at 950, 1125 and 1200°C, together with metallographic analyses were carried out to clarify the copper growth phenomenon. It is shown that penetration of liquid copper into the iron grain boundaries is the major cause of dimensional changes.

Infiltration profiles revealed that copper penetration between the iron interparticle contact points and along iron grain boundaries is a rapid process. The extent of copper penetration depends on the dihedral angle. Large dihedral angles hinder, and small angles promote copper penetration into the grain boundaries. Dihedral angle analysis shows that the addition of 0.6 wt.% graphite reduces the number of zero dihedral angle from 27 to 3° and increases the mean dihedral angle from 9.8 to 41.5°. The dihedral angle was lowest at 1125°C and then increased to higher values as the system approached its equilibrium condition. Elementally mixed (E.M) Fe-Cu compacts showed a rapid expansion at the copper melting point. However, graphite additions reduced compact growth by increasing the mean dihedral angle.

In order to reduce the copper growth phenomenon, iron powder was coated with a thin layer of copper by an immersion coating (I.C) technique. The dilatometric curves revealed an overall shrinkage in the I.C compacts compared to their corresponding E.M compacts. Multiple regression models, showed that temperature had the most effect on dimensional changes and density had the most contributing effect upon the copper penetration area in the infiltrated powder metallurgy compacts.

Keywords: Powder Metallurgy, Liquid Phase Sintering, Infiltration, Brazing.

To the family of my boyhood

and

To the family of my manhood

Acknowledgements

The author would like to express his deep gratitude to Mr. L.W. Crane for his continuing help and invaluable discussions throughout the duration of this research. My sincere thanks also to the staff and research students of the Mechanical and Production Engineering Department for their technical advice.

Finally, the author is indebted to his wife for her help in preparation of this thesis and to his parents for their support and encouragement.

List of Contents

List of Figures

List of Tables

1. Introduction

1. Introduction

Sintered steel components are currently produced in the density range 6.5-7.2 Mgm^{-3} which corresponds to 83-92% of solid density. Strength and associated properties are directly proportional to density. If this sector of powder metallurgy is to grow, it is necessary to move to the production of components of high density and strength, capable of carrying higher stresses. Methods of achieving enhanced properties include liquid phase sintering and infiltration. Liquid phase sintering is widely used for consolidating ceramic and metallic products to final shapes. The main advantages of this production method are low sintering temperatures, fast densification and homogenization, high final densities and resulting microstructures that often provide physical or mechanical properties superior to those of solid state sintered materials. Densification during liquid phase sintering is based on the rearrangement and shape change of solid constituents. Chemical homogenization is rapid during liquid phase sintering between the solid particles. In good wetting conditions, the liquid phase is pulled by capillary forces into particle necks and small pores. The sintering of hard metal alloys is a well established application of liquid phase sintering. Because of the great hardness of the carbide particles which constitute the bulk of a hard metal powder, it is quite impossible to press the powders to a density higher than about 60% of theoretical, yet on sintering, a perfect, pore free compact can be obtained. The development and exploitation of liquid phase sintering in ferrous powder metallurgy has largely been in systems where limited solubility exists between the components, such as, Fe-Cu and Fe-Cu-C alloys. Copper powder additions to iron powder are used in industry to produce high strength sintered steel parts. The copper content ranges from 1 to 10% depending on the preparation conditions, the ultimate tensile strength required

and the applications of the sintered parts. The infiltration process is of importance in powder metallurgy as a method of reducing porosity in a compact and improving mechanical properties. A porous metal compact is first prepared and is then brought into contact with molten metal (eg. copper) which fills the pores. In practice, this is accomplished by either dipping the compact in the liquid metal (infiltrant), or by placing powder or powder compact of the infiltrant, on the top of the base metal compact, and then heating the assembly to a temperature between the melting points of the two metals. At infiltration temperature the filling of the pore volume is accomplished within a short time. In practice however, the systems are maintained at the infiltration temperature for a considerably longer period. The reactions, taking place during this so called soaking period are thus analogous to those taking place in liquid phase sintering. A common disadvantage of the copper addition in infiltration and liquid phase sintering is the pronounced swelling during sintering which reduces the dimensional accuracy. This effect has been subject to investigation in the past. However, the actual mechanism of dimensional changes has been a matter of controversy. It is considered that the utilization of one of the new family of microprocessor controlled dilatometers would provide accurate monitoring of the dimensional changes of Fe-Cu and Fe-Cu-C compacts during liquid phase sintering.

Another area where interaction of liquid copper plays an important role, is in brazing, in which a filler metal is drawn by capillary action into the space between the parts to be joined. Brazing has several advantages in the joining of powder metallurgy (P/M) parts, compared to other joining methods. For example, the relatively low temperature thermal cycle has less metallurgical effect on the microstructure and mechanical properties, and that there is less distortion. There is also generally a cost saving in brazing which is due to the lower heat input, and also

the ease of production using replaced braze, which is an ideal method for the joining of small P/M parts. There is however one major problem to be overcome when brazing P/M components. This is that the interconnected porosity which is inherent in parts with more than about 8% total porosity, draws the molten brazing alloy and the flux away from the joint by capillary action. Brazing alloys that resist being drawn into the pores are available at a cost. Another operation to overcoming the problem is to process the compact to give less than 5% porosity, however this is technically difficult and expensive for iron and low alloy steels. Infiltration of the compacts prior to brazing can reduce the problem of braze metal penetration. The drawback with this method of joining is that, rigorous temperature control is needed so that the brazing temperature does not exceed the melting point of the P/M part and does not fall below the melting point of the infiltrant. It is therefore clear that interaction of liquid copper with sintered iron compacts is important in liquid phase sintering, infiltration and brazing.

Each of the topics discussed above, has been studied in isolation by previous researchers. It is now considered that a detailed review of available information, with particular emphasis on cross referencing experimental findings and theories, would prove to be rewarding. Also, an experimental programme which has a fundamental broad based approach, rather than an approach to solve a specific problem should be fruitful. Thus, a fundamental approach to the interaction of liquid copper with iron compacts, is considered to be necessary to obtain a better understanding of the situation and solve the problems still existing in industrial applications.

2. Literature Survey

2. Literature Survey

One of the fundamental properties of a liquid surface is that it tends to contract to assume the smallest possible area. This tendency is shown in the near spherical form of a drop of liquid on a solid surface. Plateau(1983) has studied the forms assumed by liquid surfaces, under the condition of zero gravity. He showed that the surfaces always assume a curvature such that :

$$1/R_1+1/R_2= \text{CONSTANT} \quad .....(2.1)$$

where R_1 and R_2 are the radii of curvature of the axes at any point.

It is a geometrical fact that surfaces for which the relation (2.1)holds are surfaces of minimum surface area.

Liquids are distinguished from the solids by their fluidity, ie the freedom of the molecules or atoms to move independently. In the body of liquid or solid, each molecule is surrounded by others on every side, and is therefore subject to uniform attraction in all directions. However at a surface, conditions are entirely different. Because there are very few molecules outside, the molecules at the surface are attracted inward by their neighbours. Hence every surface molecule is subject to a strong inward attraction perpendicular to the surface (Figure 2.1). This inward force causes the surface to contract to the smallest possible area.

2.1 Surface Tension and Surface Free Energy

When two fluids ,or a fluid and a solid (or gas), are in contact with one another, they are in general separated by a thin boundary layer called an *interface,* whose properties are different from the two original phases. Nevertheless as pointed out by Young (1805), the system behaves as though it consists of two homogeneous

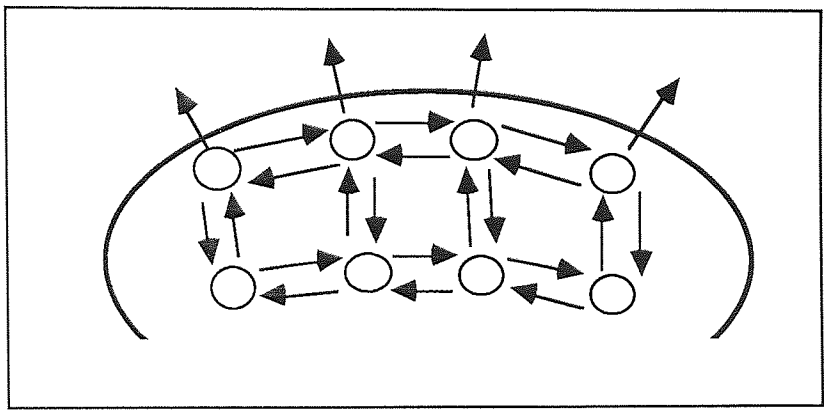

Figure 2.1 - Attractive forces within the molecules.

fluids separated by a uniformly stretched membrane of a very small thickness.

In order to define the surface tension, imagine a curve AB (Figure 2.2) with point P, dividing AB into two regions. If across an element (dl) of AB, region 2 exerts a force (σ dl) tangential to the surface, then σ is called the surface tension at that point. The surface is said to have uniform tension if:

a) σ is perpendicular to the dividing line at each point, and

b) σ has the same value at all points on the surface.

Surface tension has the dimension of force per unit length and is usually expressed as Nm^{-1}.

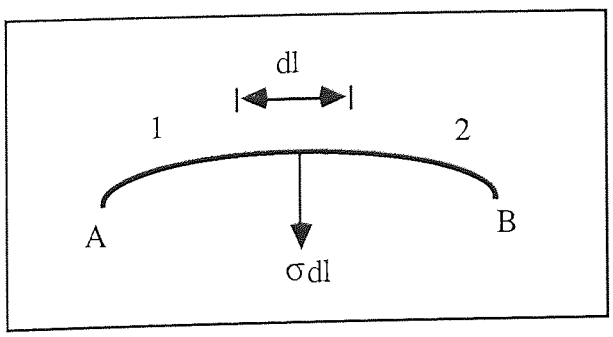

Figure 2.2 - Definition of a surface tension.

The unbalanced forces on the surface result in free energy of the surface. In addition to minimizing the surface area of the liquid, atoms and molecules in the surface layer will arrange themselves so as to give minimum overall energy. This means that the characteristic surface energy of a substrate depends markedly on the type of bonding. The energy is lowest for strongly directional covalent bonding, where molecules orientate to turn the strongest bonds inward (0.015-0.04 Jm^{-2} for most organic liquids), and highest for relatively symmetrical metallic bonding (0.3-2.0 Jm^{-2} for liquid metals). Ionic compounds such as molten salts and oxides, have surface energies between those of organic liquids and those of molten metals (0.05-0.2 Jm^{-2} , Milner, 1958).

The orientation of the molecules near the surface means that the surface layers will have a different atomic arrangement from the liquid, and the chemical composition may also be different, owing to the preferential segregation of impurities, alloying elements and absorbed vapour. Since in soldering and brazing , the liquid metal is never pure, it is necessary to have some knowledge of this effect. The generally accepted theory is that the constituent which has the lowest surface free energy in the pure state will segregate to the surface of the mixture or alloy (Adam, 1968).

In liquid phase sintering and infiltration processes, penetration of liquid copper along the interparticle contact areas and microporosities, depends to some extent on the capillary forces. These forces may be calculated from the equation of Young and Laplace.

2.2 The Equation of Young and Laplace.

A vertical thin capillary tube immersed in a wetting liquid lead to a phenomenon known as capillary rise. The height of the liquid which penetrates up the tube against gravity force depends on tube diameter, contact angle and interfacial

energies. The capillary attraction is increased by a smaller capillary tube diameter. This means that in a compact, the liquid will flow into the smaller pores first. Based on a study of liquid phase sintering of Fe-Al system Lee and German (1985), reported that if the aluminium powder has a relatively large particle size, then on melting it will flow into the neighbouring pores and create a large pore at its initial site. The created pores are easier to remove in the subsequent sintering process, if the aluminium powder has a small particle size. Thus, smaller particle sizes are beneficial because of smaller pores, better homogeneity and better capillarity.

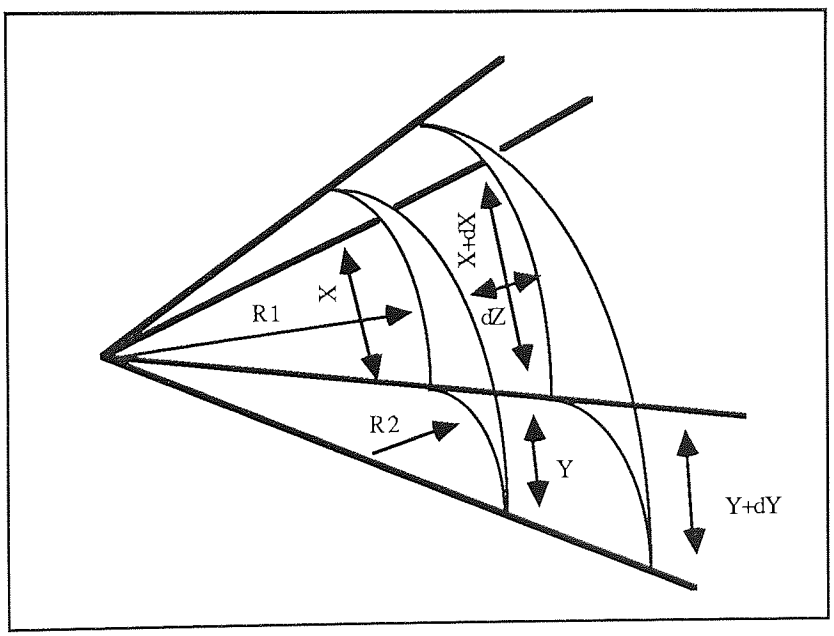

Figure 2.3 - Section of a curved surface showing the radii of curvature.

The basic equation of capillarity was first given in 1805 by Young and Laplace. They confirmed that it is necessary to involve two radii of curvature at right angles to describe a curved surface. For a spherical surface the radii are equal. Figure 2.3 shows a small section of a curved surface. If the surface is displaced by a small distance, dX outward, the change in area, ΔA will be:

$$\Delta A = (X + dX)(Y + dY) - XY = XdY + YdX$$

The work done in forming this additional amount of surface is then:

$$\text{Work} = \gamma_L \ (XdY + YdX) \quad \ldots\ldots\ldots\ldots\ldots\ldots (2.2)$$

Where γ_L= surface free energy of the liquid per unit area.

In order to create the curvature, there will be a pressure difference of ΔP across the surface. It acts on the area XY, and through a distance dZ. The corresponding work is thus:

$$\text{Work} = \Delta P \ XYdZ \quad \ldots\ldots\ldots\ldots\ldots\ldots (2.3)$$

From a comparison of similar triangles, it follows that:

$$\frac{X + dX}{R_1 + dZ} = \frac{X}{R_1}$$

$$\text{Or} \quad dX = \frac{XdZ}{R_1}$$

and

$$\frac{Y + dY}{R_2 + dZ} = \frac{Y}{R_2}$$

$$\text{Or} \quad dY = \frac{YdZ}{R_2}$$

where R_1 and R_2 are the radii of curvature.

For equilibrium at the surface, the work terms must be equal to each other. By equating and substituting for dX and dY:

$$\Delta P = \gamma_L \ (1/R_1 + 1/R_2) \quad \ldots\ldots\ldots\ldots\ldots\ldots (2.4)$$

Equation 2.4 is the equation of Young and Laplace which is also called the equation of capillarity.

For the case of a sphere, both R_1 and R_2 are equal, so:

$$\Delta P = 2 \gamma_L / R$$

For the case of a plane surface, the two radii are infinity, therefore:

$$\Delta P=0 \quad \text{(ie no pressure difference across a plane surface)}$$

The equation of capillarity suggests that, the ease with which capillary forces can act upon a liquid depends on the surface tension of the liquid.

There are a number of different methods of measuring surface tension. The values thus obtained should, and do in most cases, come out to be the same, irrespective of the method used, although difficulties in the mathematical treatment of complex phenomena can lead to some errors. Two of the methods are explained below in the next section.

2.3 Methods of Measuring Surface Tension

2.3.1 Capillary Rise Method.

Using the equation of Young and Laplace, an approximate value of surface tension can be found. Imagine a liquid surface in a capillary gap between parallel plates (Figure 2.4). The liquid molecules adjacent to the solid are acted upon by the forces of the solid as well as the forces towards the liquid. Thus, the liquid surface will be curved at the line of contact with the solid. The pressure difference across the curved interface is given by:

$$\Delta P= \gamma_L \ (1/R_1 + 1/R_2)$$

If H is the height of liquid above a flat liquid surface then:

$$\Delta P= \Delta\rho \ gH$$

where $\Delta\rho$=difference in density between the liquid and gas phase and g is the acceleration due to gravity.

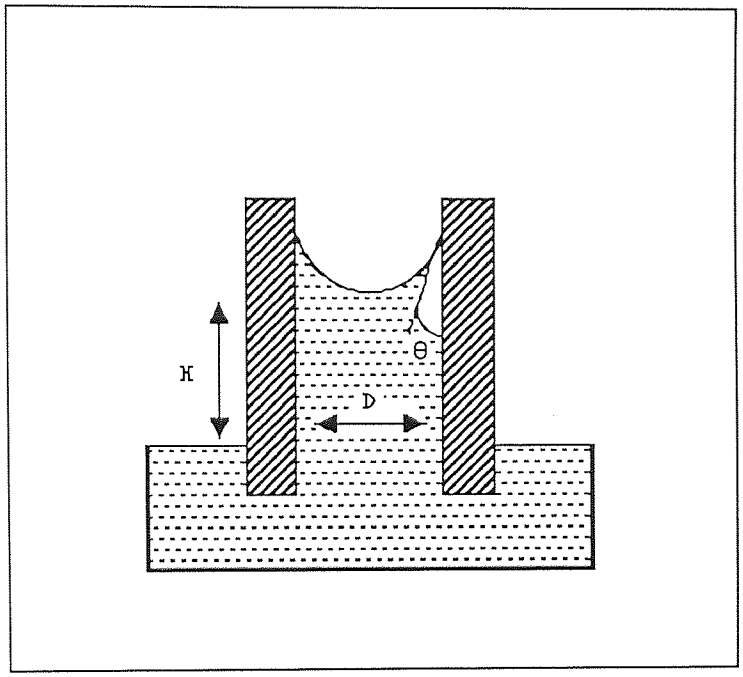

Figure 2.4 - Cross section of parallel plates with capillary gap in between.

Since "gas " is air, it has a very low density compared to molten metals. Therefore, $\Delta\rho$ is taken as ρ, the density of the molten metal.

For parallel plates, $R_1 = D/2\cos\theta$ and R_2=infinity

$$\rho\, gH = \gamma_L\ (2\cos\theta / D + 0)$$

$$H = \text{capillary rise} = \frac{(2\gamma_L \cos\theta)}{(\rho g D)}$$

$$\text{and} \quad \gamma_L = \frac{(\rho g H D)}{(2\cos\theta)}$$

2.3.2 The Ring Method.

This method is widely used and involves the measurement of the force needed to detach a wire, in the form of a ring, from a liquid surface. It was first investigated in 1919 by du Nouy.

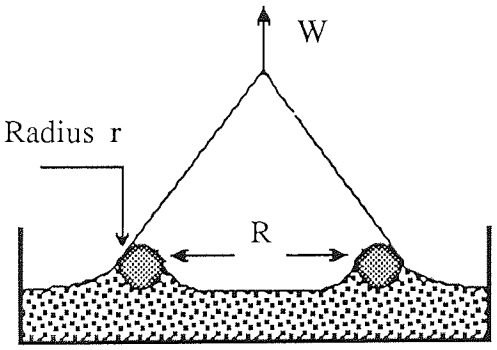

Figure 2.5 - Ring method for measuring surface tension.

An approximation to the detachment force from Figure 2.5 is given by:

Force= (surface tension) x (the periphery of the surface detached)

$$W_{total} = W_{ring} + 12.56R\,\gamma \quad \text{.....(2.5)}$$

Later, Harkins and Jordan (1930) reported that the above equation gives some error and proposed an empirical correction factor as follows:

$$\text{correction factor } f = (\gamma/P) = f\,(R^3/V\,,\ R/r\,)$$

where P= ideal surface tension calculated from Equation 2.5

V= volume of the meniscus

Figure 2.6 shows the curves of Harkins and Jordan. It indicates that the simple equation may be in error by up to 25%. The detailed theory behind the method is

quite complicated, but it has been worked out by Milner(1958), who showed that the calculated values of 'f' agree with the experimental ones to within an accuracy of about 0.25%.

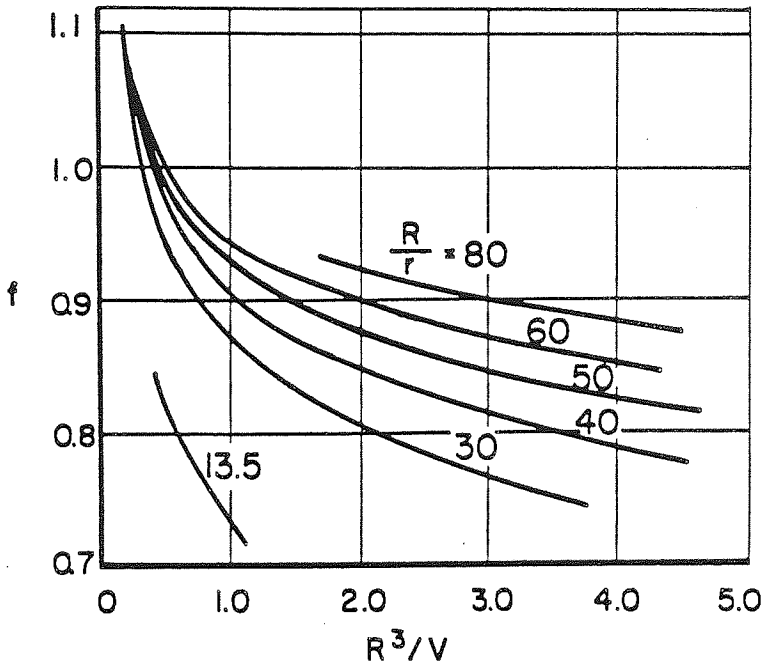

Figure 2.6 - Correction factor curves for the ring method.

There are other methods of measuring the surface tension, namely, maximum bubble pressure method, dynamic method and the drop weight method. Discussion of these techniques is considered to be not relevant to this study.

2.4 Spreading of Liquid Copper on a Solid Surface

Spreading is the kinetic process associated with wetting. The spreading of a liquid over a solid is important in liquid phase sintering and infiltration. Study of the spreading of liquids over solid surfaces is difficult. There are many factors which

affect the spreading behaviour such as, contamination, mechanical agitation, segregation and crystallographic orientation. When analysing the spreading behaviour of liquid copper, it is noticed that reference is required to both the static and the dynamic theories:

1. Thermodynamic or static theory, which defines the shape which the liquid will assume in order that the system as a whole has a minimum surface free energy. The argument is given below.

Suppose that a drop of liquid copper is resting on a solid surface. The forces involved and the contact angle it makes with the surface are shown in Figure 2.7. If the droplet is static at equilibrium then:

$$\gamma_{SV} = \gamma_{SL} + \gamma_{LV} \cos\theta \quad \text{.....(2.6)}$$

where γ_{SV} = interfacial tension between solid and vapour

γ_{SL} = interfacial tension between solid and liquid copper

γ_{LV} = interfacial tension between liquid copper and vapour

θ = contact angle

While the above relationship is theoretically important, it is of little practical importance. Allen (1984), reported that the surface energy of a solid covered with a layer of absorbed vapour is lower than that of a bare surface by an amount known as the *spreading pressure* , π, therefore:

$$\gamma_{SV} = \gamma_{SO} - \pi$$

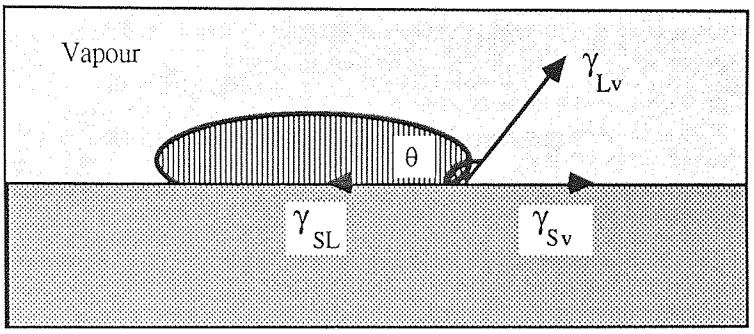

Figure 2.7 - Surface tension exerted upon liquid metal resting on a flat surface.

γ_{SO} is the surface energy of a clean solid surface. π, is always positive, although depending upon the natures of the vapour and solid, may range from negligibly small (eg: hydrocarbon oil on polyethylene), to considerable (eg: water on oxide metals).

The Young's equation can then be rewritten as:

$$\gamma_{SO} - \pi = \gamma_{SL} + \gamma_{LV} \cos \theta$$

In vacuum and at high temperatures, the vapour phase is not present, therefore $\gamma_{SV} = \gamma_{SO}$ and the π term can be omitted.

This relationship applies for contact angles less than, equal or greater than 90 degrees. There are methods of measuring the contact angles which will be dealt with later in this chapter.

2. Dynamic theory, which defines the rate at which the liquid will approach its final equilibrium state. This has been investigated by Milner (1958), where, by assuming a Reynolds Number of less than 1000 (ie streamline flow), he came up with the

following formula:

$$R = \eta \, (dU/dY) \times (\text{area travelled})$$

where:

R= resistance force to spreading

U=velocity

Y=direction perpendicular to motion

η=viscosity

The liability of a molten copper to flow can be estimated by a term called "spreading coefficient".

2.4.1 Spreading Coefficient of one Liquid on Another

Spreading of a liquid on another has been studied by Harkins (1952) and Bikerman (1958). If a small drop of oil is placed on water surface, it maintains its form as a drop, floating in a depression on water surface as shown in Figure 2.8. By equating the horizontal components of the tensions we obtain:

$$\gamma_{wv} = \gamma_{ov} \cos \theta_1 + \gamma_{wo} \cos \theta_2 \ldots\ldots\ldots (2.7)$$

For spreading of liquid to proceed, θ_1 and θ_2 should approach zero. So the relation $\gamma_{wv} > \gamma_{ov} + \gamma_{wo}$ must be satisfied.

Thus the spreading coefficient C, of oil on water will be:

$$C = \gamma_{wv} - (\gamma_{ov} + \gamma_{wo}) \ldots\ldots\ldots\ldots\ldots (2.8)$$

The general condition for any oil to spread on water is that C must be either positive or zero.

2.4.2 Spreading Coefficient of Liquid Copper on a Solid.

If γ is surface free energy per unit area then, from Equation 2.6

$$\gamma_{SV} = \gamma_{SL} + \gamma_{LV} \cos \theta \ldots\ldots\ldots\ldots\ldots (2.9)$$

where symbols S , L and V refer to solid and liquid and vapour respectively.

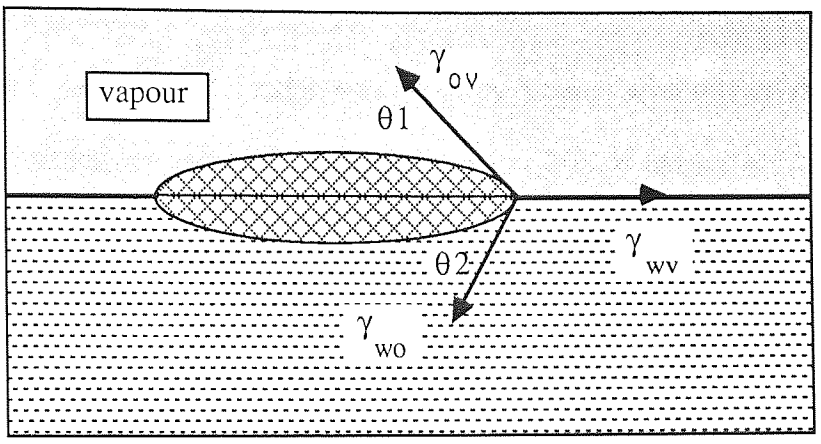

Figure 2.8 - Surface tensions exerted on a drop of oil floating on a water surface.

By a similar analogy to the spreading of a liquid on another, we may then write the spreading coefficient of liquid copper on a solid surface (Figure 2.7).

$$C_{SV} = \gamma_{SV} - (\gamma_{LV} + \gamma_{SL}) \quad \text{.....(2.10)}$$

By combining Equation 2.10 with 2.9, the final relation for coefficient of spreading of liquid copper (C_{Sv}) is obtained.

$$C_{SV} = \gamma_{LV} (\cos \theta - 1) \quad \text{.....(2.11)}$$

This equation suggests that:

1. For perfect spreading, the contact angle will be zero.
2. The more negative the value of C_{SV}, the poorer is the spreading of the liquid copper over the solid surface.

2.5 Contact Angle

It is observed that in most instances a liquid placed on a solid will not wet it completely, but will form a drop having a definite angle of contact between the liquid and solid phases. The degree of wetting is characterized by the contact angle. Good wetting corresponds to low contact angle, while poor wetting corresponds to

high contact angle.

The first equation for contact angle was given by Young, who related the contact angle to surface tension at three interfaces (Equation 2.6). If the surface of the solid is rough , Young's equation is applicable to each element of the surface, but the observed angle between the liquid/air surface and the apparent surface of the solid will vary with the position of the line of contact. It has been proposed by Wenzel (1936) that Young's relation can be written as;

$$R(\gamma_{LV} - \gamma_{SL}) = \gamma_{LV} \cos\theta \quad \text{.....(2.12)}$$

Where R is the ratio of true to apparent area of solid. Shuttleworth (1948) and Good (1952) have both given thermodynamic justification of Wenzel's formula. However, Bikerman (1957) criticised Young's equation on the grounds that the equilibrium conditions are discussed only with respect to forces parallel to the surface, and that *no* account is taken of the component $\gamma_{LV}\sin\theta$ which is normal to the solid surface. Lester (1961), gave an analysis of the stresses in the region of the three-phase boundary and concluded that the component $\gamma_{LV}\sin\theta$ caused a distortion of the solid surface which, if the solid is easily deformable, may be large enough to reject the validity of Young's equation.

These considerations emphasize that the experimentally observable quantity is θ the contact angle, whose value depends entirely on the nature of gas/liquid, gas/solid and solid/liquid interfaces. It is, for example, very much affected by the presence of absorbed molecules and impurities at these sites. It also depends on whether the boundary is advancing or receding, which is called *hysteresis of contact angle* described below. Once the state of interfaces are fixed, then the contact angle has a definite value.

2.5.1 Hysteresis of Contact Angle

After lengthy study, Adam (1968) stated that, the contact angle of a liquid which has spread outward over a smooth solid surface exceeds the contact observed after the liquid has retracted from the surface. This difference between the values of advancing and receding contact angles is generally attributed to the absorption of molecules of liquid upon the solid surface and is known as hysteresis of the contact angle. To distinguish such adsorption hysteresis from hysteresis due to surface roughness, it is proposed to use the term *molecular hysteresis*. The true contact angle is only observed on a smooth surface. The contact angle observed after the liquid has spread over a rough surface can exceed the angle observed after the liquid has receded over the surface. This effect may be called *capillary hysteresis*, to differentiate it from molecular hysteresis.

2.5.2 Factors Affecting Contact Angle

There are three main features affecting the contact angle.

2.5.2.1 Greasy Layers

The contact angle can be increased by a layer of grease of no more than one molecule thick. It has been shown that (Langmuir, 1920) a glass plate brought up through a water surface covered by a monomolecular film of some fatty substance had its contact angle very much increased, compared to that of a perfectly clean plate.

2.5.2.2 Surface Roughness

The effect of surface roughness on the contact angle was discussed by

Wenzel(1936). He stated that, if the true area of a rough surface is 'n' times greater than its nominal area, the observed contact angle, θ_o, is related to the true contact angle, θ_t, which is the angle observed on a smooth surface, by the expression:

$$\cos \theta_o = n \cos \theta_t$$

where n= roughness ratio

Therefore,when the true contact angle is less than 90°, the liquid wets the solid surface. The relationship between the true contact angle and the roughness ratio, which gives an observed angle of just equal to zero, is plotted in Figure 2.9 .

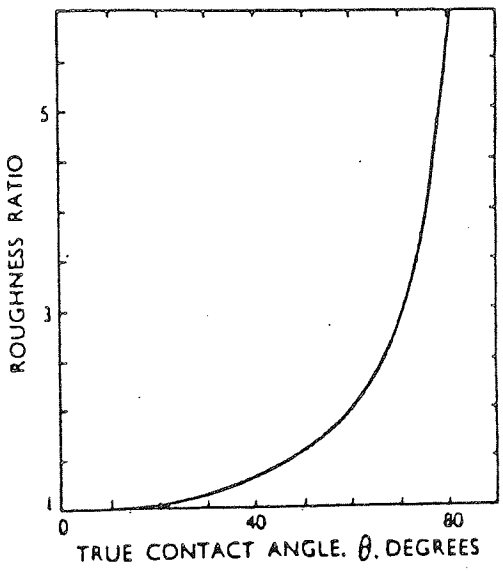

Figure 2.9 - Relationship between the true contact angle and the roughness ratio.

2.5.2.3 Moisture on the Surface

If certain substances are allowed to crystallize in contact with water, the contact angles against the water are often lower than when the crystallization takes place in air. This might be due to water molecules becoming entrapped in the surface layers of the solid and increasing the attraction between the surface and water. Such penetration into the surface layers, with consequent change in the contact angles, is

a very commonly observed phenomenon. The extent of the effect depends on the surface porosity of the solid, and also on the nature of the liquid.

2.5.3 Measurement of Contact Angle

There are two commonly used techniques for the determination of contact angle between molten metals and solid metals. The first involves allowing a drop of molten metal to spread and reach equilibrium on a solid metal, quenching and directly measuring the contact angle. This technique may result in some error due to dimensional changes on cooling and difficulty in determination of the angle exactly at the line of contact. A better method is to immerse a plate of the solid in a bath of the liquid and then tilt the plate until the liquid surface is seen by optical techniques to be perfectly in line with the plate. The inclination of the plate to the horizontal is then equal to the contact angle.

2.6 Wetting and Non-Wetting

Good wetting is important in liquid phase sintering, infiltration and brazing. Wetting is mainly a physical phenomenon but is strongly associated with a chemical reaction at the interface (Burdon, 1949), and is aided by the solubility of the solid in the liquid, formation of intermediate compounds and interdiffusion. In a typical powder metallurgy compact, a wetting liquid will attempt to occupy the lowest energy position, thus, it preferentially flows to smaller capillaries which have the highest energy per unit volume. When there is insufficient liquid to fill all the pores, the wetting liquid will attempt to pull the particles together to minimize the free energy. This effect gives rise to the rearrangement stage and rapid initial densification in liquid phase sintering (Naidich et al., 1965). The rearrangement of

particles depends on a large attraction force. This may be achieved with small particle size and small contact angle. At large contact angles, repulsive forces exist and swelling of a compact can occur on melt formation.

As previously discussed, solid is said to be perfectly wetted by a liquid, if the contact angle θ is zero. If an equilibrium is established, the relation of θ to surface tensions is given by Young's equation (Equation 2.6).

$$\cos\theta = \frac{\gamma_{SV} - \gamma_{SL}}{\gamma_{LV}}$$

Considering the powder wettability situation, if the right hand side of the equation equals or exceeds unity, liquid copper will wet the iron particles. In order to achieve this, γ_{SV} should be large, while γ_{SL} and γ_{LV} should be small. Often γ_{SL} is large in practical systems, especially where the surfaces are rough. For industrial processes such as brazing and liquid phase sintering, sufficient wetting is achieved with contact angles of less than 20°. It is clear that if θ is to be large, γ_{LV} and γ_{SL} must be large, and γ_{SV} small. In practice a contact angle of 90 degrees or greater is regarded as a sufficient criterion of non wetting, though the larger the value of θ, the less coalescence will there be of the liquid copper to the iron surface.

In the study of wetting behaviour of Fe-Cu system, factors affecting the wetting driving forces must be taken into account.

2.6.1 Wetting Driving Force

Baily and Watkins (1951-52) found that mutual solubility or formation of intermetallic compounds at the liquid-solid interface are necessary conditions for good wetting. However, Schatz (1957) attributed the driving force for wetting to the free energy of alloying. When the alloying reaction is exothermic, this theory would lead to the conclusion that, wetting may occur if a sufficiently thick layer of

alloy is formed. Later, Wassink (1967) extended the previous theories by doing his wetting experiments with either liquid copper or silver on solid iron. He stated that, if the mutual solubility between the solid and liquid was high, the interfacial tension will be low and thus solid metal will be wetted by the liquid metal. Milner (1958) suggested that, surface oxides were responsible for poor wetting. Thus, γ_{SV} is closely controlled by surface oxides. Therefore, oxides are to be removed if good wetting is required. However, Eremenko et al. (1970), reported that wetting of liquid metals on oxides increases with the oxygen affinity of the liquid metal and wettability will decrease as the oxide stability increases. They concluded that an inverse relationship exists between the contact angle and the free energy of oxide formation.

Temperature and fluxes, are two other factors affecting wetting which are discussed below.

2.6.2 Effect of Temperature

The mobility of surface atoms increases with temperature. Becker (1933) has shown this clearly by measuring the change in thermionic emission on tungsten caused by an absorbed layer of barium. The barium was deposited on one side of a flat tungsten ribbon, which was periodically heated to about one thousand degrees Kelvin, for short periods. The thermionic current was then measured. In the beginning, all the emission was from the side on which barium had been deposited. Later, the emission began and increased from the back of the ribbon until, it was finally equal to that from the front. The rate of migration of the source of emission (ie the barium atoms) from the front to the back increased with increasing temperature.

2.6.3 Effect of Fluxes

The wetting of metals has been reviewed by Daniels and Macnaughtan (1937). They state that a flux will assist the spreading of a drop of molten copper if it causes a reduction in the surface tension of the drop, and quote work by Coffmann and Parr (1927) and by Latin (1938) in which the extent to which the surface tension of a drop is reduced in various liquid fluxes was measured. Daniels and Macnaughtan, later pointed out that, joint penetration in soldering is high, if the surface tension of the liquid is high. But they found some difficulty in reconciling the facts that an effective flux promotes both spreading and joint penetration. Latin (1938), noted that around tin and solder drops which were heated in contact with copper in zinc-ammonium chloride flux, blue coloured areas were formed. He came to the conclusion that the blue colour was due to tin which had been deposited from the flux and had subsequently alloyed with the copper. He stated that this action might account for the greater spreading observed in zinc-ammonium chloride flux in comparison with that of a resin flux.

So far, we have considered the major criteria for wetting and spreading of liquid copper. We may now enter into the application of interaction of liquid copper with sintered iron compacts. Three major areas are covered namely, liquid phase sintering, infiltration and brazing.

2.7 Liquid Phase Sintering

Liquid phase sintering was defined by German (1985), as sintering involving a coexisting liquid and particulate solid during some part of the thermal cycle. The liquid may be transient or persistent during sintering, depending on the solubility

of the liquid phase in the solid.

Major advantages of liquid phase over solid phase sintering are:

1) faster sintering processes.
2) faster and more efficient atomic diffusion.
3) rapid compact densification due to the presence of a wetting liquid.
4) reduction of interparticle friction, resulting in rapid rearrangement of solid particles.
5) dissolution of sharp edges and corners on particles leading to better packing.

Bockstiegel (1962), investigated the improvement in liquid phase sintered tensile strength of iron compacts. Figure 2.10, illustrates the effect of copper additions on tensile strength and elongation. He concluded that the increase in strength was mainly due to the solution strengthening effect of copper upon ferrite and better interparticle bonding. Commonly used commercial systems involving liquid phase formation during sintering are listed in Table 2.1.

Another commercial application of liquid phase sintering is the production of self lubricating bronze bearings by sintering compacts made from a mixture of copper and tin powders. The final porosity must be controlled by proper selection of initial particle shape and size distributions, compacting pressures, sintering temperatures and the rate of heating of the compacts (Dowson, 1984).

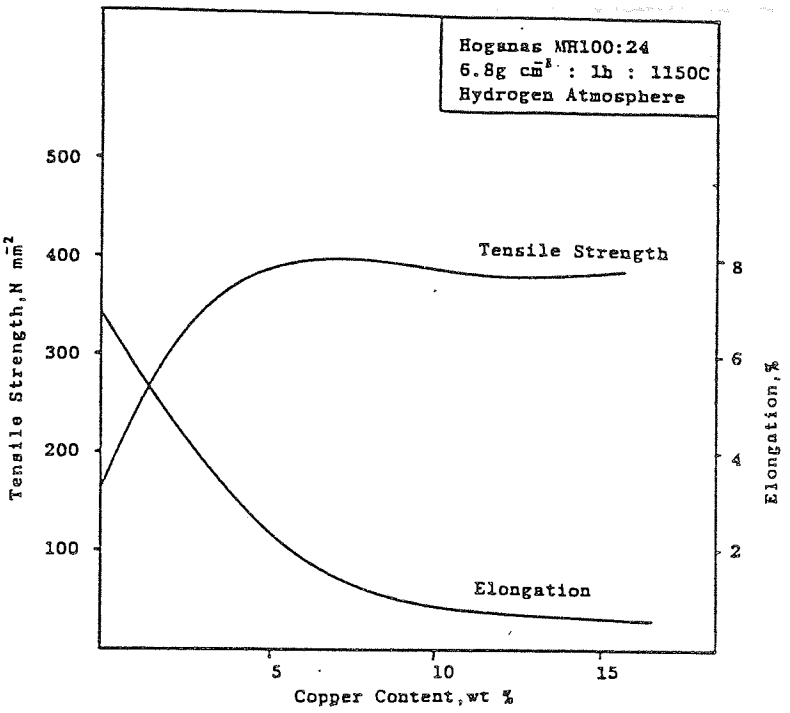

Figure 2.10 - The influence of copper on the mechanical properties of sintered iron - copper compacts.(Bockstiegel, 1962).

In liquid phase sintering, there are at least three phases present: liquid, solid and vapour. Therefore, there are several interfaces and energies associated with them. The several diffusivity, solubility and viscosity effects, together with multiple phases have made the study of the mechanisms in liquid phase sintering very difficult.

System	Application
W-Ni-Fe (Kwon etal, 1981) (Makarova etal, 1964)	radiation shields - weights
Ag-Cu-Sn-Hg (Bates and Knapton, 1977)	dental amalgam for fillings
Fe-Cu-C (German and D'Angelo, 1984) (Danninger, 1987)	structural components and gears
WC-Co (James, 1977) (Nordgren etal, 1988)	cutting and machine tools
TiC-Fe-Mo-Ni-V (Lograsso and German, 1987)	high temperature components
Cr-Co-Fe (Green and Wong, 1981)	permanent magnets

Table 2.1 - some systems involving liquid phase sintering.

2.7.1 Stages of Liquid Phase Sintering.

The first attention to liquid phase sintering was given by Price et al. (1938), and subsequently developed by Lenel (1951) and Kingery (1959). Kingery suggested three stages for sintering in the presence of a liquid phase namely: rearrangement, solution reprecipitation and solid state sintering.

2.7.1.1 Rearrangement of Particles

Figure 2.11 shows a schematic sequence of three overlapping stages of liquid phase sintering (Huppmann and Petzow, 1979: German, 1985). Initially, the mixed powders are heated to a temperature where a liquid forms. The capillary pressure will tend to slide the particles over one another, resulting in a maximum packing (Khan and Cizeron, 1984). Therefore, substantial rearrangement of the neighbouring particles can take place with an ultimate arrangement of solid particles in a way to maximize the density. The liquid phase present, wets the particles and enhances densification by drawing them together. The reduction of porosity occurs as the system minimizes its surface energy. Kingery (1959), suggested that the driving force for rearrangement is provided by the existence of pores *within* the liquid. He developed an equation to calculate this pressure in Fe-Cu compacts (Equation 2.13).

$$P = -\frac{2\sigma_{LV}}{r} \quad \ldots\ldots\ldots \quad (2.13)$$

where:

P = pressure

σ_{LV} = liquid / vapour interfacial energy

r = pore radius

Using this equation, he found that in an Fe-Cu system containing pores of 1μm diameter, a pressure of 5 MPa is exerted upon the compact. The amount of densification attained by rearrangement is dependent upon the amount of liquid, particle size and respective solubilities. Usually finer particles give better packing on rearrangement. The process of rearrangement can be inhibited by high green density or irregular particle shape. Also the particle contacts resulting from compaction form solid state bonds during heating, thereby preventing rearrangement.

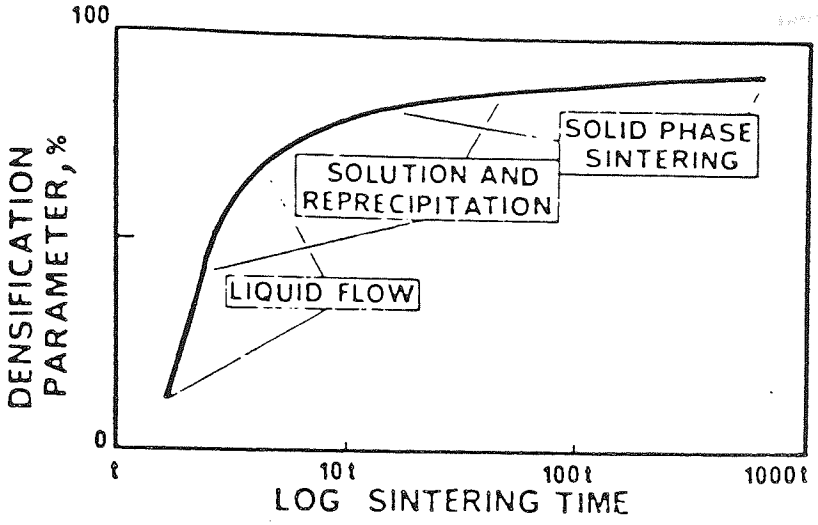

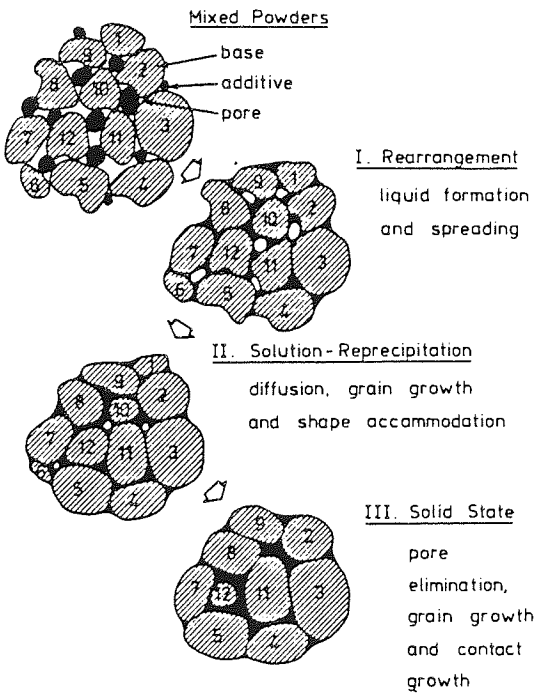

Figure 2.11 - Schematic sequence of the stages of liquid phase sintering (German, 1985)

Kingery (1959), suggested that 35% by volume of liquid was necessary to achieve full densification of the compacts provided that some mutual solubility exists between the liquid and solid. In a later work, Sebastian and Tendolkar (1979), investigated the mechanism of liquid phase sintering in the W-Cu system and showed that complete densification by rearrangement can occur in this system at a contact angle of 6 degrees. It should be noted that no solubility exists in the W-Cu system and this slowed down the rate of densification.

One of the important parameters in the rearrangement stage is the volume fraction of the liquid. At a high volume fraction, complete densification of the compact is possible by rearrangement and pore filling on liquid formation. At a low volume fraction, other processes like solution -reprecipitation must be active for full densification.

Eremenko et al. (1970), studied the insoluble systems of WC-Cu, W-Cu, and W-Ag. They demonstrated that maximum densification occurs at approximately 50 vol.% of liquid. In many practical liquid phase sintering systems, liquid quantities are kept to below 20 vol.% to avoid shape distortion of the compact during sintering.

Other important parameters are particle size and shape. The effect of particle size was investigated by Cannon and Lenel (1953) for Fe-Cu compacts. Figure 2.12, shows little densification by rearrangement was observed for the coarser particle size, while greater densification by rearrangement occurred with the finer particles. Hence, a finer particle size is beneficial for the production of high strength components. Irregular particles undergo less rearrangement due to greater friction force and greater interlocking between the particles.

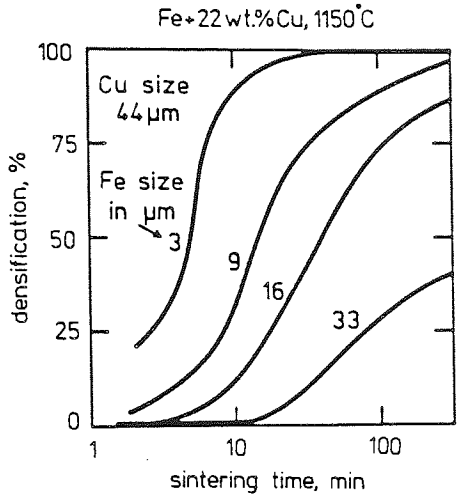

Figure 2.12 - Densification in the initial stage of liquid phase sintering for Fe-Cu compacts with various particle sizes of iron; a large iron particle eliminates rearrangement (Cannon and Lenel, 1953).

2.7.1.2 Solution and Reprecipitation.

The solution and reprecipitation process occurs concurrent to the rearrangement stage. However, the kinetics of rearrangement are initially so fast that these other events are overshadowed. As densification by rearrangement slows, solubility and diffusivity effects become dominant. It has been shown by Cannon and Lenel (1953), that dissolution and reprecipitation process occurs, provided that at least a limited solubility of the solid in the liquid phase is present. If not, this stage of densification will not occur. Densification occurs more slowly by this mechanism than by particle rearrangement, because of the dependence on atomic diffusion. The large grains assume a more regular shape, while the small ones (ie, with strongly convex curvature) disappear (Price et al., 1938), due to higher surface energy to volume ratio. Figure 2.13 shows a model of densification by this mechanism (Huppmann and Petzow, 1980).

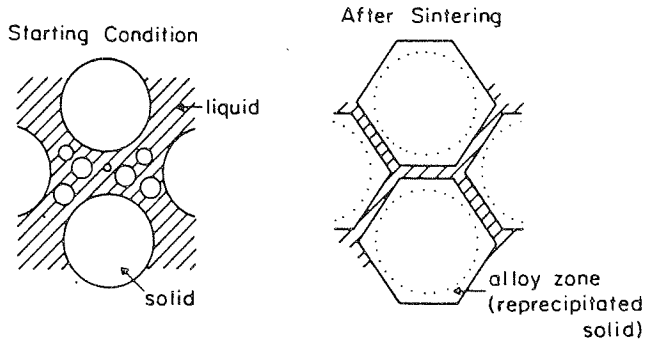

Figure 2.13 - A model of densification by solution reprecipitation, during liquid phase sintering (Huppmann and Petzow, 1980).

The driving force for material transport results from increased compressive stresses and hence from enhanced chemical activity and higher solubility in the contact zone. As a result, material is removed from the contact points. This chemical activity relationship is given by Kingery (1959) as follows:

$$\text{Ln}\frac{a}{a_o} = \frac{2KV_o\,\sigma_{LV}}{RTr} \quad \ldots\ldots (2.14)$$

where:

a = increased chemical activity.

a_o = standard chemical activity

K = pressure constant

V_o = initial volume of the compact

R = universal gas constant

T = absolute temperature

r = pore radius within the liquid

This densification mechanism causes the contact points to be flattened therefore it is

called *contact flattening*.

The localized increase in activity causes the solid substance to be carried away and precipitated again at locations of lower stresses. This results is an approach of midpoints of particles and therefore, shrinkage (Lenel, 1948). However, Huppmann and Petzow (1979), suggested that the presence of chemical concentration gradient provides a driving force, greater by a factor of two orders of magnitude, than the driving force arising from the reduction of interfacial energy. WC-Ni and WC-Cu-Ni mixtures were among the mixtures chosen for their experiments. The level of the liquid phase was kept constant at 12% by volume, which means that during sintering the content of liquid varied only slightly due to different solubilities. Microstructural changes, other than the particle flattening model of Kingery (1959), were also demonstrated.

Based on a model for sintering tungsten with nickel additions, Gessinger and Fischmeister (1972), reported that growth of the intergrain neck by diffusion through a solid diffusion path contributes to densification. The neck growth results in grain shape changes and centre to centre approach of the grains. Whalen and Humenik (1967), pointed out that contact flattening does not explain grain growth and the simultaneous decrease in the number of grains. According to Gessinger et al. (1973), often the neck growth is not obtained in systems lacking solid solubility in the liquid. Thus, solid state diffusional flow appears to be uncommon. Further, when grain growth is inhibited, there is no shape accommodation (Yoon and Huppmann, 1979). These observations support a mechanism explained by Kaysser et al. (1985), where shape accommodation takes place by dissolution of small grains and re-precipitation on large grains with little centre to centre approach. However, considering that the initial stresses at interparticle contact points are quite

large by virtue of their small size, it seems reasonable that contact flattening is initially an important mechanism for densification (Eremenko et al., 1970).

2.7.1.3 Solid State Sintering or Coalescence.

Coalescence is another name for solid state sintering. This stage of liquid phase sintering has been investigated by Makarova (1965) and later reviewed by Courtney (1977). Densification is slow in this last stage because of the existence of a solid skeleton. The rigidity of the skeleton prevents further rearrangement. The driving force of solid state sintering is provided by the tendency of the system to minimize their interface energies. Grain coalescence begins with the formation of a connecting bridge between grains of similar crystallographic orientation (Makarova et al., 1964).

German and Churn (1984), reported the final stage densification rate may be estimated from the following equation:

$$\frac{d\rho}{dt} = \left[\frac{3D\,C\,\Omega}{k\,T\,R^2}\right]\left[\frac{\xi}{(1+\xi)}\right]\left(\frac{2\gamma}{r - P_p}\right) \quad \ldots\ldots (2.15)$$

Where, ρ is fractional density, t is time, D is diffusivity of solid in liquid, C is solid concentration in liquid, Ω is atomic volume, k is Boltzmann's constant, R is solid grain size, ξ is a geometric term, γ is liquid - vapour surface energy, r is the pore radius, P_p is gas pressure in the pore.

The dimensionless geometric term, ξ, depends on grain size, pore size and number of pores per unit volume N, as follows:

$$\xi = \left[\frac{4\,\pi\,N\,R^2\,r}{3}\right] \quad \ldots\ldots \ldots\ldots \quad (2.16)$$

Because of high diffusivity through the liquid phase, densification in the final stage should be rapid as the pore size and porosity decrease. However, Kingery et al. (1961), suggested that factors such as decomposition products from the sintering component, trapped gas in the pore and reaction products involving the atmosphere, can inhibit final densification. Sintering in a non soluble atmosphere will result in a trapped gas in the pores which will inhibit densification.

German (1985), suggested three possible mechanisms of coalescence between contacting grains as shown schematically in Figure 2.14.

These mechanisms were as follows:

1- solid state diffusion by grain boundary migration.

2- grain boundary migration by diffusion across an intermediate thin liquid layer.

3- solution - reprecipitation from the small grain to the large grain.

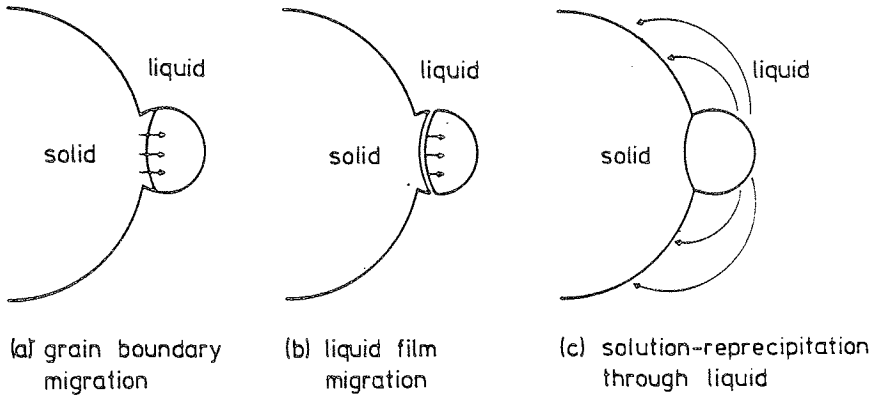

Figure 2.14 - The three possible mechanisms of coalescence between contacting grains; (a) solid state grain boundary motion (b) liquid film migration, and (c) solution reprecipitation through the liquid.

It has been claimed that solid state diffusion by grain boundary migration is the most frequently observed mechanism (Courtney and Lee, 1980). However, in most cases of solid state sintering, a co-operative solution - reprecipitation process is also necessary (German, 1985).

Finally, the three stages of liquid phase sintering may be summarised as shown in Table 2.2.

Stage	Function
1- Rearrangement	Flow of liquid metal and its penetration between interparticle contacts, repacking, rapid densification, sliding of particles.
2- Solution - reprecipitation	Shape accomodation, diffusion controlled densification, neck formation.
3- Solid state sintering or coalescence.	Neck growth, pore coarsening, grain growth, rigid structure.

Table 2.2 - Summary of the mechanisms occurring during three stages of liquid phase sintering.

2.7.2 Iron-Copper System

The iron-Copper phase diagram has been reviewed by Rivlin (1984) and its relationship to the sintering of Fe-Cu compacts has been studied by Elliot (1959). Figure 2.15, shows the Fe-Cu phase diagram. As the compact is heated to the sintering temperature, interdiffusion of iron and copper particles occurs. The intersolubilities also increase with temperature, particularly after α to γ transformation of iron. Copper melts at 1084°C but iron has been taken into solution, so melting is not complete until 1094°C is exceeded. The molten copper wets the iron particles very rapidly.

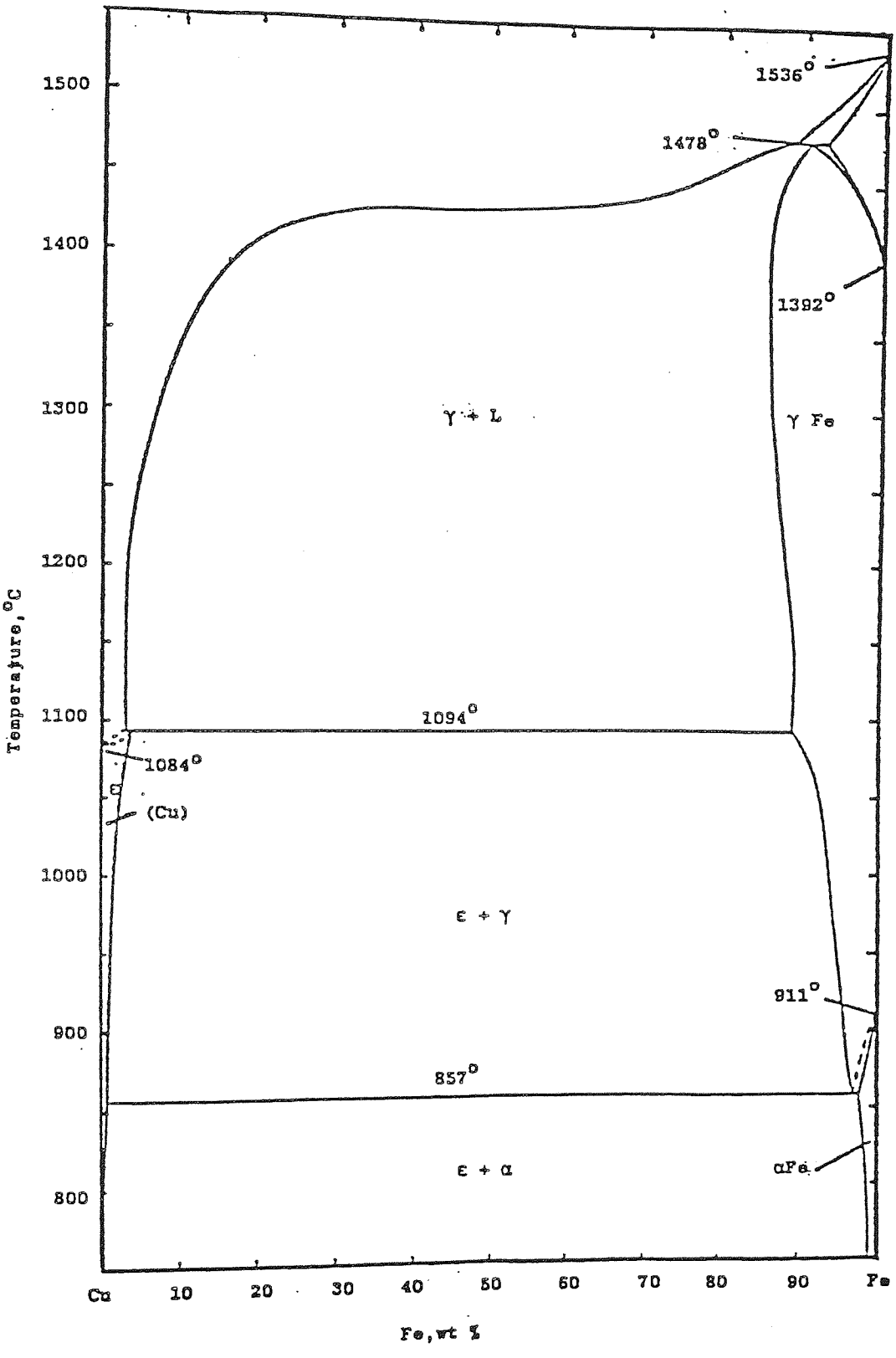

Figure 2.15 - The iron - copper equilibrium diagram (Rivlin 1984).

Rivlin (1984), stated that the maximum solubility of copper in iron is 10%, under equilibrium conditions. However, Trudel and Angers (1975), suggested that the maximum copper solubility in iron is no more than 8%. According to Berner et al.(1974) and Ohno (1973), the molten copper becomes saturated with iron within a few seconds of melting. As can be seen from the phase diagram (Figure 2.15), the intersolubilities of iron and copper are reduced upon cooling so that eventually, α+ ε (ie Fe-Cu) and ε (copper) phases are developed.

2.7.3 Precipitation Hardening

Smith et al. (1933), reviewed and investigated the precipitation hardening of copper steels. They concluded that steels containing 0.7 to 1.5% copper are capable of being hardened by precipitation, if normalized from 800°C and aged for 4 hours at 500°C, to cause precipitation of copper retained in metastable solution by normalising treatment. Based on his studies, no quenching was necessary to induce precipitation hardening. As an example of mechanical properties, Smith (1933) showed that , a steel containing 1.45% copper and 0.2% carbon had a tensile strength, hardness, and elongation of 743 MNm^{-2}, 277 HB and 23.5% respectively, in which no quenching was involved. However, Phadke and Davies (1977), suggested that quenching is necessary in order to achieve precipitation hardening effects. In the later work, alloys containing 2, 4 and 6% copper were sintered at 1150% for 1 hour, water quenched and aged at 500°C for various times. The peak hardness was less than that claimed by Smith (1933), being at 190 HB.

2.7.4 Copper Growth

Fe-Cu based materials have a technically troublesome feature in that a substantial growth referred to as "copper growth phenomenon", may take place during sintering. In practice a large dimensional change is difficult to control. As a result, it may not be possible to obtain parts having the required dimensional accuracy. Also the density of compacts pressed under high pressure drops to such a degree during sintering that the method is not used for the production of structural parts. Various attempts have been made to suppress the copper growth phenomenon, for instance, it has been proposed to attain such suppression by the addition of carbon (Trudel and Angers, 1974) or nickel (Kothari, 1967). However, an additive giving completely satisfactory results is still not found. Trudel and Angers (1974), made dilatometric studies of Fe-Cu-C compacts and reported the reduction in copper growth due to a 1.0% carbon addition. The copper content ranged from 0 to 12.8%. The experimental conditions are summarised in Table 2.3.

However, Asaka (1983), suggested that the addition of carbon has an effect "only to some extent" and that is only when the copper content is less than 5%. He reported that it was impossible to attain a desired dimensional change if copper content was more than 5%. Asaka (1983), concluded that the addition of 1.5% boron to Fe-4Cu compacts, is the most effective way to reduce the copper growth phenomenon. Boron diffuses into iron thereby preventing the diffusion of copper into the iron lattice. Further work on the Fe-Cu-C, based on dilatometric investigations are considered to be necessary.

Reference	Iron Powder	Copper Powder	Sinterung Conditions			Compaction Pressure - MPa	Carbon Addition
			Temperature(°C)	Time(min)	Atmosphere		
Trudel and Angers(1974)	Water Atomised	Electrolytic	1120	30	40% H_2 40% N_2 20% Co	618	1 wt% graphite
Trudel and Angers(1975)	Water Atomised Atomet 28	Amax HB	1120	30	Same as Above	650	–
Dautzenburg and Dorweiller(1985)	Not Given	Not Given	1120	20	Not Given	Not Given	0 - 1.2wt.%
Bockstiegel (1959)	Reduced Sponge	Electrolytic	1150	60	Gettering Technique	Not Available	1 wt.% graphite

Table 2.3 - Experimental Data Relating to Trudel & Angers (1974, 1975), Dautzenberg and Dorweiller (1985) and Bockstiegel (1959).

2.7.5 Iron-Copper-Carbon System.

The ternary Fe-Cu-C phase diagram for the portion of the diagram representing the state of alloys containing less than 30% copper was investigated by Ishiwara et al. (1929). Later Parameswaren et al. (1979), investigated the Fe-Cu-C ternary diagram for the region 950 to 1500°C and developed refined methods of thermal analysis to obtain accurate data for the invariant temperatures of the stable system. It is agreed that at a typical sintering temperature of 1120°C, carbon decreases the solubility of copper in γFe. However, the effect is very small as shown in Figure 2.16.

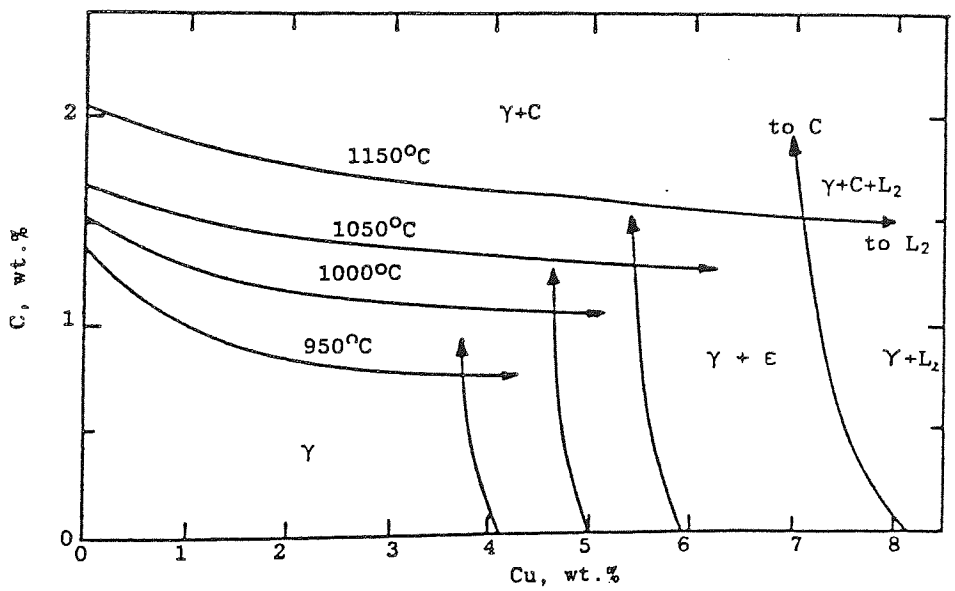

Figure 2.16 - Iron rich corner of the Fe-Cu-C ternary equilibrium diagram at 950, 1000, 1050 and 1150°C (Parameswaren, 1979).

2.7.5.1 Carbon Solution in Iron

Trudel and Angers (1974), suggested that carbon solution in γFe continues during isothermal sintering at 1120°C and is complete within $1/_2$ hour. Dautzenberg and Dorweiller (1985), reported that when heating up from room temperature, the carbon solution was complete prior to reaching the melting point of copper. Hansen and Anderko (1958), reported that the copper solubility for carbon is 0.00015 wt % at 1300°C. This amount of solubility is negligible, therefore copper should have little effect upon the amount of carbon available to diffuse into iron.

During cooling, similar precipitation effects to those mentioned for Fe-Cu phase diagram occur. However, at around 720°C the (γFe) to (α-Fe_3C) eutectoidal reaction occurs, the amount of pearlite being proportional to the carbon level. The final microstructure consists of grains of Fe-Cu solid solution and pearlite, surrounded by the copper rich ε phase.

In commercially sintered Fe-Cu-C compacts, evidence of a ternary liquid phase is not usually observed, although Bockstiegel (1959), suggested that an iron rich ternary eutectic liquid phase is formed, which improves densification of Fe-Cu-C compacts. Majima and Mitani (1977), produced differential thermal analysis data and metallographic evidence to support the existence of a ternary liquid phase during sintering. However, Parameswaren (1979), could find no such phase in his study of phase equillibria in Fe-Cu-C alloys.

2.7.5.2 Carbon Absorption Mechanisms.

There are two theories concerning carbon transfer and absorption. One is that carbon is directly transferred by diffusion through the contacts between iron and graphite (Dautzenberg, 1977) and (Pozdnyak, 1963).

The other theory is that (Gummeson, 1968) and (Gummeson and Stosuy, 1967) the transfer of carbon takes place through the formation of a gas phases in the

following stages:

a) Carbon oxidation, giving carbon monoxide.

$$C + \frac{1}{2} O_2 = CO \quad \text{.....(2.17)}$$

b) Adsorption of carbon monoxide on the iron surface.

c) Catalytic cracking of carbon monoxide at the iron surface.

$$2\,CO = CO_2 + C \quad \text{..... (2.18)}$$

d) Diffusion of the nascent carbon atom into the iron lattice.

e) Regeneration of carbon monoxide.

$$CO_2 + C = 2CO \quad \text{..... (2.19)}$$

The above reactions continue until carbon (which may be in the form of graphite) is exhausted or the matrix is saturated. However, Banerjee and Mukunda (1984), based on sintering experiments in hydrogen and vacuum with compacts of different densities and permeabilities, concluded that the existing theories were not adequate to explain the transfer mechanism of graphite in iron compacts. Instead they suggested in their next paper (Banerjee and Mukunda, 1984), that carbon transfer from graphite takes place through interparticle contact areas, after the absorbed oxygen from graphite particle surfaces has been removed. The chemisorbed oxygen is almost completely removed in the form of CO and CO_2 when graphite is heated in vacuum at temperature between 800 and 1300°C. During heating, stable equilibrium conditions hold, excess carbon is then present as graphite. However, upon cooling metastable equilibrium conditions exist, due to greater tendency for cementite nucleation rather than graphite. Finally therefore, at room temperature, the microstructure of an Fe-Cu-C compact, consists of Fe_3C either as pearlite or as boundary cementite depending upon the initial graphite addition.

2.7.6 Effect of Carbon upon Strength of Iron Compacts.

It is clear that carbon additions increase the sintered strength of Fe compacts. Squire (1974), studied the effect of different size of graphite particles upon tensile strength of iron compacts (Figure 2.17). Finer graphite particles provided better strengthening effect and homogeneity.

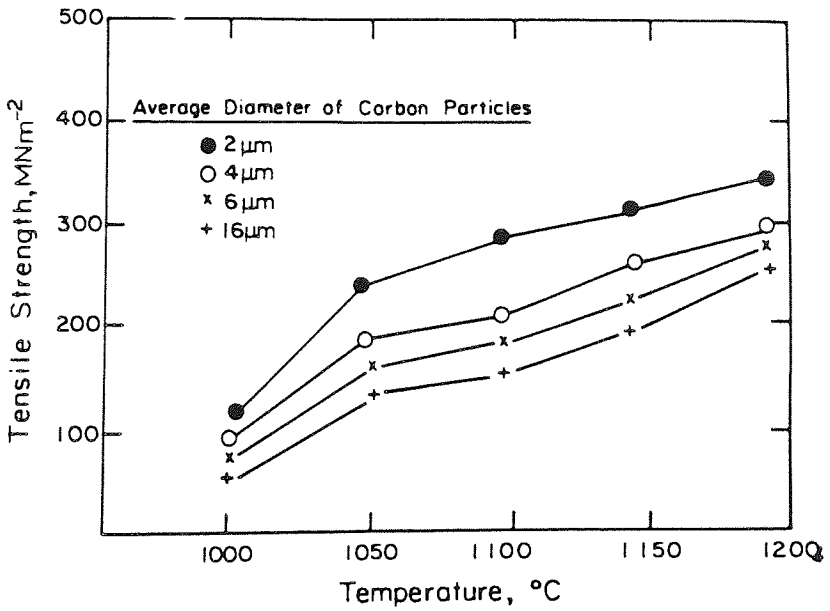

Figure 2.17 - Effect of sintering temperature for 1 hour on strength of sintered Fe-C powder mixture; C was added at various particle sizes at 1% concentration. These data illustrate benefits from homogeneous additions of sintering enhancers (Squire, 1974).

Squire's experiments were based on 1.0wt.% graphite additions and sintering was performed in the austinitic region (1200°C max). Other researchers (Cambel and Lund, 1974), suggested that sintering above the solidus temperature was more beneficial. Sintered densities of 91% of the theoretical maximum were claimed when sintering loose Fe-0.95 wt.% C powders for 1 minute at 1425°C. Compact distortion occurred at this temperatures, as would be expected with the large volume

of liquid present. Only limited mechanical property evaluation is given by the authors. The effect of carbon addition on sintering characteristics and microstructure of high speed steel was studied by Maulik and Price (1987). Addition of 0.1% carbon shifted the effective sintering temperature from 1260 to 1230°C. Densities of the order of 99% were achieved after cold compaction and vacuum sintering of annealed, atomised powders.

2.7.7 Dihedral Angle

Dihedral angle, is the angle which exists at the junction of a liquid phase and a grain boundary (Figure 2.18).

The relationship between the grain boundary interfacial energy, solid / liquid interfacial energy and dihedral angle has been studied by Smith (1948). He suggested that if the two interphase boundaries are not subject to crystallographic influences (ie $\gamma_{S_1L} = \gamma_{S_2L} = \gamma_{SL}$), then:

$$\gamma_{gb} = 2\,\gamma_{SL}\cos\left(\frac{\phi}{2}\right) \quad \ldots\ldots \quad (2.20)$$

where:

γ_{gb} = grain boundary interfacial tension

γ_{SL} = solid/ liquid interfacial tension

ϕ = dihedral angle

An alternative derivation of the above equation can be obtained by summing the horizontal components in Figure 2.18. At equilibrium, the sum will equal zero. Figure 2.19 shows some examples of the manifestation of different dihedral angles. The liquid phase assumes different shapes for different angles.

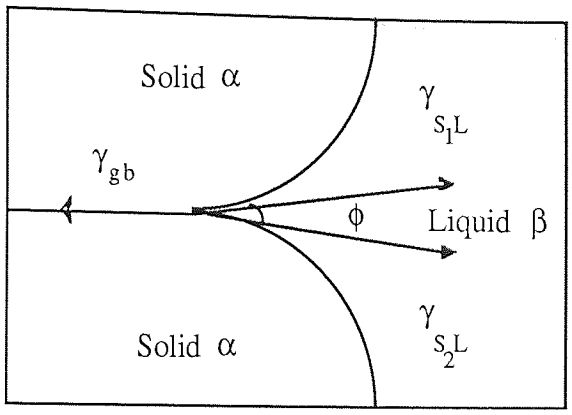

Figure 2.18 - Dihedral angle and surface energy equilibrium between two intersecting grains (α), with a partially penetrating liquid phase (β).

2.7.7.1 Measurement of Dihedral Angle.

If a section of a sintered compact is prepared for metallographic examination, dihedral angles could be measured. However, the dihedral angle may not be simply measured on a two dimensional micrograph.

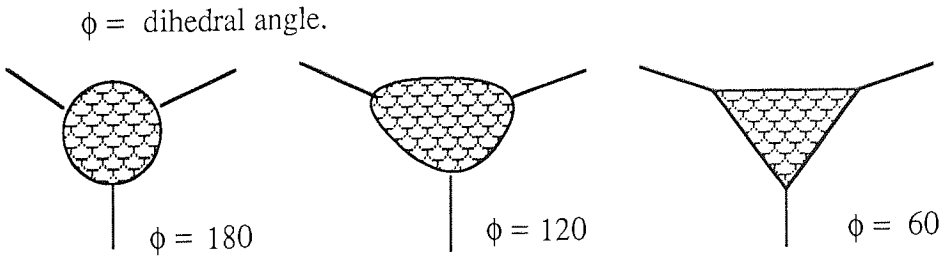

Figure 2.19 - The effect of dihedral angle on the liquid shape at the intersection of three solid grains.

The metallographic microspecimen is a plane section cut at random through a three dimensional structure, and that an angle between two planes may appear on this section as any value between 0° and 180°, though with greatly differing probabilities. Jamil and Chadwick (1985), reported that the most frequent angle

may be taken as being the true dihedral angle. However, Harker and Parker (1945), claimed that this method is correct, only if the true dihedral angle is around 120°. The angle at any intersecting plane can be calculated by the formula given by Harker and Parker (1945), as follows:

$$\text{Tan } \alpha = \frac{2 \text{ Sin}\phi \text{ Cos}\beta}{\text{Sin}^2\beta \, (\text{Cos } 2\eta - \text{Cos } \phi) + 2 \text{ Cos}\phi} \quad \ldots\ldots(2.21)$$

where: ϕ = true dihedral angle

α = observed angle

η and β = solid polar coordinates

Riegger and Van Vlack (1960), used Harker and Parker's equation and showed that the mean dihedral angle as measured on two dimensional sections is the best estimate of the true angle, with a typical error of ±5°. The statistical accuracy of the dihedral angles produced is illustrated in Figure 2.20. These curves suggest that at least 100 observed angles are needed in order to establish 95% confidence in the accuracy of the measurements.

2.7.7.2 Factors Affecting Dihedral Angle.

Densification in liquid phase sintering depends on both the contact angle and the dihedral angle, they in turn depend on the interfacial energies within the system. In reality, these energies change during solution-reprecipitation and up to the solubility limit. The dissolution reaction decreases the solid / liquid interfacial energy. This behaviour is predicted by the model of Aksay et al. (1974).

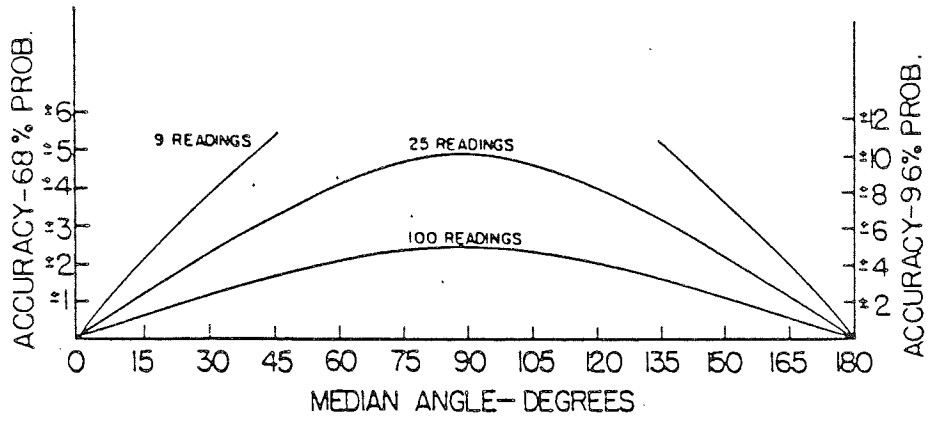

Figure 2.20 - Statistical accuracy of random dihedral angle measurements (Riegger and Van Vlack, 1960).

Sintering temperature, time and atmosphere together with the presence of alloying elements and contaminants would certainly affect the dihedral angle of the system. The equilibrium interfacial energy and dihedral angle is approached on completion of the densification mechanisms and solubility limits during liquid phase sintering. The interfacial energies of Fe and Fe-Cu compacts have been studied by several researchers (Roth, 1975: Hondros, 1965: Van Vlack, 1951: Hough and Rolls, 1971). The values of interfacial energies obtained by various test methods are shown in Table 2.4.

Material	Measuring Temperature	Measuring Method	γ mJm^{-2}	Reference
Fe in Argon	1480	-	985	Roth (1975)
Fe in Hydrogen	1480	-	860	Roth (1975)
Fe in Argon-10% H_2 (1)	1450	Z.C	795	Hondros (1965)
Fe in Hydrogen (2)	1105	D.A	850	Van Vlack (1951)
Fe-Cu in Argon (3)	1100	S.D	444	Hough and Rolls (1971)
Fe-Cu in Argon (3)	1130	D.A	444	Hough and Rolls (1971)
Fe-Cu in Argon (4)	1100	S.D	387	Hough and Rolls (1971)
Fe-Cu in Argon (4)	1130	S.D	301	Hough and Rolls (1971)
Fe-Cu in Nitrogen (2)	1105	D.A	430	Van Vlack (1951)

(1) contaminated
(2) Fe is saturated with Cu & S
(3) Fe is saturated with Cu
(4) Fe is saturated with Cu. The authors calculated γ_{SL} with $\gamma_{SV} = 1970$ mJm^{-2} as value of Fe wetting experiment.

S.D = sessile drop
Z.C = zero creep
D.A = dihedral angle
γ_{SV} = specific interfacial energy of solid / vapour.

Table 2.4 - Interfacial Energies of Iron and Copper.

2.7.8 Mechanism of Dimensional Change.

One of the first published papers concerning dimensional changes of iron-copper compacts was written by Gummeson and Forss (1955). Since then, many papers have been written on this subject. Krantz (1969) and Elliot (1959) have reported that copper growth increased with the amount of copper added. This is clearly shown in Figure 2.21.

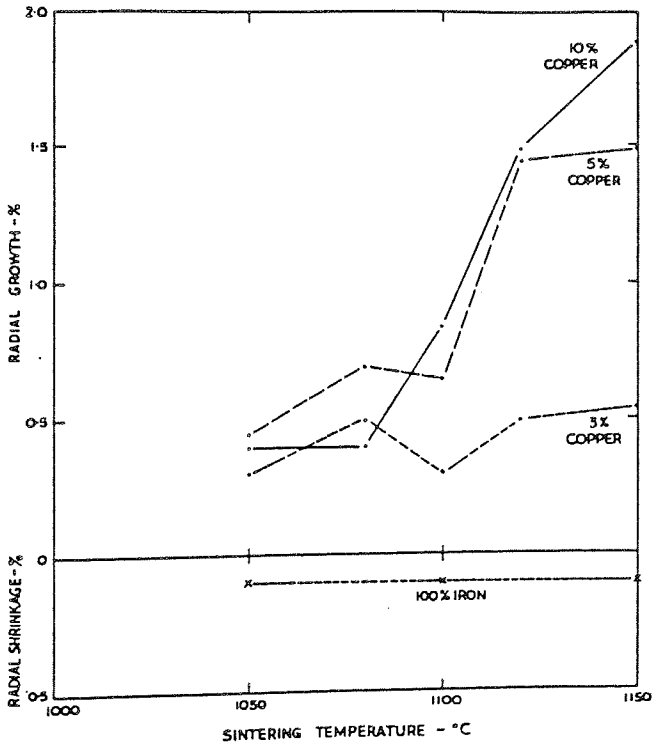

Figure 2.21 - Sintering temperature versus growth of Fe-Cu compacts with a sintering time of 15 minutes (Elliot, 1959).

Bockstiegel (1959), showed that at copper levels greater than the solubility limit of copper in iron (ie ~8%), an excess of liquid phase is present during the sintering

process. The presence of this liquid phase allows solution-precipitation processes to operate which causes shrinkage during liquid phase sintering. In a further work, Bockstiegel (1962), suggested that the observed volume increases during sintering of Fe-Cu compacts was due to diffusion of copper into iron lattice. However, Berner et al. (1974) and Phadke and Davies (1977) demonstrated that swelling above the melting point of copper could not be explained by diffusion alone. They attributed the dimensional change to penetration of liquid copper along the grain boundaries of the solid iron particles.

Berner et al. (1974) also claimed that several other processes contribute to dimensional changes during the sintering cycle. These process are listed as follows:

1- Shrinkage due to solid state sintering of iron particles during the heating cycle and at areas not penetrated by copper rich liquid phase during the isothermal sintering.

2- Expansion due to volume diffusion of copper into the iron lattice.

3- Expansion due to the flow of liquid copper into γFe interparticle regions.

4- Shrinkage due to sintering mechanisms.

At present, the above points are still considered to be the major factors which affect the copper growth phenomenon. However, it is not yet well established which process is the rate controlling factor and contributes most to swelling.

Krantz (1969), reported that the grain boundary diffusion is most likely to be the rate controlling factor of copper growth, since it is ~10^5 times faster than volume diffusion. The exact contribution of liquid flow and diffusion of copper into iron has been a matter of controversy. A recent work has been by Kaysser et al. (1980), who carried out their experiments on iron and copper spheres. They itemized the contributions to dimensional changes into four main groups. Copper penetration

into iron interparticle contacts, and into the grain boundaries, copper diffusion into iron at interparticle contact sites and via the grain boundaries. These mechanisms of copper growth are illustrated by a model which is shown in Figure 2.22.

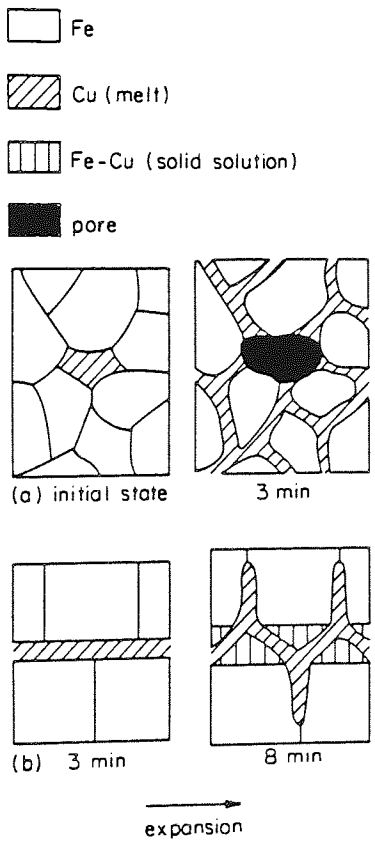

Figure 2.22 - Two mechanisms of swelling in Fe-Cu system. Swelling occurs because of; (a) particle separation and (b) grain boundary penetration (Kaysser et al., 1980).

2.7.8.1 Penetration of Iron into Iron Particle Contacts

As soon as copper melts, it fills the gaps between iron particle contacts. This provides for the rearrangement of the solid particles and an overall change in the structure of iron skeleton. This has also been confirmed in 1973 by Ohno, during his experiments on a rotating iron bar in liquid copper.

2.7.8.2 Penetration into Grain Boundary.

Penetration of liquid copper into the grain boundaries is a slow process, therefore it is more likely to occur for sintering times greater than 5 minutes. It has been shown by Smith (1948) that, for a liquid to penetrate a grain boundary, the following relationship must be satisfied:

$$\gamma_{gb} > 2\gamma_{SL} \ldots\ldots (2.22)$$

Which means that, the grain boundary interfacial energy must be more than twice the solid / liquid interfacial energy for complete wetting of the grain boundary. This will be described in more detail later.

2.7.8.3 Diffusion of Cu into Fe.

This is the slowest of the mechanisms, and is dependent on a number of variables. The volume of iron particles increase with diffusion of copper . The solid / liquid interfaces move in the direction of the movement of the melt during the diffusion process. Shewmon (1963), suggested that this movement can be calculated from the following equation:

$$\Delta l = \frac{S}{100}\left[1 - \text{erf}\left(\frac{1}{2D_V t_s}\right)\right] dl \quad .....(2.23)$$

where:

S = solubility of copper in Fe

D_V = volume diffusion coefficient

t_s = sintering time

Δl = change in thickness of the interface

dl = change in the length of the interface

Kaysser et al. (1980), suggested that if the average thickness of the liquid layers

between the iron interparticle contact area is not changed by the diffusion process, the volume change of Fe-Cu compacts may be derived from the equation:

$$\frac{\Delta V}{V_0} = S_V \times \Delta l\ (t_s) \times 100 \ldots\ldots (2.24)$$

Where S_V is the specific surface area of iron particles. Since diffusion is very slow process, it is significant at long sintering time of 60 minutes or more. A typical industrial sintering time for iron base components is 20-30 minutes.

The work of Kaysser et al. (1980) indicates that both liquid penetration and volume diffusion of copper play a significant roll in the overall growth. However, it has been reported that (Bozhko, 1968), stresses produced during a welding operation can affect the diffusion of molten copper into iron. Stresses are caused by thermal gradients imposed during welding a steel specimen. When the specimen is immersed in molten copper, the diffusion of molten copper in the steel is considerably increased. Phadke and Davies (1977), reported similar views to that of Kaysser et al. (1980), but concluded that the penetration into the grain boundaries has the highest contribution to the copper growth phenomenon.

2.7.9 Effect of Carbon upon Copper Solubility and Wetting.

Gummeson and Forss (1955), reported that carbon lowered the growth of Fe-Cu compacts by reducing the solubility of copper in iron. They also concluded that volume diffusion of copper into iron is the major cause of the overall expansion. In contrast, the Fe-Cu-C phase diagram constructed by Ishiwara et al. (1926), showed carbon to have a negligible effect of the solubility of copper in iron. The results of another work by Bockstiegel (1959), suggested that shrinkage by liquid phase sintering mechanisms, is induced by the formation of an iron rich ternary eutectic.

The wetting behaviour of copper has been investigated by several workers.

On the basis of EPMA studies, Dautzenberg and Dorwellier (1985), concluded that carbon has no effect upon the wetting behaviour of a copper rich liquid phase on iron. However, on the basis of dihedral angle measurements, Berner, Exner and Petzow (1974), reported that carbon reduces the wetting of iron particles by liquid copper. It is clear that more work on the effect of carbon upon wetting and solubility effects when liquid copper is in contact with iron needs to be done.

2.7.10 Effect of Carbon upon Dihedral Angle.

It has been reported that the dihedral angle of copper on iron is greatly influenced by carbon additions to Fe-Cu compacts. Jamil and Chadwick (1985), reported that carbon additions to Fe-10 Cu compacts, progressively increased the dihedral angle. Berner et al. (1974), on the basis of sintering Fe-8 Cu-C compacts, showed that for a range of carbon of 0-1.2 wt.%, the most frequently observed dihedral angle increased from 20° to 45° as can be seen in Figure 2.23.

This leads to reduction in growth of the compacts as solution-precipitation mechanism is accelerated. Temperature dependency of the dihedral angle was also shown by Berner et al. (1974) and a minimum dihedral angle was reported to occur at 1150°C.

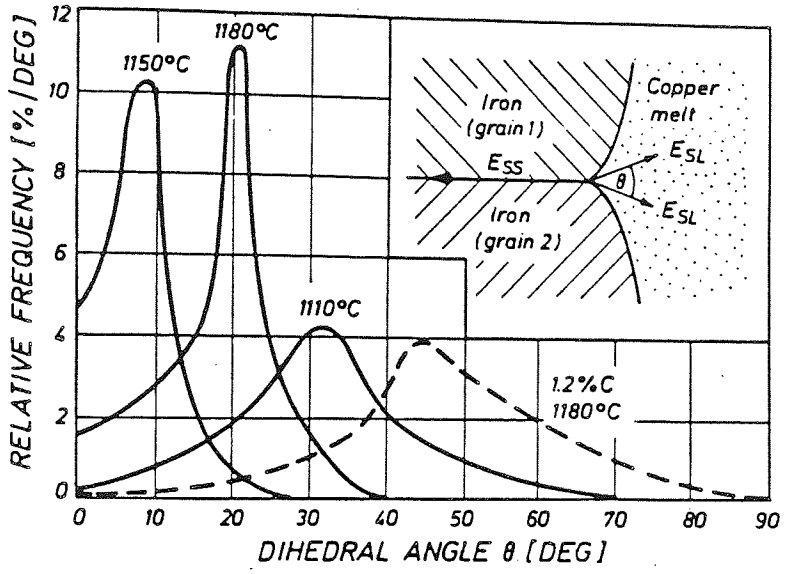

Figure 2.23 - Frequency distribution of planar dihedral angles in Fe-Cu and Fe-Cu-C compacts (Berner et al., 1974).

However, Hough and Rolls (1971) and Van Vlack (1951), measured the dihedral angles at different sintering temperatures, but did not find the temperature dependency of the dihedral angle. The comparison of their results in Fe-Cu system is shown in Figure 2.24. Berner et al. (1974), concluded that maximum swelling occurred around 1150°C where the dihedral angle was at its minimum value.

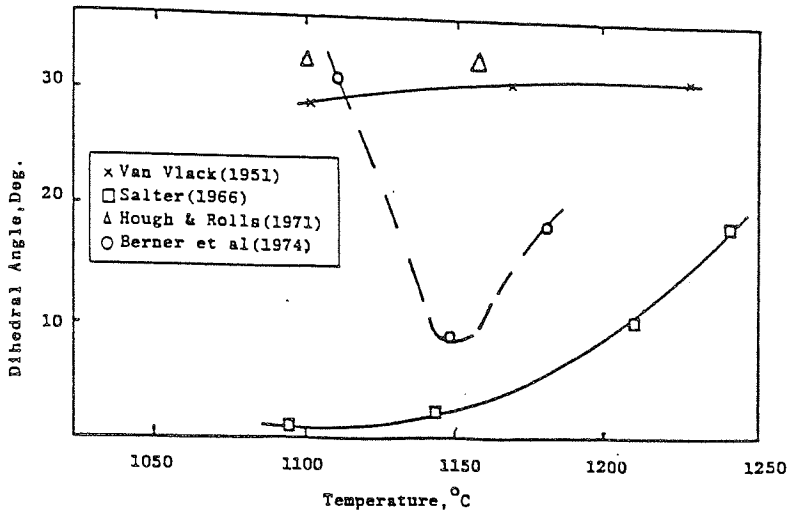

Figure 2.24 - Comparison of reported values of dihedral angle in Fe-Cu system.

Jamil and Chadwick (1985), carried out their experiments on three types of iron powder with different compressibilities and specific surface areas. Carbon was admixed in the form of fine synthetic graphite. They suggested that the iron powder with greatest specific surface area (ie Pyron iron), performed greatest shrinkage, when sintered at 1140°C in the presence of different levels of carbon additions. This is shown in Figure 2.25 and the experimental conditions are listed in Table 2.5.

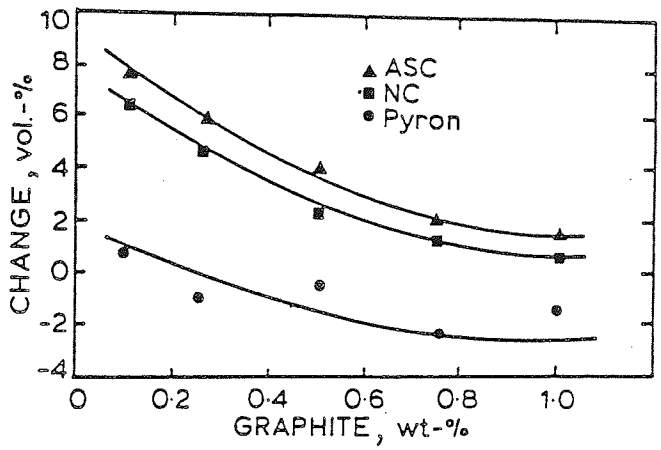

Figure 2.25 - Percentage volume change versus graphite content of sintered compacts pressed at 283 MNm^{-2}, before sintering at 1140°C for 60 minutes (Jamil and Chadwick, 1985).

Reference	Iron Powder	Copper Powder	Sinterung Conditions			Compaction Pressure MPa	Carbon Addition
			Temperature(°C)	Time(min)	Atmosphere		
Majima and Mitani (1977)	Electrolytic	Electrolytic	1150	60	Vacuum	588	1 wt. % graphite
Krantz (1969)	Domtar MP 32A	Amax HB	1120	30	40% H_2 40% N_2 20% CO	800	–
Berner, Exner Petzow (1974)	a)Air Atomized b)Water Atomized	a)Electrolytic b)Atomised	1100 -1180	180	80% N_2 20% H_2	Not Given	1.2 wt.% graphite
Jamil and Chadwick (1985)	a)ASC100 b)NC100 c)Pyron	99.2% Pure Electrolytic	1140	60	95% N_2 5% H_2	140 - 680	0 - 1 wt.% graphite

Table 2.5 - Experimental Data Relating to Majima & Mitani (1977), Krantz (1969), Berner et al. (1974), Jamil & Chadwick (1985).

2.7.11 Dilatometric Studies

Dilatometers were originally developed for obtaining the coefficients of thermal expansion of metals and materials. Today, dilatometers play a variety of roles in material characterization, particularly important in the investigation of sintering processes in powder metallurgy. The following are some examples of the areas in which they can be used:

1- Compacting pressure determination for minimum shrinkage during sintering. (high precision components).

2- Sintering temperature determination for maximum part strength without densification. (bearings and filters).

3- Determination of minimum temperature for a desired density. (for economic reasons).

4- Continuous monitoring of melt formation, phases and dimensional changes during liquid phase sintering.

Dautzenberg and Dorweiller (1985), Trudel and Angers (1974), Majima and Mitani (1977), have investigated the dilatometric behaviour of Fe-Cu and Fe-Cu-C compacts (see Tables, 2.3 and 2.5 for details of the experimental conditions).

Figure 2.26, shows the dilatometric curves for Fe-Cu compacts produced by Trudel and Angers (1975). When the melting point of copper was reached the compacts expanded, an effect which became more pronounced with higher copper contents. Figure 2.27 shows the dilatometric curves of Fe and Fe-C compacts. Trudel and Angers (1974), reported that this expansion is due to carbon solution into γFe.

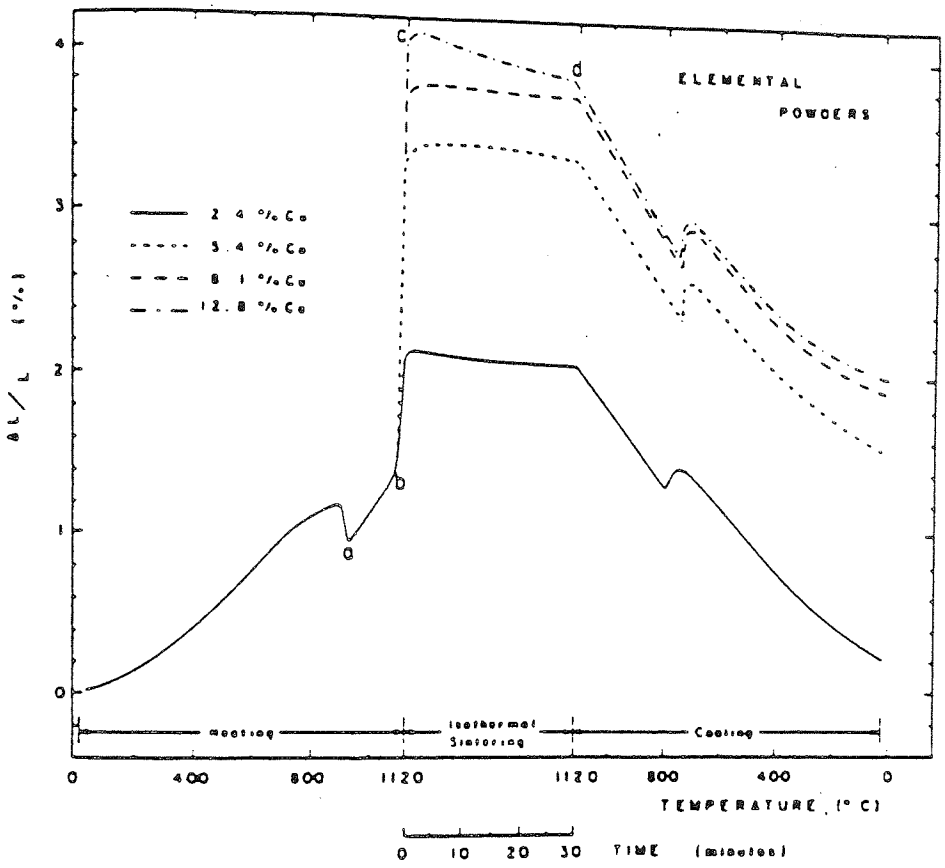

Figure 2.26 - Dilatometric curves of compacts made from elemental Fe-Cu powder (Trudel and Angers, 1975).

Furthermore, comparison shows an overall shrinkage effect of carbon. Mead and Brichenall (1956), claimed that self diffusion coefficient of γFe increases as the carbon content is increased from 0 to 1.0 wt.%. It then appears that self diffusion may play an important role in the overall shrinkage of carbon containing compacts. Trudel and Angers (1974), suggested that grain boundary pinning action is the major factor in the shrinkage enhancement.

Figure 2.28, shows the dilatometric curves for Fe-Cu-C compacts. If this Figure is compared to Figure 2.26, a reduction in growth is clearly observed. Based on EPMA studies, Trudel and Angers (1974) showed that liquid copper did not penetrate the iron grain boundaries in the presence of carbon.

Another set of dilatometric curves showing different effects to those of Trudel and Angers (1974 and 1975), were produced by Dautzenberg and Dorweiller (1985). Figure 2.29 shows, the expansion of the γ iron lattice of the Fe-C compact, as being due to carbon absorption. The maximum expansion occurred at the end of heating the Fe-1.2%C compact is less than the expansion reported by Trudel and Angers (1974), for Fe-1.0%C compact.

Figure 2.30, illustrates dilatometric curves for Fe-Cu-C compacts produced by Dautzenberg and Dorweiller (1985). It reveals that at low carbon additions the copper growth makes a more pronounced addition to the expansion due to carbon absorption than is shown by the results of Trudel and Angers (1974) (Figure 2.28). Overall expansion is greatly reduced at high carbon contents. Moreover, the dilatometric curves of Fe-1.2C and Fe-5Cu-1.2C are almost identical. A change in the sintering mode during isothermal sintering was observed by Dautzenberg and Dorweiller. Such a change was not observed by Trudel and Angers (1974).

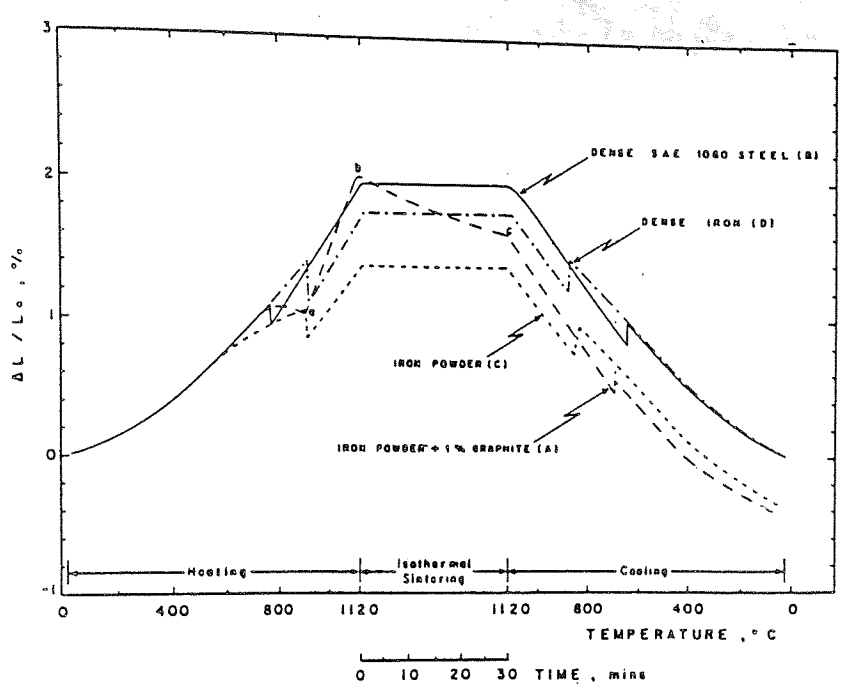

Figure 2.27 - Dilatometric curves of dense iron, dense SAE1080 steel and compacts made of iron powder mixed with 1% graphite. Sintering atmosphere was a mixture of 40% H_2 , 40% N_2 and 20% CO. (Trudel and Angers, 1974).

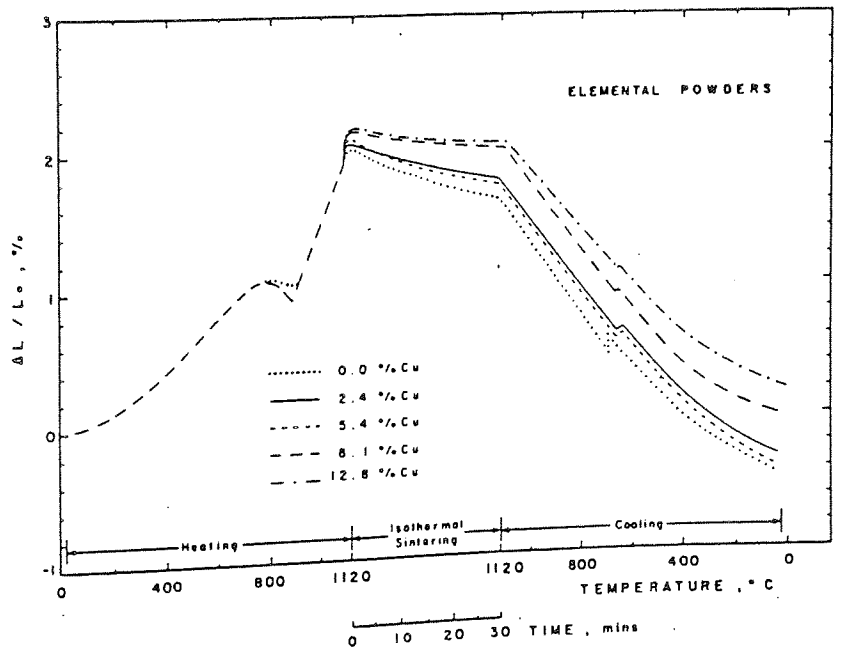

Figure 2.28 - Dilatometric curves corresponding to sintering of compacts of iron powder mixed with various additions of copper and 1% graphite, sintered in a mixture of 40% H_2 , 40% N_2 and 20% CO. (Trudel and Angers, 1974).

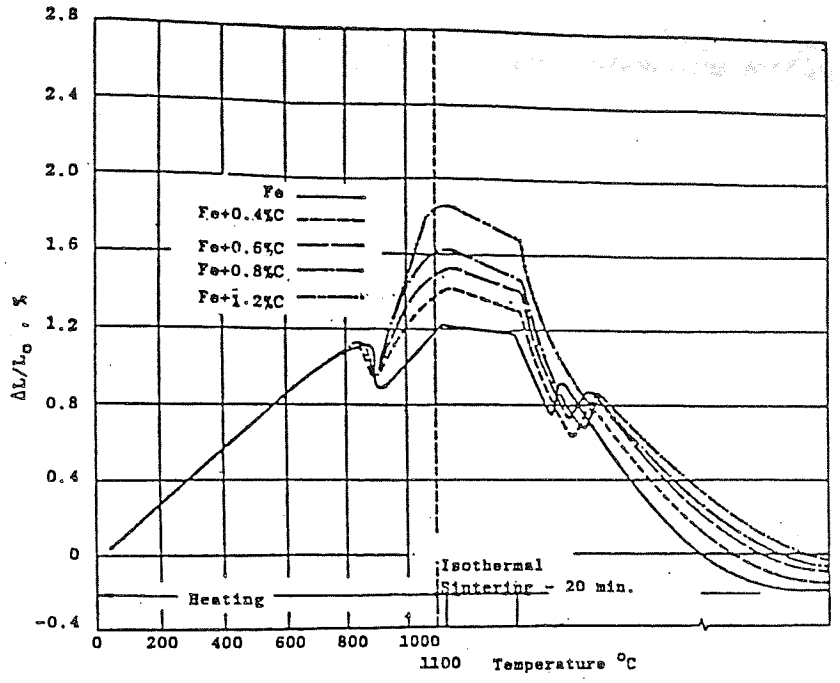

Figure 2.29 - Dilatometric curves of Fe-C compacts (Dautzenberg and Dorweiller, 1985).

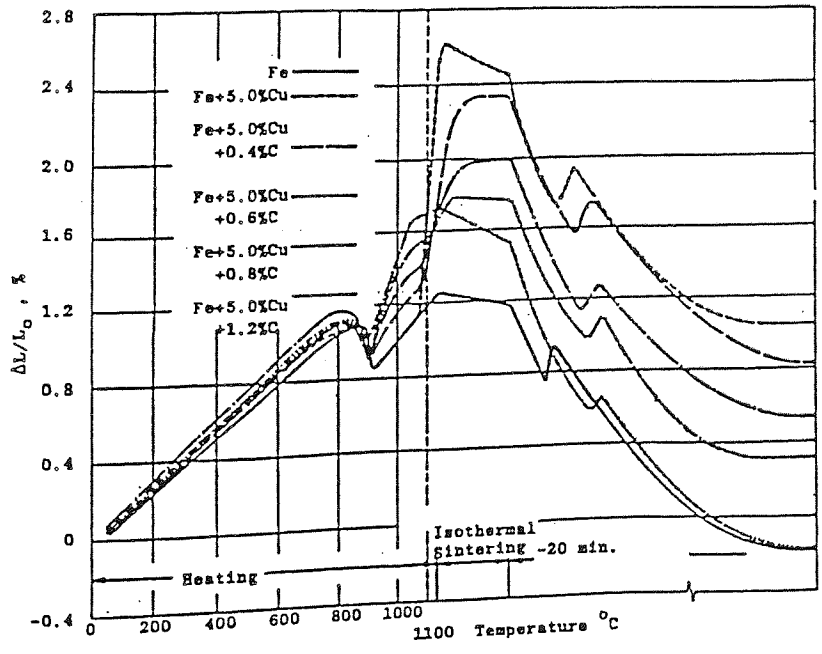

Figure 2.30 - Dilatometric curves of Fe-Cu-C compacts (Dautzenberg and Dorweiller, 1985).

It can be seen from the above two studies that there remains some conflict regarding the mechanisms affecting dimensional changes during the sintering cycle of Fe-Cu-C compacts. Further work in this matter is considered to be necessary.

2.8 Infiltration

Copper infiltration of iron compacts during sintering has been in use for about forty years. Over the years, many researchers [(Veidis, 1976), (Rennhack, 1961), (Snape, 1974)], have studied the effect of copper infiltration and have shown that it considerably improves hardness, electrical conductivity, machinability, yield and impact strength, by complete filling of the pores. Figure 2.31, shows the sequence in an infiltration process.

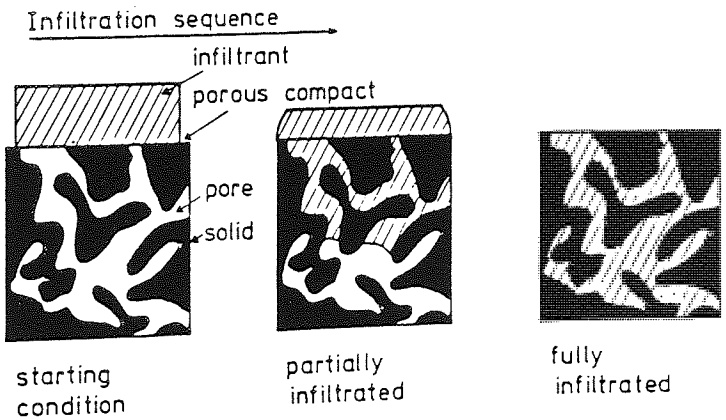

Figure 2.31 - A view of the infiltration sequence where a molten metal forms on the surface of a porous compact and fills the pores based on capillarity (German, 1985).

Penetration of the liquid into the pore relies on gravity and capillary action. A liquid with a low contact angle is drawn into the open pore structure of the compact. Usually, the liquid is formed from a solid preform or paste which is melted on the surface of the compacted skeleton. One of the earliest publications appears to be that of Schwarzkopf (1954). He suggested two types of systems relative to infiltration:

Type A- System of metals that are insoluble in each other at infiltration and room temperature. (eg, W-Cu or W-Ag). Materials of this type combine the wear resistance characteristics of the higher melting point element, with the good electrical conductivity and ductility of the lower melting point element. Uses are for heavy duty contact materials. To preserve the favorable characteristics of the components, it is necessary that no alloying takes place.

Type B- Systems of metals that exhibit partial solubility at infiltration temperature. (eg, Fe-Cu or WC-Co). Materials of this type interact at the infiltration temperature, thereby increase the strength and toughness of a structural sintered component. Mechanism of strengthening is by partial solubility of the higher melting point component (Fe) into the lower melting point component (Cu) (Schwarzkopf, 1954).

Shaler (1965), investigated the infiltration process of type B above, and established the requirements of a successful infiltration.

2.8.1 Basic Requirements of Infiltration.

Shaler (1965), suggested that the following conditions must be met for effective infiltration:

1- Reaction between solid and liquid should be such that an alloy of a greater specific volume than their combined pre-infiltration specific volume is not formed, otherwise the alloy may block the capillarities and prevent further infiltration.

2- During solidification of the liquid metal, the volume changes should not result in the formation of excessive porosity. This would result in reduced strength and increased stress concentration in the compact.

3- Time of infiltration must be short enough to be economical.

In addition to the above condition, Lumpkins (1985), added that, mutual solubility between the solid and liquid must be limited. This is necessary for proper flow of infiltrant into the pores. With extensive mutual solubility the liquid will only be absorbed into the skeleton matrix. Figure 2.32 illustrates the phase diagrams of alloy systems that may or may not be suitable for infiltration.

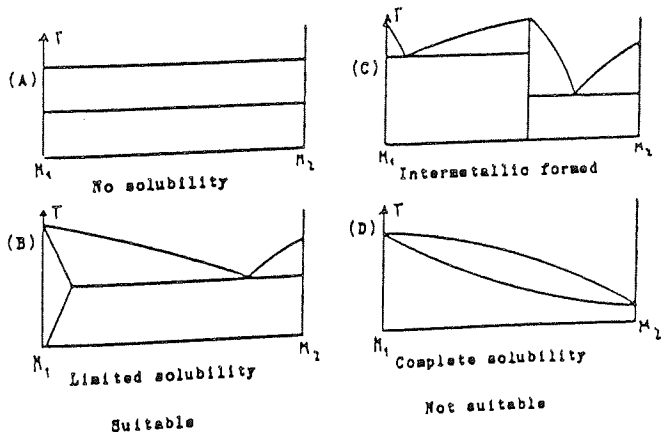

Figure 2.32 - Suitability of binary alloy systems for infiltration: (A) and (B) are suitable ; whereas (C) and (D) are not suitable for infiltration (Lumpkins, 19985).

The primary fundamental characteristic for infiltration to proceed, is good wetting. A common atmosphere for sintering is endogas, with a typical cycle of 1/2 hour at 1100°C. This atmosphere is cheap and has a modest reducing potential. Veidis (1974), reported that the more reducing the atmosphere, the better the wetting and liquid penetration. Matthews (1983), developed an equation to calculate the amount of infiltrant needed for optimum infiltration. These equations were similar to MPIF standard 49 equations (1982).

There are certain drawbacks to infiltration. Goetzel and Shaler (1964), reported that the process is very sensitive to surface contamination, making the use of various surface cleaning treatments inevitable.

Craters are often seen on the surface exposed to the infiltrating liquid. These craters are due to erosion which occurs with the non uniform dissolution of the solid in the liquid infiltrant. Careful selection of the amount of infiltrant is important. Excessive quantities of the liquid will cause slumping and separation of the solid skeleton. On the other hand, insufficient liquid results in residual pores and incomplete wetting.

2.8.2 Infiltration Index.

In order to have a knowledge of the extent by which a compact is penetrated by liquid metal, Shaler (1965), developed an infiltration index, I (Equation 2.25), based on a simple idealised model of surface free energy changes during infiltration.

$$I=2\pi r^2\left\{\left[\frac{1}{\psi}-\frac{2}{1+\sin\theta}+\frac{t\cos\theta}{r}\right]\gamma_L+\frac{t}{2}(P_1-P_2)\right\} \quad \cdots\cdots \quad (2.25)$$

where: I = infiltration index

r = pore radius

ψ = porosity

θ = contact angle

γ_L = surface tension of the liquid

P_1 & P_2 = pressure exerted upon the liquid layer and liquid in the pore respectively

Shaler (1965), stated that, whether a compact can be infiltrated depends on infiltration index, I. If I is positive, infiltration proceeds and as soon as I becomes negative, infiltration ceases. Shaler's (1965) theory, is based on many assumptions which makes the above relation difficult to be applicable for practical situations. Some of his assumptions are listed below:

1- liquid and solid metal do not react.

2- pores are of equal radius.

3- gas phase is not present.

4- liquid and solid have zero thermal expansion coefficients.

Lisovskii (1974), suggested that the liquid must have a low viscosity and must wet the solid. Moreover, the pores should be open and interconnected, thus, the solid skeleton should have at least 10% porosity.

Once the liquid metal finds its way from pore to pore in the porous compact, it may penetrate into the grain boundaries of the solid.

2.8.3 Penetration into the Grain Boundary

Assume that a quantity of liquid is resting at the entrance of a grain boundary (Figure 2.18). If the two solid and liquid interphase boundaries are not subject to crystallographic influences, then according to Smith (1948):

$$\gamma_{gb} = 2\gamma_{SL}\cos\left(\frac{\phi}{2}\right) \cdots\cdots (2.26)$$

γ_{gb} = grain boundary interfacial energy

γ_{SL} = solid / liquid interfacial energy

ϕ is called the dihedral angle, which may have a value from 0 to 180 degrees. It can be deduced from the above equation that :

a) If $2\gamma_{SL} > \gamma_{gb}$, ϕ will be positive and the grain boundary is not wetted by the liquid.

b) If $2\gamma_{SL} = \gamma_{gb}$, ϕ will be 120°, which is a no wetting situation.

c) If $2\gamma_{SL} < \gamma_{gb}$, ϕ will be zero and hence the liquid will be sucked into the grain boundary. This formula is applicable in liquid phase sintering, infiltration and brazing. It has been used by many researchers for solving industrial problems such as, liability of steels to penetration by molten copper during brazing.

2.8.4 Liability of Iron and Steel to Copper Penetration.

Evidence has been found that when certain types of steel are brazed with copper or copper base alloys, the molten copper penetrates along the grain boundaries in the steel (Asnis and Zamkov, 1961). The copper may penetrate in a limited way in isolated regions or it may form a complete network along the grain boundaries. The reason why molten copper penetrates into steel during welding or brazing has been studied by several researchers. Asnis and Zamkov (1961), reported that copper penetration occurs due to thermal tensile stresses. Bozhko (1968), deposited copper on pure iron by the MIG process and concluded that wetting stresses were responsible for the observed copper penetration. He suggested that silicon

containing steels were less prone to copper penetration due to the repelling action of silicon to the molten copper.

A more plausible study was carried out by Asnis (1965). He deposited copper on different kinds of steel ranging from fully austenitic to fully ferritic and then heated the samples. He concluded that the presence of ferrite reduces the penetration of copper into the steel and further showed that if the ferrite content of an austenitic / ferritic steel is over 30%, penetration is totally eliminated. The findings of this study were later confirmed in another publication (Kastkin and Tsaryuk, 1965). Sitnik (1975), studied copper penetration by tensile testing of specimens with blind holes of 2.0 mm diameter and 1.0 mm deep drilled in the middle into which copper alloy was pressed. They showed that the austenitic class of steels had the highest strength at 1200°C, indicating they had greater resistance to copper penetration. The amount of ferrite in his samples were greater than 30%.

2.8.5 Factors affecting infiltration.

a) Temperature- Chen and Klar (1980), investigated the effect of temperature on infiltration kinetics with copper as infiltrant. They pointed out that, changing the temperature from 1104°C to 1127°C *did not* result in increased infiltration efficiency. However, they suggested that the following parameters were significant:

b) Time- infiltration efficiency is increased with an increase in processing time.

c) Atmosphere- dissociated ammonia, gives more beneficial effect than using an endogas atmosphere. This is due to cleaner surfaces produced by the much greater reduction potential.

d) Porosity- penetration of liquid copper into the porosity is dependent on pore

size and shape. the smaller the pores, the greater the capillary forces.

There have been contradictory results published by other authors. For instance, Kondo et al.(1981), investigated the infiltration of Fe-Al compacts with liquid copper. They not only rejected the previously reported relationship between infiltration efficiency and pore size, but also reported that, the infiltration efficiency increased with an increase in temperature from 1130 to 1180°C.

Another process in which interaction of liquid copper is important, is brazing.

2.9 Brazing

Fabrication of powder metallurgy (P/M) parts has been practiced in industry for many years. P/M parts were initially joined to either another P/M part or a wrought part, using a mechanical method, such as nuts and bolts. This method proved to be very expensive. Fusion welding has been tried, but the main problem is distortion of the P/M parts.

A cheap, low distortion method could be joining by brazing. This is because the temperature for brazing is relatively low and therefore, variation in base metal structure is limited. Brazing is a process in which metal parts are joined by mean of forces of interatomic attraction across a joint, developed from a brazing alloy (often a copper based alloy), so that it flows and wets the adjacent surfaces. However, due to the porosity of a powder metallurgy compact (~10-20%), precautions must be taken to avoid "loss" of the brazing alloy from the joint by infiltration into the substrate. One other drawback is that, substantial infiltration of the brazing alloy, may result in erosion which affects its appearance, precision and strength.

Experiments by Pritchard (1964), show that methods of joining other than brazing, were impracticable for P/M compacts. For instance, oxyacetylene welding resulted

in burning before molten metal flow. Others (Knopp, 1975), brought the effect of powder, alloy additions and lubricant on the porosity so that to eliminate interconnecting pores.

Infiltrating the compacts prior to brazing was proposed by Ford Motor company Limited(U.K Patent, 1484641, 1977). A sandwich is made (Figure 2.33), and the whole assembly is heated in a furnace. The brazing alloy contained 8.5 % Mn, 4.0 % C and the balance Fe. Mn is necessary because it lowers the eutectic point of the brazing alloy and hence the flow temperature. The level of carbon in the compacts was proposed to be less than the level of carbon in the brazing material. This might be due to the fact that high carbon levels may produce fusion in the compact.

The whole assembly is taken into a furnace where it is pre-heated at 1400°F for about 20 minutes. Then at 2000°F the Cu melts and infiltrates the porous substrate. The brazing alloy is then melted and joins the compacts together. The problem with this method of joining is that rigorous temperature control is needed so that the brazing temperature does not exceed the melting point of P/M part and does not fall below the melting point of copper. Relatively long sintering (brazing) time is also spent (as long as 3 hours).

The type of the brazing alloy depends on the application of the type of the part being used. Too high a brazing temperature may lead to diffusion of carbon into the surrounding ferrite grain whereby graphite is replaced by pearlite, this may have an adverse effect on the mechanical properties. Too low a brazing alloy melting point is also not desired since it may melt away in the applications subjected to heat (eg: heat engines). In these cases a brazing alloy is needed which has a melting point of between 810-930°C.

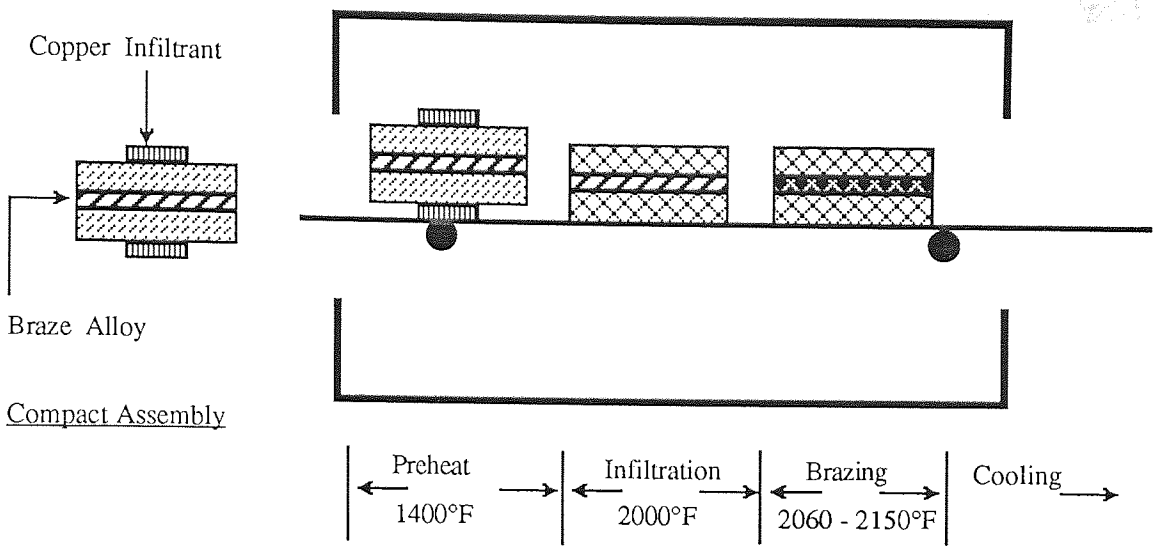

Figure 2.33 - Simultaneous infiltration and brazing of a P/M compact.

Johnson and Co. (U.K Patent, 1444521, 1976), invented such brazing alloy which contained, 50% Cu- 24.5% Mn- 24.5% Zn and 1.0% Ni. The composition of the alloy is such that when molten, it does not penetrate into the pores. Lap joints were produced and were subjected to a shear stress of 144.8 MNm^{-2} without breaking. A tensile specimen comprising two pieces of cast iron brazed in end to end relationship was also subjected to a tensile loading and the fracture occurred a 510.23 MNm^{-2}.

In another patent (U.K patent, 1360890, 1974), the same company investigated the use of boron in the brazing alloy. They made two different brazing alloys and investigated their influence both alone and in combination on the mechanical properties of the brazing joint. The two brazing alloys are:

Alloy (A)	60 - 70 % Cu
	6 - 12 % Ni
	18 - 34 % Mn

Alloy (B)

3.5 - 5.5 % Si

2 - 4 % B

Balance Ni

After performing a number of tests, they noticed that some combinations gave weak bonds, some experienced no flow and some others had the problem of pore penetration by the liquid metal. The only combination which resulted in a strong bond, good flow and good uniform radius was 55% of alloy (A) plus 45% of alloy (B). The parts assembled with this brazing alloy were sinter-brazed for 30 minutes at 2050°F in an atmosphere of dissociated ammonia. The parts were then subjected to tensile test. The strength range of 179.27 - 268.9 MNm^{-2} was obtained.

Later the effect of boron was investigated by Alloy Metals Co. (U.K Patent, 1547117, 1979), who included silicon and rare earth material in their brazing alloy. The brazing metal can be in the form of paste, powder, foil or tape depending on the type of joint and the processing conditions. Rare earth metal is added as a "deoxidiser" to promote wettability of joint, finer grains and improving the microstructure. Silicon is added which reduces the melting point if added at level of about 6%. The brazing metal which allowed brazing without penetration, contained 19-20 % Mn - 6.0 % Si - 5.0 % Cu - 1.0 % B - 0.02 % C - 0.1 % Rare Earth (Yttrium, Lanthanum or Mischmetal).

The brazing temperature employed is lower than that of the patented alloy previously mentioned, being at 1850°F. The sintering was performed either in vacuum or dry hydrogen atmosphere. Other industrial applications using wet endothermic or dissociated ammonia atmospheres were also employed. The low melting point of the said brazing material, permits brazing carbon and low alloy steels which require relatively low brazing temperatures.

A similar brazing material, with the trade name of Anchorbraze (AB72), has been developed which is designed so that the penetration of liquid metal into the pores is limited. It can be applied as paste or preform depending on the sintering (brazing) atmosphere (Johnson, 1975). Correct joint clearance is mandatory to develop the necessary capillary forces and draw molten material into the interface area. Typical clearance range may be from 0.05-0.14 mm varying with the degree of porosity in the part being brazed.

A study of Ag-Cu brazed joint strength of sintered steel has been reported by Suezawa (1977). Two different types of brazing materials were used in his experiments: a) BAg8 (ie 72.0% Ag + 28.0% Cu), and b) A sandwich of BAg8 with pure Cu in between. The result showed that BAg8-Cu-BAg8 filler metal had less tendency of penetration into the pores than BAg8. This may be due to the precipitation of some Cu compounds form the combined filler metal in the joint, causing reduced fluidity of molten BAg8. Suezawa(1977), also investigated the relationship between depth of the filler metal penetration and the change in degree of porosity. This is shown in Figure 2.34 in which higher penetration occurred with increasing porosity.

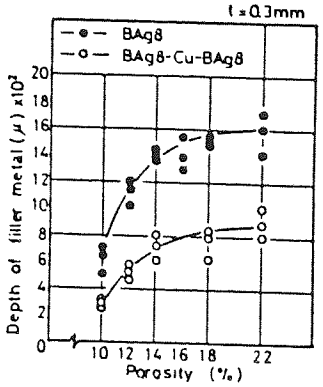

Figure 2.34 - Relation between depth of filler metal and sintered steel porosity (Suezawa, 1977).

Pettersson (1951), revealed that the force of penetration of molten metal into the pore space between sand grains is calculated as follows:

$$K = \left(\rho g h + P_0 - P_1\right) \pi \gamma^2 + 2 f \pi \gamma \cos \theta \quad \ldots\ldots (2.27)$$

where:

K = penetration Force of molten metal

P_0 = atmosphere Pressure

P_1 = back Pressure of inner space of sand grains.

g = radius of inner space section among the sand grains.

f = surface Tension of molten metal.

q = contact angle of molten metal with the sand grains.

r = density of molten metal.

h = head of molten metal.

g = acceleration of gravity.

It is clear that the penetration force of molten metal into the sand grains is stronger since the gap between the sand grains is larger and that the penetration is deeper. Therefore it is unreasonable to apply the equation to Suezawa's (1977)

experiments. However, on the basis of this equation, it is possible to confirm the depth of molten filler metal penetrating into the sintered steel, and its effect observed to indicate nearly the same tendency as shown in Figure 2.34. The brazing operation by Suezawa (1977) was done *after* the parts had been sintered. Sintering was done at 1150°C for 45 minutes in an atmosphere of dry hydrogen (dew point -42°C). The subsequent brazing operation was done at 840°C for 10 minutes in a dry hydrogen atmosphere. Finally, Suezawa (1977), performed tensile and impact tests on the specimens. The results showed that the joint strength is very much dependent on the braze material and joint clearance. Best clearance was ~0.2-0.3 mm for highest impact strength results and for highest tensile strength values a joint clearance of ~0-0.1 mm was recommended as shown in Figures 2.35 and 2.36.

All the above methods of brazing have to be done in furnaces with temperature controlled so that it lies within a certain range. Otherwise the required benefits are not obtained. Furthermore components of very large mass can't be brazed in standard furnaces and special furnaces have to be designed to meet the requirement. This adds to the cost and makes it uneconomical. In a patent (U.K patent, 2007137, 1979), a method to overcome this problem is proposed which involves plating the porous substrate with a thin layer of nickel and then brazing to a solid with a silver alloy. It is essential that the brazing temperature does not exceed the flow temperature of nickel.

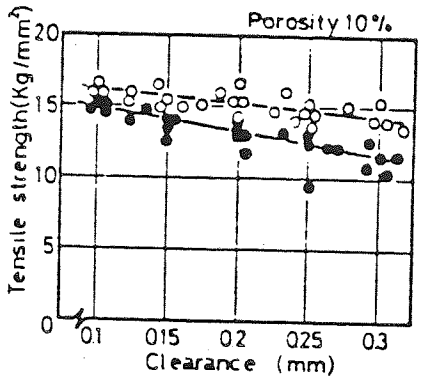

Figure 2.35 - Relation between tensile strength of brazed joint and joint clearance at 10% porosity (Suezawa, 1977).

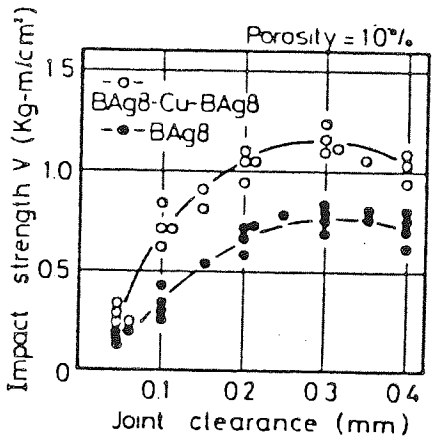

Figure 2.36 - Relation between impact strength of brazed joint and joint clearance at 10% porosity (Suezawa, 1977).

From the foregoing discussion it is concluded that copper penetration is prevented either by adding controlled amounts of additions to the brazing alloy or filling the porous substrate by other means, prior to brazing operation.

2.10 Concluding Summary

Having considered the data and experimental results of the published literature, it can be suggested that there remains some conflict regarding the sequential dimensional changes, effect of carbon on solubility, dihedral angle and wetting in Fe-Cu and Fe-Cu-C compacts. The mechanisms of swelling and preventative measures have been investigated by previous researches but with contradictory results. Bockstiegel (1962), proposed that volume increase in Fe-Cu compacts was caused by solid state diffusion of copper into iron grains, leaving large stable pores at the original molten copper sites. However, Berner et al. (1974), investigated the swelling kinetics and made dilatometric measurements of Fe-Cu compacts and concluded that diffusion alone could not be responsible for the rapid volumetric growth during sintering. They suggested that the growth of these compacts was caused by the penetration of liquid copper into the interparticle contact points.

Various attempts have been made to prevent the copper growth phenomenon. Trudel and Angers (1974), reported a reduction in copper growth due to a 1.0% carbon addition. However, Asaka (1983), suggested that the addition of carbon has an effect only to a limited extent and that is when the copper content is less than 5%. Further work in this matter with a copper content above and below 5% would be enlightening. It was suggested that carbon reduced growth because the solubility of copper in iron was reduced (Elliot, 1959). Krantz (1969), contested the solubility hypothesis on the basis that the Fe-Cu-C ternary phase diagram study by Ishiwara et al. (1926), showed that carbon had a negligible effect upon the solubility of copper in γFe. The major cause of the reduction in growth was given by Krantz (1969), as being due to a reduction in the grain boundary penetration by the liquid copper and dihedral angle changes. The work of Krantz (1969), appears

to be valid, however, there are few unified theories to explain the role of carbon in reducing grain boundary penetration.

Berner et al. (1974), made dihedral angle measurements and reported that carbon reduces the wetting behaviour of copper. However, Dautzenberg and Dorweiller (1985), carried out EPMA studies and suggested that carbon has no effect on the wetting of iron compacts by copper. On the basis of comparing the dilatometric investigations of Trudel and Angers (1974), with Dautzenberg and Dorweiller (1985), an element of inconsistency is observed in the dilatometric traces.

It was thus decided that a broad based study of the interaction of molten copper with iron powder compacts was necessary to attempt to clarify the various anomalies. This study would include infiltration, liquid phase sintering, wetting and flow, dilatometry and dihedral angle measurement.

3. Experimental Procedure

3. Experimental Procedure

3.1 Powder Characteristics

3.1.1 ASC 100.29 Iron Powder.

The powder chosen for this experiment as the base metal was a commercially available atomised powder manufactured by Hoganas AB of Sweden. The trade name stands for:

A= Atomised
S= Super
C= Compressibility
100= Mesh size (~150 μm)
29= Apparent density is 2.9 Mgm^{-3}

The powder has a very low specific surface area (25 m^2Kg^{-1}), and little internal porosity.

Figure 3.1 shows a Scanning Electron micrograph of ASC 100.29.

It has a highly irregular shape, which makes a good interlocking between the particles during compaction,hence a good compressibility and high green strength due to particles being soft and easily deformed .

According to the manufacturers (Hoganas, 1980), a density of 7.0 Mgm^{-3} can easily be achieved from 500 Mpa compaction pressure. The physical data and chemical analysis of this powder is included in Appendix A.

3.1.2 Copper Powder.

The copper powder which was used in the experiments, is of grade BB4, manufactured and supplied by the BSA limited.

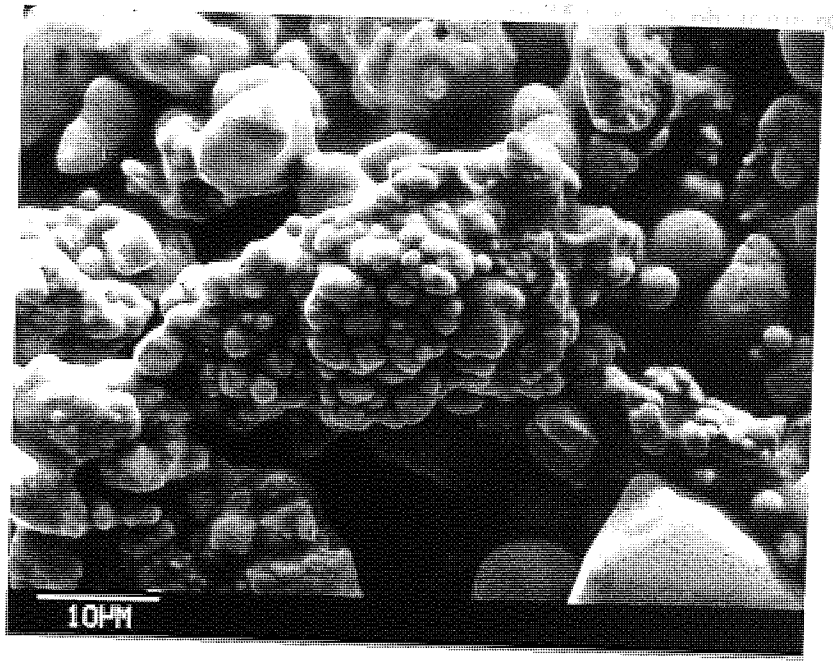

Figure 3.1 - SEM micrograph of ASC100.29 iron powder. x 2K

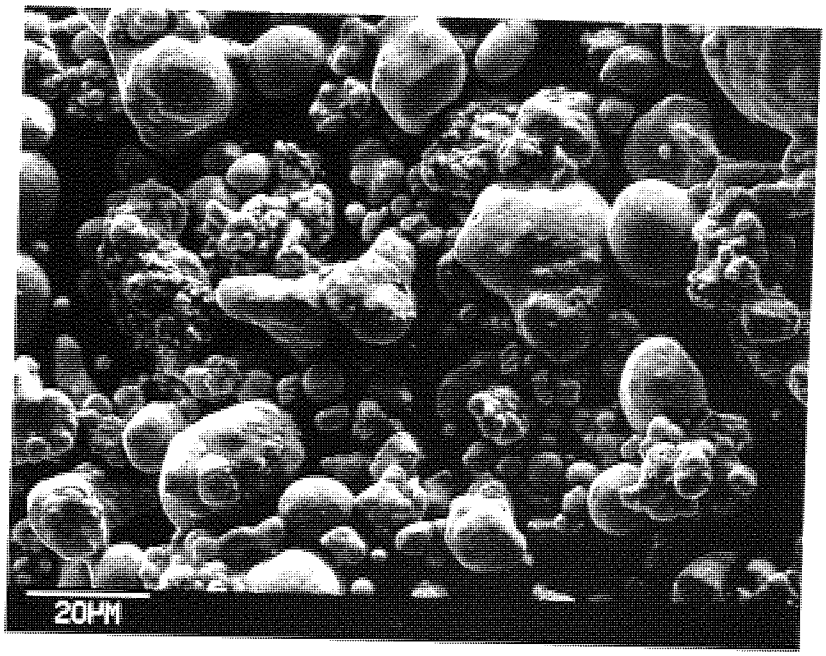

Figure 3.2 - SEM micrograph of atomised copper powder. x 1K

It is a very fine powder with the size of less than 45 μm. A photomicrograph of the copper powder is shown in Figure 3.2.

3.1.3 Anchorbraze 72

This is a commercially available brazing powder which was used in the preliminary experiments. It is a brazing alloy used for joining ferrous P/M parts and is claimed (Johnson, 1975), to prevent the molten brazing alloy flowing into the adjacent pores of the component. The particle sizes are between 40 and 200 mesh and an average apparent density of 2.0 Mgm^{-3} (Appendix A).

3.1.4 Carbon additions to the powders were made in the form of synthetic graphite powder. It is an extremely fine powder and was found to be more consistent than "natural graphite" which can contain high levels of impurities (Gummeson and Stousy,1986). This powder was readily available in the required form from Laboratory Chemicals Suppliers.

One advantage of using graphite is that it is smeared in a very thin layer over the iron particles during mixing. This gives maximum surface reaction both for reducing oxide films and diffusing into iron particles.

3.1.5 Zinc Stearate $Zn(C_{36}\ H_{70}\ O_4)$

A saturated solution of zinc stearate in diethyl ether was used for die wall lubrication. Carr and Kearns (1967) have recommended this lubricant for iron based compacts.

However, the characteristics of an extreme pressure Esso oil were also investigated as a die wall lubricant. Samples compacted with this lubricant, generally

experienced higher ejection loads (Figure 3.3). For example a load of 4.4 KN was needed to eject a specimen compacted to 6.65 Mgm^{-3}, whereas an ejection load of only 2.5 KN was sufficient to eject an identical sample when zinc stearate lubricant was used in the experiments.

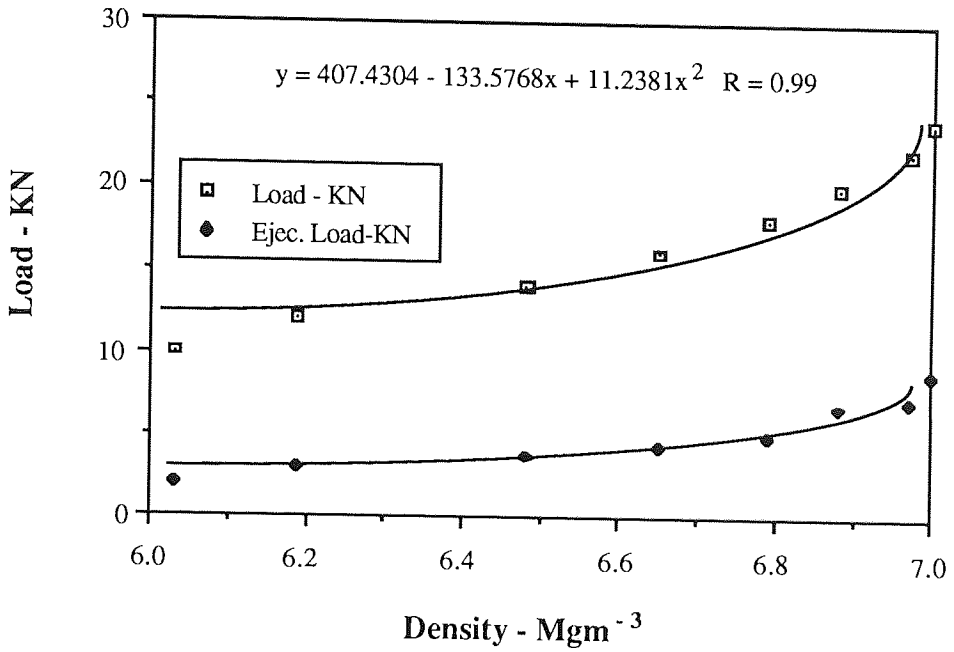

Figure 3.3 - Ejection load and load / density relationship using Esso oil IL2731 lubricant.

It has been found that (Heckel, 1967), die wall lubrication is superior to admixed lubrication for the following reasons:-

a) die wall lubricant virtually eliminates the lubricant "burn off", hence less associated restrictions on heating rates.

b) lower furnace operating costs, savings in replacements and maintenance cost of mesh belts and muffles.

c) sintering mechanism is enhanced, by avoidance of undesired products of lubricant burn off on the particle surfaces.

During sintering, zinc stearate is melted at 140°C and decomposes at 390°C (Ward, 1977). The decomposition consists of two stages. The first corresponds to the rapid removal of the hydrocarbon radical. The second occurs at higher temperatures and is associated with carbon deposition.

Recent work(James, 1987) has shown that extreme pressure oils (eg Esso grade 2731) can also be used instead of stearates for die wall lubrication. Comparison of some P/M lubricants are summarised in Table 3.1. Lubricant breakdown level is said to be the minimum compact density at which scoring was detected.
Generally die wall lubrication is preferred to admixed lubrication. However, for mass production, specially designed dies are needed which are very expensive to make and run. Therefore this lubrication system is only feasible if a production run of between 250000 and 500000 parts off from one toolset is achieved.

Lubricant	Comment	Lubricant Breakdown Level Mgm^{-3}
1. 20% zinc stearate 10% stearic acid in	mixture coagulates during use	6.9
2. 5% zinc stearate in equal values of butyle stearate and Chlorothene	mixture retains fluidity during use	6.85
3. Butyle Stearate	relatively low viscosity retained during use, freezing point is just below room temperature.	6.55
4. Garia A (EP oil)	viscosity similar to butyle stearate.	6.7
5. Esso IL2731	relatively low viscosity	7.2

Table 3.1- Comparison of powder metallurgy lubricants.

3.2 Preparation of Test Piece.

In order to simulate the experiments to brazing, infiltration and also liquid phase sintering , and facilitate copper penetration in the compacts, a purpose built tool set was made.

It was made of a through hardened high speed steel, heat treated to a hardness of 700 HV. All cylindrical samples had a nominal diameter of 12mm except the samples for dilatometric experiments which had flat ends and a diameter of 7.6 mm. Figure 3.4 illustrates the method of producing the compacts. Ejection of the samples were achieved by removing the top punch, with the bottom punch forcing the compact out of the cavity.

3.2.1 Mixing and Blending

Accurately weighed proportions of powders were placed in a screw top jar so that it filled to not more than 2/3 of the jar to allow for optimum mixing. The jar was then fitted in the cylinder end of double cone blender, and rotated repeatedly. This has been shown by the previous studies to be a satisfactory method of blending metal powders (Hill, 1979).

Carbon and copper additions were also made to the iron powder. The optimum mixing time under laboratory conditions was found to be (Ward, 1977) 20 minutes. Different levels of copper and carbon were investigated which are all summarised in Table 3.2.

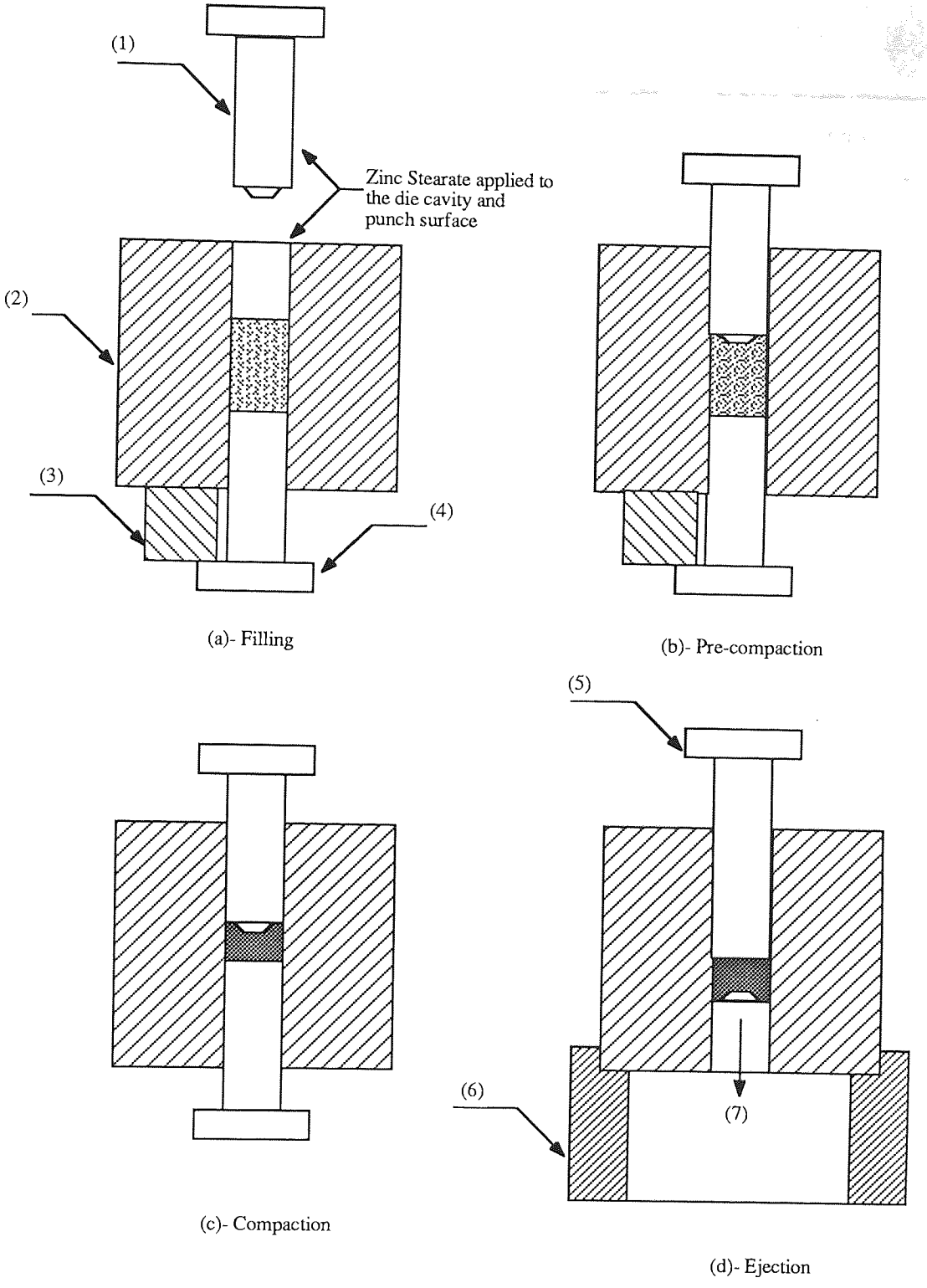

1- Top Punch
2- Die
3- Copper Block
4- Bottom Punch
5- Ejection Punch
6- Ejection Block
7- Compact

Figure 3.4 - Schematic diagram showing method of producing powder metallurgy compacts.

Experiment	Carbon%	Copper%	Shape
Infiltration studies	0.15 , 0.6	2%, elemental	cylinders
Solubility and wetting experiments	0.15 , 0.55 , 1.0	2,4% elemental	sheet metal
Dilatometric experiments	0.15 , 0.6	2,4,8% elemental and copper coated	cylinders

Table 3.2- Experimental conditions in infiltration, solubility and dilatometric experiments.

3.2.2 Compacting

Die wall lubrication was applied by brushing a small amount of saturated solution of zinc stearate in diethyl ether into one die cavity and corresponding punches, prior to compaction. This was necessary to minimize die wall friction during compaction and reduce the ejection stress of unlubricated powders. A linear relationship for powder compaction has been suggested by (Heckel, 1961), Equation 3.1.

$$\ln\left(\frac{1}{1-D}\right) = KP + A \quad \text{.....(3.1)}$$

Where K and A are constants and D is the relative density (ie the ratio of the compact density to the density of the solid metal). K is related to the ability of the material to flow plastically with an increase in pressure, and A is related the particle size and shape.

This relationship presents powder compaction as a linear relationship, however, experiment suggests that it is not linear. Three stages are proposed which are as follows:

stage 1 - filling of the die under gravitational forces. The amount of densification in indicated by the apparent density.

Stage 2 - individual particle movement and rearrangement under the effect of the upper punch and at low pressures before interparticle bonding becomes appreciable.

Stage 3 - bulk deformation of particles under high pressures.

A 50 tonne Avery Denison universal testing machine was used for compacting the cylinders. The required load for compaction was read from a previously determined pressure/ density curve (Figure 3.5), and the powder charge to the die was weighed to an accuracy of three decimal places of grams. The die was supported by a chock when the bottom punch was inserted. After charging the powder and inserting the top punch, the chock was removed.

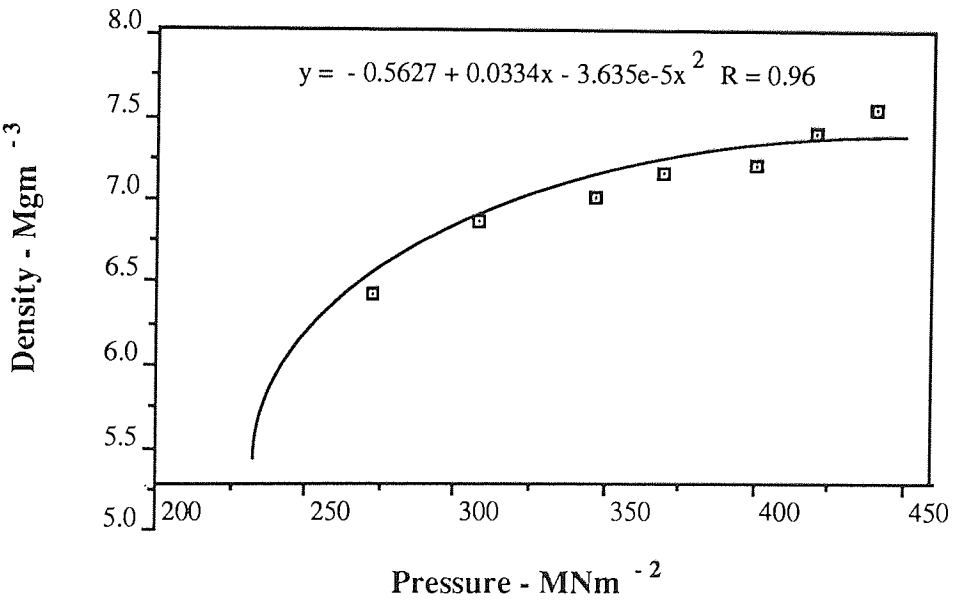

Figure 3.5 - Pressure / density relationship of the experimental compacts.

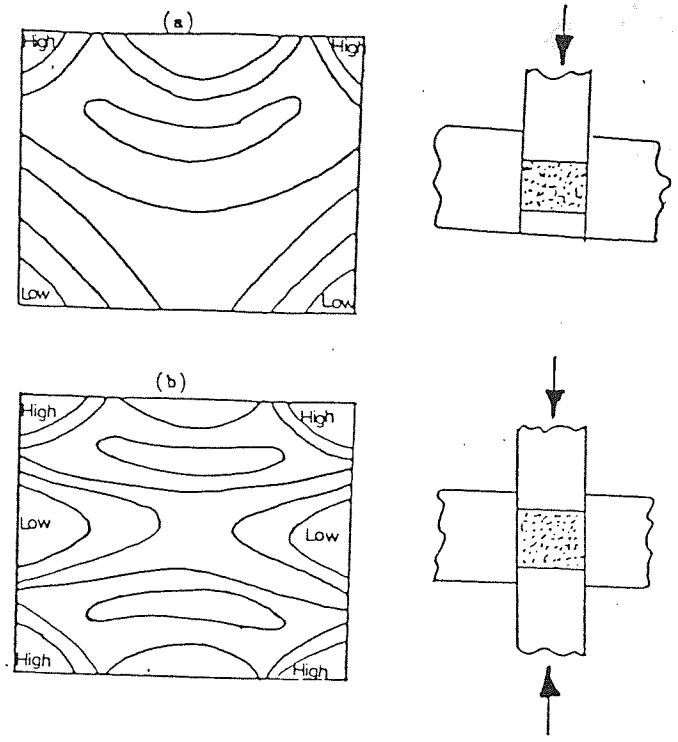

Figure 3.6 - Density contour maps in the compacts subject to single and double end compaction.

The load was applied slowly, up to the required level, held for about 10 seconds and released. This method of compaction results in double action pressing of the compacts. Figure 3.6 illustrates the density variations within the compacts when subjected to single and double end compaction.

After ejection, the dimensions and the weight were accurately measured and recorded. The density of the compacts could then be calculated using Equation 3.2.

$$\text{Density} = \frac{\text{Mass of the cylinder}}{\text{Volume of the cylinder (-Volume of the semi-cone}^{*})} \quad \ldots\ldots\ldots(3.2)$$

* Only for infiltration experiments.

3.2.3 Sintering

The specimens were sintered in a Scot-Vac vacuum furnace which consists of a water cooled chamber, lined with insulating materials and heated using graphite elements. The vacuum furnace is illustrated in Figure 3.7. Prior to sintering, the samples were left, overnight in a vacuum desicator. This helps reduce sample contamination.

The samples were placed in an alumina boat in the centre of the furnace. The furnace was evacuated by the use of a rotary pump until a vacuum of $5*10^{-1}$ torr was indicated on the Pirani gauge. The diffusion pump was then turned on and allowed to warm up for approximately 20 minutes.

When the vacuum was better than $5*10^{-1}$torr the rotary pump was turned to backing and the baffle valve opened slowly. After the vacuum was greater than 10^{-1} torr, the heating power was switched on and heating current set at 140 Amps. Finally, the desired temperature on the Ether digital control was set and the overtemperature policeman set to about 120 degree above the desired temperature. During sintering, a vacuum of 10^{-3} torr was maintained.

Experiments were carried out at 960, 1125, 1200 degrees centigrade, with an error of ±5 Degrees. The heating rate being kept constant. The sintering times were 3, 20, and 60 minutes. After sintering, the heat was switched off and compacts were cooled under vacuum.

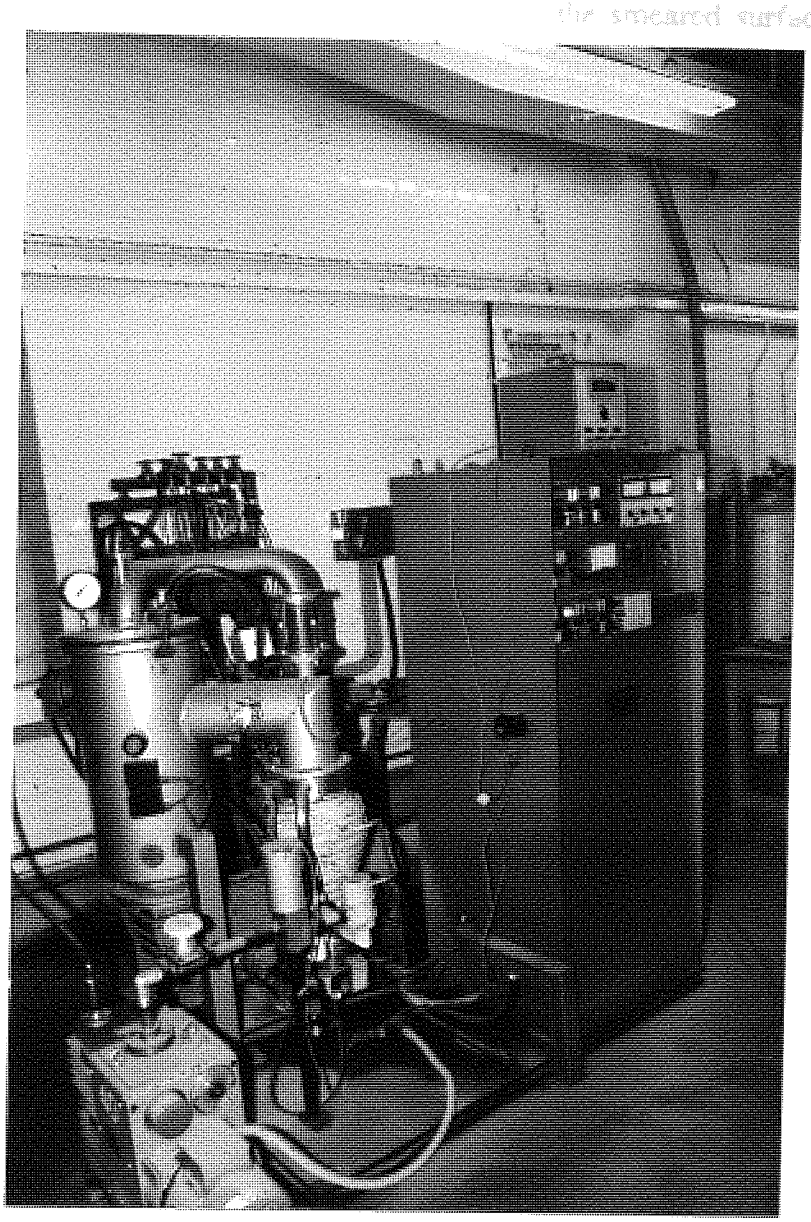

Figure 3.7 - The Scot - Vac vacuum furnace.

3.2.4 Metallography

The cylindrical specimens were sectioned longitudinally and mounted in bakelite. After about half a millimeter from the surface was ground off, they were ground on Silicon carbide grinding disks down to the finest grit size, P1200. The samples

were then deeply etched in 4% Nital to remove the smeared surface, washed thoroughly in alcohol and dried. They were subsequently placed in Inhibisol and ultrasonically cleaned for 15 minutes to remove any entrapped air, oil or other contamination.

It is difficult to examine the pore structure in the sintered material due to the flow of metallic matrix into the adjacent pore during polishing on fine pads. To overcome this problem, the specimens were impregnated with Araldite (Appendix B) and allowed to harden. The specimens were then reground on the fine 6 micron and 1 micron polishing wheels (Table 3.3), after being washed with ND150 (detergent). The micros were finally checked under an optical microscope to make sure that all the scratches had been removed.

Trade name	Pad size	Kind	Comments
Pan K	6 micron	Napless	Tends to retain the diamond abrasive for longer time.
Lec cloth-B	1 micron	Napped	Good final polish achieved.

Table 3.3 - List of the examined fine polishing pads.

Several etchants were investigated, out of which, 2% Nital (nitric acid in alcohol) proved to be the best. The studied etchants are all summarised in Table 3.4 .

Etchant	Comments
50% Ammonia +50% Hydrogen Peroxide.	Bubbles evolved from the specimen, but no clear microstructure was revealed.
Ferric Chloride	Mainly attacked copper regions. Microstructure not clear.
Dichromate	Not satisfactory.
2% Nital	Satisfactory - Mainly attacked iron.

Table 3.4 - List of the investigated etchants.

3.3 Preliminary Experiments

3.3.1 Copper Penetration.

Having considered liquid phase sintering, infiltration and brazing in isolation, a fundamental unified approach was considered so that the mechanisms operating the three processes could be interrelated. As a starting point, 0.15 grams of copper powder was placed in the top cavity of iron compacts (Figure 3.8) and infiltrated at 1125°C for 10 minutes in vacuum (volume of the cavity was 146.34 mm^3). The melting point of copper is 1084°C, well below the sintering temperature. The height and diameter of the samples were 11.0±1 and 12.70±0.01 mm respectively. The penetration of liquid copper into the iron compacts were then studied by optical and scanning electron microscopy.

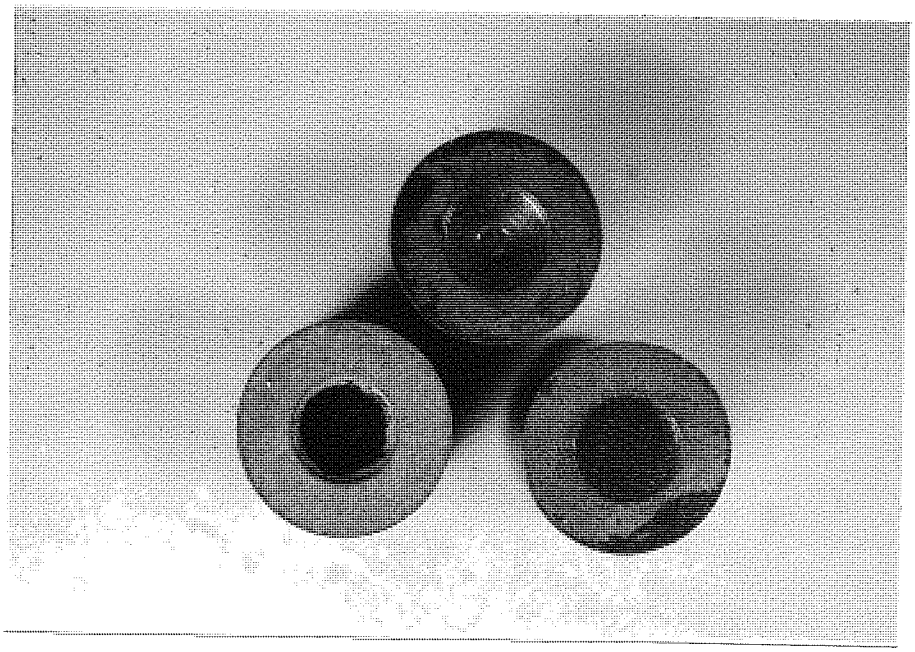

Figure 3.8 - Top view of the experimental samples.

3.3.2 Heat Tinting

In order to reveal copper diffusion path into iron matrix, a heat tinting technique was employed. This was done by heating the specimens to about 300°C while resting on a hotplate in still air for one hour. The idea was to oxidise the iron matrix so that it appears dark. The copper diffusion could be seen clearly under the optical microscope.

3.3.3 Anchorbraze Study

Optical photomicrographs revealed that at the sintering temperature, above the melting point of copper(1084°C), all of the copper powder melted and penetrated (infiltrated) into the iron compact. This is considered to be a disadvantage when brazing.

A commercially available brazing material "Anchorbraze" (Johnson, 1975) was replaced by copper, sintered at 1125°C for 10 minutes in vacuum. The photomicrographs showed that the brazing material did not penetrate into the iron compacts. This confirms the claims of the inventors of Anchorbraze.

3.4 Main Study

3.4.1 Copper Penetration Profile

Several samples were prepared to study the effect of time, temperature and compact density on copper penetration profiles. The weight of the samples were in the order of 9.0±0.2 grams. The variables are summarised in Table 3.5.

Variables	Range
Temperature °C	1100 - 1200
Density Mgm^{-3}	6.4 - 7.4
Time, minutes	5 - 40

Table 3.5 - Variables in copper infiltration experiments.

The objective of these experiments were to investigate:

1. Diffusion of copper and change in dimensions of the samples under different conditions.
2. Changes in copper penetration area and maximum depth of copper infiltration.
3. Changes in the dihedral angle of copper on iron particles.

In order to find which one of the experimental variables has the most effect on copper infiltration, a statistical analysis of the data was necessary. Sintering of the specimens was done according to section 3.3.1. After sintering, the specimens were sectioned, polished and etched so that the area of copper penetration could clearly be seen. Photomicrographs of the penetrated regions were prepared using a Polyvar optical microscope, all at the same magnification.

3.4.2 Double and Two Step Infiltration

Two different infiltration techniques namely double infiltration and two step infiltration were carried out to examine their effect on copper penetration profiles and dimensional changes. The green compacts with the copper infiltrant in the top cavity, were placed into the vacuum furnace and infiltrated. The infiltrating conditions were as follows:

Process	Condition
Double infiltration	Heat to 1125°C Hold for 20 minutes Cool to 700°C Heat again to 1125°C Hold for 20 minutes Cool to room temperature
Two step infiltration	Heat to 960°C Hold for 20 minutes Heat to 1125°C Hold for 20 minutes Cool to room temperature

Table 3.6 - Process conditions for double and two step infiltrated experiments.

3.4.3 Multiple Regression Analysis

The data obtained from the experiments explained in section 3.4.1 were fed into a statistical package, " Statworks", on an Apple Macintosh computer. The dimensional change was taken as the dependent variable and density, temperature and time were taken as the independent variables.

The aims of this analysis were to:

a) evaluate which one of the sintering variables contributes most to the dimensional changes.

b) calculate the regression coefficient.

c) observe if there is any pattern when plotting the residuals.

d) finally, write a formula to predict the dimensional behaviour of the compacts.

The way the data were analysed was based on "stepwise correlation". This means each independent variable was first considered individually, then two variables and finally all three variables were taken into account. The effect of each variable was then investigated, making two assumptions :-

a) There is a linear relationship between dependent and independent variables. (ie a regression line)

b) No correlation exists between independent variables.

The information obtained included, regression coefficients, t-statistic, F-ratio, coefficient of determination, correlation matrix and residual.

3.4.4 Dihedral Angle Measurements

The angle which the liquid copper makes with the iron grain boundary is called the dihedral angle. The specimens containing carbon and those sintered at different temperatures were subjected to dihedral angle analysis. The specimens were placed

on a projection microscope and the eyepiece, objective lens and bellows settings adjusted to give a magnification of 2000 times, which was sufficient for a clear observation of the dihedral angles within the microstructure. 120 individual angles were measured in each specimen. It is predicted by past workers (Riegger, 1960) that if greater than 100 readings are taken, an accuracy of better than ±5° should result at 96% confidence level. Hence, reasonable accuracy in the determination of the dihedral angle should occur.

3.4.5 Oxidation Treatment of Compacts

One of the major problems associated with joining powder metallurgy parts during brazing, is the penetration of the brazing material (commonly copper), into the compact by capillary action induced by the interconnected pores. This is believed to be a principal factor contributing to the failure of the soldered and brazed bond between sintered iron articles.

3.4.5.1 Oxidation Experiments.

Oxidation treatment of the compacts was considered to be a possible method of preventing this problem. The idea was to block the interconnected pore network with oxide, making the component impervious to liquid copper. Specimens were weighed to an accuracy of 0.0005 grams and were sintered in a Scot Vac furnace at 1125°C for 20 minutes in vacuum. The green densities of the samples were 6.90±0.05 and 6.40±0.05 Mgm^{-3}. They were then oxidised in a muffle furnace in air at 500°C for 3, 5, 30, 75, 130 minutes. After the samples were oxidised, accurate measurement of weight gain (due to formation of oxidation products) was performed and samples cooled in a vacuum dessicator to prevent any subsequent

oxidation. Finally, the top cavities of the samples were filled with copper powder and sinter-brazed in the tube furnace at 1125°C for 20 minutes in high purity argon. The extent of copper penetration and possible oxide layers were then studied.

It is considered (Regel, 1963) that at temperatures up to 570°C, the oxide layer consists mainly of magnetite (Fe_3O_4). Above 570°C, wustite (Fe0) can be produced, but this oxide will decompose eutectoidally during cooling to give a duplex structure of magnetite and iron (Smithells 1967). This structure is claimed to have corrosion resistance inferior to that of the layers produced below 570°C (Regel, 1963). A diagrammatic representation of the oxide layers is shown in (Figure 3.9).

Fe_2O_3= Haematite - highest oxide - formed below 570°C

Fe_3O_4= Magnetite - formed around 570°C

FeO = Wustite - lowest oxide - formed above 570°C

3.4.5.2 Auger Electron Spectroscopy and Diffractometry.

In order to identify the oxide layers, Auger Electron spectroscopy was performed on a sample, sintered at 1125°C in vacuum and oxidised at 500°C for 130 minutes. The surface of the specimen was etched for 30, 120 and 150 minutes to remove the surface contamination. The trace of intensity versus kinetic energy of the Auger electron was produced on a chart recorder. The experimental conditions are given in Table 3.7.

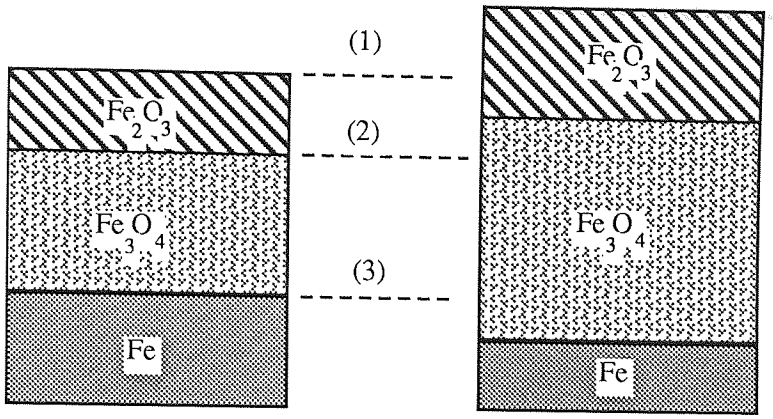

a)At 500°C

b)When cooled to room temperature from 500°C.

(1) haematite-atmosphere interface advances.

(2) magnetite-haematite interface advances.

(3) iron-magnetite interface retracts.

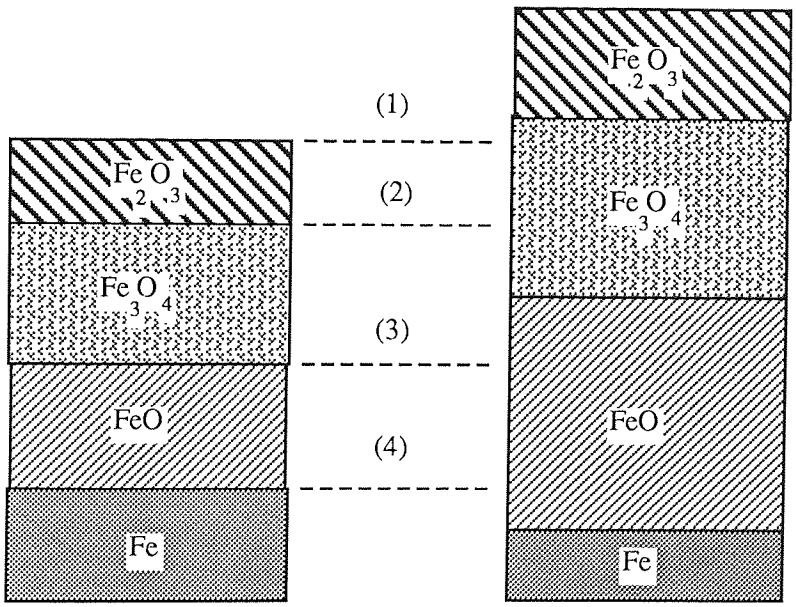

c) Above 570°C

d) When cooled to room temperature from a temperature above 570°C.

(1) haematite-atmosphere interface advances.

(2) magnetite-haematite interface advances.

(3)wustite-magnetite interface advances.

(4) iron-wustite interface retracts.

Figure 3.9 Diagramatic representation of the oxide layers at 500°C and above 570°C

Voltage	3 KV
Current	250 mA
Mode	FRR
Scan Width	1250 eV
Scan Time	300 s
Sensitivity	0.2 nV

Table - 3.7 - AES operating conditions.

Since this technique was dependent on only the first few atomic layers, another analysis was considered necessary to support the auger results. X-ray diffractometry was found to be an ideal technique to identify the type of oxides present on the surface. Continuous scanning over 10 to 100 degrees was used for this test which took 1.5 hours. The data output of the count rate versus 2θ angle was collected in graphical form on the chart recorder. General operating conditions for the X-ray set are shown in Table 3.8.

X-ray tube	Co
Radiation	Co K
Wavelengh	1.791 Å
Potential	30 KV
Current	30 mA
Beta filter	Iron
Scanning range	10 - 100°
Divergence slit	1°
Recieving slit	4°
Detector	Proportional counter
Chart speed	10 mm/min.
Scan speed	1° per min.

Table 3.8 - XRD operating conditions.

3.4.6 Thermomechanical Analysis.

The experiments described previously provided results "after" the sintering runs were over. It was considered necessary to study the dimensional and phase changes of iron -copper compacts "during" the sintering process. This was achieved by using a thermomechanical analyser in its dilatometric mode. Valuable information was obtained regarding dimensional changes in all stages of sintering, especially when the temperature reached the melting point of copper.

3.4.6.1 Thermomechanical Analyser,(TMA)

The schematic layout of the TMA is shown in Figure 3.10.

It is a versatile and sensitive instrument designed to measure the dimensional changes of a sample in the range from room temperature to 1500°C. It consists of:

a) Furnace- The furnace is automatically raised and lowered by means of a switch motor drive. The furnace element support tube of alumina is wound with nichrome wire, and it is all mounted in a water cooled jacket. A tap water supply was fitted with, a pressure reducing value, to give a flow rate of 30 litres per hour.

b) Probe assembly - The probe assembly is made up of the screw height adjuster for the probe unit, alumina tube and alumina probe unit. The probe unit comprises the linear variable differential transducer core.

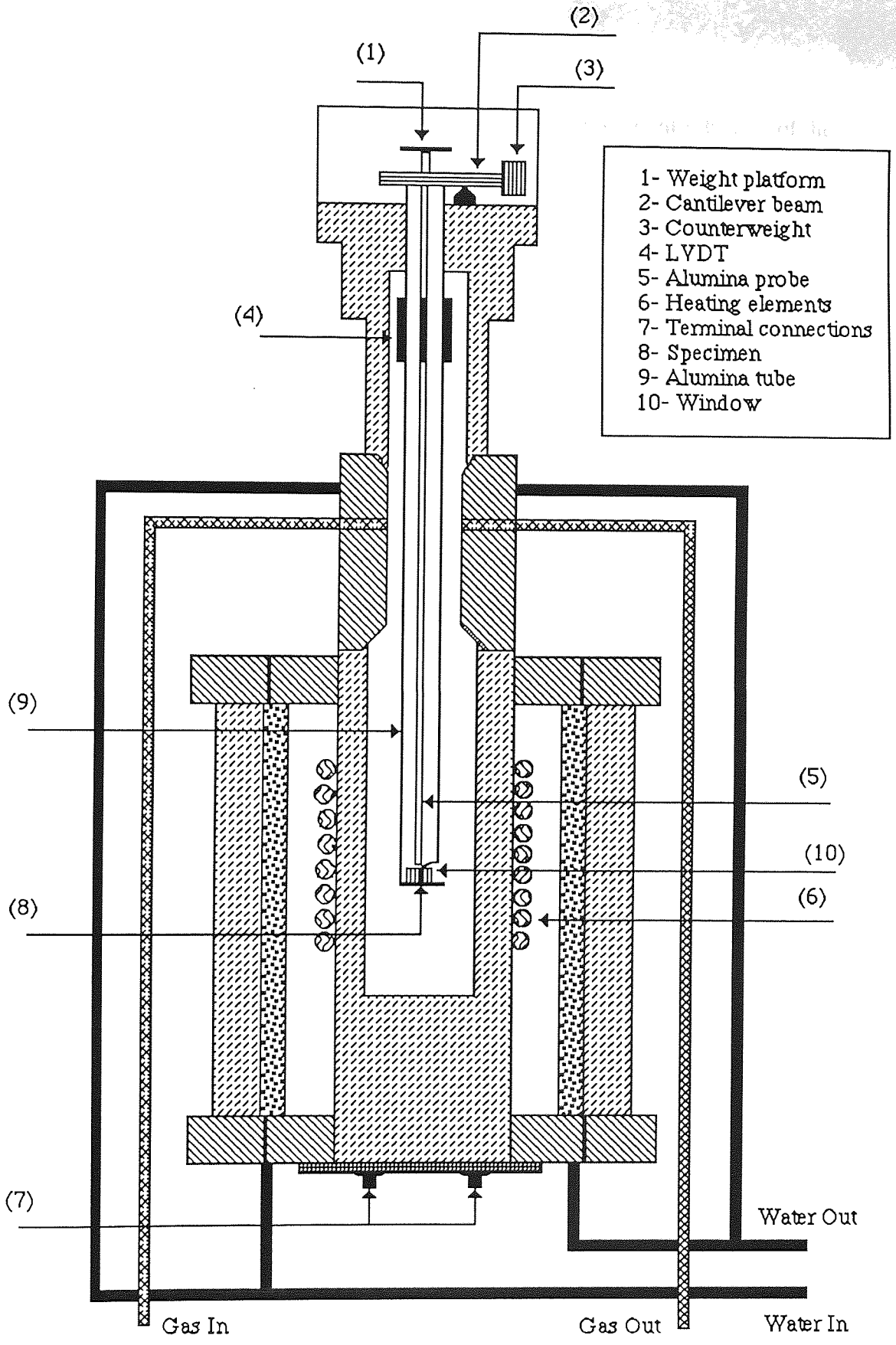

Figure 3.10- Schematic layout of the thermomechanical analyser.

c) Balance unit, comprises a weight platform which enables the introduction of the required load to the probe and a balance arm,which carries a counter weight to counter balance the weight of the probe itself. A load of 2 grams was applied throughout the experiments.

d) Temperature controller.

The furnace temperature was controlled by using a micro-processor driven programmer / controller, using a Platinum / Platinum+13% Rhodium thermocouple. Temperature control is achieved by setting the Proportional, Integral and Differential (P. I. D) values on the programmer. Control terms were entered via a keyboard.

3.4.6.2 TMA Experiments.

Cylindrical samples of nominal diameters of 7.6 mm were placed under the alumina probe in the alumina tube, and the furnace raised. The system was then left on for approximately 20 minutes to stablise the LVDT. The experimental conditions are summarised in Table 3.9.

From the TMA traces it was noticed that that there is a discrepancy between the furnace and sample temperatures due to a thermal lag. This is made in the form of a graph (Figure 3.11). For comparison, some TMA tests were repeated in $90\%N_2/10\%H_2$ atmosphere, to evaluate the effect of atmosphere.

Variable	Range	Unit
Temperature	960 - 1200	℃
Density	6.0 - 7.4	Mgm^{-3}
Copper	2 - 8	%
Carbon	0.15 - 0.6	%
Heating rate	20	$°C\ min.^{-1}$
Cooling rate	40	$°C\ min.^{-1}$
Load	2	Gram
Chart speed	10	$mm\ min.^{-1}$
Water flow rate	30	$litre\ hr.^{-1}$
Gas flow rate	160	$cm^3 min.^{-1}$
Sintering time	20	min.

Table 3.9 - TMA experimental conditions.

Dilatometer traces of the experiments were then recorded on a pre-calibrated chart recorder. In most sintering experiments, an inert atmosphere of HP Argon was maintained. Analysis of the trace impurities within the atmosphere is shown in Table 3.10.

Argon	99.998	Min.
Moisture	3 vpm	Max.
Oxygen	3 vpm	Max.
Nitrogen	3 vpm	Max.
Hydrocarbons	1 vpm	Max.

Table 3.10 - Analysis of trace impurities in argon.

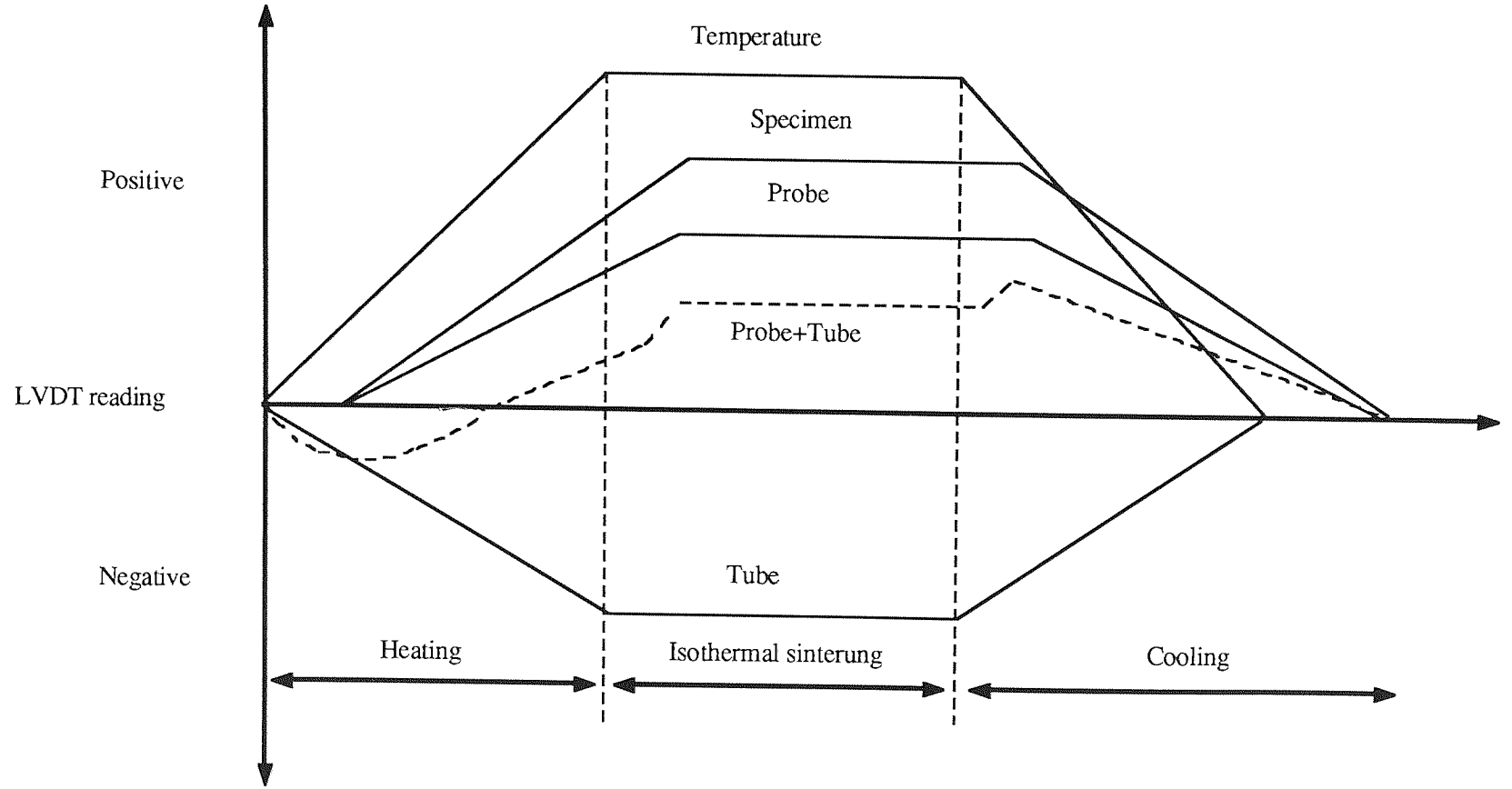

Figure 3.11 - Diagramatic representation of expansion / contraction of the specimen, probe and tube assembly of the TMA during sintering.

3.4.6.3 Baseline Drift Measurements.

During heating, the alumina tube surrounding the specimen expands at a higher rate than the specimen. Therefore, the net expansion detected by the probe is only a certain fraction of the actual specimen expansion. Moreover, since a high heating rate is employed (20°C min^{-1}), the alumina probe and specimen holder tube will expand at different rates (Figure 3.11).

It was necessary to correct all the TMA traces for their corresponding baseline drift. Three baseline runs were obtained with no samples and with the probe touching the floor of the alumina tube, from room temperature to 960, 1125 and 1200°C at a heating rate of 20°C min^{-1}. A computer programme was then developed to collect the TMA data and correct them for their baseline drift (Appendix C). The programme was capable of first selecting the sintering temperature and then choosing its corresponding data for correction from the resident data bank. A separate programme was written to read the corrected data and use it to draw the TMA graphs (Appendix C).

3.4.6.4 Calibration of the LVDT

The calibration of the LVDT was carried out using a wrought Armco iron sample over a range of 18-1125°C. The change in length was measured between the temperatures T_2 and T_1 giving $\Delta l_{T_1}^{T_2}$(observed). They were then corrected for baseline drift and compared to the calculated values of $\Delta l_{T_1}^{T_2}$(calculated) from Table 3.11. The calibration factor, K, was finally calculated for the instrument from the ratio:

$$K = \frac{\Delta l_{T_1}^{T_2}(\text{calculated})}{\Delta l_{T_1}^{T_2}(\text{observed})} \quad \text{.....(3.3)}$$

Temperature	Change in Length (mm)
18	0.000
169	0.066
884	0.539
915	0.359
1125	0.748
1125	0.762
900	0.375
868	0.552
456	0.251
18	0.000

Table 3.11 - TMA calibration values for Armco iron.

If the K value lay between 0.98 and 1.02, the instrument was considered to be calibrated. If it was outside the limits, the potentiometer output was altered by the percentage of the K factor.

3.4.7 Immersion Coating Experiments

The TMA traces depicted rapid growth of Fe-Cu compacts especially at the melting point of copper. Measures were taken to restrict copper growth phenomenon, in which the most successful method was to "coat" the iron powder with copper prior to compaction and sintering.

3.4.7.1 Preparation of the Solution and Powders.

10% copper sulphate solution was made up to one litre distilled water and stirred until dissolved. 200 grams of ASC 100.29 iron powder were poured into a copper sulphate solution and constantly agitated by a motor driven paddle for one minute. The paddle had been lacqured to prevent copper deposition onto the blades. The solution temperature was maintained at 20°C for better control of the reaction. Atomic absorption spectroscopy (section 3.4.6.3), revealed that the coated powder contained 10.9% copper. The experiment was repeated for 5 and 3% copper sulphate solution to obtain a copper deposition of 6.2 and 4% respectively (Figure 3.12).

Figure 3.13 shows the optical photomicrograph of the copper coated iron powder. A very thin layer of copper covered the iron particles. Sintered microstructures of the elementally mixed Fe-Cu, and copper coated iron compacts are shown in Figure 3.14.

The coating mechanism is as follows:

As soon as iron powder is introduced into the solution, the exchange of copper and iron ions occur. Hence, the colour of the solution changes from blue to grey, and the colour of iron powder from grey to red. Major displacement reactions are:

$$Fe^{o} + Cu^{2+} = Fe^{2+} + Cu^{o}$$

Half equations are:

$$Fe^{o} = Fe^{2+} + 2\,e^{-} \text{ (Iron ions going into solution)}$$

$$2\,e^{-} + Cu^{2+} = Cu^{o} \text{ (Copper depositing onto iron powder)}$$

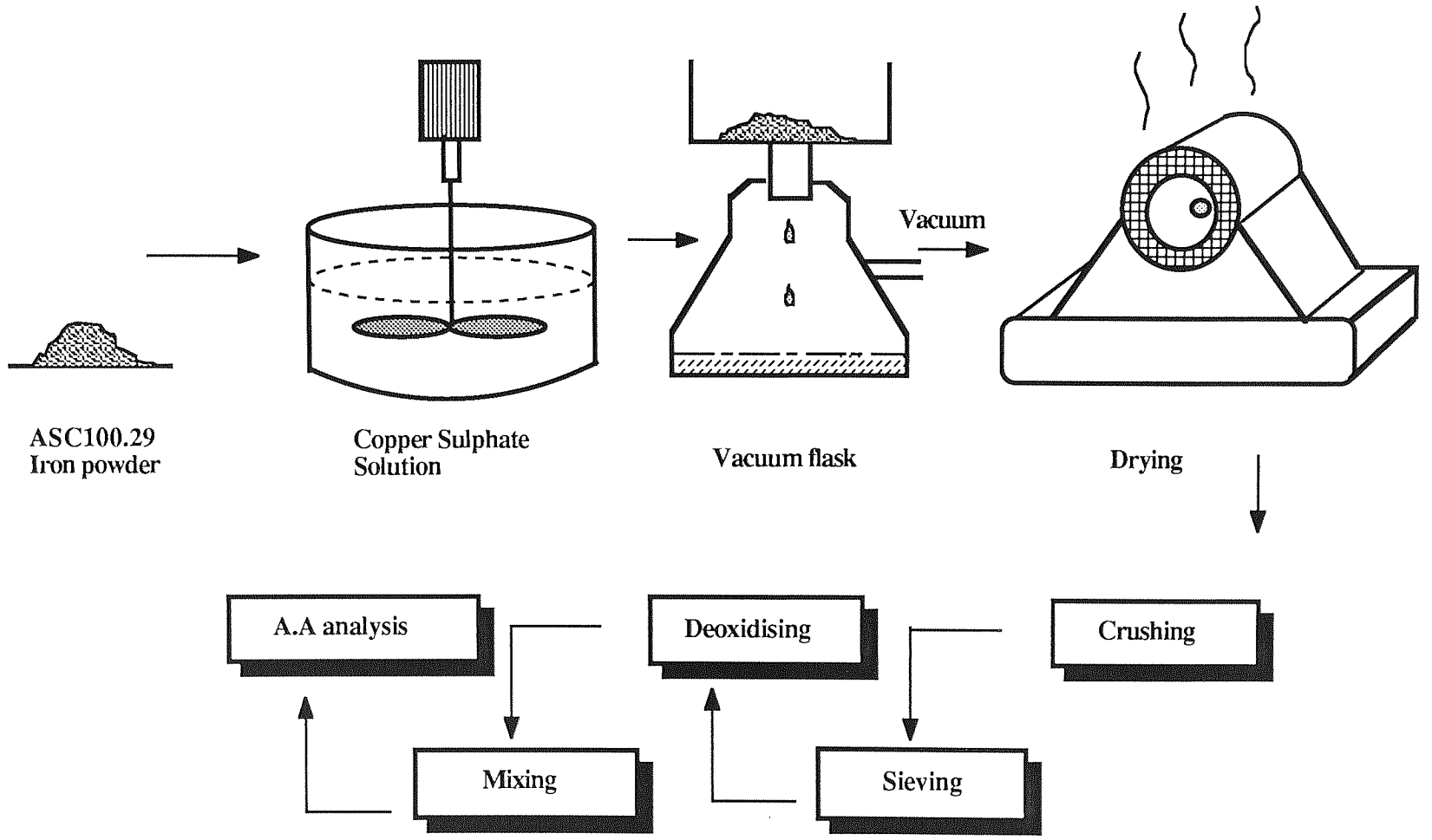

Figure 3.12 *Block diagram of the immersion coating process.*

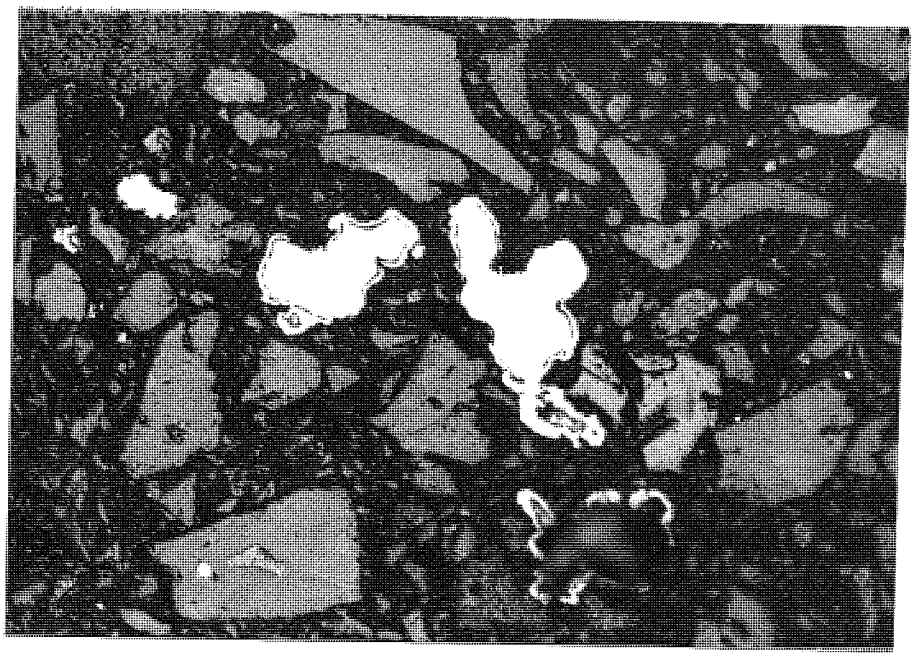

Figure 3.13 - Optical photomicrograph of Fe powder, coated with copper after immersion coating in 5% $CuSO_4$ solution for 1 minute.

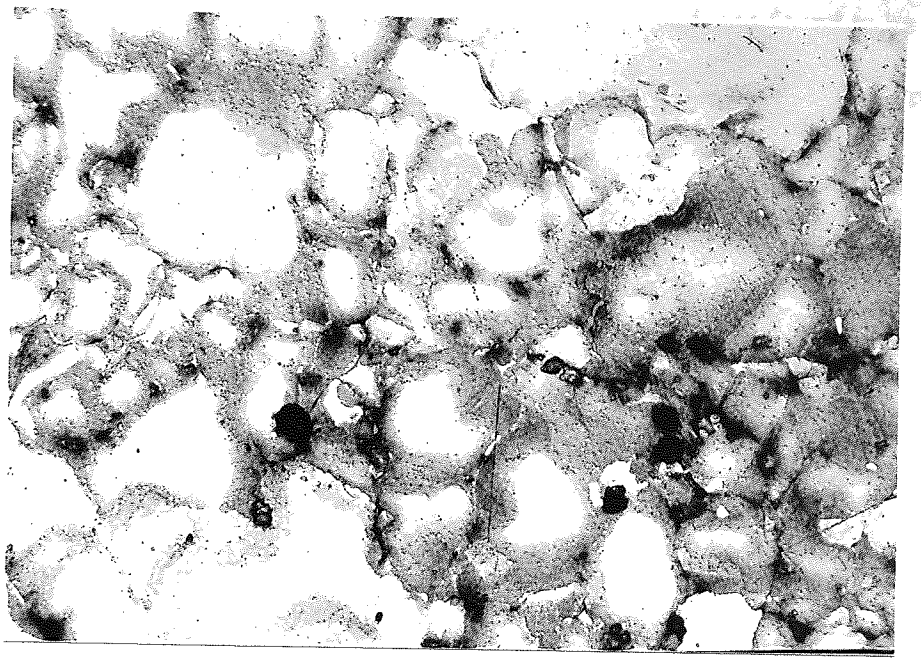

a) Fe-4Cu, elementally mixed. x490

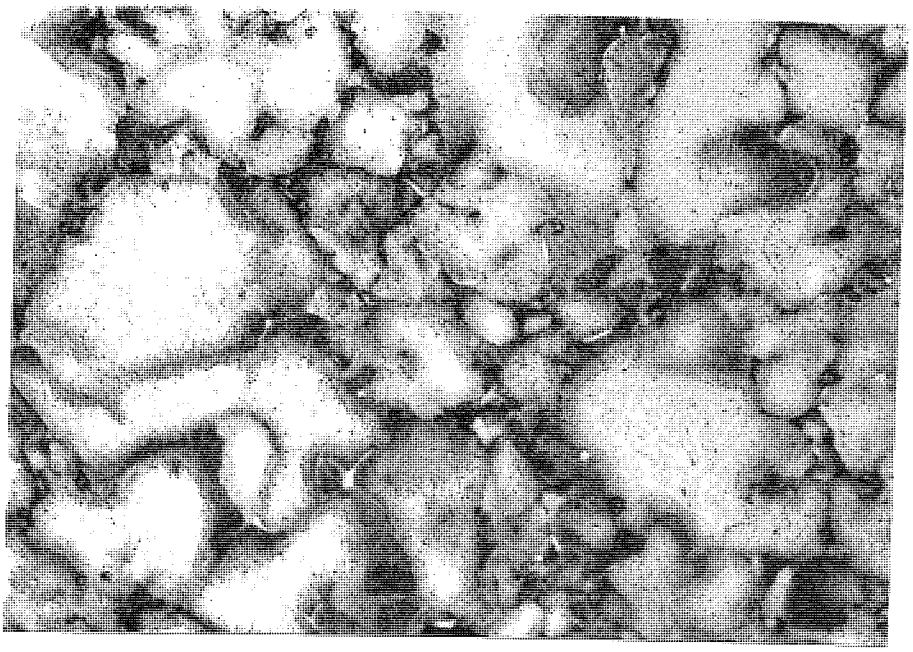

b) Fe-4Cu, immersion coated (I.C) x490

Figure 3.14 - Sintered microstructure of Fe-4Cu compacts.

The pH of the solution was measured using a pH meter, and was found to be 3.21, showing that the copper sulphate solution was acidic. This was already expected due to the highly polarizing nature of Cu^{2+}. This acidity would then result from the following reaction:

$$Cu^{2+} + H_2O = (CuOH)^{+} + H^{+}$$

$$Fe^{2+} + H_2O = (FeOH)^{+} + H^{+}$$

The pH of the solution after the immersion coating process was 3.46. The increase in the pH could be due to the following reaction:

$$Fe^{o} + 2H^{+} = Fe^{2+} + H_2$$

Thus, hydrogen is evolved and the pH raised because H^{+} ions are consumed in the above reaction. It can be deduced that the greater the surface area of the iron powder (ie finer), the quicker will be the above reaction and the more the pH is raised.

3.4.7.2 Post Coating Treatments.

The coated powder was immediately washed in distilled water and drained in a vacuum flask. It was then dried in an air circulating furnace at 80°C for 1/2 hr and crushed. Sieve analysis of the coated powder is compared with ASC100 iron in Table 3.12.

Particle Size (P) μ m	Content (%)	
	Copper Coated Powder	ASC100.29 Iron Powder.
P>150	3.3	10 max.
150>P>90	35.1	}60-80
45<P<90	38.9	
P<45	22.7	10-30

Table 3.12 - Sieve analysis of ASC100.29 and copper coated iron powder.

The sieved powder fractions, with the coarse powder fractions discarded, were then mixed for 20 minutes using a double cone blender and finally deoxidised in a tube sintering furnace, at 300°C under a reducing atmosphere of 90%N_2 / 10%H_2 and a gas flow rate of 0.015 m^3 hr^{-1}.

The tube sintering furnace is shown in Figure 3.15. The gas was dried in three stages. The first stage was a hydrogen catalyst to remove oxygen. The second was silica gel and the third magnesium perchlorate. In order to prevent sucking back of the moisture, two water bottles were installed through which excess gas was bubbled. Before reduction, the furnace was flushed out with the gas at high flow rate of 0.03 m^3 hr^{-1} for 10 minutes. The powder was then taken into the hot zone of the furnace by means of a wire attached to the tray containing the powder. After reduction, the powder was cooled by pulling the tray into the cooling zone.

It has been suggested (Nowotarshi, 1984), that the amount of oxide removed from copper powder, at various temperatures, was proportional to the hydrogen

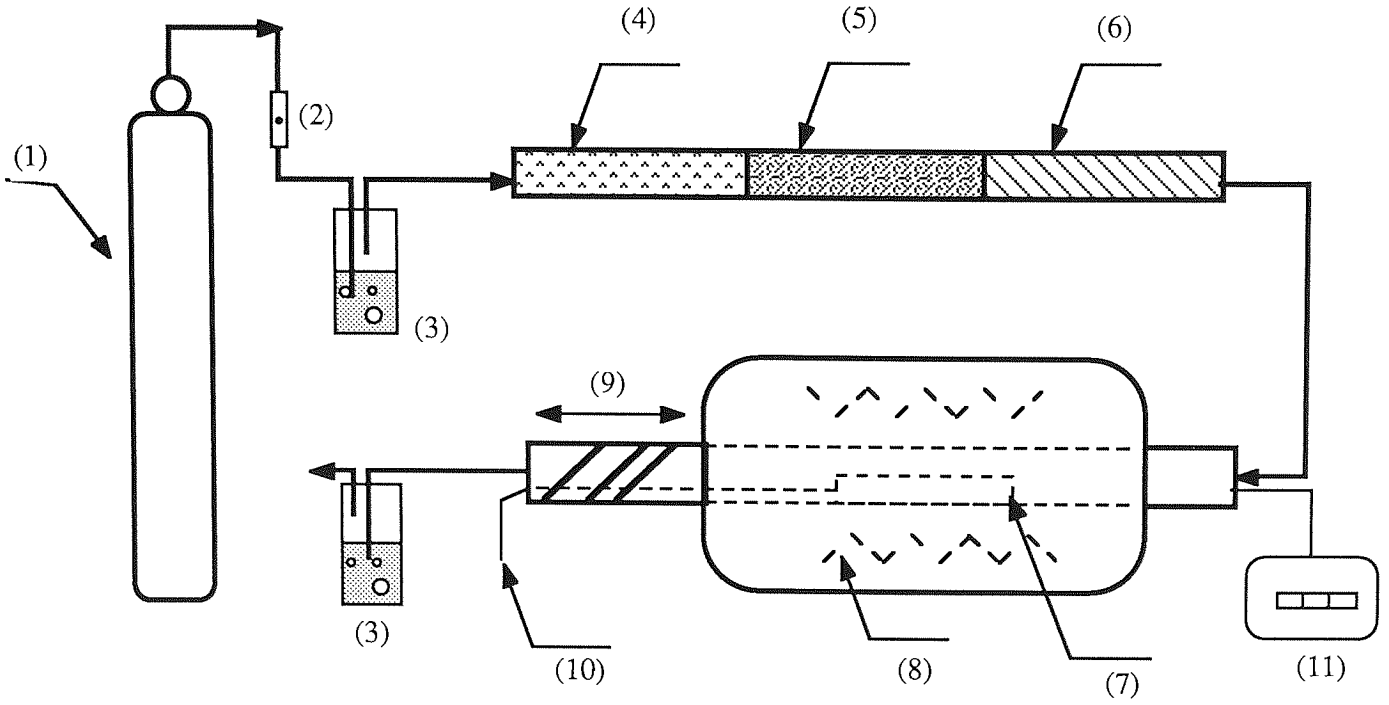

1- gas cylinder
2- gas flow meter
3- water bottle
4- hydrogen catalyst (removes oxygen)
5- silica gel (drying agent)
6- Magnesium perchlorate (drying agent)
7- specimen tray
8- nichrome heating elements
9- cooling zone
10 wire
11- temperature indicator

Figure - 3.15 Layout of the tube sintering furnace.

concentration in the atmosphere but independent of the gas flow rate. In the mentioned study, a hydrogen concentration of between 1 to 10% and a gas flow rate of 0.14 to 0.57 m^3 hr^{-1} were investigated. The coated powders were finally analysed to determine the copper levels deposited.

3.4.7.3 Atomic Absorption Spectroscopy.

The copper levels were measured accurately using atomic absorption spectroscopy. Initially iron and copper standards were made from iron and copper nitrates to 5 ppm concentration (ie. 1 mlitre of the solution in 200 mlitre distilled water). Next, one gram of the coated powder was dissolved in 50% nitric acid, made up to one litre (1000 ppm) solution and diluted so that a solution of the concentration of 4 ppm of the coated powder in made. It was important that the concentration of the coated powder solution (analyte) be less than that of the standards. The solution were then ready for analysis.

In the atomic absorption technique, a chopped exciting beam from a hollow-cathode lamp, emitting the spectrum of the analyte, scans a flame into which a solution of the analyte has been injected. The beam, now weakened by absorption by the analyte atom in the flame, passes through a monochromator, which isolates a single line of the analyte spectrum. A photocell, amplifier and readout device then measure the intensity of the analyte line. A signal obtained in the same manner but with the copper standard only (no absorption), permits the calculation of percent absorption, which is an indication of copper concentration in the solution.

3.5 Supplementary Study

3.5.1 Optical and S.E.M Examination

The microspecimens were initially examined in etched and unetched conditions with a Polyvar optical microscope in order to visualize:

a) Copper diffusion regions.

b) Copper infiltration profiles

c) Effect of carbon upon copper diffusion and infiltration.

d) The dihedral angles.

For comparison, a single magnification was employed.

The micro specimens were also examined at higher magnification, using a Stereoscan Cambridge "S150" Scanning Electron Microscope (S.E.M), to reveal the pore morphologies. The S.E.M, had a "Link system 860" energy dispersive X-ray analysing attachment, which provided:

a) Spot analysis, giving localised concentration of the elements.

b) Line concentration profile of copper within the iron matrix.

c) Rapid quantitative and semi-quantitative analysis, although this was found to be inaccurate for elements below 0.25% concentration.

d) X-ray image analysis, to identify the copper concentration regions.

The above is achieved by accelerating a beam of electrons through a potential of ~20 KV, focused to a point on the specimen. On hitting the specimen surface, some of the incident electrons are "backscattered" with almost no loss in energy. Other "secondary" electrons are emitted from the surface due to interaction with the electron beam. These emitted electrons are thrown out in all directions and some are intercepted by scintillation counter or solid state detectors. The signal from the detector is amplified and used to modulate the intensity of the beam on a cathode ray tube(C.R.T) which is scanned in a fixed raster synchronised with the electron beam

on the specimen. Thus, as the focused beam passes over the specimen, points which emit more electrons appear bright whereas other parts are dark on the screen. The brightness of the image depends on the number of electrons emitted which in turn depends on the atomic number of the element under the beam. Since the atomic numbers of the elements of the study (copper and iron) are close to each other (29 and 26 respectively), contrast between the two elements was not achieved. Thus, another cambridge S.E.M "S2a" which had a backscattered electron detector attachment was used where high resolution and good contrast was needed.

Secondary electron emission depends to some extent on the atomic number of the elements on the material surface but mostly on the surface topography. Additional preparation of the metallographic specimens was required prior to S.E.M examination, that is, gold plating on the specimen surface. This was done to prevent vaporization of Araldite when subjected to bombardment of the electron beam which produces localized heating to about 200°C. Where chemical analysis was to be performed, Araldite was dissolved in "dichloro ethane" prior to the examination.

3.5.2 Electron Probe Microanalysis (EPMA)

As mentioned in the previous section, S.E.M will not provide an accurate chemical analysis of a sample. A Cambridge EPMA, "Mark 5", was used for accurate elemental analysis, down to a level of 0.1%. The greater sensitivity is because the EPMA is optimized for the generation and detection of X-rays, rather than for producing electron images. The EPMA also has an optical microscope so that the specimen can be examined in reflected light before the region to be analysed is

chosen. The instrument settings are listed in Table 3.13.

Gas proportional counter	Argon
Condenser lens	0.42 Amp.
Final condenser lens	20 KV
Beam current	135 μA
Electron gun	20 KV
Crystal	Lithium Floride (LIF)

Table 3.13 - Electron probe microanalyser settings.

X-ray of a particular energy will be reflected off the planes of atoms in the crystal at a particular angle. High energy X-rays reflect at small angles and low-energy X-rays at large angles. The actual angle can be calculated from the Bragg equation:

$$\text{Sin } \theta = \frac{n\lambda}{2d} \quad \text{.....(3.4)}$$

where:

$$\lambda = \frac{12.4}{E} = \text{X-ray wavelength , in Å.}$$

θ= The Bragg (or reflection) angle.

d= Interplanar spacing of the set of crystal planes used for reflection, in Å.

n= An integer

E= X-ray energy, in KeV

For a given d, and θ, only X-rays of a fixed wavelength will be diffracted into the X-ray detector (Figure 3.16), the rest, just pass through the crystal and will be invisible. The probe was mainly used for quantitative analysis of copper and iron, which was carried out as follows:

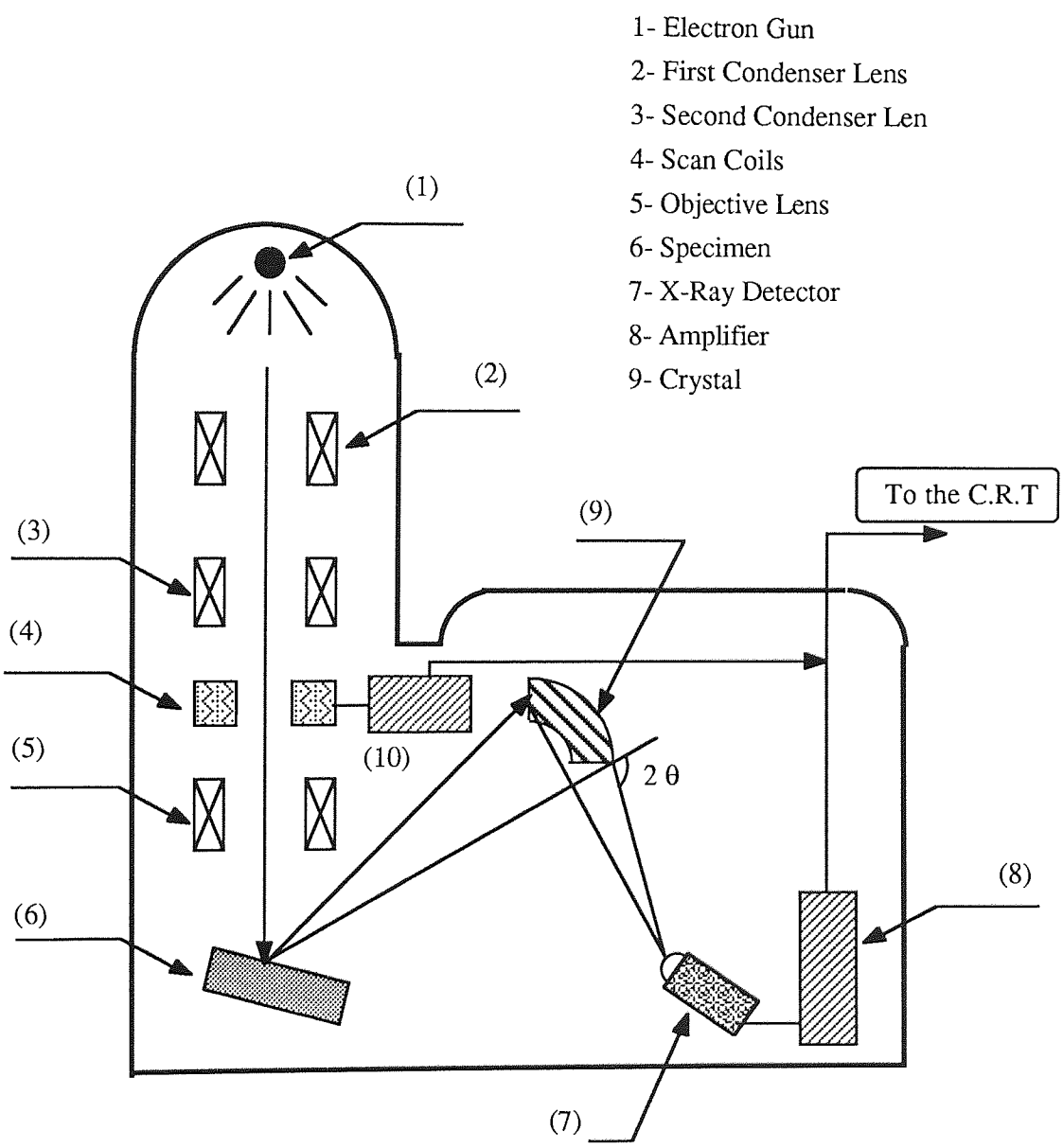

Figure 3.16 - Schematic Layout Of The E.P.M.A , Showing The Bragg Angle.

A strong emission peak with no overlaps from other elements present was selected by adjusting the crystal spectrometer and the X-ray count-rate, P, measured. The angle was offset by 2 degrees, either side of the peak and the background X-ray, B, was measured. The maximum count rate, MC, in the peak was then calculated as:

$$MC\ (Specimen) = P - B$$

Prior to which a dead time correction (lost counts), was added to the peak. The same procedure was repeated for the standard to get the maximum count rate of the standard, MC (standard). The concentration of the element, CN (element), was obtained from the equation:

$$CN\ (Element) = \frac{MC\ (Specimen)}{MC\ (Standard)} \times CN(Standard) \quad .....(3.5)$$

Where CN (standard) is the concentration of the element in the standard.

CN (element) was not the true concentration of the analysed element. This is because X-rays may be absorbed or even augmented in their passage through the surface into the spectrometer. Hence, necessary corrections were made for atomic number (Z), absorption (A) and fluoresence (F). This was done, using a "ZAF 4" programme on a computer to get the true mass concentration.

4. Results

4. Results

4.1 Anchorbraze Study.

In the initial experiments a commercially available brazing alloy, "Anchorbraze", was used in conjunction with plain iron compacts. It was noticed that the brazing powder melted, but it did not penetrate into the iron matrix at the brazing temperature 1125±2°C. A quantitative SEM elemental scan analysis using the ZAF4 correction programme is shown in Table 4.1. It can be seen that it contains copper, nickel, manganese and silicon, all of which contribute in a chemical reaction with iron, thus reducing the penetration of the brazing material.

Element	Efficiency Factor	Total%
Si	0.68	1.8
Mn	0.75	6.6
Fe	0.85	23.2
Ni	1.19	37.8
Cu	1.38	30.4

Table 4.1 - Quantitative elemental scan of Anchorbraze after brazing for 3 minutes.

Figure 4.1, illustrates with a photomicrograph the interface between Anchorbraze and iron at 1K magnification. X-ray images of the constituent elements reveal that, nickel and copper were mainly confined to the surface but manganese could diffuse well into iron matrix.

Table 4.2, lists the alloying constituents of the areas shown in Figure 4.2 after brazing. Area 1, the white phase, consisted of 79.9% copper, whilst area 2, (grey) and area 3, (dark), consisted mainly of iron. The amount of Anchorbraze in area 3

was negligible.

Element (%)	Phase 1	Phase 2	Phase 3
Si	0.0	0.5	0.2
Mn	5.8	3.5	0.2
Fe	8.7	78.8	98.3
Ni	5.4	10.4	0.9
Cu	79.8	6.6	0.2

Table 4.2 - Alloying constituents of the phases shown in Figure 4.2.

4.2 Copper Infiltration

The compacts were all sintered and infiltrated simultaneously. The sintering experiments were repeated for compacts undergoing the same treatment, but with no copper in top cavity of the compacts. This was done for comparison purposes. Most of the samples were eroded by the molten copper, and pits could be seen on the surface and sides of the specimens (Figure 3.8). In industrial situations, this problem can be overcome by adding 4.0% iron to copper powder (U.S patent, 3307924).

During sintering the rearrangement and solution reprecipitation mechanisms occurred. Weak iron particle contacts were broken by the liquid phase, resulting in the formation of larger pores just below copper-iron interface. These large pores were not observed further down the infiltration path.

Figure 4.3 shows an optical micrograph of a sample infiltrated at 1100°C for 3 minutes. It suggests that firstly copper melted and rapidly ran into the pores and interparticle contacts. Then dissolution of iron by liquid copper occurred quickly,

seen as dark narrow lines and finally, due to short infiltration time and low temperature, only some of the copper could penetrate into the iron matrix.

In order to investigate whether the molten copper penetrated along the grain boundaries, samples were produced in the etched condition (Figure 4.4). After 3 minutes infiltration at 1100°C, copper could only go into the pores and the iron grain boundaries. This is because copper penetration in the grain boundaries is comparatively a quick process. However, when infiltrating for 60 minutes at 1200°C (Figure 4.5), copper not only totally infiltrated but also fully diffused into iron, so that no isolated copper rich islands could be seen in the microstructure.

4.2.1 Dimensional Changes.

The effect of infiltration time, on the maximum radial dimensional changes is shown in Figure 4.6. For comparison, compacts of 6.4 and 6.9 Mgm^{-3} are included. It is evident from this figure that the lower density compacts expanded less than the higher density ones. Figure 4.7, shows the effect of sintering temperature on dimensional changes. The same trend mentioned above is again evident for compacts having densities of 6.4 and 6.9 Mgm^{-3}. Figure 4.8, illustrates the effect of sintering temperature on 6.4 Mgm^{-3} samples treated for 10 and 40 minutes. The compacts infiltrated for 40 minutes, underwent more expansion than those sintered for 10 minutes. The sample sintered for 10 minutes at 1100°C, shrank by 0.1% whereas the one sintered for 40 minutes expanded less than 0.1%, presumably due to diffusion of copper into iron.

Figure 4.9, illustrates the effect of density variation upon dimensions after infiltrating at 1125°C for 10 and 40 minutes. As the density is increased, the expansion is also increased. On the other hand, samples infiltrated for 40 minutes

revealed higher expansion of up to 0.7% for a density of 7.4 Mgm^{-3}.

Figure 4.10 shows the effect of sintering temperature on compact dimensions after infiltrating for a constant time of 40 minutes. It confirms that, at each temperature, compacts having a density of 6.4 Mgm^{-3} expanded less than those with 6.9 Mgm^{-3} density. The specimen sintered at 1100°C and with a density of 6.4 Mgm^{-3} had virtually zero expansion as compared with the one having a density of 6.9 Mgm^{-3}. The graph of percentage change in dimension versus the sintering temperature is shown in Figure 4.11.

The densities were being kept at a nominal value of 6.9 Mgm^{-3}. It compares the dimensional behaviour of the specimens with the different sintering times of 10 and 40 minutes. Two points emerge from this figure. First, the specimen infiltrated at 1100°C for 10 minutes had a shrinkage of 0.1% whereas the one with an infiltration time of 40 minutes had an expansion of more than 0.2%. Second, the graphs meet at a point representing the infiltration temperature of 1200°C.

Compacts containing 0.15 and 0.6% graphite were made to a density of 6.9 Mgm^{-3} and infiltrated for 10 minutes, at various temperatures. The results are shown in Figure 4.12. Interestingly, the specimens containing no graphite exhibited greatest expansion and specimens containing 0.6% graphite recorded shrinkage at 1100°C. The specimens with 0.15% graphite had characteristics between the two mentioned limits.

The comparison in the dimensional behavior of infiltrated compacts with those not infiltrated with copper and sintered at various temperatures for 10 minutes, is shown in Figure 4.13. With increase in sintering temperature, samples with copper, expanded up to 0.6% at 1200°C. Comparatively, samples with no copper shrank down to about 0.2% at 1125°C and underwent no significant change up to 1200°C. Hence, sintering at 1125°C was sufficient for maximum shrinkage for

plain iron compacts.

The effect of sintering time upon dimensional changes of infiltrated specimens compared to the plain iron specimens is shown in Figure 4.14. The same trend as illustrated in Figure 4.13 is quite evident, except that, the variation in sintering time from 5 to 40 minutes does not seem to affect the amount of shrinkage for non-infiltrated specimens.

Figure 4.15, illustrates the dimensional changes which occurred in plain iron compacts of varying densities, after sintering at 1125°C in vacuum. Specimens sintered for 40 minutes, underwent more shrinkage than those sintered for 10 minutes. Moreover, the rate of expansion was greatest in the compacts with densities of 6.9 to 7.4 Mgm^{-3}.

Figure 4.16, depicts the effect of variation in sintering temperature on the dimensional stability of plain iron compacts. Specimens having a density of 6.4 Mgm^{-3} experienced more shrinkage than those having a density of 6.9 Mgm^{-3}. The maximum shrinkage recorded was 0.21% belonging to a specimen sintered at 1150°C for 40 minutes in vacuum. No further change in dimensions occurred from 1150°c to 1200°C.

The overall dimensional changes of the samples are shown, in the form of bar charts in Figures 4.17 and 4.18. The sample's specification is shown in Tables 4.3 and 4.4. On the vertical axis, the specimen labels can be seen. The prefixes B and C, denote samples in the infiltrated and non-infiltrated conditions respectively. Hence labels B1 and C1 refer to samples which had undergone the same treatment but in two different conditions.

The maximum expansion of about 1.0% belonged to a sample infiltrated at 1200°C for 10 minutes and having a density of 6.90 Mgm^{-3} {Figure 4.17(b), sample B20}. Whereas maximum shrinkage was exhibited by a 6.34 Mgm^{-3} plain iron specimen,

sintered at 1200°C for 40 minutes {Figure 4.18(b), sample C24}.

Label	Density Mgm^{-3}	Dimensional change %	Time min.	Temperature °C
B1	6.47	0.157	5	1125
B2	6.36	0.157	10	1125
B3	6.41	0.228	20	1125
B4	6.37	0.370	40	1125
B5	6.43	-0.102	10	1100
B6	6.36	0.236	10	1125
B7	6.45	0.370	10	1150
B8	6.45	0.638	10	1200
B9	6.34	0.189	10	1125
B10	6.62	0.307	10	1125
B11	6.96	0.244	10	1125
B12	7.42	0.441	10	1125
B13	6.95	0.291	5	1125
B14	7.01	0.354	10	1125
B15	6.99	0.402	20	1125
B16	6.94	0.512	40	1125
B17	6.92	-0.071	10	1100
B18	6.92	0.331	10	1125
B19	6.91	0.709	10	1150
B20	6.92	0.961	10	1200
B21	6.38	0.047	40	1100
B22	6.38	0.457	40	1125
B23	6.35	0.622	40	1150
B24	6.37	0.867	40	1200
B25	6.92	0.276	40	1100
B26	6.91	0.591	40	1125
B27	6.90	0.843	40	1150
B28	6.95	0.930	40	1200
B29	6.35	0.402	40	1125
B30	6.58	0.418	40	1125
B31	6.90	0.694	40	1125
B32	7.38	0.685	40	1125

Table 4.3 - Sintering condition of the infiltrated compacts.

Label	Density Mgm^{-3}	Dimensional change %	Time min.	Temperature °C
C1	6.47	-0.142	5	1125
C2	6.44	-0.181	10	1125
C3	6.47	-0.150	15	1125
C4	6.45	-0.134	20	1125
C5	6.33	-0.016	10	1100
C6	6.37	-0.181	10	1125
C7	6.35	-0.173	10	1150
C8	6.34	-0.173	10	1200
C9	6.34	-0.110	10	1125
C10	6.63	-0.087	10	1125
C11	6.89	-0.095	10	1125
C12	7.41	0.047	10	1125
C13	6.89	-0.134	5	1125
C14	6.89	-0.134	10	1125
C15	6.90	-0.118	15	1125
C16	6.89	-0.134	20	1125
C17	6.90	-0.134	10	1100
C18	6.89	-0.150	10	1125
C19	6.90	-0.126	10	1150
C20	6.89	-0.158	10	1200
C21	6.34	-0.166	40	1100
C22	6.34	-0.173	40	1125
C23	6.36	-0.205	40	1150
C24	6.34	-0.205	40	1200
C25	6.90	-0.142	40	1100
C26	6.94	-0.134	40	1125
C27	6.89	-0.158	40	1150
C28	6.94	-0.189	40	1200
C29	6.31	-0.181	40	1125
C30	6.57	-0.166	40	1125
C31	6.89	-0.166	40	1125
C32	7.37	-0.095	40	1125

Table 4.4 - Sintering conditions of the non - infiltrated compacts.

4.2.2 Double and Two Step Infiltration.

The behaviour of double and two step infiltrated experiments are shown in Figure 4.19. After infiltrating at 1100°C, the double infiltrated specimen underwent an expansion of 0.1%, but the two step infiltrated specimen recorded a shrinkage of the same amount.

Figure 4.20 shows the difference in microstructure between double and two step infiltration. The structure of two step infiltrated sample shows very large copper regions compared to the double infiltrated one which showed a more homogeneous microstructure.

4.2.3 Area of Copper Infiltration.

An optical micrograph of the infiltrated area is shown in Figure 4.21. The infiltrated area appeared dark after etching for 2 minutes in 2% Nital.

Figure 4.22, illustrates the change in area of infiltration as a function of density, for 10 and 40 minutes. The experiments were done at 1125°C in vacuum. Considering those samples infiltrated for 40 minutes, an increase in density from 6.35 to 7.40 Mgm^{-3}, increased the copper infiltration area from 3250 to 5000 mm^2. Another point to note is the slope of the two lines, indicating that the rate of copper infiltration is lower when infiltrating for 10 minutes than for 40 minutes. Finally, there was not an appreciable difference in the extent of infiltration for compacts with a density of 6.35 Mgm^{-3}. Figure 4.23 illustrates the change in infiltrated area as a function of temperature, for compacts with densities of 6.4 and 6.9 Mgm^{-3}. The experiments were performed for 40 minutes in vacuum. Specimens with a density of 6.9 Mgm^{-3} experienced more copper infiltration than those with a density of 6.4 Mgm^{-3}. Moreover, the rate of infiltration was higher for the specimens with higher

density, with the two lines diverging from each other.

4.2.4 Heat Tinting.

In order to reveal the copper rich regions by another method, as a check, heat tinting was used. Figure 4.24, shows a sample infiltrated at 1100°C for 60 minutes, and heat tinted at 300°C for one hour. The copper rich phase appeared bright and iron appeared dark. As copper melts, it dissolves the surrounding iron. When the temperature is reduced, the solubility of copper in iron is decreased. As a result, iron precipitates in the form of a dark band at copper-iron interface. Since copper is not oxidised, copper diffusion appears as a bright white band, surrounding the iron.

Figure 4.25, shows a photomicrograph of back scattered electron image of the heat tinted specimen. It reveals two distinct regions:

a) Infiltrated area, containing copper in solution in iron and also in the pores. This area resisted oxidation due to its copper content.

b) Non infiltrated area, containing only iron which was oxidised. The oxide scales can clearly be seen in this figure.

4.3 Multiple Regression.

4.3.1 Dimensional Changes.

This statistical analysis was done on 32 differently processed specimens (Table 4.3), using a statistical package described in section 3.4.2.

4.3.1.1 Correlation Matrix.

Table 4.5, lists the correlation matrix. It illustrates whether there is any correlation among the independent variables.

Dimensional change	1.0	0.55	0.26	0.19
Density	0.55	1.0	-0.04	-0.039
Time	0.26	-0.04	1.0	0.03
Temperature	0.19	-0.039	0.03	1.0

Table 4.5 - Correlation matrix for the regression model of dimensional changes.

Since the numbers in the correlation matrix were very small, it can be deduced, there is no correlation between the independent variables (Edwards, 1979). Therefore, the second assumption which was made in section 3.4.2 is valid.

4.3.1.2 Analysis of Variance Table.

Source	**ΣSquares**	**D.O.F**	**Mean squares**	**F-ratio**	**Prob.>F**
Model	2.050	3	0.683	75.793	0.00
Residuals	0.252	28	0.009		
Total	2.302	31			
Coefficient of Determination			0.890		
Coefficient of Correlation			0.944		
Standard Error of Estimate			0.095		
Durbin Watson Statistics			2.275		

Table 4.6 - Analysis of variance table for the regression model of dimensional changes.

Table 4.6 gives the computer output showing the partitioning of sum of squares into the sum of squares for the model and the sum of squares for the residuals. The model sum of squares has 3 degrees of freedom, equal to the number of dependent variables. The residuals sum of squares has (n-3-1) degrees of freedom, where n is 32, the total number of experiments. Note that mean squares, is the sum of squares divided by the degrees of freedom. For the test of significance of the regression, F=75.79 with 3 and 28 degrees of freedom. This is a significant value, since there is zero probability of getting values greater than F. The F ratio is calculated from:

$$F=\frac{\text{mean square between samples}}{\text{mean square within samples}}$$

The coefficient of determination (R^2) was found to be 0.89. This coefficient explains the total variability of dimensional changes (Y), as a function of the experimental variables (X). The more closely X and Y are linearly related, the more the variability in the Y values can be explained by the variability in the X values and closer R^2 will be to 1.

The coefficient of correlation (R) was very good, being at 0.94. This means that, generally 94% of the variables lay on a straight line. The positive sign implies a positive linear correlation or a positive slope. Hence an increase in X, results in an increase in Y.

4.3.1.3 Correlation Coefficients.

Table 4.7 lists the correlation coefficients of the infiltrated samples. It can be seen that the coefficients are positive for the sintering variables. A positive sign implies large X induces large Y (Chatfield, 1983). If the coefficients had been negative,

large X results in large decrease in Y.

Variable	Coefficient	Std. Error Est.	t-Stat.	Prob.>t
Constant	-10.335	0.787	-13.138	0.00
Density	0.296	0.054	5.528	0.00
Time	0.007	0.001	6.446	0.00
Temperature	0.008	0.001	12.536	0.00

Table 4.7 - Correlation coefficients for the regression model of dimensional changes.

t-statistic values were calculated by dividing the coefficients by their respective standard error estimates. The t-statistic was 12.53 for the temperature and 5.52 for the density. This implies that the temperature had the highest and the density, the lowest effect upon dimensional changes. All the values quoted in Table 4.7 are significant since the probabilities of getting values greater than t, are zero.

Therefore, the multiple regression model, with dimensional change as the dependent variable and density, temperature and time as the independent variables can be written as:

$$Y=-10.335342 + 0.29587\ \rho + 0.007288\ t + 0.007585\ T \quad \text{..... (4.1)}$$

where ρ= density (Mgm^{-3})

t = time (minutes)

T = temperature (°C)

Y = dimensional changes %

In order to evaluate the residuals, a graph of residuals versus Y(calculated) is plotted (Figure 4.26). It was found that no actual pattern existed, justifying the regression formula.

4.3.2 Copper Infiltration Area

4.3.2.1 Correlation Matrix

Dimensional change	1.00	0.30	0.42	0.78
Density	0.30	1.00	-0.04	-0.04
Time	0.42	-0.04	1.00	0.03
Temperature	0.78	-0.04	0.03	1.00

Table 4.8 - Correlation matrix for the regression model of copper infiltration area.

The same statistical method was repeated, but this time with copper infiltration area as the independent variable. From the correlation matrix (Table 4.8), it can be seen that no correlation exists among the independent variables.

4.3.2.2 Analysis of Variance

The analysis of variance (Table 4.9), gives a value of 7.11 for the F ratio and 1% for the probability of values greater than F. Compared to the previous calculations, the coefficient of correlation (R) was only 0.65, hence 35% scatter in the experimental points.

The coefficient of determination was 0.43, compared to 0.89 of the previous multiple regression calculations. Therefore, in this case, the variability in infiltrated area can be explained to a lesser extent with the variability in the infiltrating variables. In other words, the area of copper infiltration and the sintering variables are much less linearly related than those of the dimensional changes.

Source	Σ Squares	D.O.F	Mean Squares	F-Ratio	Prob.>F
Model	8186434.66	3	2728811.55	7.1132	0.001
Residuals	10741521.67	28	383625.77		
Total	18927956.33	31			
Coefficient of Determination			0.432		
Coefficient of Correlation			0.657		
Standard Error Estimate			619.37		
Durbin Watson Statistics			2.673		

Table 4.9 - Analysis of variance table for the regression model of copper infiltration area.

4.3.2.3 Correlation Coefficients

Table 4.10 lists the correlation coefficients. Positive correlation exists among the area and independent variables. t-statistics was 4.0, 1.96 and 1.46 for density, time and temperature respectively, implying that here, density has been the most contributing factor in copper infiltration.

Variable Name	Coefficient	Std. Error Est.	t-Stat.	Prob.>t
Constant	-12530.4911	5131.9804	-2.4416	0.021
Density	1404.4624	349.1610	4.0224	0.00
Time	14.4586	7.3754	1.9604	0.059
Temperature	5.7740	3.9472	1.4628	0.154

Table 4.10 - Correlation coefficients for the regression model of copper infiltration area.

Therefore, the multiple regression model, with area of copper infiltration as dependent variable and density, time and temperature as independent variables may be written as:

$$Y' = -12530.4911 + 1404.4624\,\rho + 14.4586\,t + 5.7740\,T \ldots\ldots (4.2)$$

The graph of residuals versus Y'(calculated) is plotted in Figure 4.27.

The regression models described in Equations 4.1 and 4.2 apply only to the particular set of experimental conditions described before.

4.4 Dihedral Angle

4.4.1 Iron-Copper System

Figure 4.28 depicts the frequency of the observed dihedral angles of an infiltrated sample, treated at 1125°C for 20 minutes in vacuum. 36% of the dihedral angles lay between zero and 4.5 degrees. Out of 119 readings, 27 angles were zero. Mean and standard deviations are given in Table 4.11. The mean dihedral angle was 9.8 degrees which can be used in the calculation for the surface tension and the grain boundary energy by. using the Smith's equation:

$$2\cos\frac{\phi}{2} = \frac{\gamma_{gb}}{\gamma_{SL}} \ldots\ldots\ldots (4.3)$$

where;

ϕ = dihedral angle

γ_{SL} = solid / liquid interfacial energy Jm^{-2}

γ_{gb} = grain boundary energy Jm^{-2}

Data File: Cu only(B14)		Observations: 119	
Variable: Dihedral Angle			
Minimum:	0.00	Maximum:	41.0
Range	41.0	Median:	9.00
Mean:	9.8	Standard Error:	0.85
Variance:		86.77	
Standard Deviation:		9.31	
Coefficient of Variation:		84.23	
Skewness:		0.95	
Kurtosis:		0.55	

Table 4.11 - Statistical presentation of observed dihedral angles for the sample containing no graphite.

4.4.2 Effect of 0.15% Carbon

Figure 4.29 reveals the effect of 0.15% carbon upon dihedral angle, for a specimen infiltrated with the same conditions as the one in quoted Section 4.4.1. Surprisingly, the mean dihedral angle is shifted from zero so that 43% of the readings were between 20 and 30 degrees.

The addition of 0.15% carbon also reduced the number of zero dihedral angles from 27 to 12. The mean dihedral angle is given in Table 4.12.

Figure 4.30 depicts optical photomicrographs of an iron compact, containing 0.15% carbon and infiltrated at 1100°C for 10 minutes. It shows the three regions of a) iron / copper interface. b) copper infiltrated area and c) non-infiltrated area. After 10 minutes only part of the copper melt penetrated the compact. The level of porosity was also very low in the infiltrated region as compared to the non-infiltrated region. This compact had a shrinkage of 0.126%. Figure 4.31 illustrates the microstructure of a Fe-0.15% C compact, infiltrated at 1150°C. In this test, the molten copper fully penetrated into the pores and iron particle contact area, leaving large pores at the surface. Figure 4.31(b), shows the level of porosity was much less than the one shown in Figure 4.30(b). Figure 4.31(c) shows where the infiltration process stopped. Note that there exists a porosity gradient as a result of a decrease in copper concentration. This specimen expanded by 1.70%.

Data File: Cu+0.15 C Variable: Dihedral Angle		Observations: 120	
Minimum:	0.00	Maximum:	50.0
Range	50.0	Median:	21.0
Mean:	20.28	Standard Error:	1.07
Variance:		138.57	
Standard Deviation:		11.77	
Coefficient of Variation:		58.06	
Skewness:		0.22	
Kurtosis:		-0.25	

Table 4.12 - Statistical presentation of observed dihedral angles for the sample containing 0.15% graphite.

4.4.3 Effect of 0.6% Carbon

The effect of 0.6% carbon upon dihedral angle is shown in Figure 4.32. The mean dihedral angle has been shifted even further to a higher value. Here, 47% of the dihedral angles were between 37.5 and 52.5 degrees, making the mean dihedral angle of 41.5 degrees (Table 4.13). The grain boundary energy is then given as: Notably, adding 0.6% graphite to a plain iron compact (infiltrated with copper) has reduced the number of zero dihedral angles from 27 in the compact with no graphite additions to only 3.

Data File: Cu+0.6 C Variable: Dihedral Angle		Observations: 120	
Minimum:	0.00	Maximum:	75.0
Range	75.0	Median:	45.0
Mean:	41.64	Standard Error:	1.35
Variance:		218.75	
Standard Deviation:		14.79	
Coefficient of Variation:		35.52	
Skewness:		-0.53	
Kurtosis:		0.22	

Table 4.13 - Statistical presentation of the observed dihedral angles in the specimens containing 0.6% graphite.

Figure 4.33 illustrates the microstructure of a Fe-0.6 C compact infiltrated at 1100°C for 10 minutes. The level of free isolated copper was higher {Figure 4.33(b)} than the one shown in Figure 4.30(b). Moreover, the level of porosity in the non-infiltrated region {Figure 4.33(c)} was much lower than the one in Figure 4.30(c). Comparison in microstructure of Fe-Cu-C and Fe-Cu systems are shown in Figure 4.34. Plate (a) shows a number of small pores filled with copper and low dihedral angles. On the other hand plate (b), exhibits a large copper region, fewer porosity and large dihedral angles. Additionally, X-ray photomicrographs revealed more large segregated copper regions with Fe-Cu-0.6C system whilst copper was comparatively uniformly distributed in Fe-Cu system (Figure 4.35). Finally, the effect of carbon upon dihedral angles and solid / liquid interfacial energies are summarised in Figure 4.36.

4.4.4 Dimensional Effect

The effect of carbon addition upon dimensional changes is shown in Figure 4.37. With an increase in carbon addition from zero to 0.6%, the expansion of the specimens was reduced from 0.16 to 0.06 percent. Another point to note is that the rate of decrease in expansion is higher from zero to 0.15% carbon additions compared to an increase in carbon from 0.15 to 0.6%.

The effect of carbon additions on the infiltrated area is depicted in Figure 4.38. It is interesting to note that an increase in carbon addition resulted in an increase in the depth of copper infiltration.

4.5 Copper Concentration Profile

After quantitative concentration measurements and correction for atomic number, fluoresence and absorption, the copper concentration profiles were obtained.

Figure 4.39 exhibits the copper concentration profiles for specimens sintered at 1200°C for 10 minutes with densities of 6.99 and 6.40 Mgm^{-3}. Copper concentration and penetration was higher for the compact with higher density. The depth of penetration of which was 6.0 mm below the surface. Note that the copper concentration remained constant up to a certain depth and then dropped to a zero. On the other hand, compacts infiltrated at 1125°C (Figure 4.40) did not exhibit a region of uniform copper concentration. Instead, the concentration dropped from ~4.0% to a minimum in a linear mode. However, the compact with a density of 7.5 Mgm^{-3} confirmed greater copper penetration compared to the one with a density of 6.4 Mgm^{-3} (Figure 4.40).

The effect of infiltration temperature on copper concentration profile is illustrated in Figure 4.41. The copper concentration decreased linearly from 4.5% to 0.0% 3 mm below the surface, for the compact infiltrated at 1150°C whilst the one infiltrated at 1100°C infiltrated to a depth of 2.0mm.

Figure 4.42, depicts the copper concentration profile of compacts infiltrated at 1125°C for 5 and 20 minutes. Copper concentrations were equal on the surface, however, the copper penetration depth of the compact infiltrated for 20 minutes was twice the penetration depth for the compact infiltrated for only 5 minutes.

Comparing Figures 4.39 and 4.42, it is clearly evident that copper distribution is homogenised if the compact is treated at 1200°C (Figure 4.39), whereas a large scatter in copper concentration is recorded when infiltrated at 1125°C (Figure 4.42). However the maximum depth to which copper infiltration proceeded, remained the same in both set of tests.

4.6 Effect of Carbon on the Solubility of Copper in Iron.

The effect of carbon on the solubility of copper in iron was further studied by evaluating the copper solubility in Fe-8Cu and Fe-8Cu-0.6C compacts after sintering at 1200°C for 1 hr in vacuum. For better accuracy three count rates were taken for each element and the mean obtained. Then the dead time was added to the mean. Finally results were corrected for "ZAF" on a computer. These results are shown in Table 4.14. The EPMA settings are quoted in section 3.6.2.

Phase System	Copper wt.%	Iron wt.%
Fe- 8Cu- 0.6C	4.2	95.7
Fe- 8Cu	7.0	92.9

Table 4.14 -. EPMA Quantitative Analysis for iron and copper at Fe / Cu interface.

The above results indicate that carbon tends to reduce the solubility of copper in iron.

Using the solubility data of copper in alpha iron given by Speich et al. (1966), the heat of formation of copper from solid solution may be calculated.

The free energy of precipitation of copper, $\Delta G°$, and heat of formation of copper from iron, $\Delta H°$, per mole of copper may be written as:

$$\Delta G° = -RT \ln (K) \quad .....(4.4)$$

$$\Delta H° = \Delta G° + T \Delta S° \quad .....(4.5)$$

Where:

R= Gas constant = 8.314 J mol^{-1} K^{-1}

K= Rate constant

ΔS° = Change in entropy of precipitation of copper from iron, per mole of copper.

Assuming ideal solution:

$$K = \frac{\left[a_{Cu}^{Cu}\right]}{\left[a_{Cu}^{\alpha}\right]} \ldots\ldots\ldots (4.6)$$

Where: a_{Cu}^{Cu} = activity of pure copper

a_{Cu}^{α} = activity of copper in iron.

For an ideal solution, $a_{Cu}^{Cu} = 1$ and $a_{Cu}^{\alpha} = S$ (solubility of copper in α). Hence:

$$K = \frac{1}{S} \ldots\ldots\ldots (4.7)$$

Therefore from the above, we can state that the heat of precipitation of copper is dependent on the solubility of copper in iron.

From Equations 4.4, 4.5 and 4.7, we can write:

$$\ln (S) = \frac{\Delta H^\circ}{R} x \frac{1}{T} - \frac{\Delta S^\circ}{R} \ldots\ldots (4.8)$$

This is an equation for a straight line with $\frac{1}{T}$ as the variable, $\frac{\Delta S^\circ}{R}$ as the intercept and $\frac{\Delta H^\circ}{R}$ as the slope of the line. The corresponding data are listed in Table 4.15.

Temperature (T)	Solubility (S)	$1/T*10^3$	ln (S)
699	0.53	1.43	-0.63
730	0.72	1.37	-0.33
750	0.97	1.33	-0.03
776	1.33	1.29	0.28
832	1.57	1.20	0.45

Table 4.15 - Solubility limit of copper in alfa iron.

The straight line of $\frac{1}{T}$ versus ln(S), is shown in Figure 4.43. The heat of precipitation of copper ($\Delta H°$) , may be calculated from the slope of this line, $\frac{\Delta H°}{R}$.

$$\text{Slope} = -4.9545 = \frac{\Delta H°}{R} \quad \ldots. \ (4.9)$$

$$\Delta H° = -4.9545 * 8.314$$

$$\underline{\Delta H° = -41.19 \text{ KJ mole}^{-1}}$$

The negative heat of precipitation, means that there is a preference of Fe-Fe and Cu-Cu bonds to form rather than Fe-Cu bonds. Now, as mentioned before, carbon appears to reduce the level of copper dissolved in iron. If this occurs, the value of $\Delta H°$, will be more negative, resulting in even higher tendency of Fe-Fe and Cu-Cu bonds to form. The effect of this will be more undissolved copper regions in the microstructure.

4.7 Oxidation Treatment

Since oxide films on iron particle surfaces will greatly affect wetting and flow of molten copper, the effect of oxidation on Fe-Cu compacts was studied. Generally,

oxidised samples had a lower infiltration area than the non-oxidised ones.

4.7.1 Weight Gain

Figure 4.44 illustrates the weight gain of the compacts of different densities, after oxidation at 500°C in a muffle furnace. It shows that with an increase in density from 6.4 to 7.4 Mgm^{-3}, the weight gain as a result of oxidation was reduced from 4.3 to 1.0% for the compacts oxidised for 130 minutes. On the other hand, the rate of oxidation of higher density compacts appears to be lower than the ones with a low density. Comparing the two curves for weight gain related to density, in Figure 4.44, it is evident that convergence occurs towards higher densities. This prompted the study of copper infiltration in these compacts.

4.7.2 Copper Infiltration in the Oxidised Compacts.

Figure 4.45, shows a bar chart of penetration area after infiltrating the oxidised samples at 1125°C for 10 minutes in a tube furnace. The compacts oxidised for 30 minutes, showed a penetration area of 3916 mm^2 compared to 4868 mm^2 for the non-oxidised compacts. Moreover, with an increase in the pre-oxidation time, the infiltration area decreased considerably.

Figure 4.46 shows the optical photomicrograph of a 6.92 Mgm^{-3} specimen, oxidised at 500°C for 130 minutes. Severe oxidation was noticed at the surface of the compact, but little or no oxide was seen in the core. A duplex layer of oxide was observed especially on the surface of the compact {Figure 4.46(a)}. Thinner or no duplex layer was seen underneath {Figure 4.46(b)}. The oxide layer also contained some porosity and cracks associated with it. Finally, most surface pores were totally blocked by the oxidation product.

4.7.3 Auger Electron Spectroscopy (AES).

The oxide layers responsible for weight gain and reduction in copper penetration were identified using Auger Electron Spectroscopy (AES) technique.

Figure 4.47 exhibits a typical Auger trace after the surface contamination had been etched away for 150 minutes. AES is extremely surface sensitive. The phases of the oxide layers were determined from the traces as follows:

1- Peaks were measured for iron and oxygen, then divided by their sensitivity factor.

For oxygen..... 85/0.4 = 212.5

For iron..... 35/0.22 = 159.1

Oxygen to Iron Ratio = 212.5/159.1 = 1.33

This suggests that there are 1.33 molecules of oxygen for one molecule of iron, ie $Fe_1\ O_{1.33}$. If the coefficients are multiplied by three, we get Fe_3O_4. However, it was revealed that since the oxygen sensitivity factor is higher than that of iron, it is likely to be removed when etching the surface with ions. Therefore, X-ray diffraction technique was considered to give more accurate results since the surface atoms are not removed by ions.

4.7.4 X-ray Diffraction (XRD).

Table 4.16 exhibits the Bragg angles, intensity and d-spacings of a compact oxidised at 500°C for 130 minutes. The d-spacings were calculated from Bragg formula, and the phases were looked up from Powder Diffraction File (1978). The identified phases were: magnetite(Fe_3O_4), haematite(Fe_2O_3) and alpha iron. The peak with the highest intensity belonged to magnetite.

4.8 Thermomechanical Analysis

4.8.1 Dilatometry at 960°C

Figure 4.48, shows the effect of temperature on dimensional changes of plain ASC100.29 iron compacts up to and during the isothermal sintering at 960°C. At this temperature the copper powder was present in the solid state, therefore the mechanism of any expansion is due to grain growth and solid state diffusion. Figure 4.48 shows that the compact with the lower density expanded less than the higher density compact. Both compacts continued to grow from room temperature up to ~900°C, where they underwent shrinkage due to α to γ transformation. No appreciable expansion was recorded during the isothermal sintering temperature. However, when the compacts were cooled, they initially experienced shrinkage, expanded at α to γ transformation and started shrinking again at the end of the transformation.

Figure 4.49 depicts the effect of density on the dimensional changes occurring in Fe-4Cu compacts. Compacts expand steadily up to 1.0% at 900°C. It should be born in mind that the amount of shrinkage is less in copper containing compacts than in plain Fe compacts (Figure 4.48) at the α to γ transformation point. When cooled to room temperature, the compact with a density of 6.8 Mgm^{-3} shrank more than the one at 6.0 Mgm^{-3} density.

2 θ	Intensity	d Spacing	Phase
35.2	33	2.958	M
35.7	18.5	2.918	H
38.8	12	2.693	H
41.5	61.5	2.525	M,H
43.4	13.5	2.425	H
50.5	23.5	2.097	M
52.5	18	2.022	H,Fe
63	18	1.712	M
67.3	26	1.614	M
74.3	35	1.481	M,H
76	21	1.453	H
77.2	34	1.434	Fe
77.4	30	1.431	Fe
79.2	20	1.403	Fe
80.3	20	1.387	H
99.7	15.5	1.170	Fe
100	12	1.168	Fe

Table 4.16 - X-ray diffraction data of a compact oxidised at 500°C for 130 minutes.

M= magnetite , H= haematite , Fe= alpha iron.

Figure 4.50 illustrates the effect of different levels of copper addition on dimensional changes during heating and cooling. The compact containing 8% copper expanded considerably more than the one containing 2% copper. However, when cooled to room temperature, both recorded the same amount of overall shrinkage.

The comparison between dilatometric behaviour of elementally mixed (E.M) and

immersion coated (I.C) Fe - 4Cu compacts is made in Figure 4.51. It appears that a dramatic difference in the sintering and densification mechanism exists between the two types of compacts. First thing to notice is that the rate of expansion of the I.C compact is much lower than the E.M compact. Secondly, the I.C compact, began to shrink after reaching a temperature of about 600°C whilst the E.M specimen was still expanding. In both cases α to γ transformation was completed at 920°C. Overall, on return to room temperature, the I.C specimen showed a shrinkage of 1% compared with 0.2% to that of the E.M specimen.

Figure 4.52 illustrates the effect of 0.6% graphite addition on dilatometric characteristics of E.M and I.C powders. Similar trend to those seen in Figure 4.51 is shown, with an additional feature that graphite addition tends to inhibit growth. However, the promotion of shrinkage by the graphite addition appears to be much greater in the E.M compacts. Also, the presence of graphite lowered the α to γ transformation temperature of E.M, whereas that temperature was not altered in the I.C specimen.

The effect of different levels of graphite addition on I.C compacts is depicted in Figure 4.53. During the heating period and up to 960°C, the dimensional changes in each compact were similar. After 20 minutes sintering time, the specimen with no graphite addition showed slightly more expansion than those containing graphite. Overall, the specimen containing 0.6% graphite revealed the greatest shrinkage.

4.8.2 Dilatometry at 1125°C

Figure 4.54 illustrates the dimensional changes of pure Armco iron and a plain ASC 100.29 iron compact. The behaviour was similar up to α to γ transformation

temperature. During transformation, the iron compact shrunk more than the solid iron cylinder. When cooled to room temperature, the solid iron had zero dimensional change, whilst the iron compact recorded a shrinkage of 0.4%. The effect of density of Fe - 4Cu compacts on dimensional changes was investigated and compared to solid iron cylinder, the results are given in Figure 4.55. When the melting point of copper is reached (1084°C), the dilatometric graphs reveal that a rapid expansion occurs, which is more pronounced for specimens with higher densities.

An investigation of 2, 4 and 8% copper additions (Figure 4.56), revealed that at the melting point of copper the expansion is more pronounced for the specimen with higher copper contents. Fe - 8Cu specimen expanded up to 3% during isothermal sintering, but this fell to 2.0% while cooling to room temperature. More over, during isothermal heating, the rate of expansion for Fe - 8Cu was higher than the other two. In other words, copper growth was completed at the end of isothermal sintering in Fe - 2Cu, whilst it was still proceeding in Fe-4Cu and Fe - 8Cu compacts.

Figure 4.57 illustrates the effect of graphite on elementally mixed Fe - 4Cu compacts. It reveals that below the melting point of copper graphite did not have much effect on the change of dimensions but did lower the α to γ transformation temperature. From the point of copper melting, graphite clearly inhibited the growth caused by copper. Moreover, γ to α transformation in the Fe-4Cu-0.6C specimen started at a temperature at which the transformation was complete in the Fe-4Cu compact.

The dimensional changes of E.M and I.C compacts are shown in Figure 4.58. The I.C compact showed an initial expansion up to ~600°C, from where it started to shrink. At ~900°C the shrinkage was more rapid while α to γ transformation was

taking place. At the end of transformation and after the point of copper melting, the specimens showed an expansion which was more pronounced with the E.M specimen. No dimensional change was observed during isothermal sintering of I.C compact and it also showed the overall shrinkage of 0.5% when cooled to room temperature.

This experiment was repeated, on samples containing 0.6% graphite. It was revealed that (Figure 4.59), graphite addition reduced the expansion of E.M specimen more than the I.C specimen. During α to γ transformation, the I.C specimen shrunk much more than the E.M specimen. During isothermal sintering (20 minutes), the E.M compact expanded, while the I.C compact shrunk.

Figure 4.60 depicts the dilatometric curves of the I.C compacts at 960°C and 1125°C. The effect of density of I.C specimens on dimensions is shown in Figure 4.61. The same trend as with the E.M compacts is seen. The compact with a density of 6.8 Mgm^{-3} underwent less shrinkage. All compacts revealed shrinkage during the isothermal sintering of 20 minutes.

The effect of graphite on I.C compacts are shown in Figure 4.62. During the isothermal heating period, the rate of shrinkage of Fe-4Cu-0.6C compact was greater than that shown by the one containing no graphite. The compact with 0.6% graphite showed a maximum shrinkage of 0.8%, 0.2% more than that of the compact containing no graphite. Figure 4.63 shows the effect of superimposition of dilatometric traces of a plain iron compact, pure solid iron and an Fe - 4Cu compact (elementally mixed) at 1125°C. The compacts had a density of 6.40±0.05 Mgm^{-3}. At α to γ transformation plain iron and Fe -4Cu compacts shrunk about the same amount, but the solid iron cylinder revealed less shrinkage. From 920°C to 1125°C, the rate of expansion of pure solid iron was higher than that of the plain iron compact. On the other hand, the Fe - 4Cu compact exhibited a rapid expansion

at the melting point of copper (1084°C), to reach a maximum expansion of ~2.0%.

4.8.3 Dilatometry at 1200°C

Figure 4.64 depicts the dilatometric traces of pure solid iron and solid iron containing 0.2% carbon. Increasing the isothermal heating temperature from 1125°C to 1200°C increased the expansion of pure solid iron cylinders from 0.75% to ~0.95%. 0.2% carbon addition reduced the α to γ transformation temperature and caused an overall shrinkage of almost 0.2% in the solid cylinder.

Figure 4.65 shows the dilatometric curves of Fe-2Cu, Fe-4Cu compacts and pure solid iron cylinder at 1200°C. Comparing the results with those presented in Figure 4.64, copper containing compacts showed a shrinkage during the isothermal sintering of 1200°C. A compact of similar constitution shows an expansion when sintered at 1125°C.

4.8.4 The Effect of Atmosphere.

All the dilatometric work presented in the previous section were the results of experiments performed in a protective atmosphere of high purity argon. To obtain "markers", and industrial relevance, selected experiments were repeated with $N_2/10H_2$ atmosphere. Figure 4.66 illustrates the atmosphere effect on plain iron compacts. It reveals that the $N_2/10H_2$ atmosphere promotes more shrinkage than argon especially during isothermal sintering.

Figure 4.67 shows the dilatometric curves of Fe-0.6C compacts at 1125°C. The same effect as that shown in Figure 4.66 is seen, except that 0.6% graphite causes 0.4% overall shrinkage in both atmospheres. Dilatometric curves of Fe-4Cu, elementally mixed specimens is shown in Figure 4.68. Up to the point of copper

melting, the specimens behaved in a similar way, but during isothermal sintering, the one sintered in HP argon registered higher shrinkage, which was retained at room temperature.

Figures 4.69 and 4.70 show the dimensional changes of Fe-4Cu and Fe-4Cu-0.6C immersion coated compacts respectively. It reveals that sintering atmosphere did not have any effect on the final dimensions after the complete sintering cycle. However, the ones sintered in $N_2/10H_2$, registered more expansion during the heating period, and more shrinkage during isothermal sintering and cooling periods.

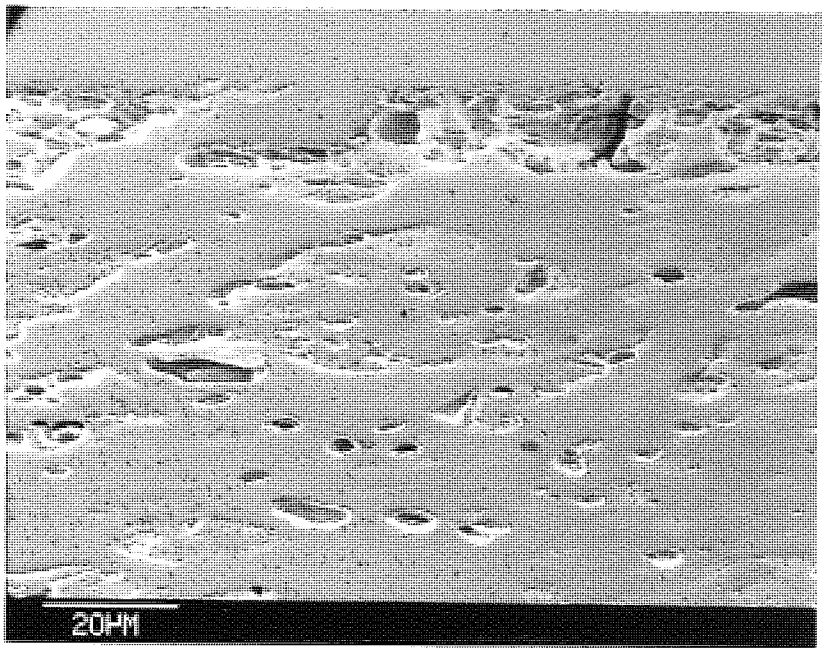

a) Electron image of Anchorbraze in contact with iron. x 1K

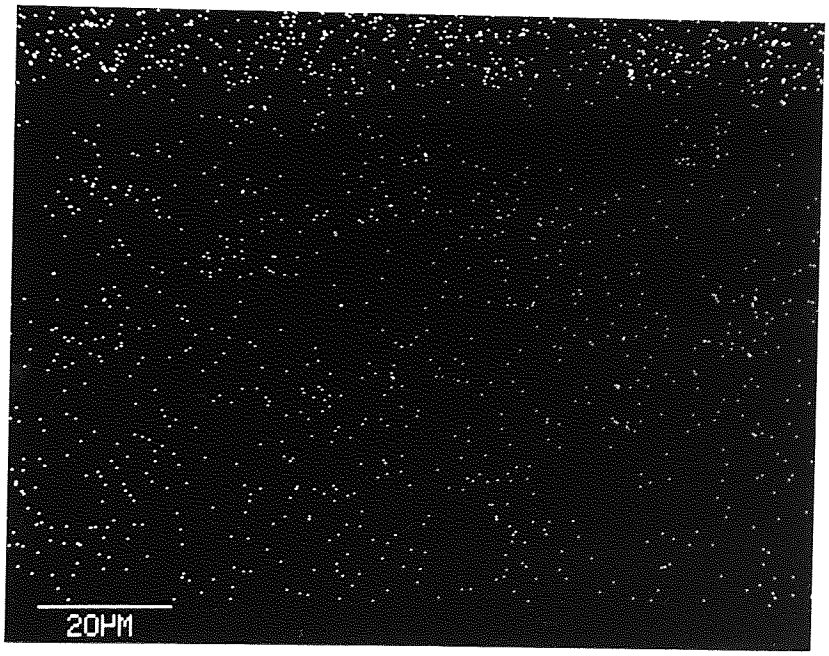

b) Ni X-ray map x 1K

Figure 4.1 - SEM and X-ray images of the interface between Anchorbraze and iron.

c) Cu X-ray map x1K

d) Mn X-ray map x 1K

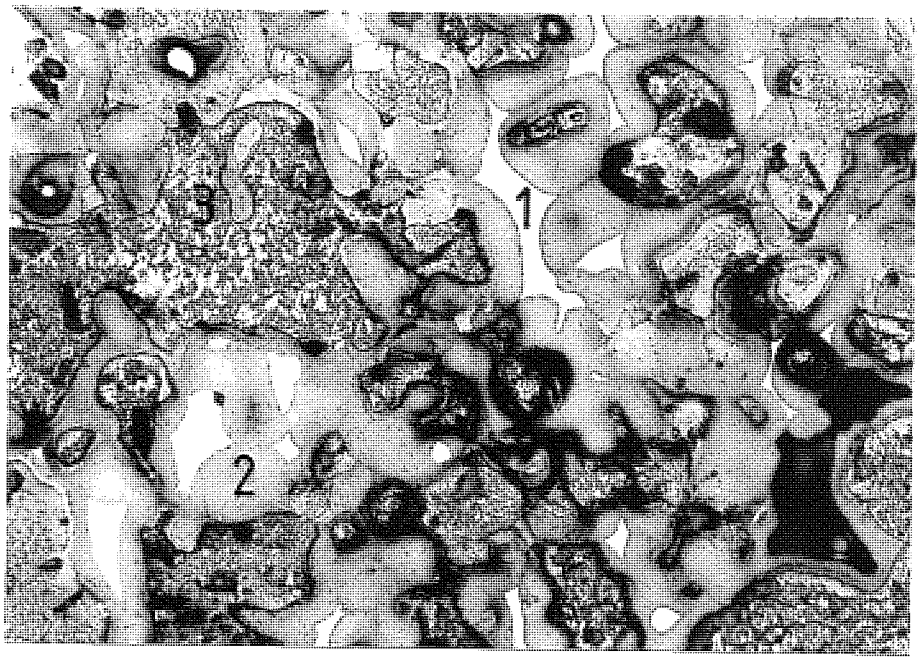

Figure 4.2 - Photomicrograph showing alloying zones just below Anchorbraze / iron interface. Etched 2% Nital. x 490

1- Copper rich phase

2- Alloying region, containing Ni, Si, Mn, Cu and Fe

3- Fe skeleton

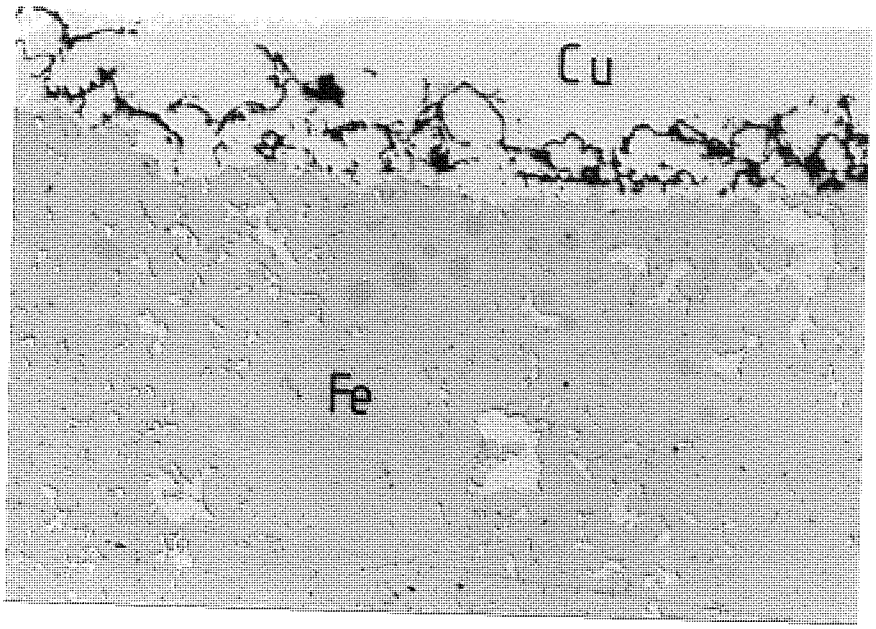

a) x 198

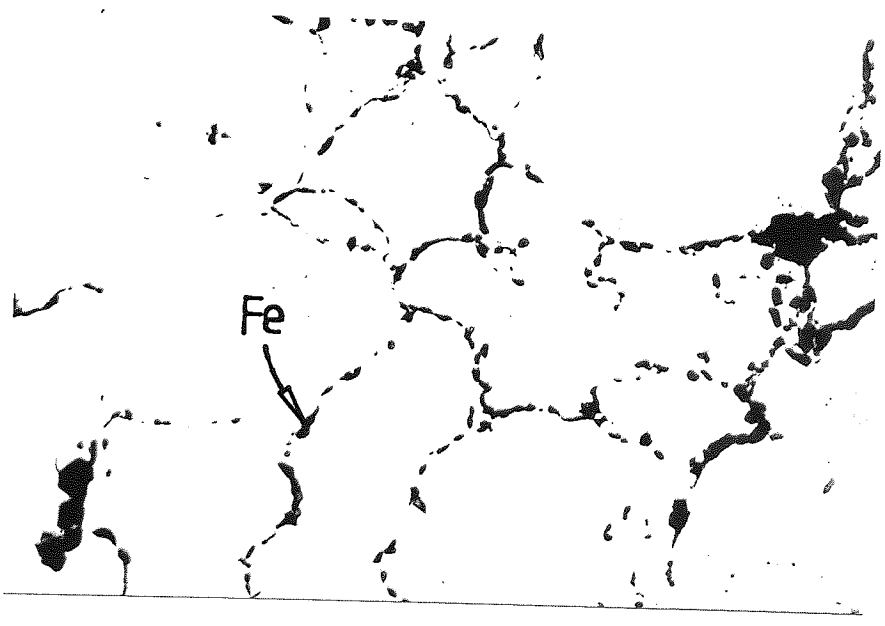

b) x 980

Figure 4.3 - Optical photomicrograph of a sample infiltrated at 1100 °C for 3 minutes, showing iron precipitates.

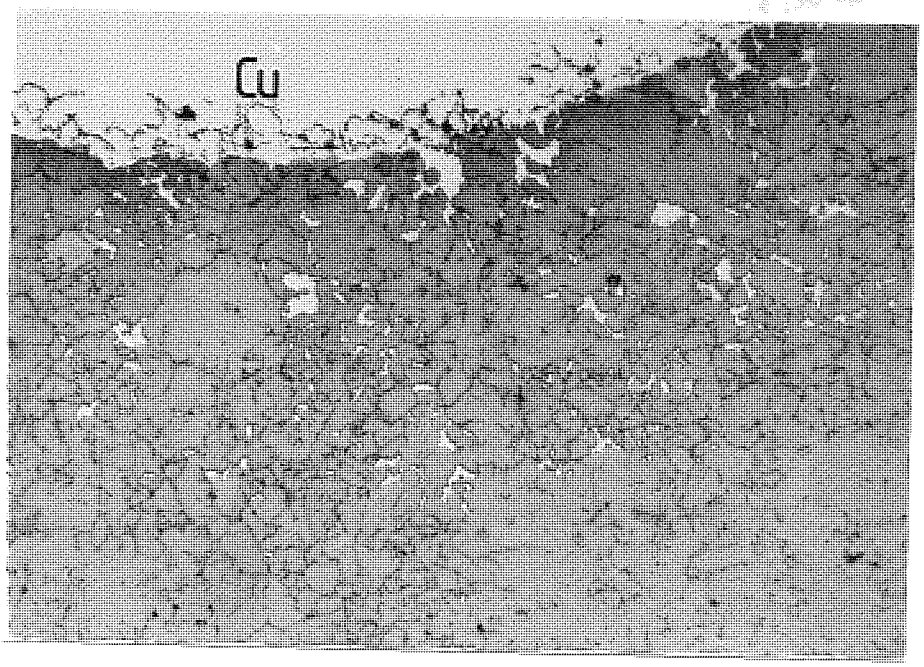

a) x 98

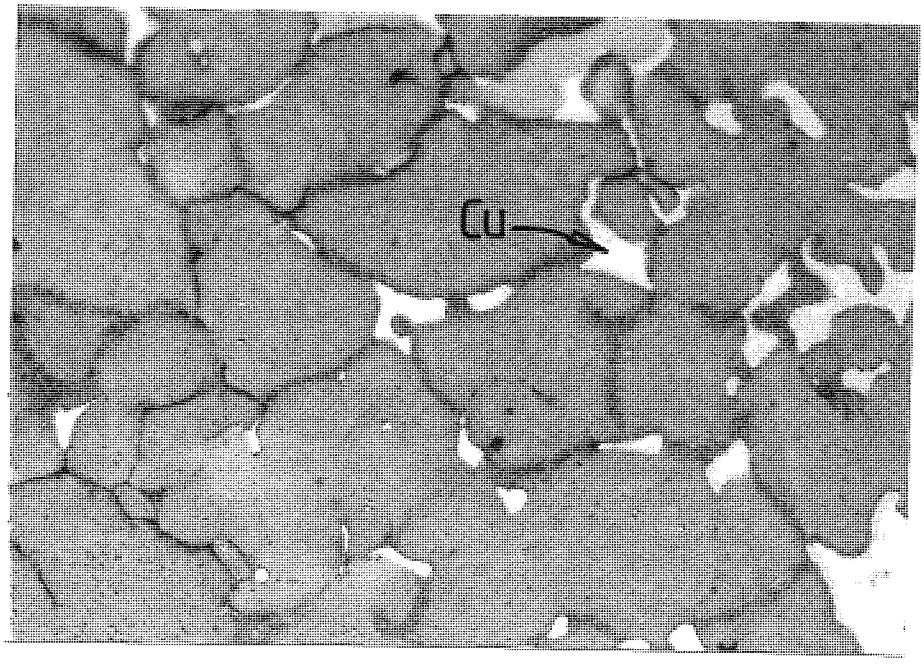

b) x 980

Figure 4.4 - Optical photomicrograph of a sample infiltrated at 1100 °C for 3 minutes, showing copper penetration along grain boundaries.

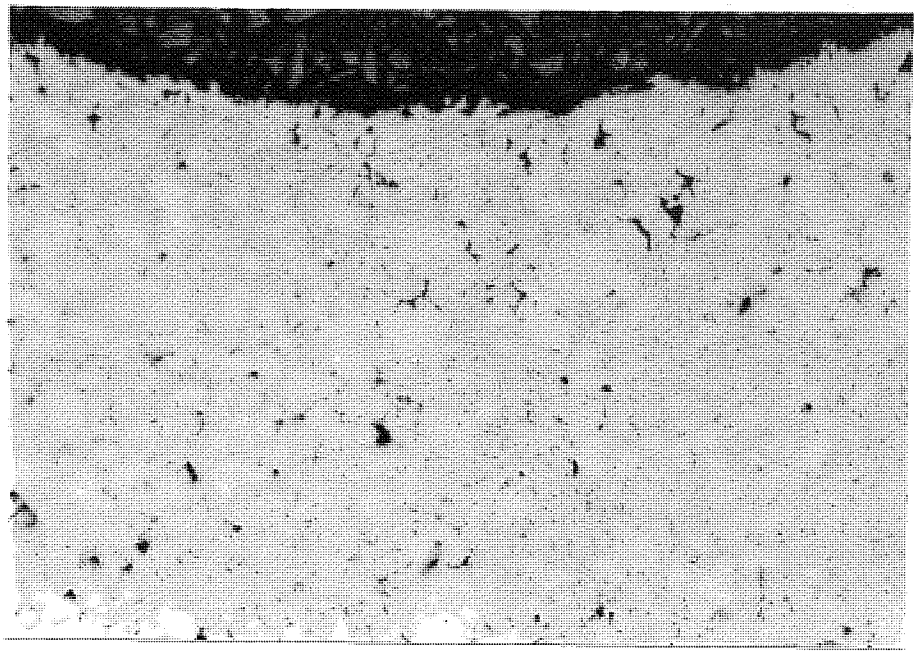

a) x 98

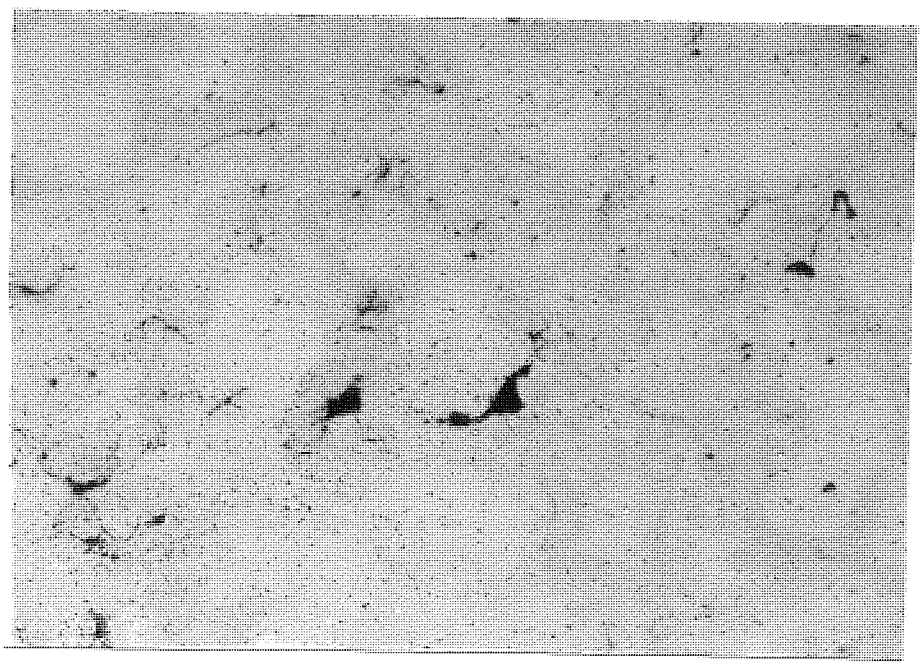

b) x 980

Figure 4.5 - Optical photomicrograph of a sample infiltrated at 1200°C for 60 minutes, showing complete copper diffusion in iron.

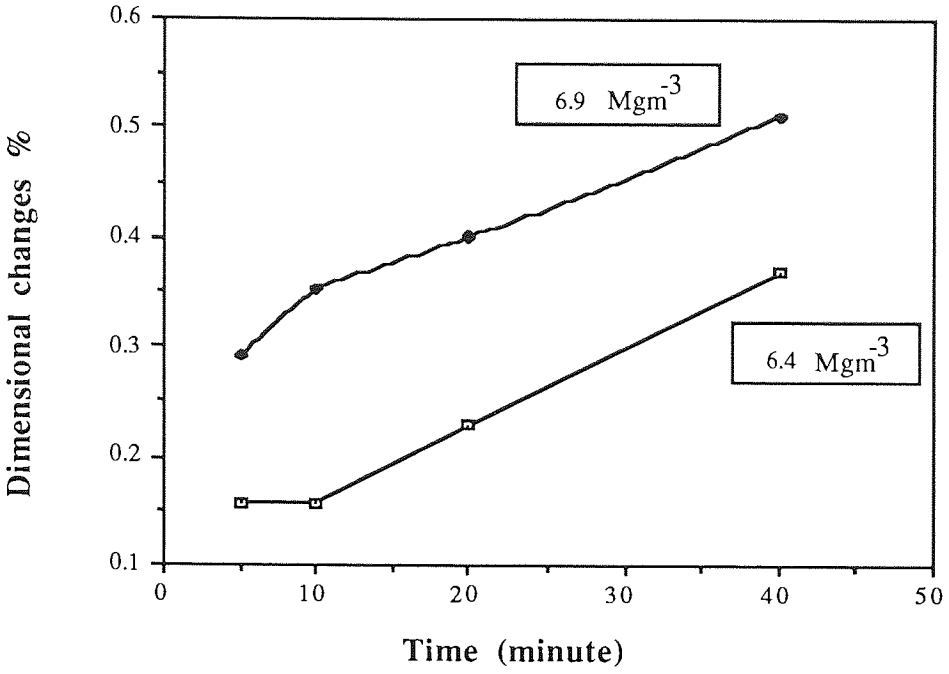

Figure 4.6 - The effect of infiltration time on dimensional changes in samples isothermally sintered at 1125 °C.

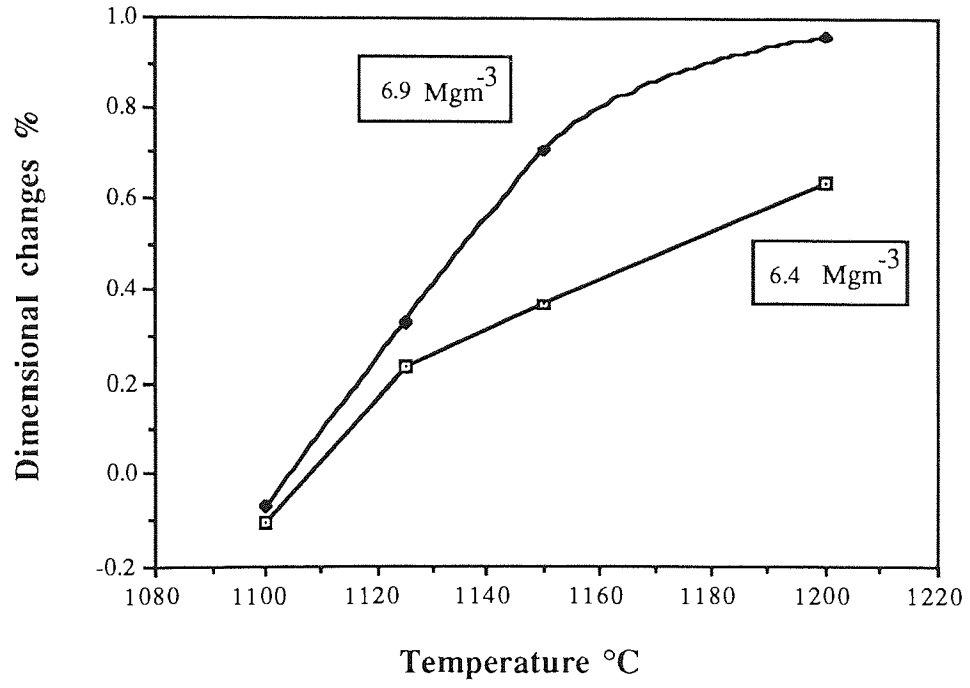

Figure 4.7 - The effect of sintering temperature on dimensional changes in samples sintered for 10 minutes.

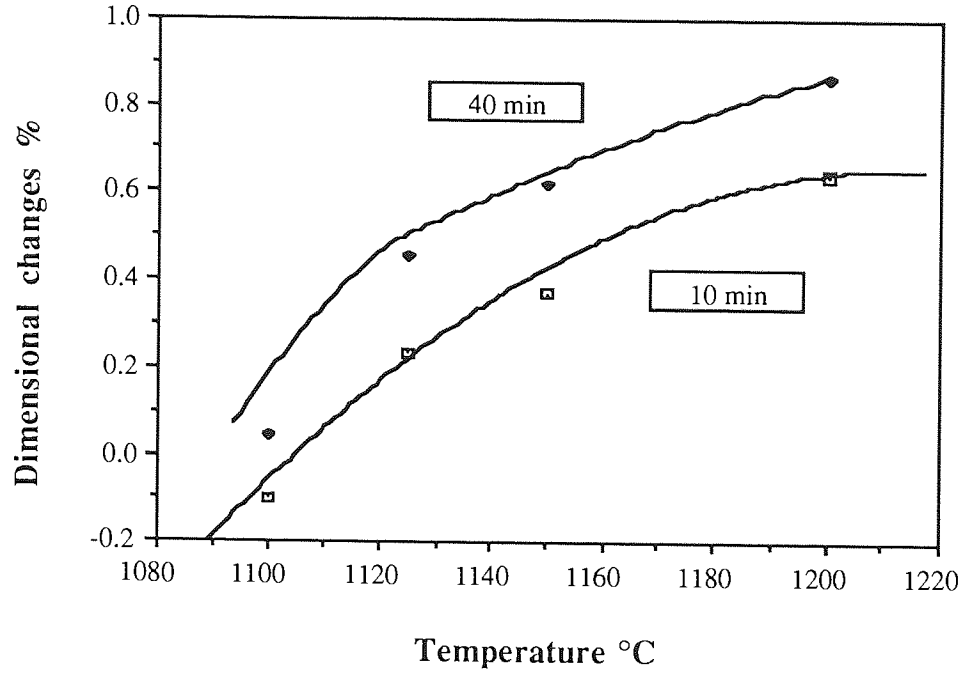

Figure 4.8 - The effect of sintering temperature on dimensional changes in samples with a density of 6.4 Mgm^{-3}

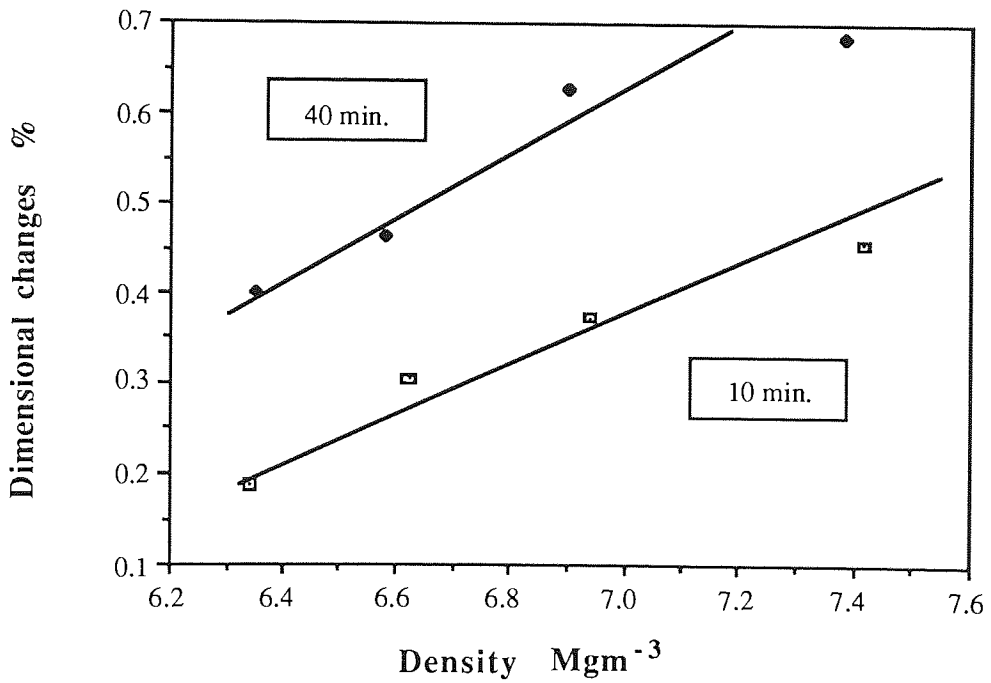

Figure 4.9 - The effect of density upon dimensional changes after sintering at 1125°C for 10 and 40 minutes.

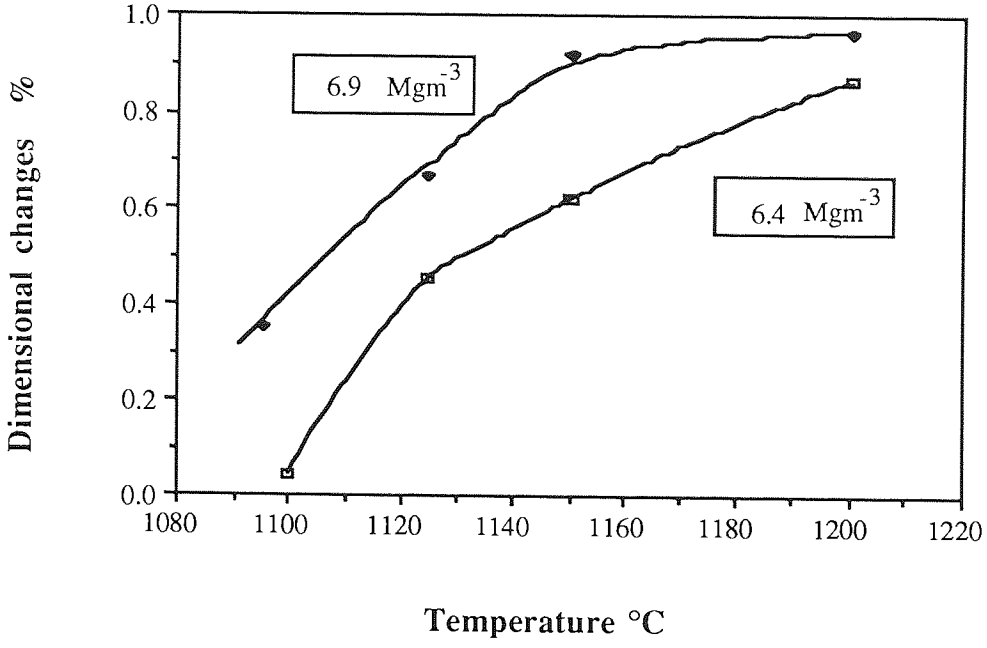

Figure 4.10 - The effect of sintering temperature on compact dimensions after infiltrating for 40 minutes.

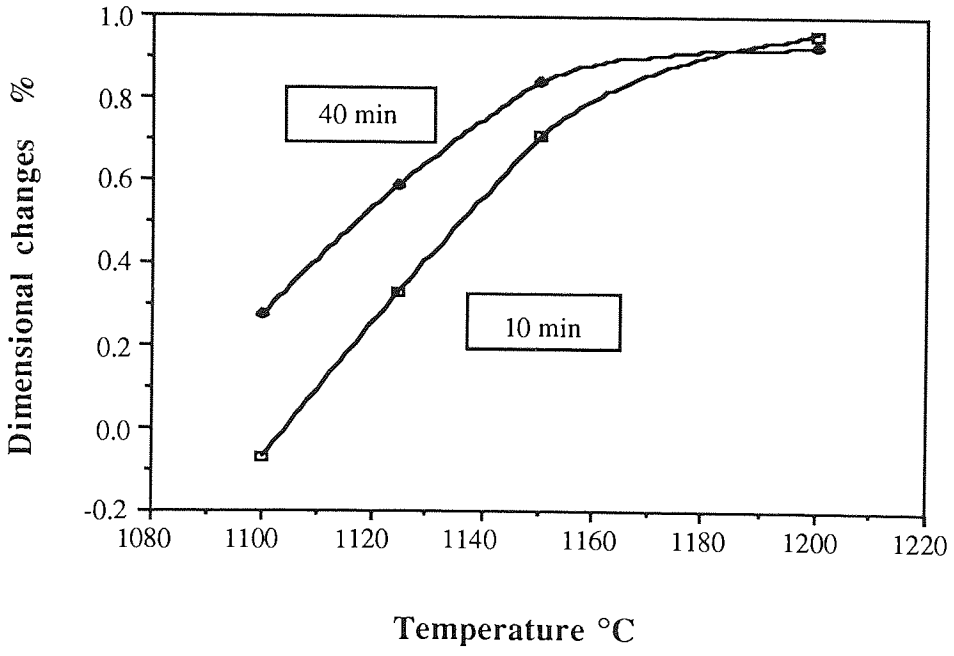

Figure 4.11 - The effect of sintering temperature upon dimensions of compacts with a density of 6.9 Mgm^{-3}

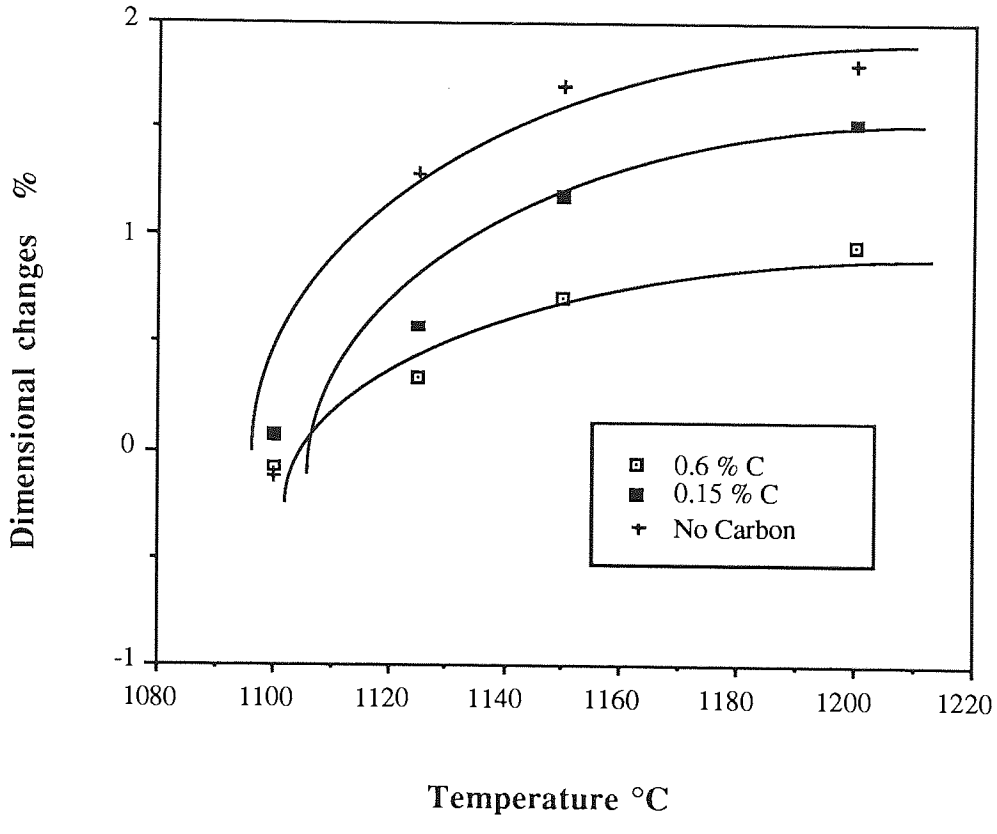

Figure 4.12 - The effect of sintering temperature upon dimensions of carbon containing compacts.

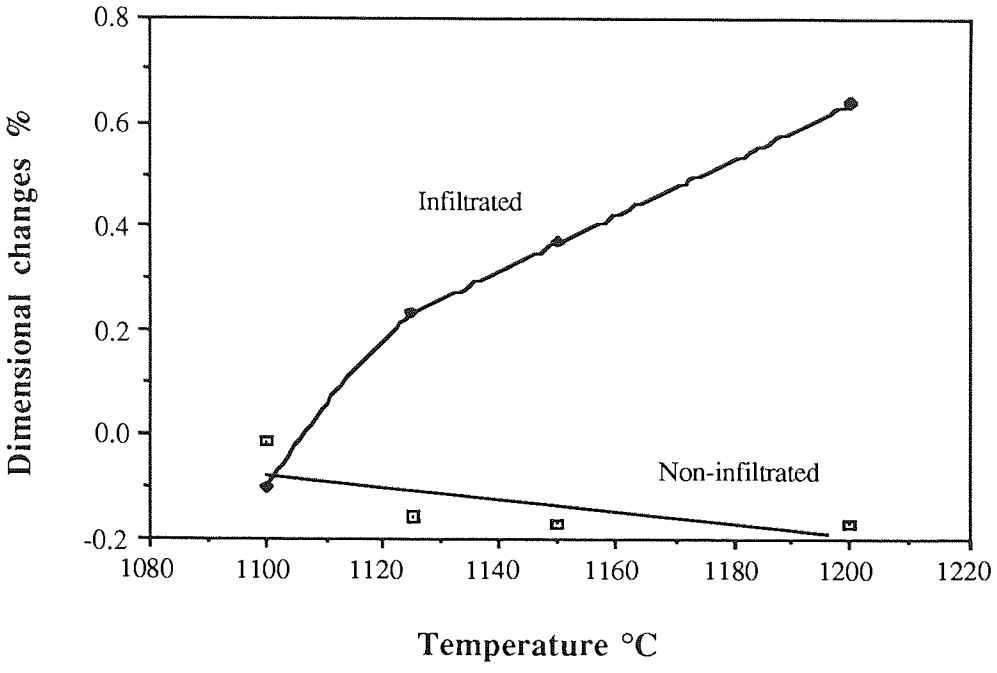

Figure 4.13 - Comparison in the dimensional behaviour of the infiltrated and non - infiltrated compacts.

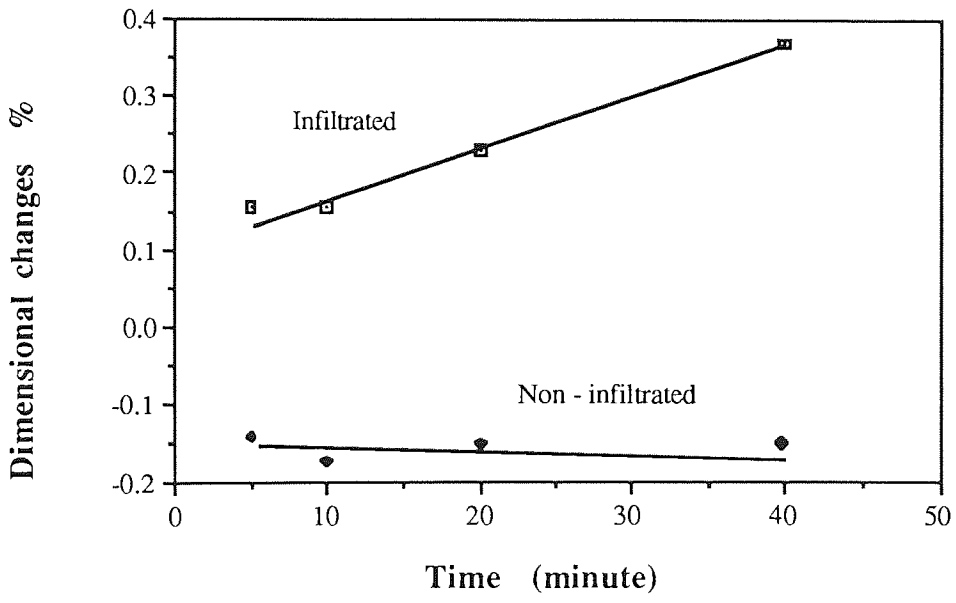

Figure 4.14 - The effect of sintering time upon dimensions of infiltrated specimens compared to plain iron compact, isothermally infiltratrd at 1125 °C.

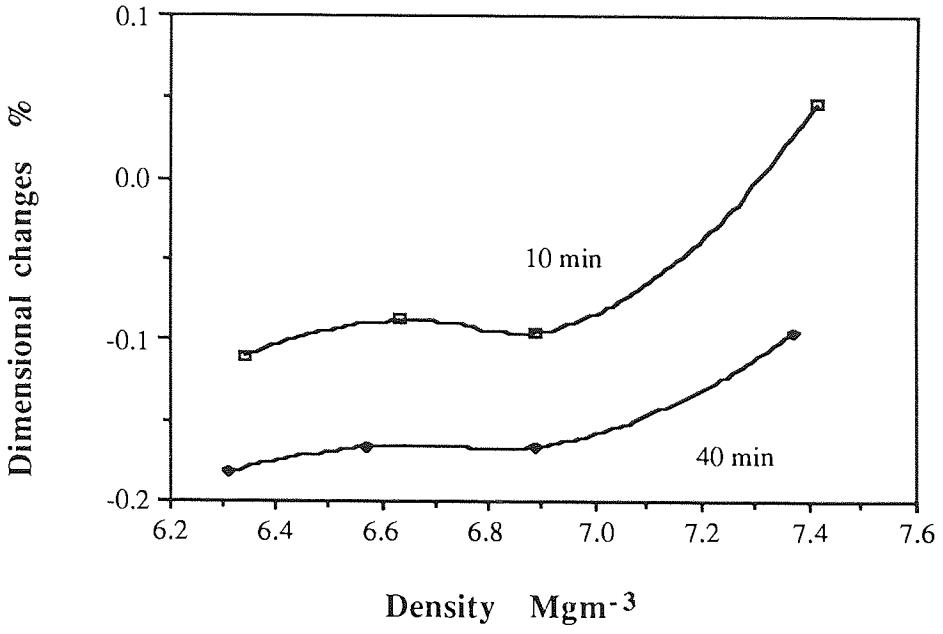

Figure 4.15 - Dimensional behaviour in plain iron compacts of varying densities, isothermally sintered at 1125°C.

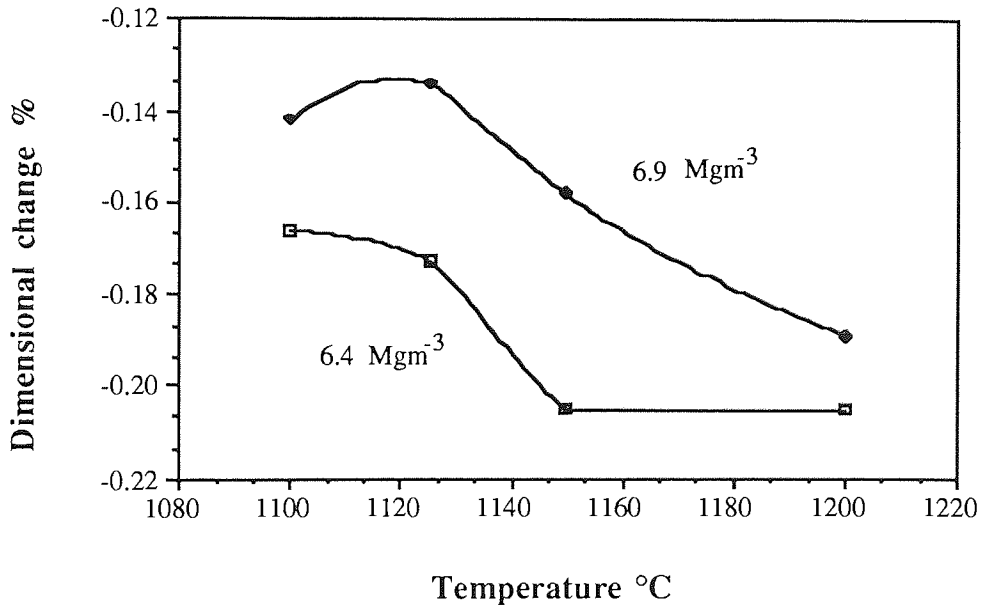

Figure 4.16 - The effect of temperature on dimensions in plain iron compacts.

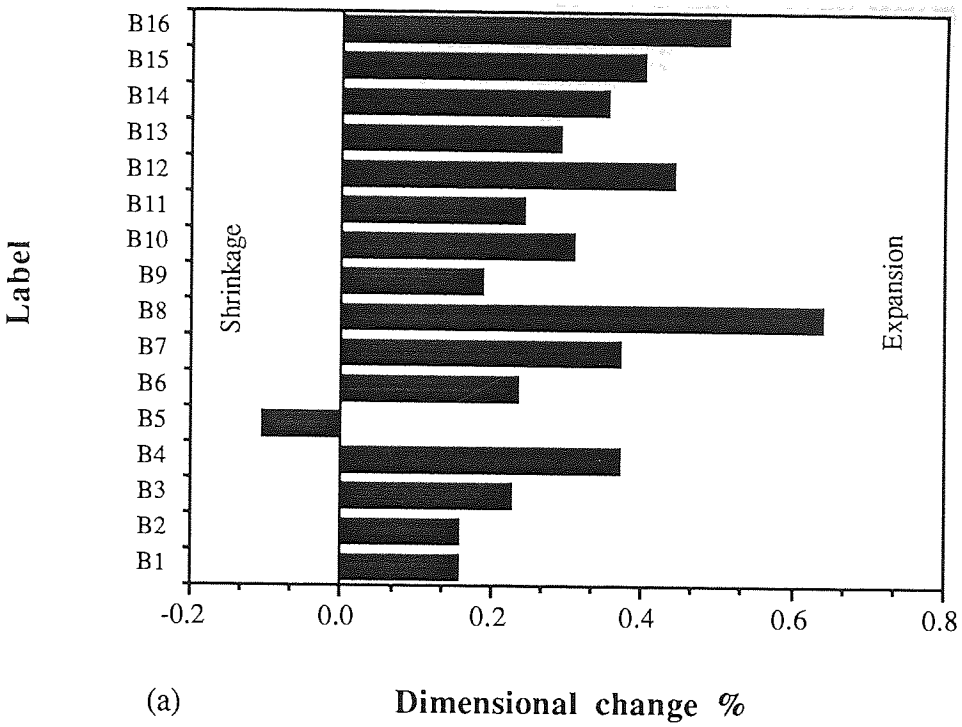

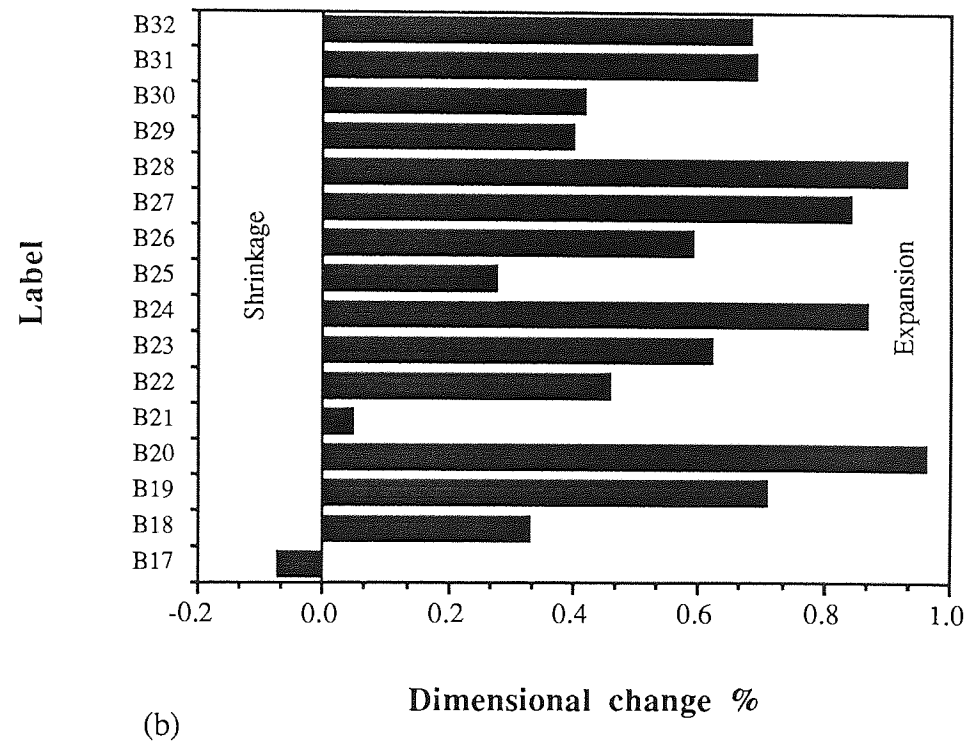

Figure 4.17 - Shrinkage / expansion in the infiltrated compacts. Experimental conditions are given in table 4.3.

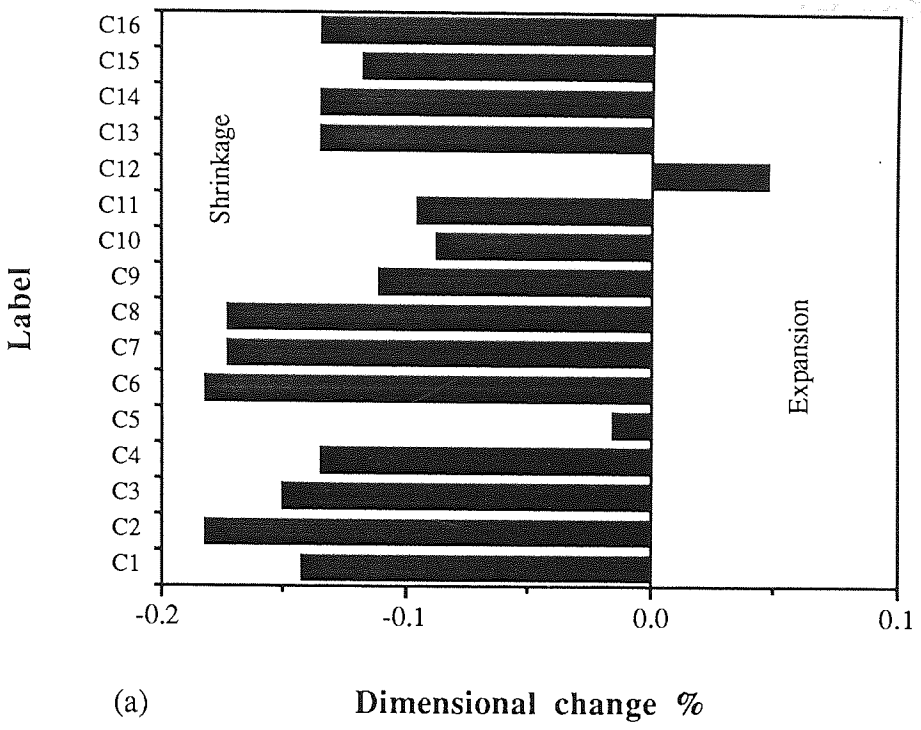

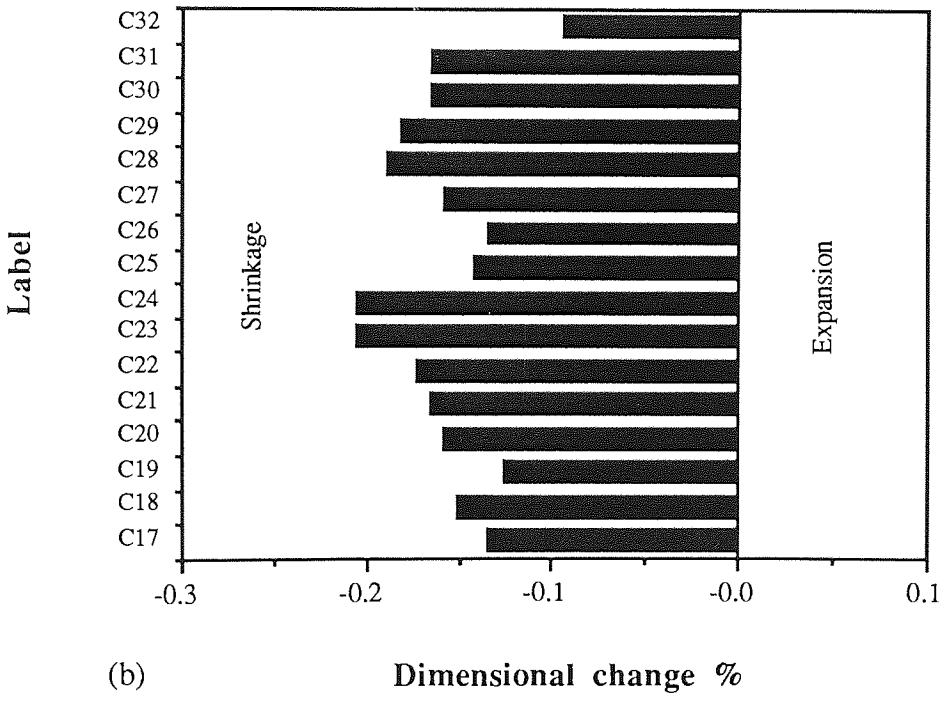

Figure 4.18 - Shrinkage / expansion in the non - infiltrated compacts. Experimental conditions are given in table 4.4.

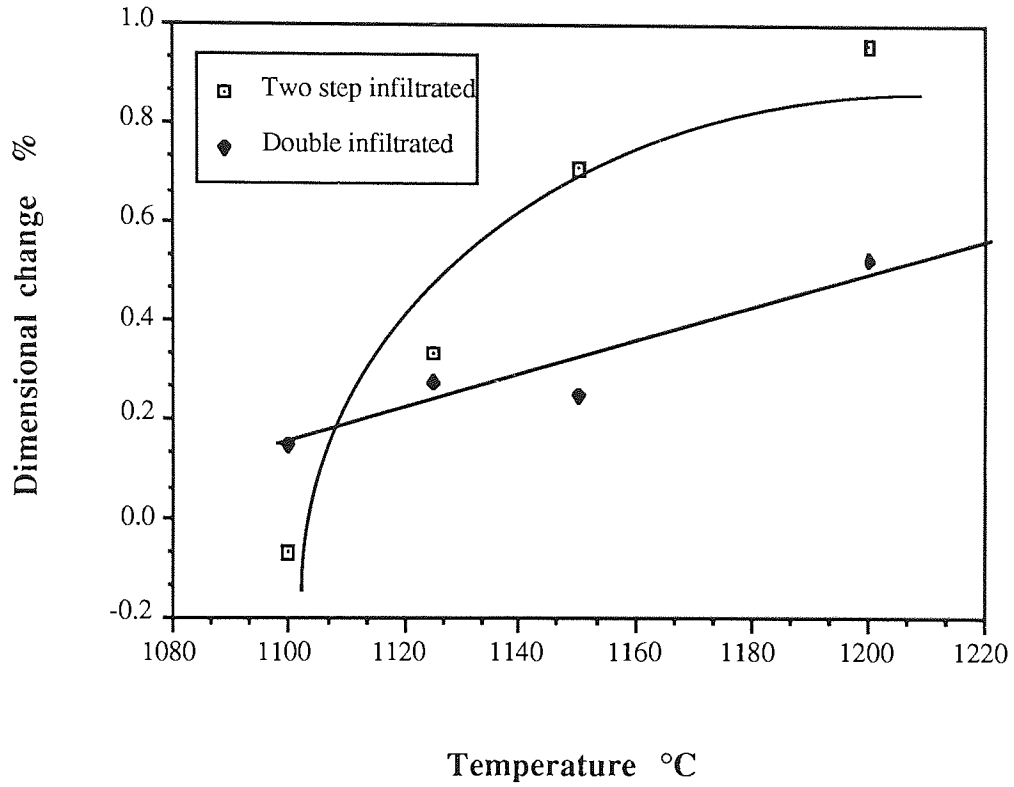

Figure 4.19 - Dimensional belaviour of double infiltrated and two step infiltrated compacts.

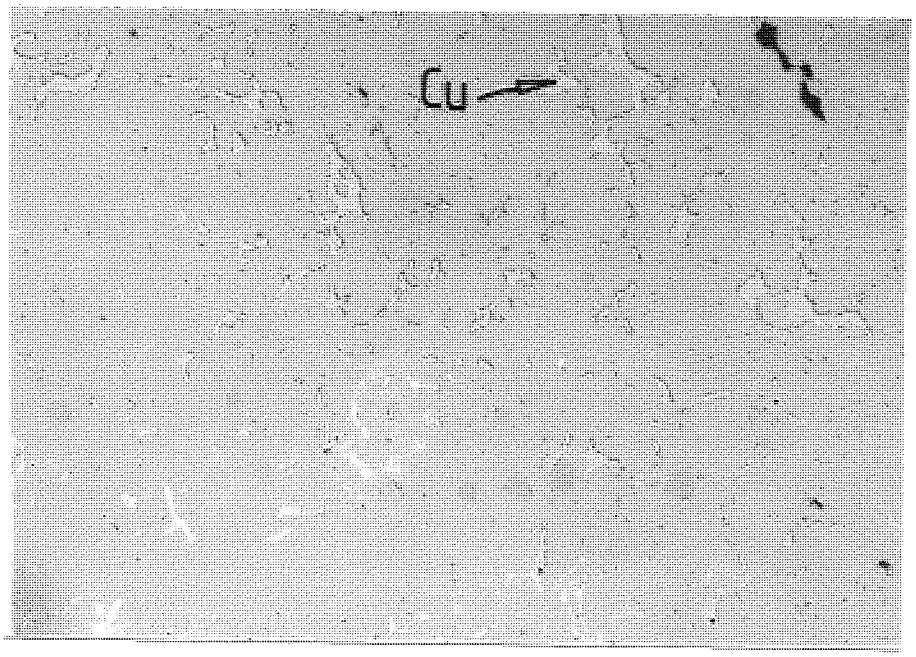

a) Two step infiltration x196

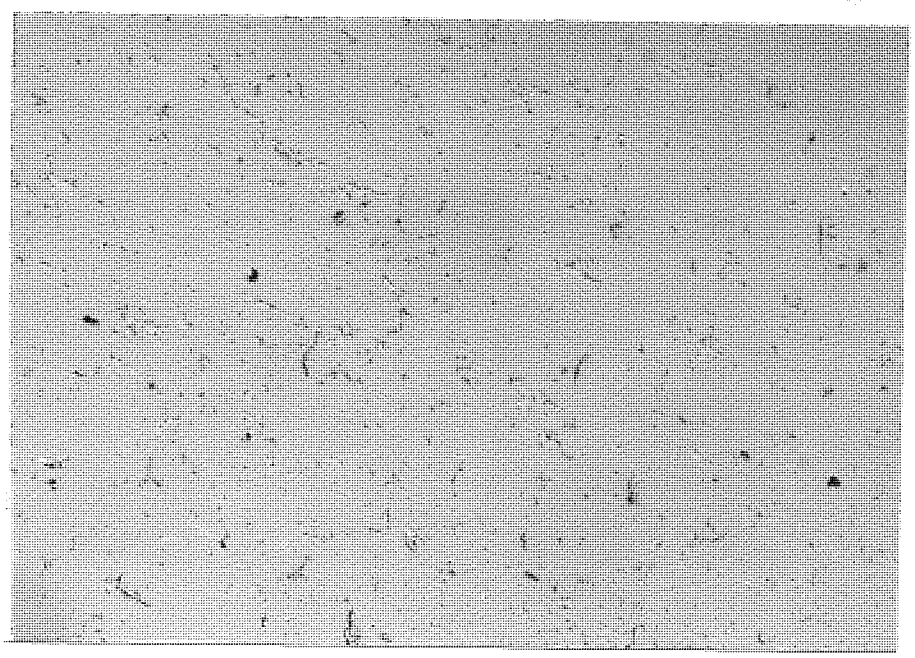

b) Double infiltration x196

Figure 4.20 - Effect of Cu on the microstructure of Fe in double and two step infiltrated compacts.

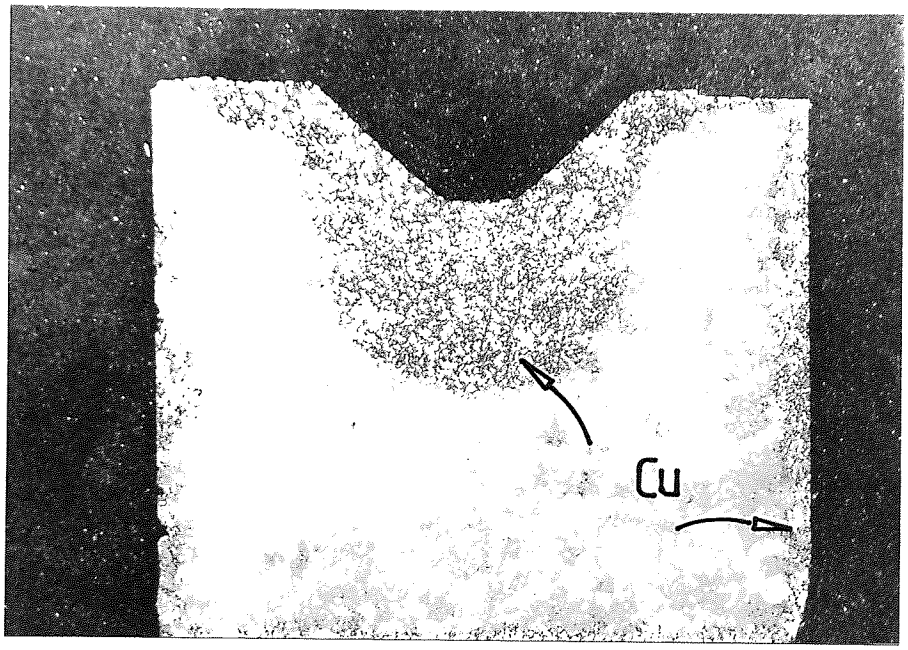

Figure 4.21 - Copper infiltration profile of a sample sintered at 1125°C for 30 minutes in vacuum. Density = 6.9 Mgm^{-3}

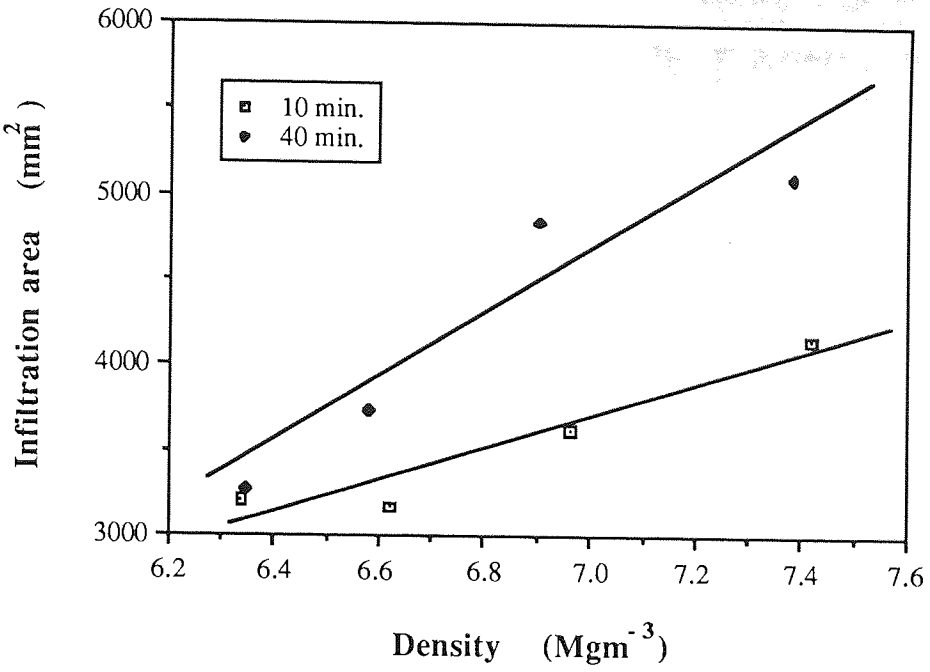

Figure 4.22 - The effect of density on infiltration area in the compacts isothermally infiltrated at 1125 °C.

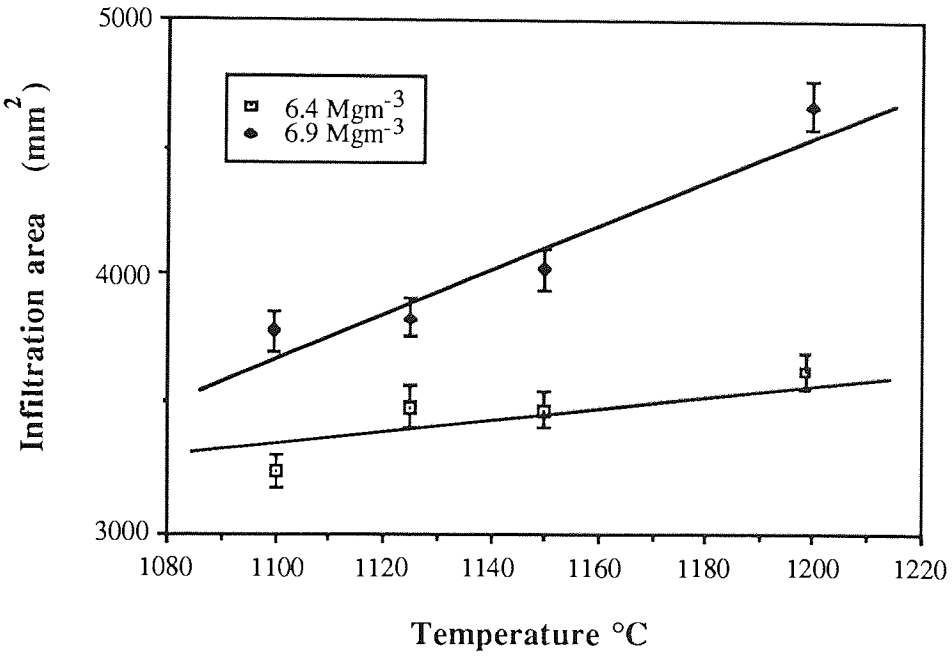

Figure 4.23 - The effect of temperature on infiltration area in compacts sintered for 40 minutes.

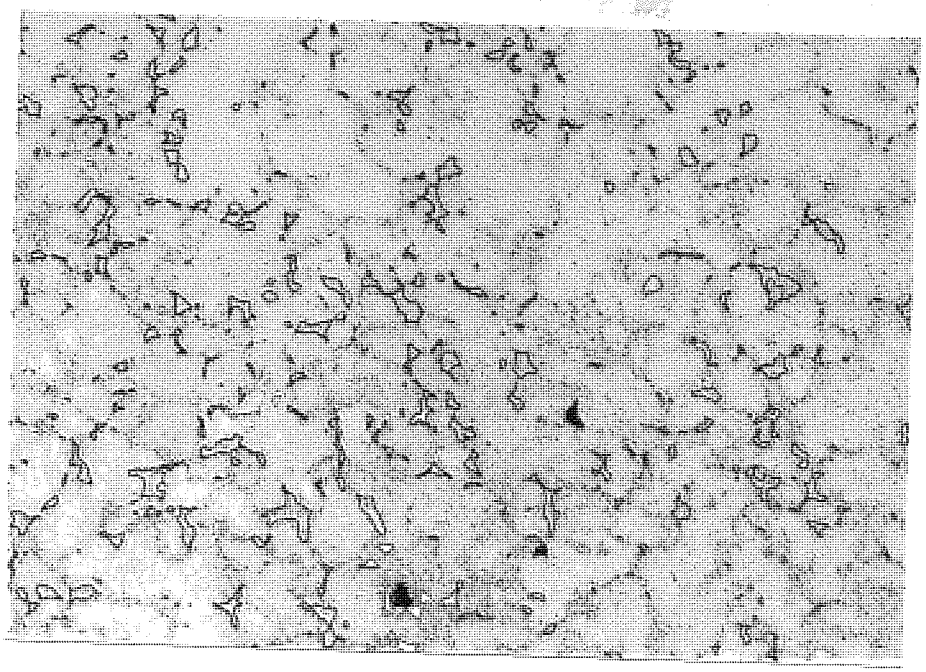

a) x 196

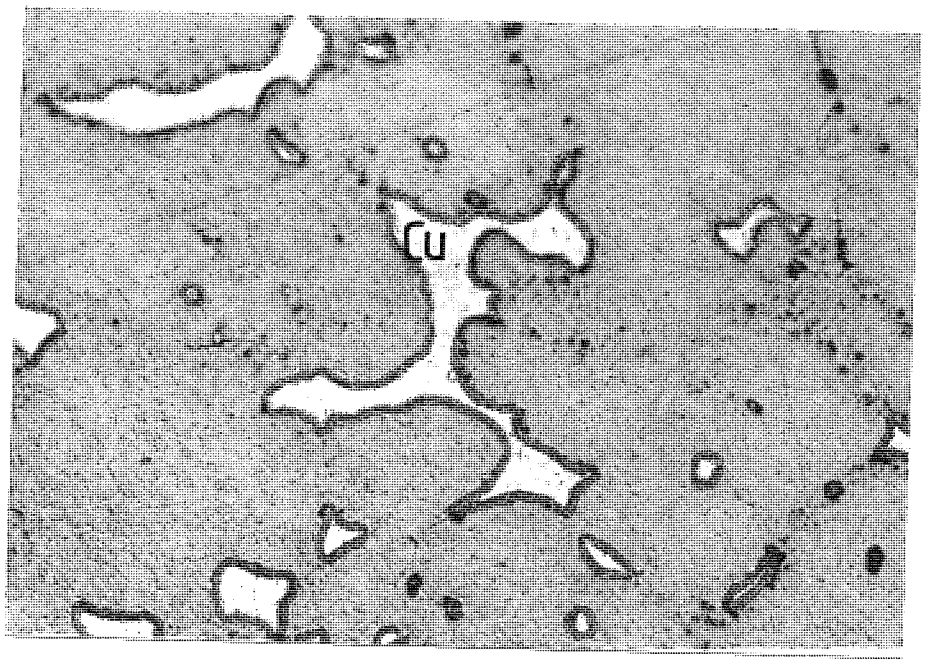

b) x 980

Figure 4.24 - Optical photomicrograph of a compact infiltratedat 1100°C for 60 minutes and heat tinted at 300°C for 1 hour.

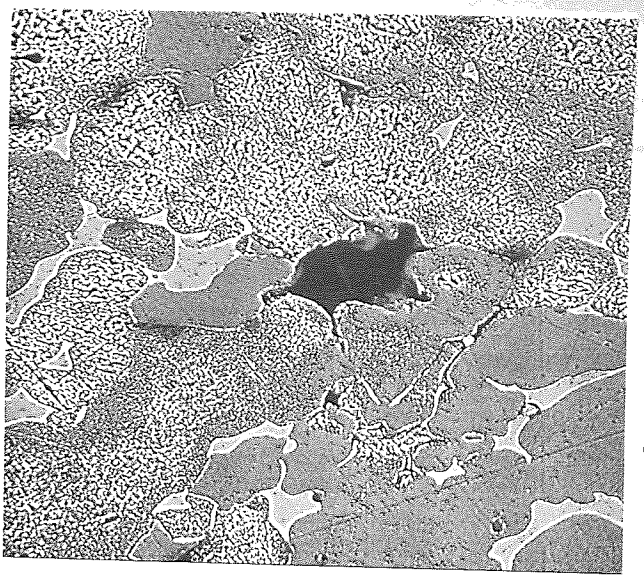

a) Pore morphology

x 500

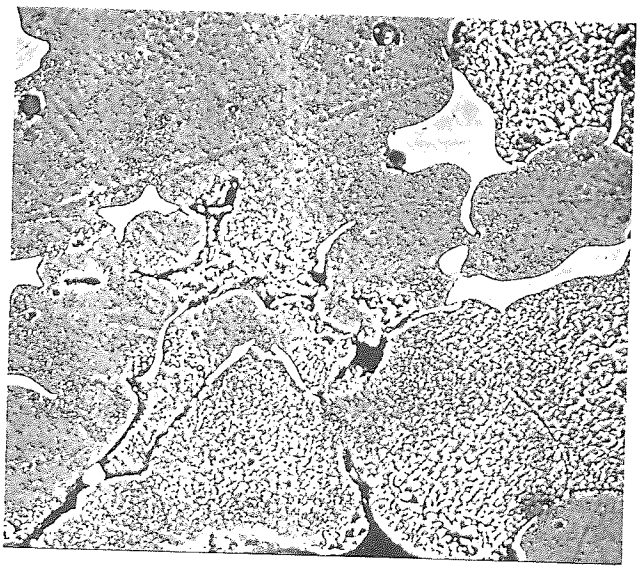

b) Copper rich region

(less oxidised)

x 1280

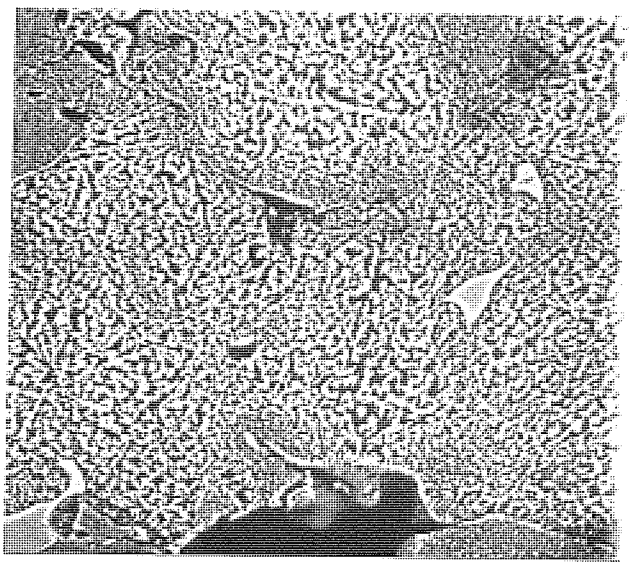

c) Iron rich region

showing oxide scales

x 1280

Figure 4.25 - Backscattered electron image of the heat tinted specimen

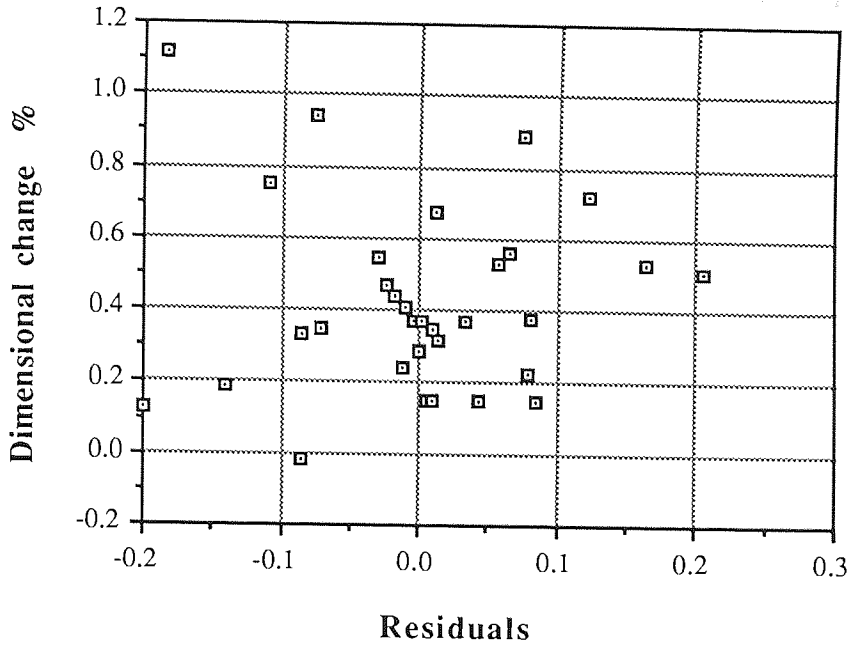

Figure 4.26 - The residual error in the dimensional change multiple regression model.

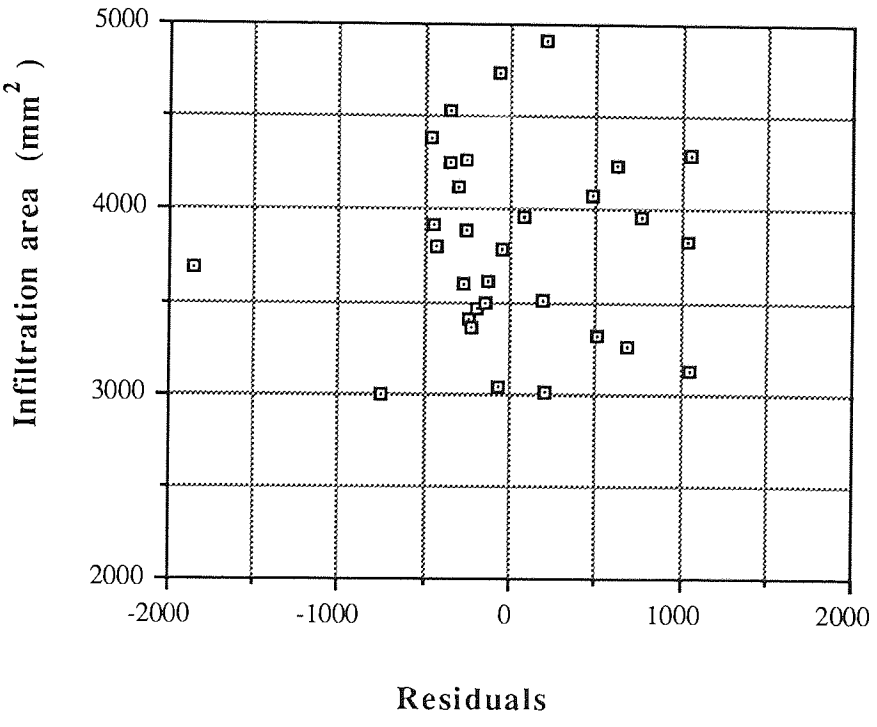

Figure 4.27 - The residual error in the infiltration area multiple regression model.

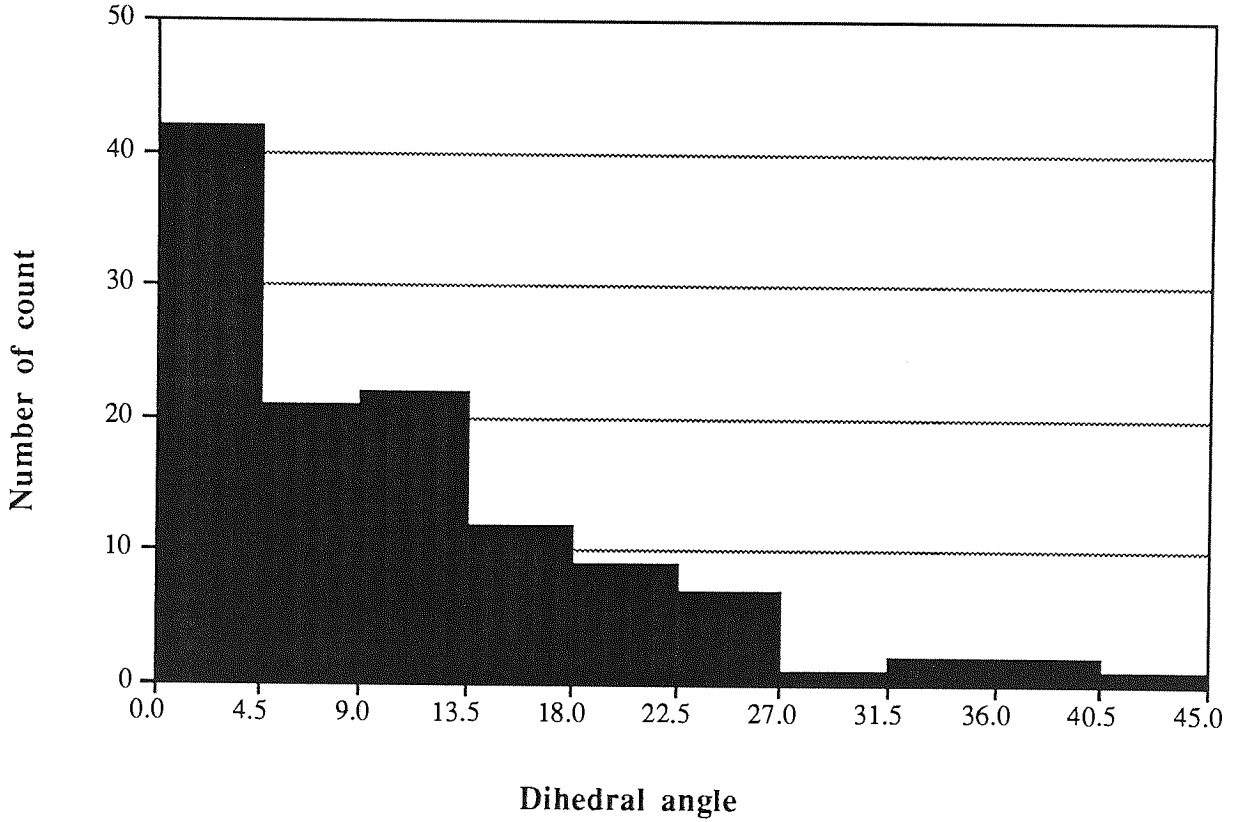

Figure 4.28 - Frequency of the observed dihedral angles of a plain iron compact infiltrated at 1125 °C for 20 minutes.

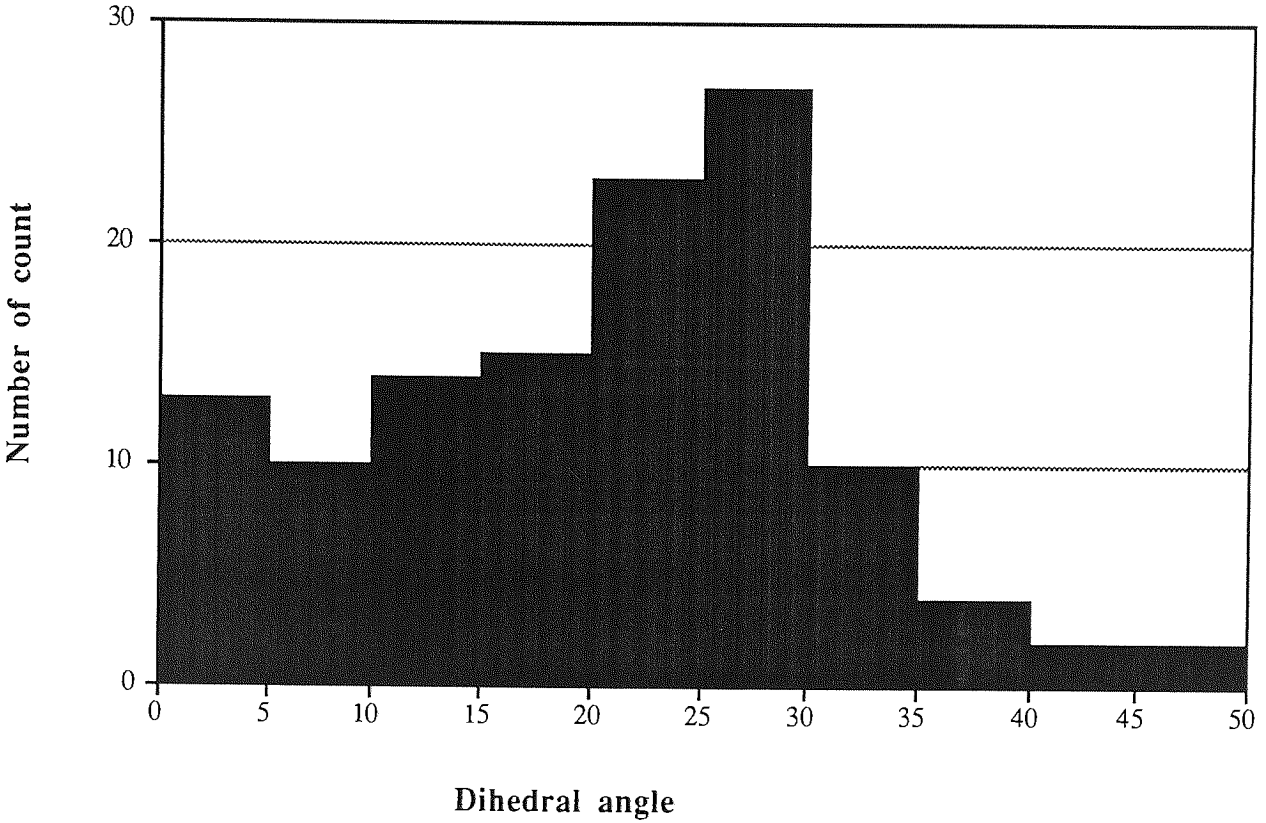

Figure 4.29 - Frequency of the observed dihedral angles of a Fe-0.15C compact infiltrated at 1125 °C for 20 minutes.

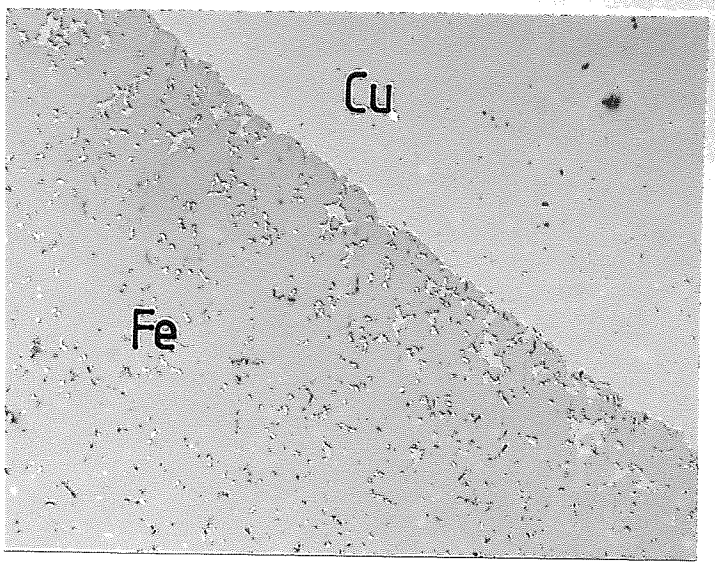

a) iron / copper interface x 196

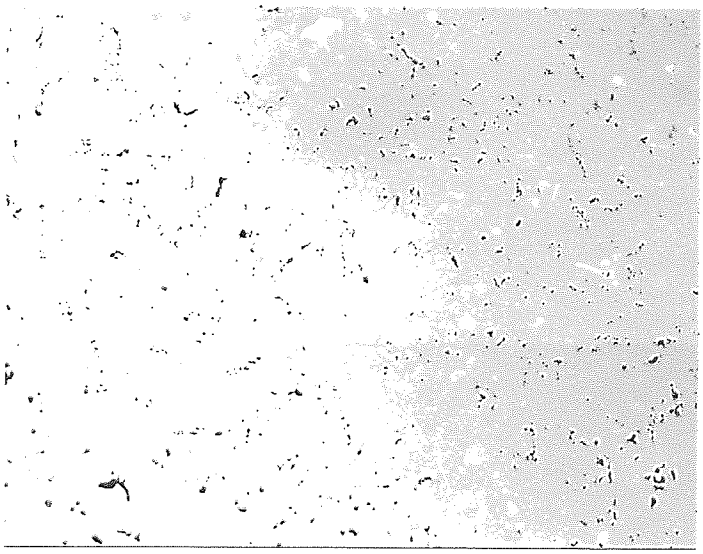

b) copper infiltrated area. x 196

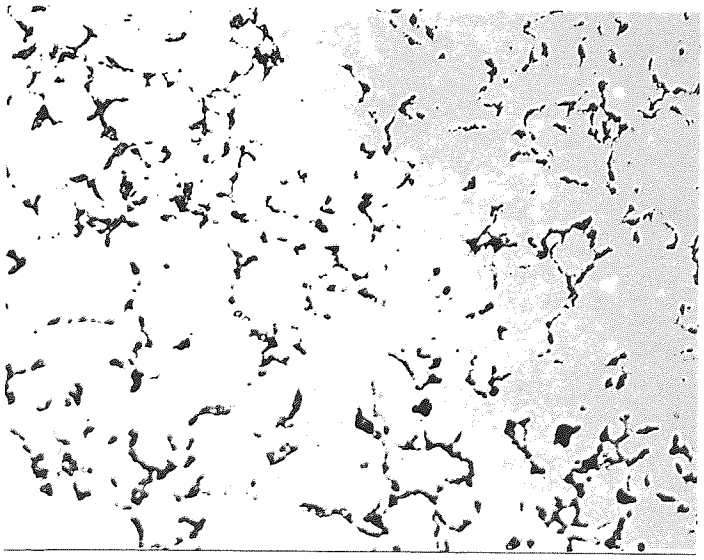

c) Non-infiltrated area x 196

Figure 4.30 - Optical photomicrograph of a Fe-0.15C compact, infiltrated at 1100°C for 10 minutes. Density = 6.85 Mgm^{-3}

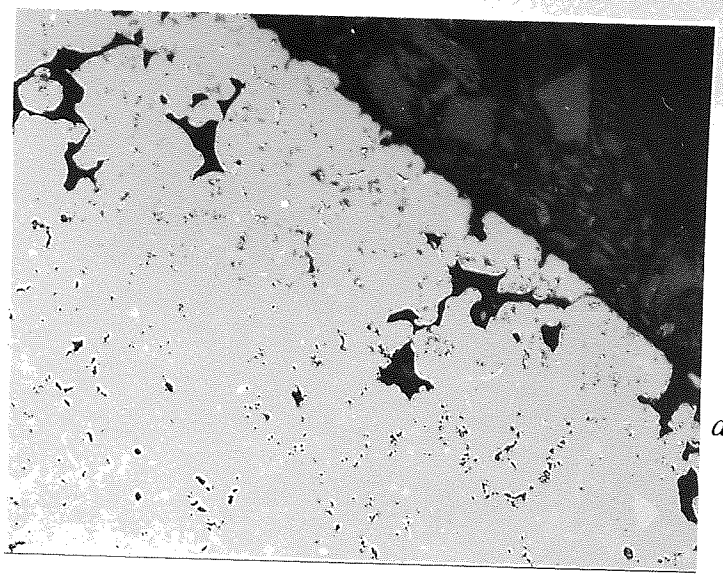

a) Copper / iron interface. x 196

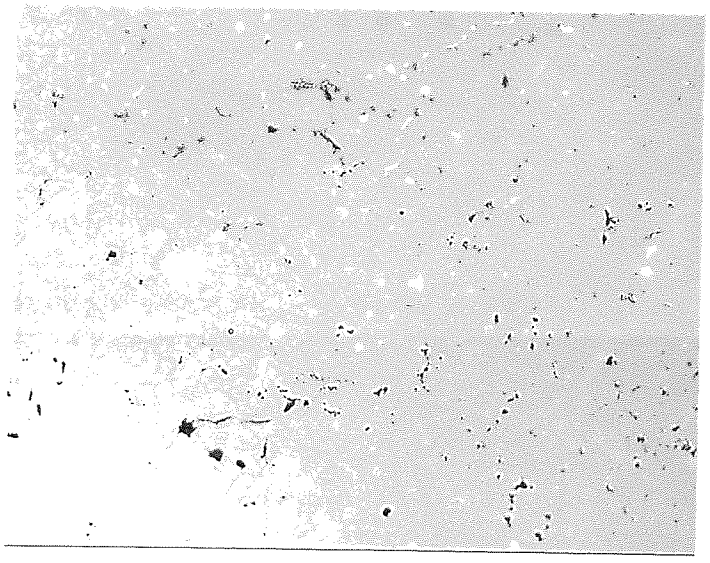

b) Copper infiltrated area. x 196

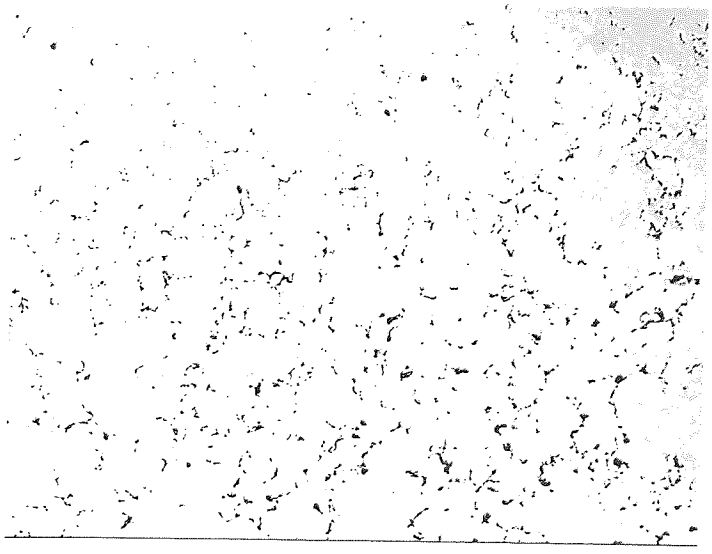

c) Boundary between the infiltrated and non-infiltrated regions. x 196

Figure 4.31 - Optical photomicrograph of a Fe-0.15C compact, infiltrated at 1150°C for 10 minutes. Density = 6.74 Mgm^{-3}

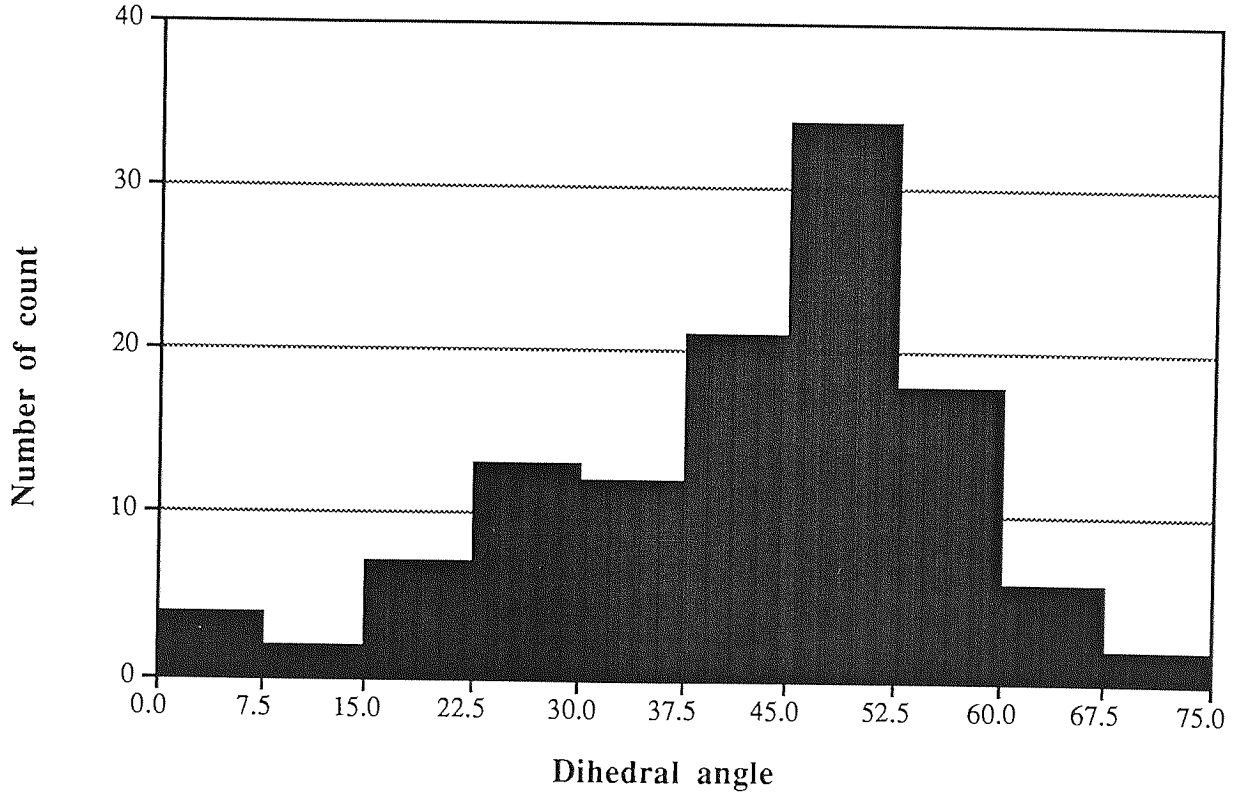

Figure 4.32 - Frequency of the observed dihedral angles in a Fe-0.6C compact infiltrated at 1125 °C for 20 minutes.

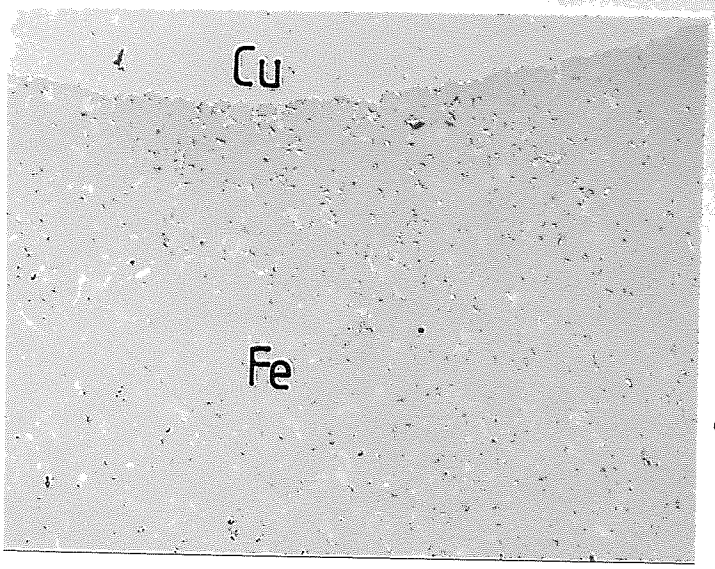

a) Copper / iron interface. x 98

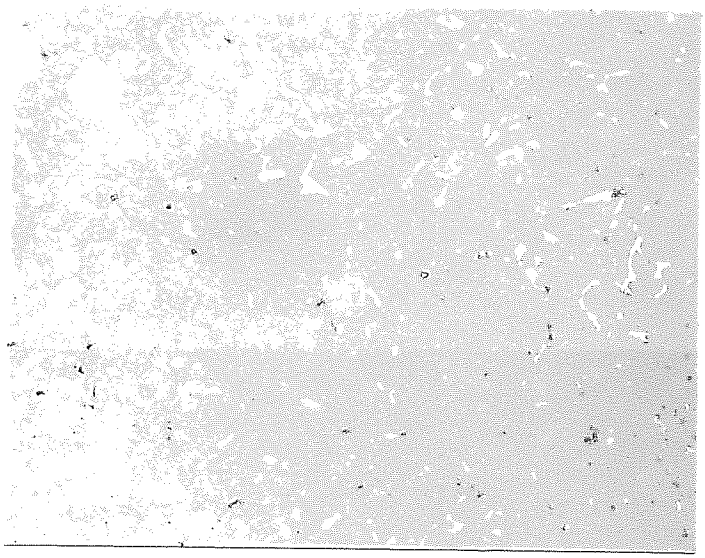

b) Infiltrated region x 196

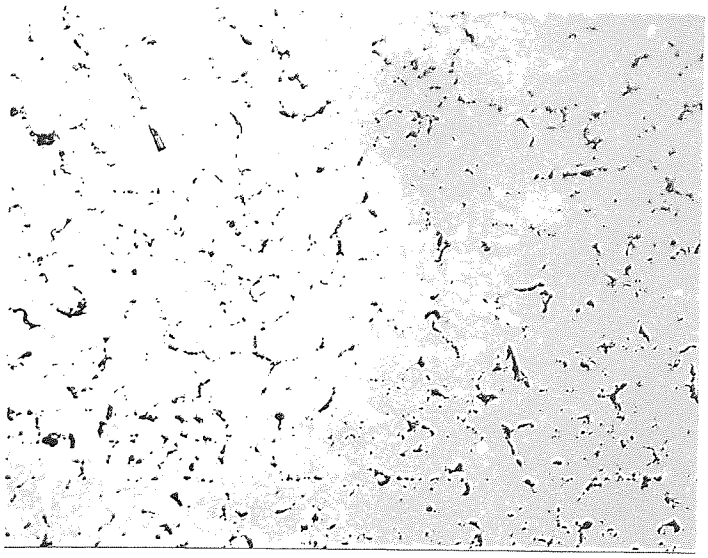

c) Non-infiltrated region. x 196

Figure 4.33 - Optical photomicrograph of a Fe-0.6C compact, infiltrated at 1100°C for 10 minutes. Density = 6.99 Mgm^{-3}

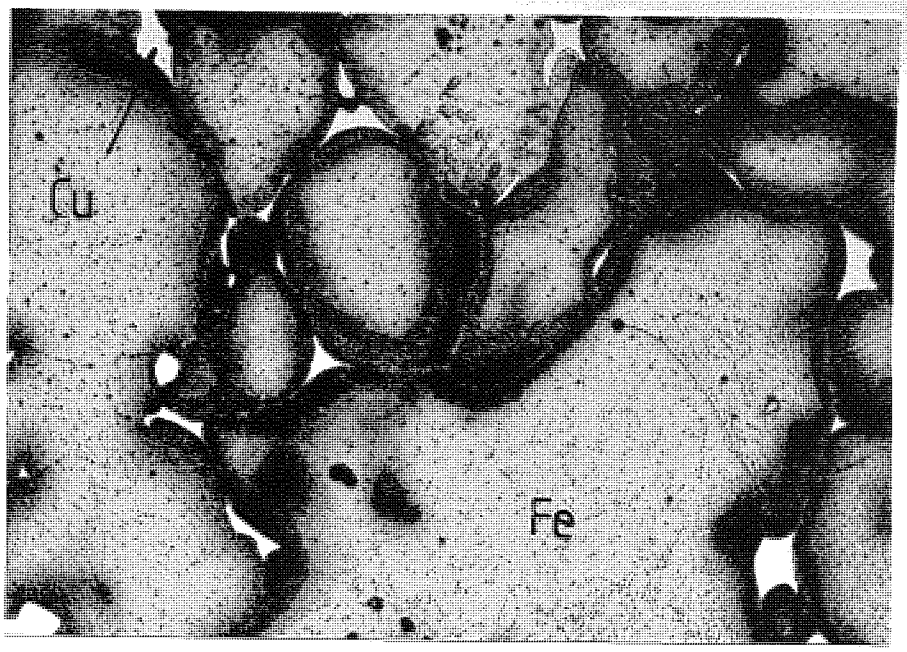

a) No graphite. x 980

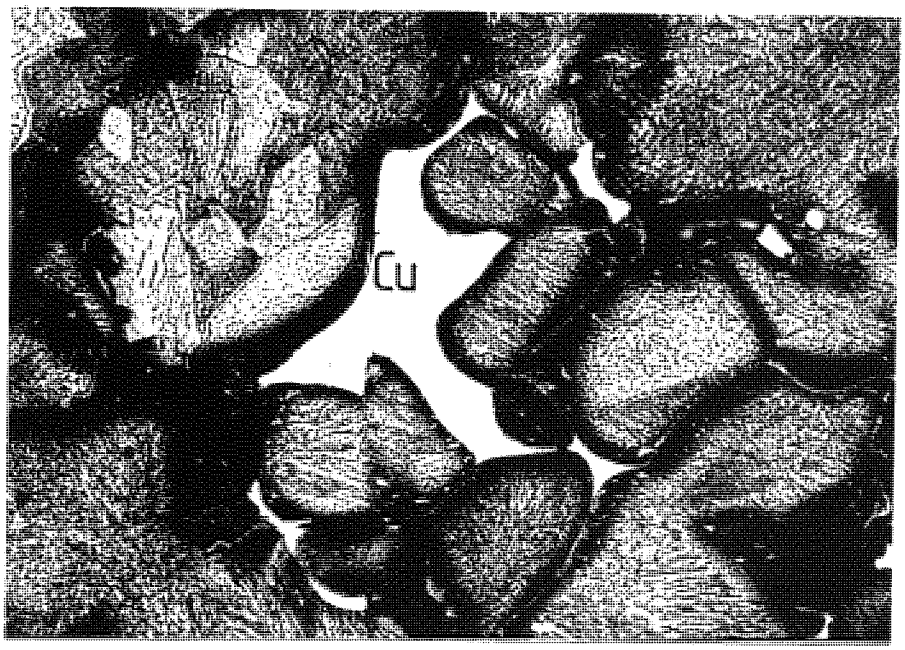

b) 0.6% graphite. x 980

Figure 4.34 - The effect of graphite on dihedral angle of the copper infiltrated compacts.

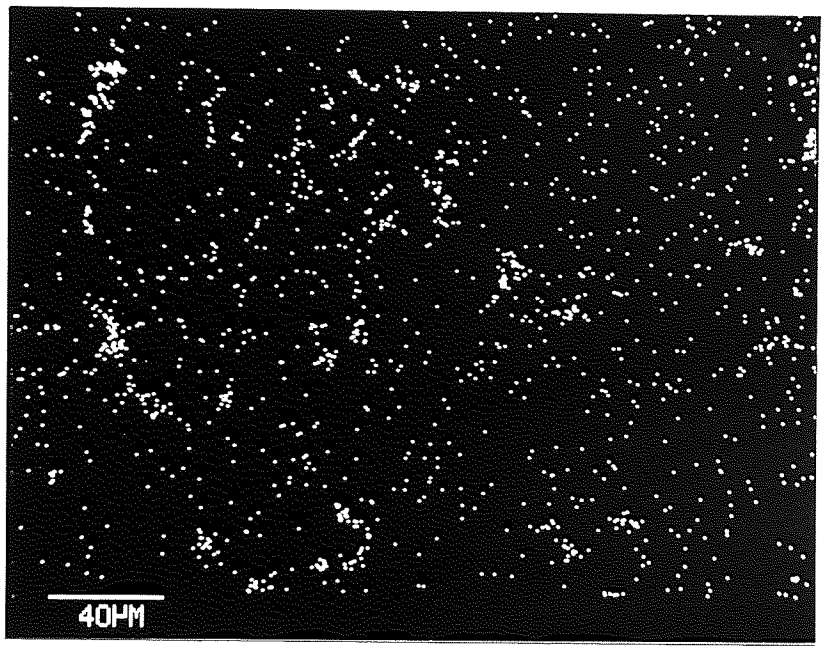

a) No graphite. x 500

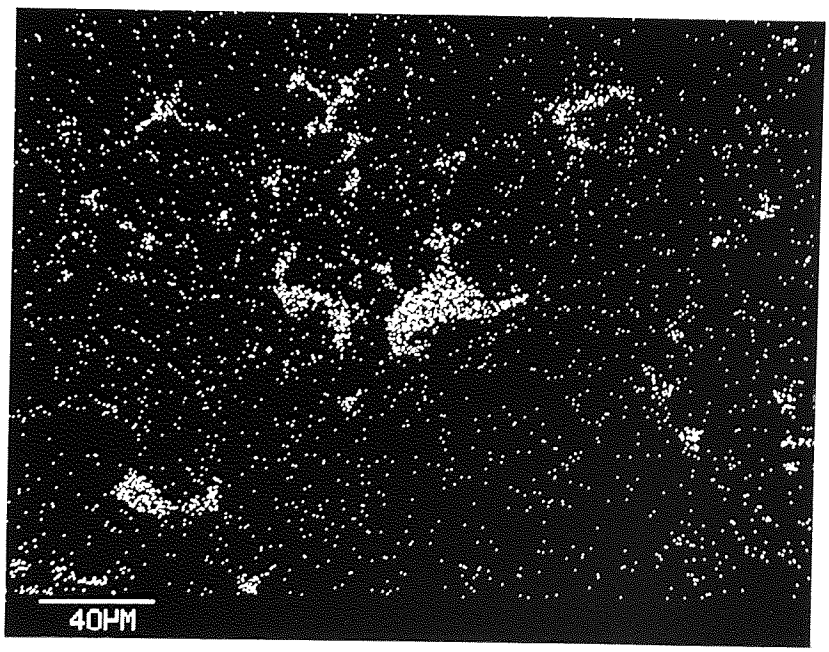

b) 0.6% graphite. x 500

Figure 4.35 - X-ray photomicrographs of Fe-Cu and Fe-Cu-C compacts.

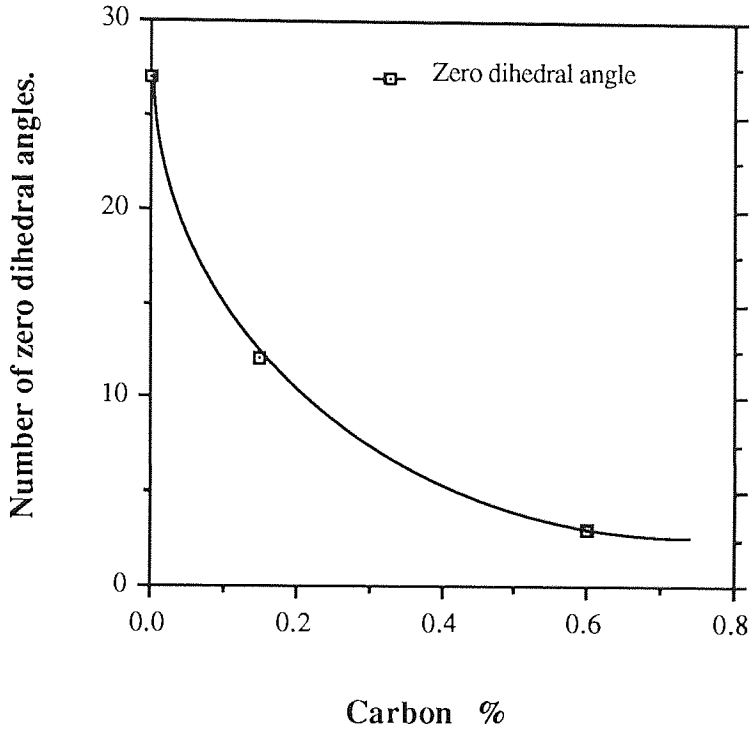

Figure 4.36 - The effect of carbon upon dihedral angle of copper infiltrated compacts.

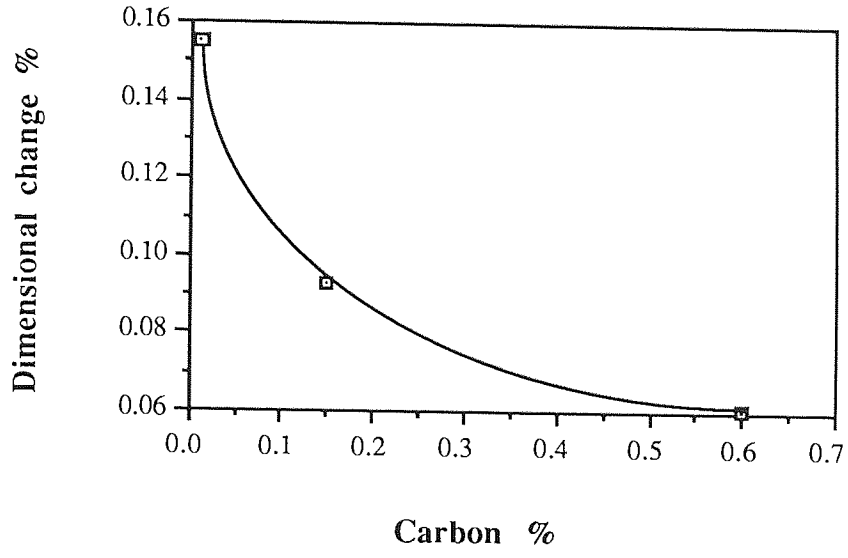

Figure - 4.37 - The effect of carbon upon dimensional changes of copper infiltrated iron compacts.

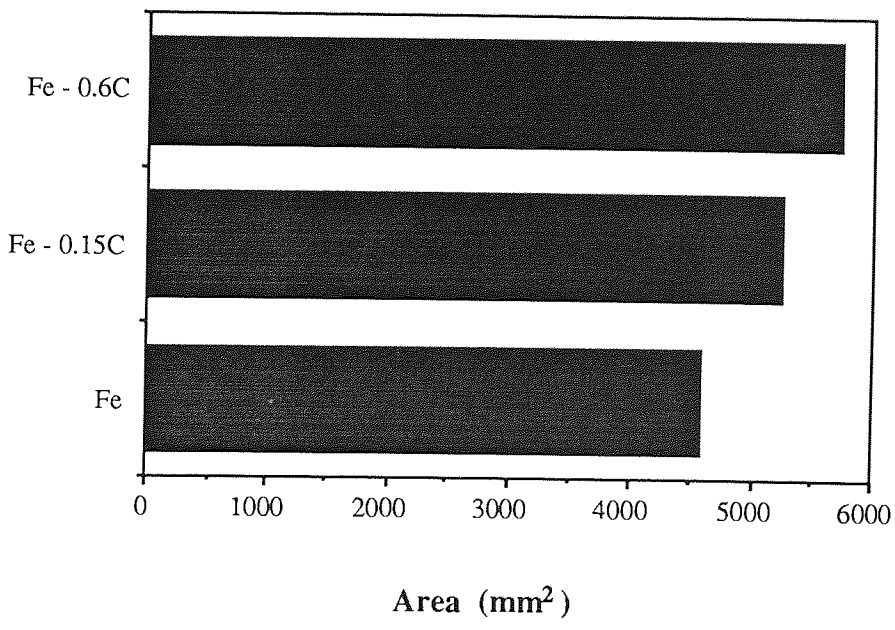

Figure 4.38 - The effect of graphite upon infiltration area.

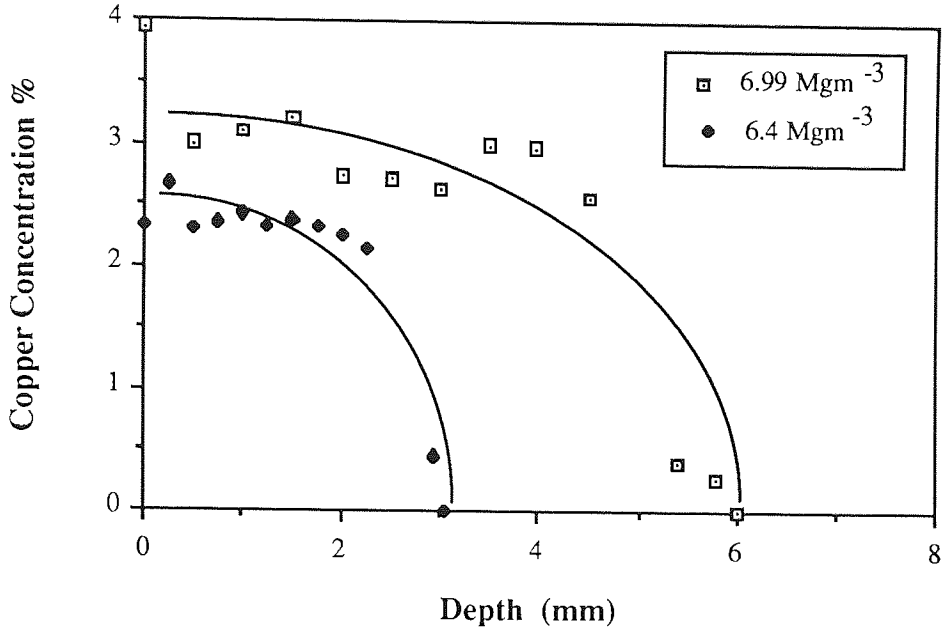

Figure 4.39 - Copper concentration profile for specimens sintered at 1200°C for 10 minutes.

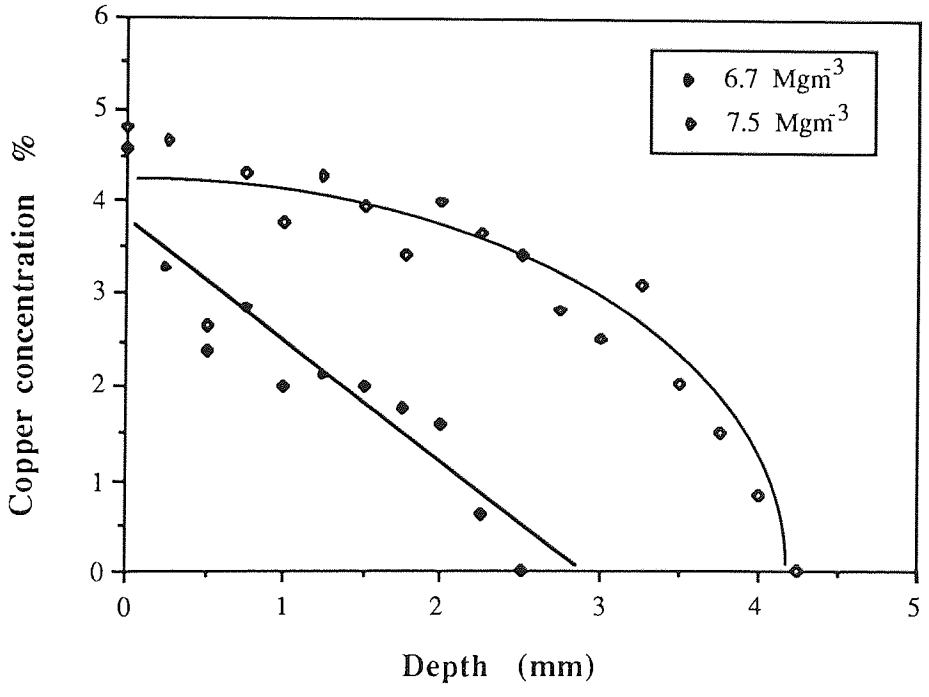

Figure 4.40 - Copper concentration profile in specimens sintered at 1125C for 10 minutes.

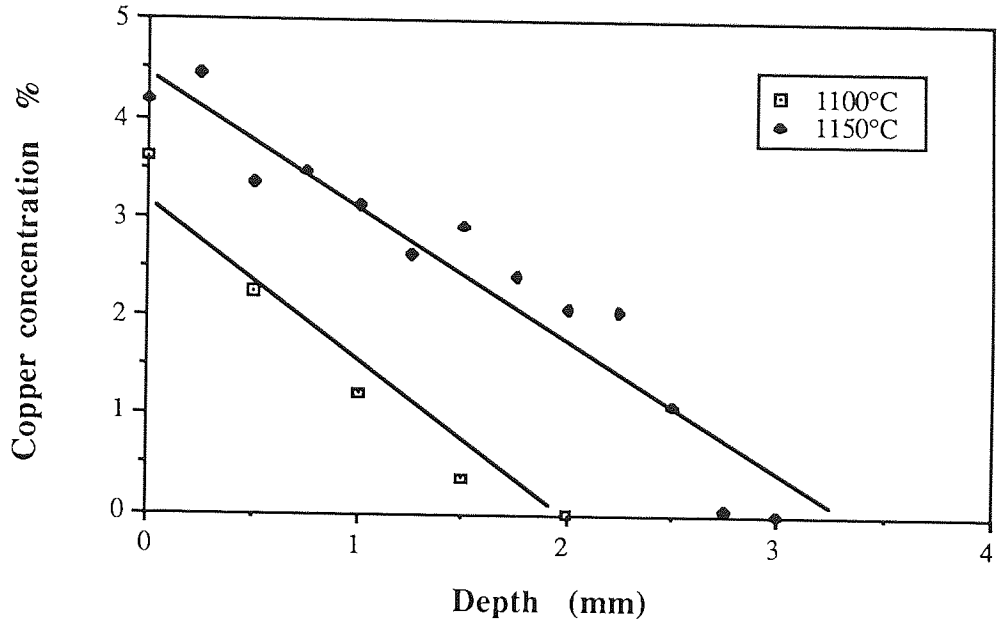

Figure 4.41 - The effect of infiltration temperature on copper concentration profile. Infiltration time =10 minutes. Density = 6.4 Mgm^{-3}

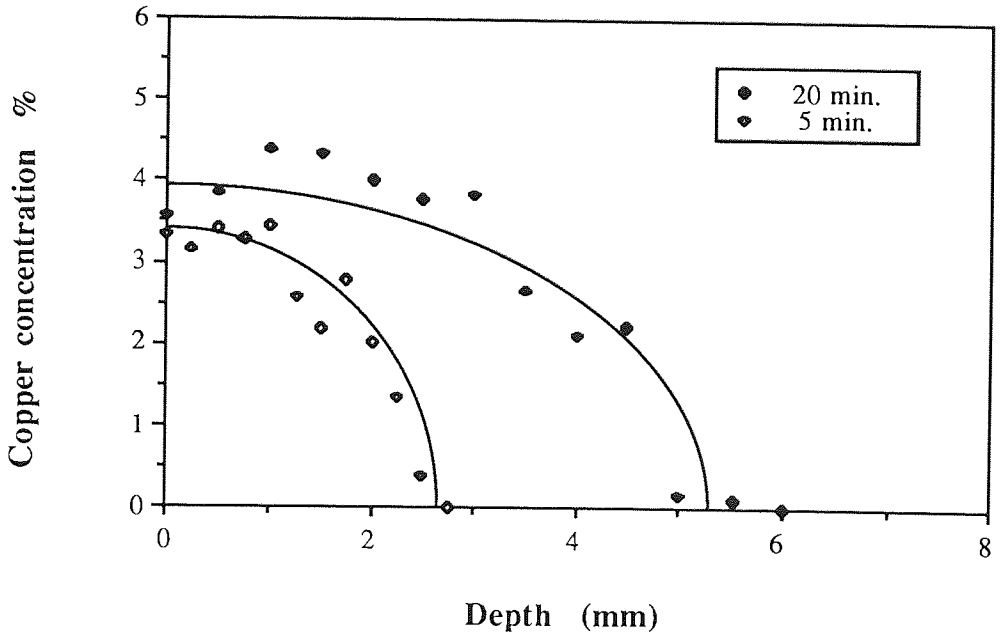

Figure 4.42 - The effect of infiltration time on copper concentration profile. Infiltration temperature = 1125°C. Density = 7.0 Mgm^{-3}

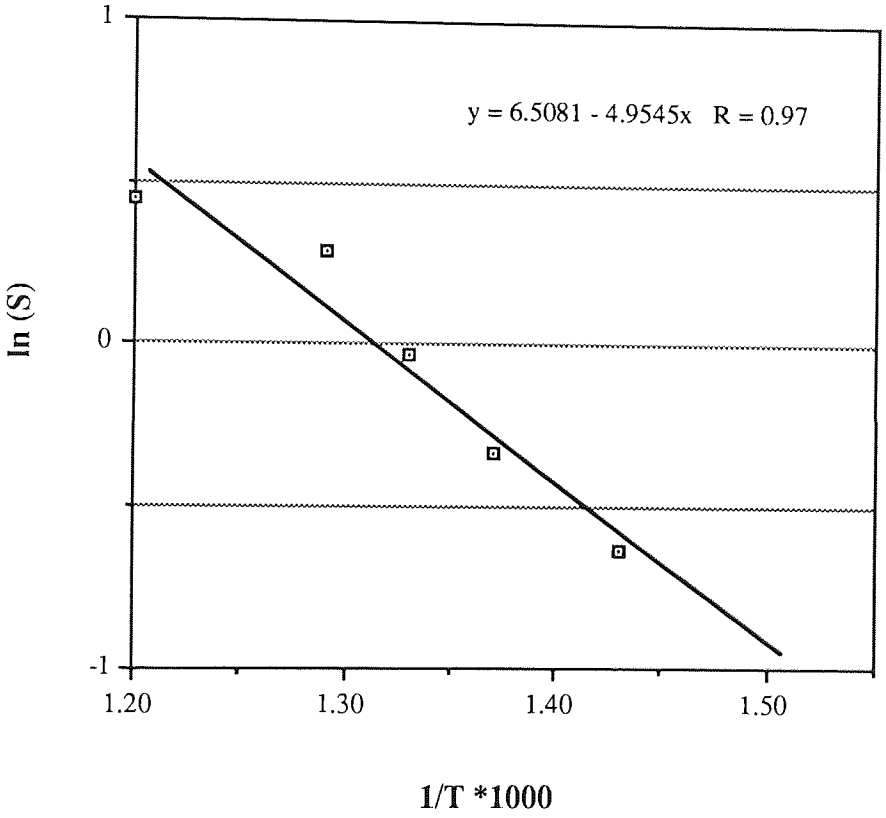

Figure 4.43 - Relationship between temperature and solubility of copper in alfa iron.
S = Solubility T= Temperature (°C)

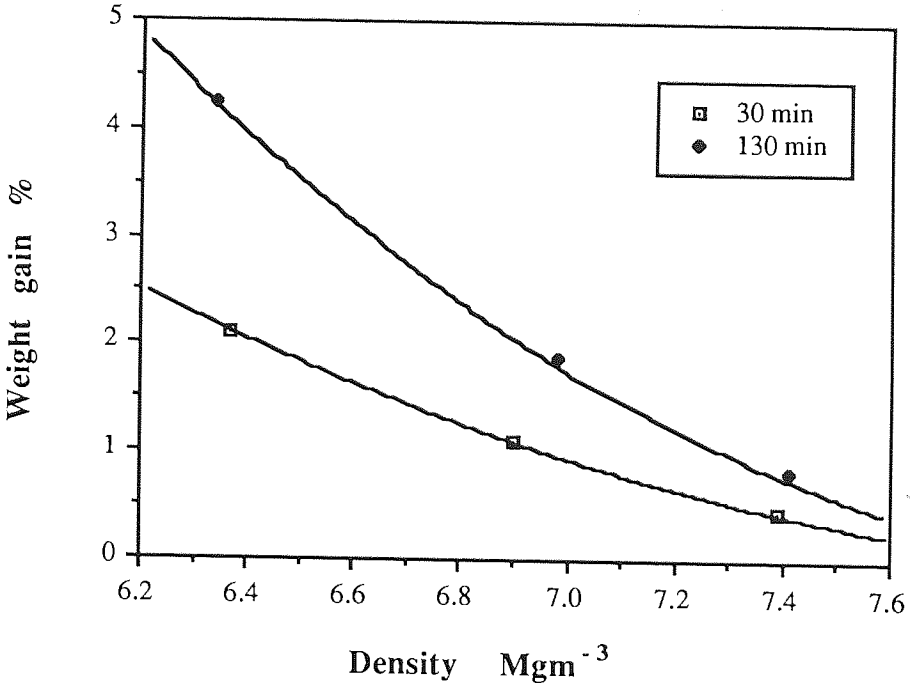

Figure 4.44 - The effect of compact density on weight gain after oxidation at 500°C in air.

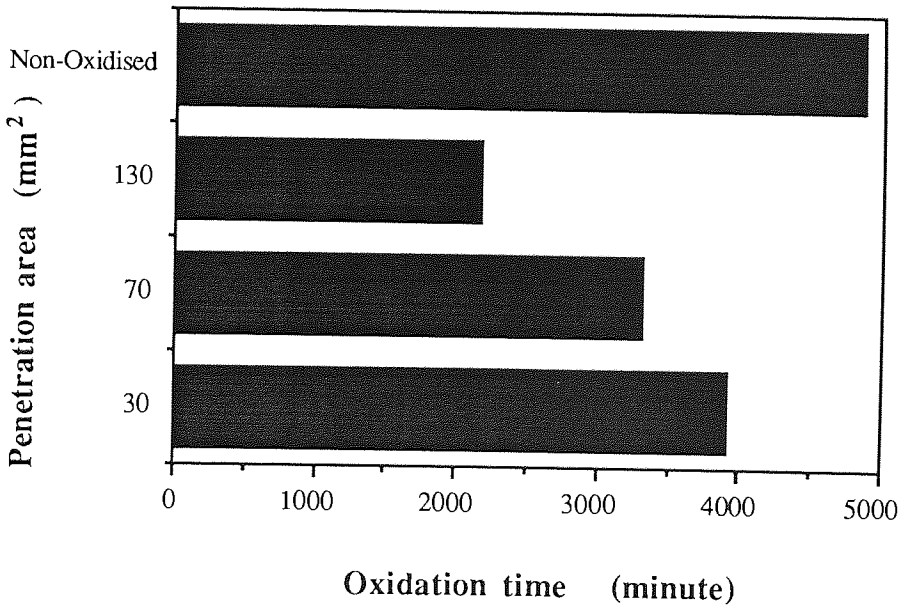

Figure 4.45 - Histogram showing the copper penetration area in the oxidised cpmpacts. Oxidation temperature = 500°C

a) Edge and top surface, showing the duplex layer x 980

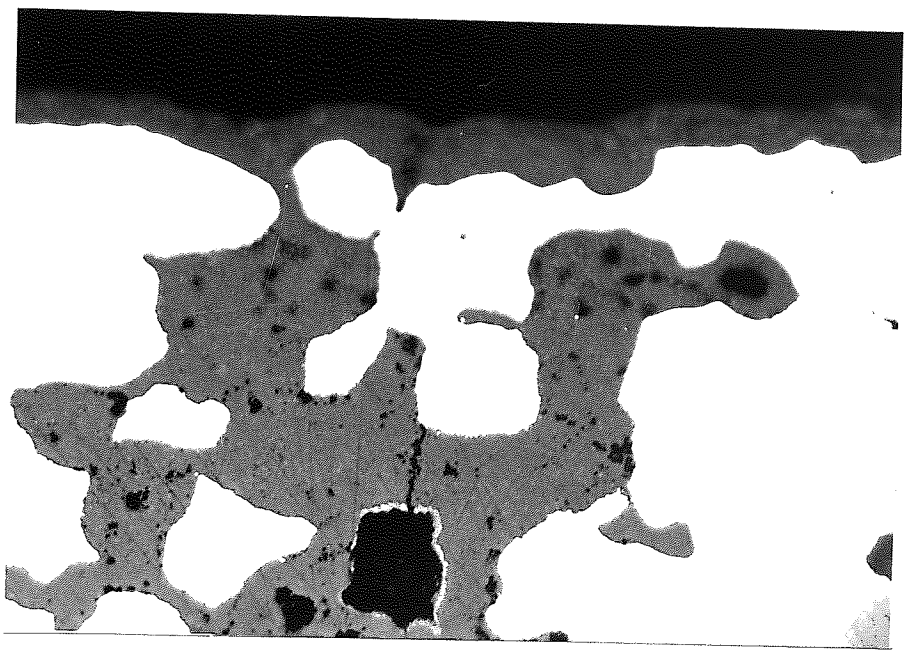

b) Pore blocked by the oxidation product. x 980

Figure 4.46 - Optical photomicrograph of a compact oxidised at 500°C for 130 minutes. Density = 6.92 Mgm^{-3}

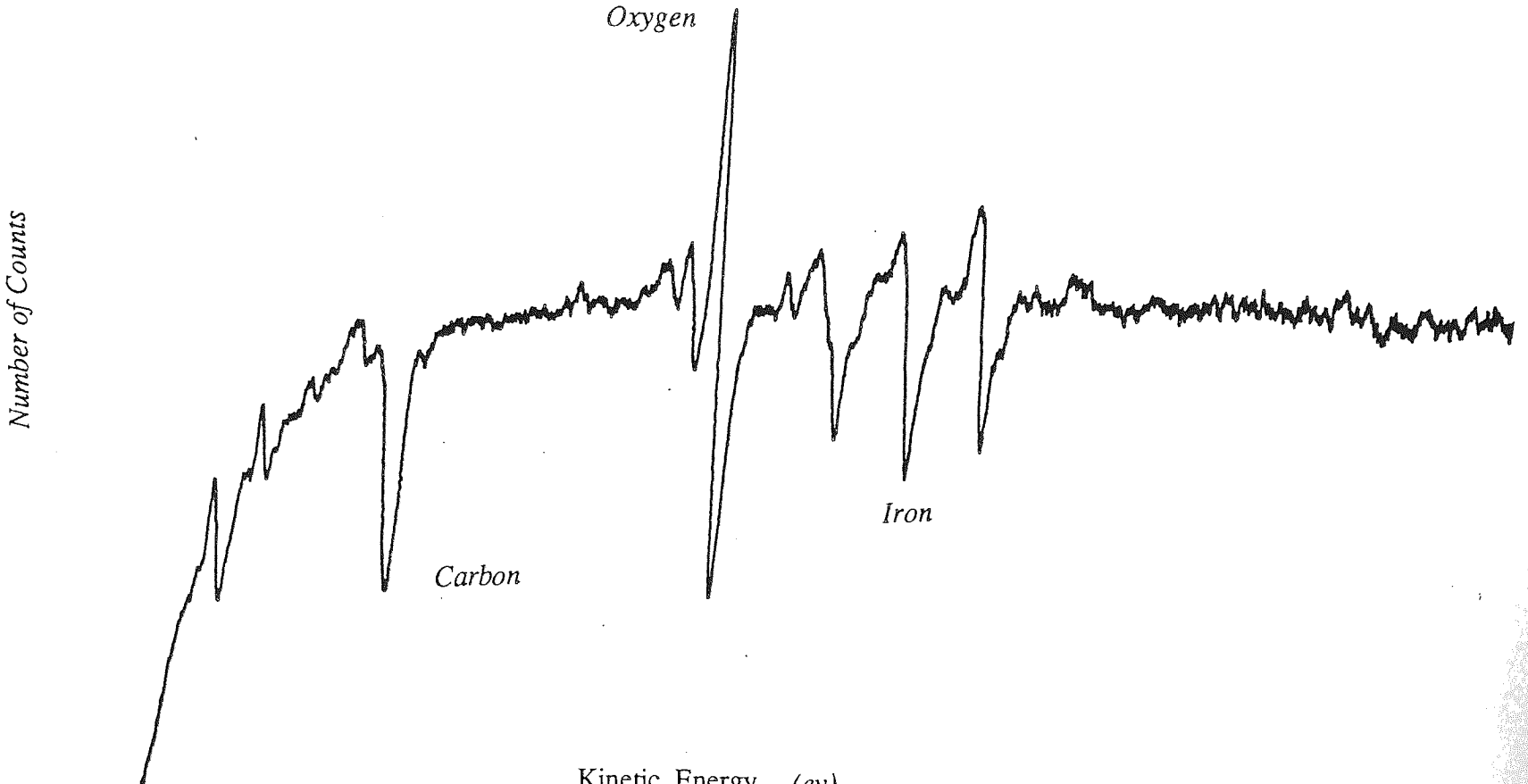

Figure 4.47 - A typical Auger trace of the oxide surface.

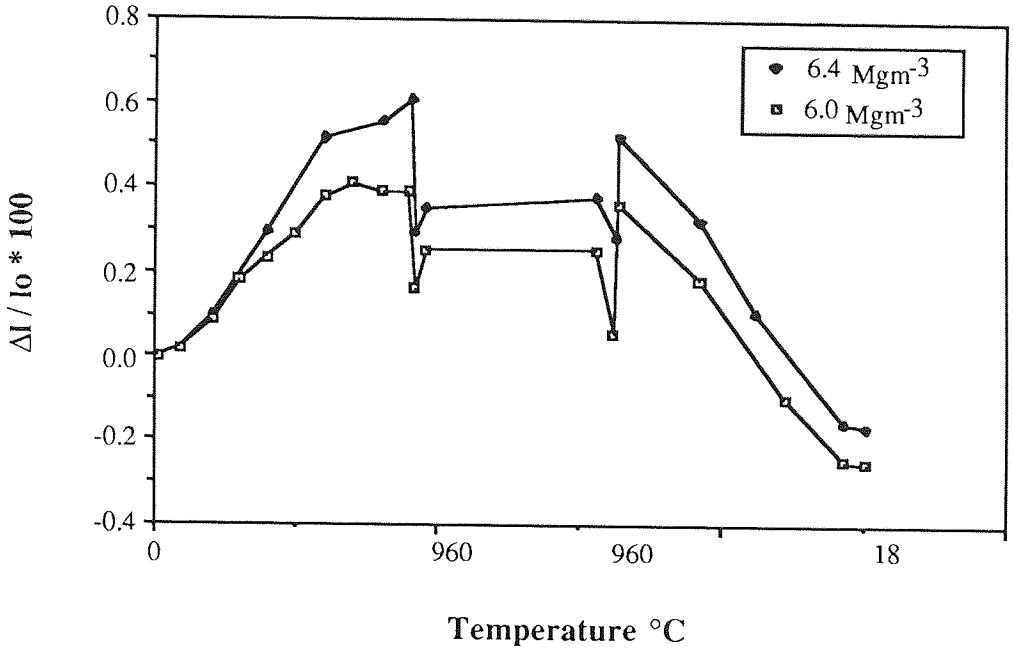

Figure 4.48 - The effect of density upon dilatometric curves of plain iron compacts sintered at 960 °C.

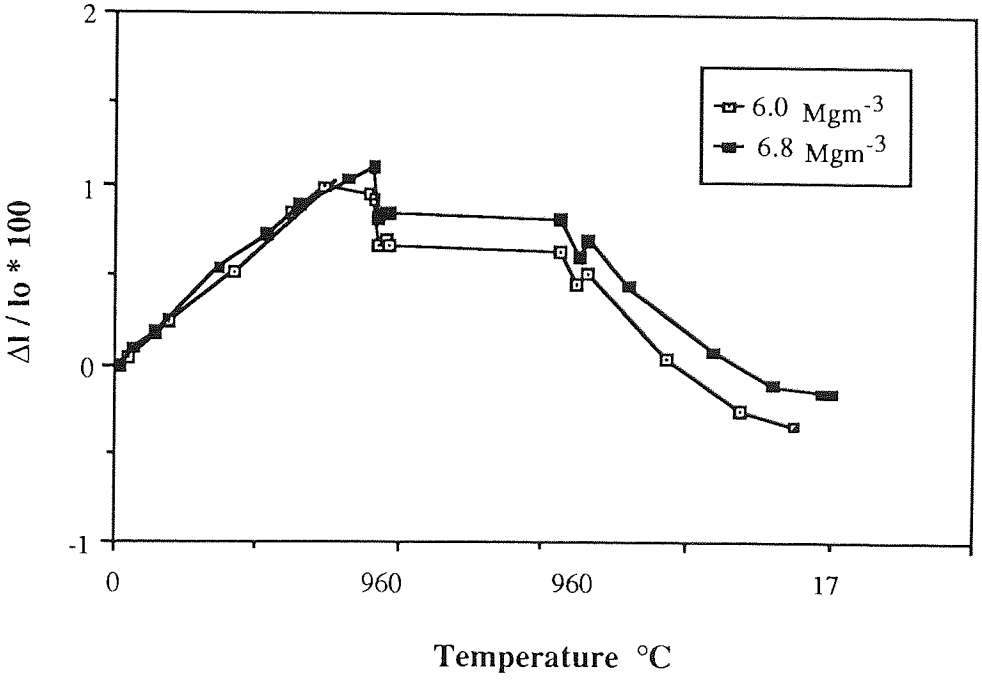

Figure 4.49 - The effect of density upon dilatometric curves of Fe-4Cu compacts sintered at 960 °C.

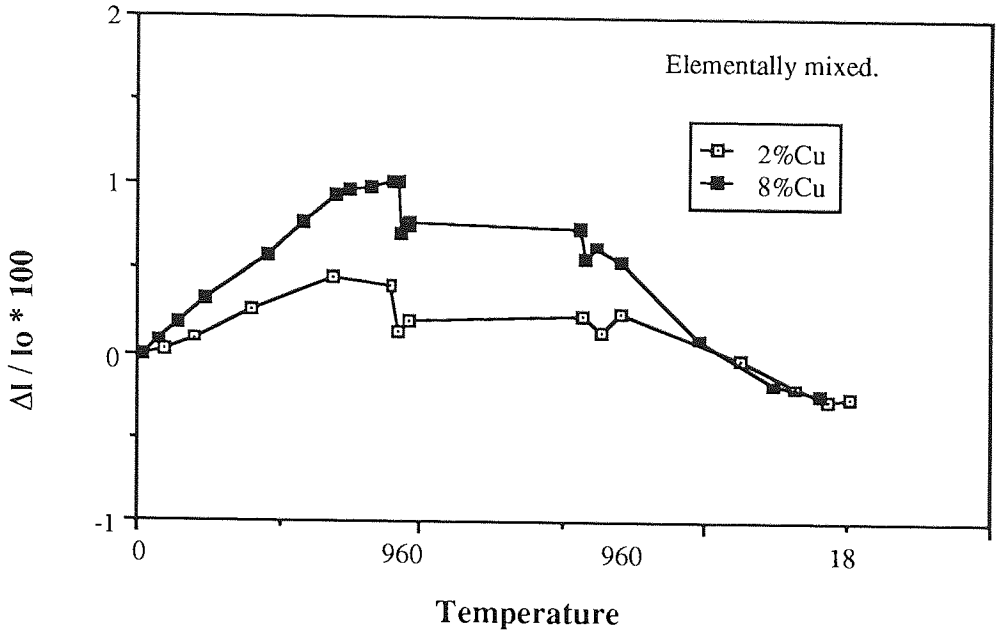

Figure 4.50 - The effect of different levels of copper additions upon dimensional changes in sample sintered at 960 °C. Density = 6.4 Mgm^{-3}

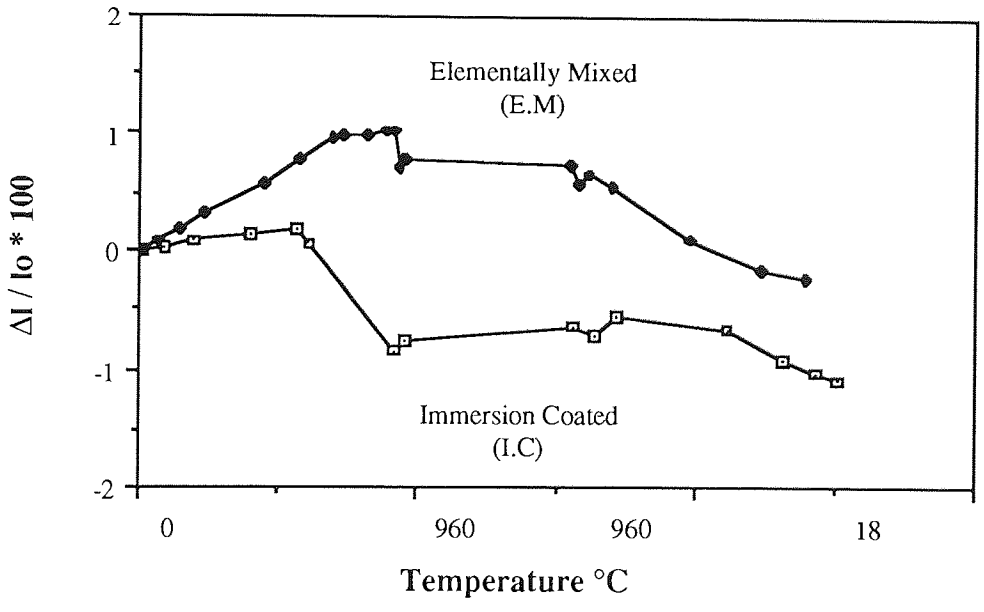

Figure 4.51 - TMA traces of 4% copper coated and elementally mixed Fe-Cu compacts sintered at 960 °C.

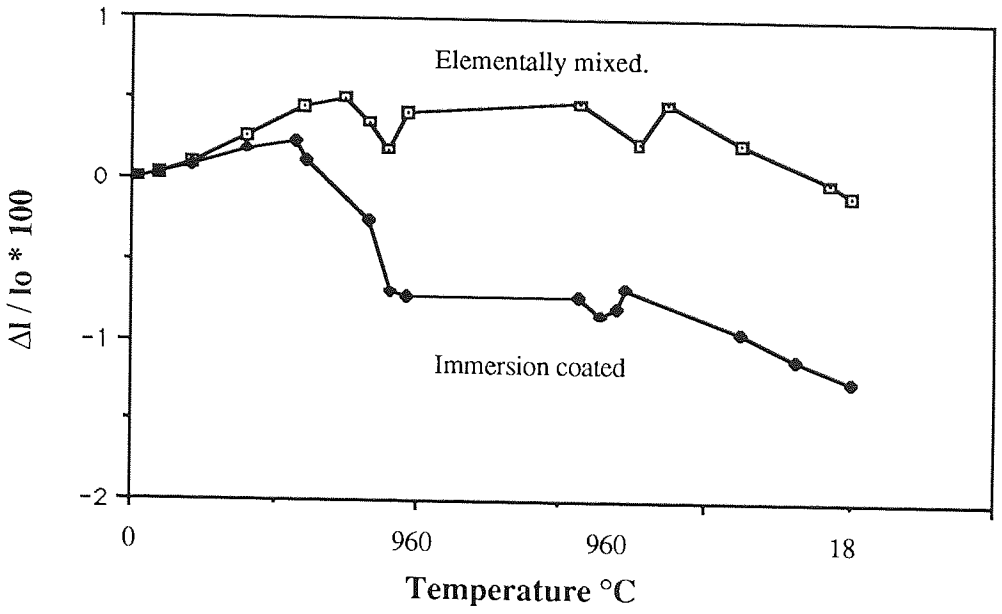

Figure 4.52 - TMA traces of copper coated and elementally mixed Fe-4Cu-0.6C compacts sintered at 960°C.

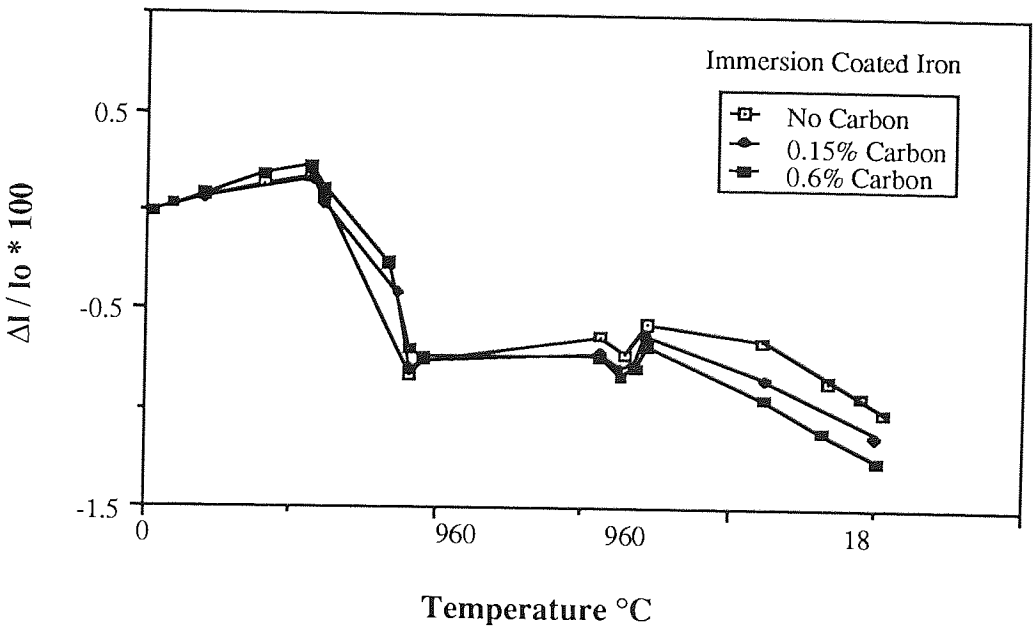

Figure 4.53 - The effect of carbon upon dimensions of copper coated Fe-Cu compacts sintered at 960°C.

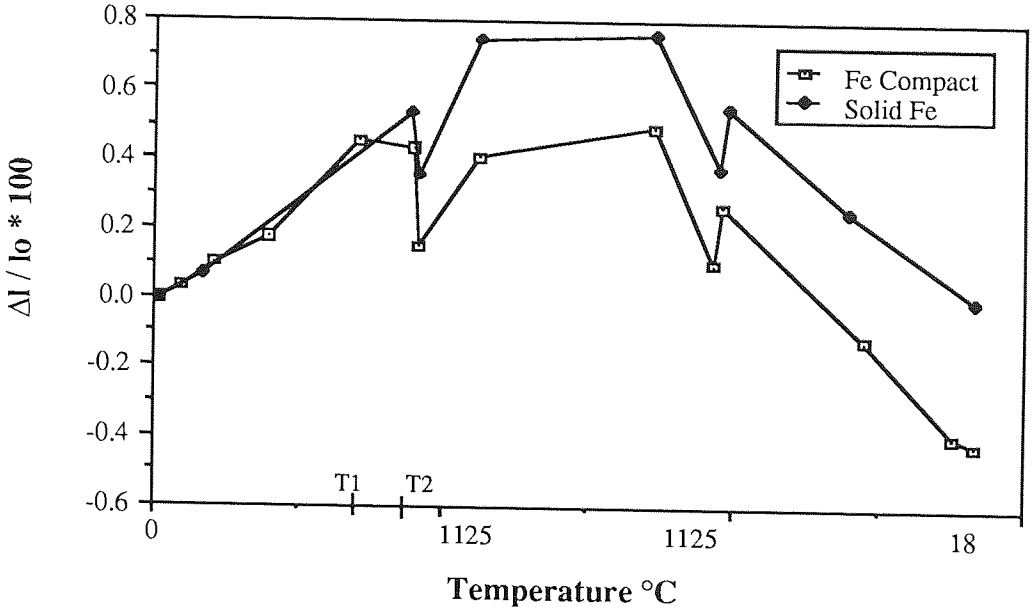

Figure 4.54 - Dilatometric curves of pure Armco iron slug, and plain iron compact.

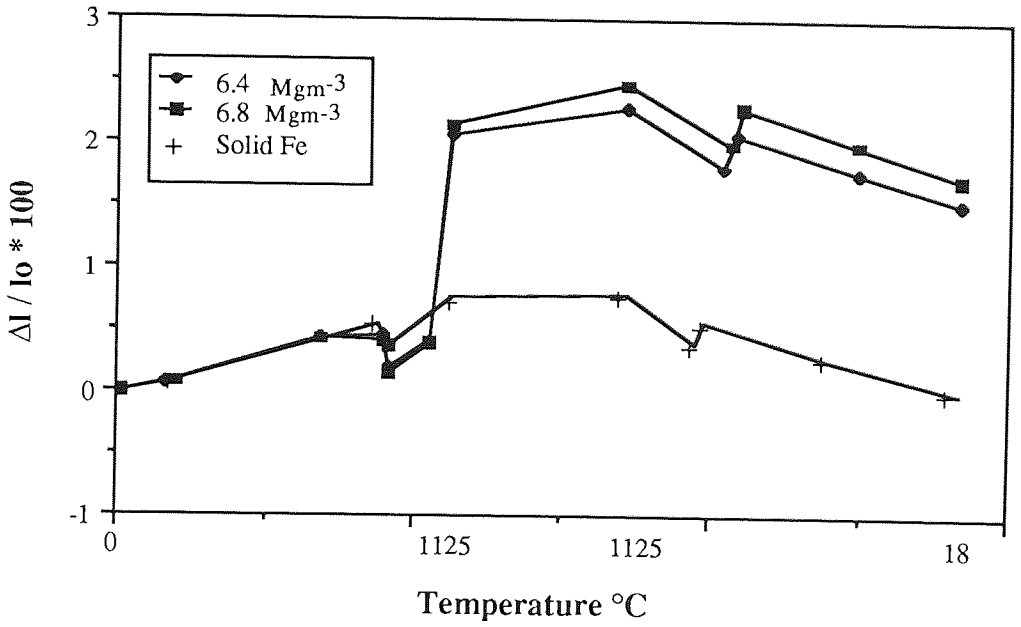

Figure 4.55 - The effect of density upon dilatometric curves of Fe-4Cu compacts at 1125°C.

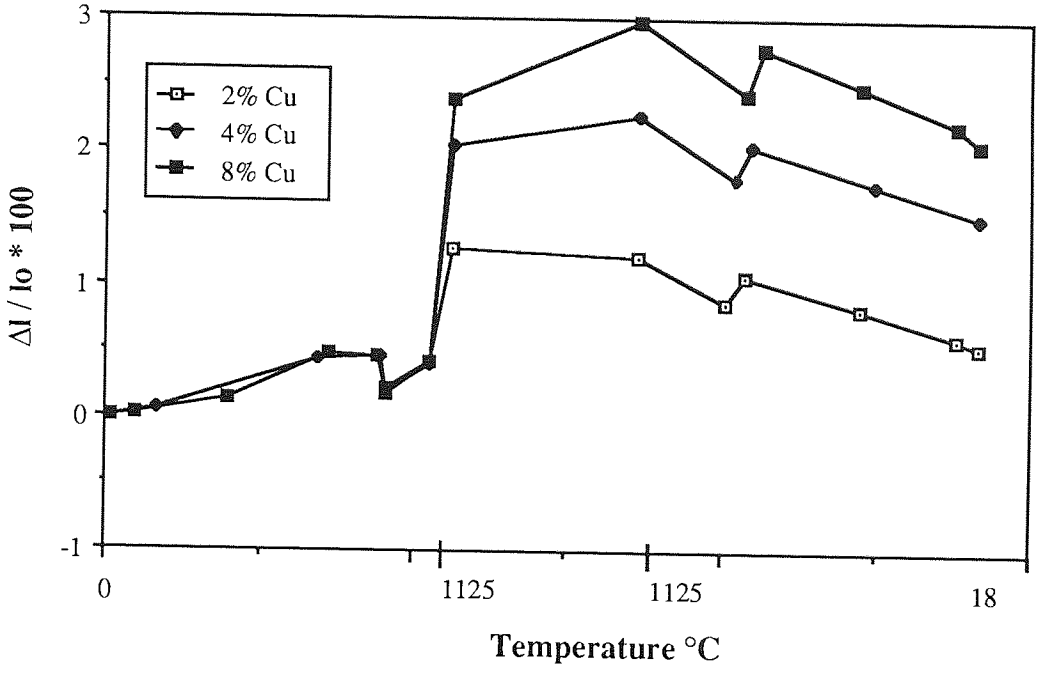

Figure 4.56 - The effect of copper upon dimensions of Fe-Cu compacts at 1125°C.

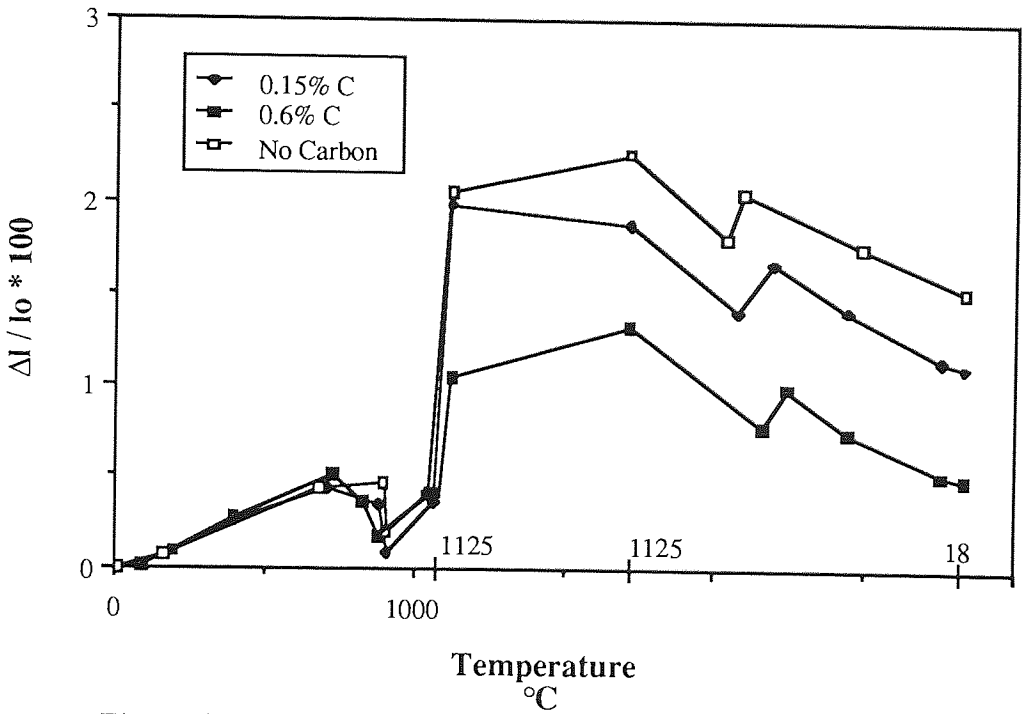

Figure 4.57 - The effect of graphite upon dimensions of Fe-4Cu elementally mixed compacts.

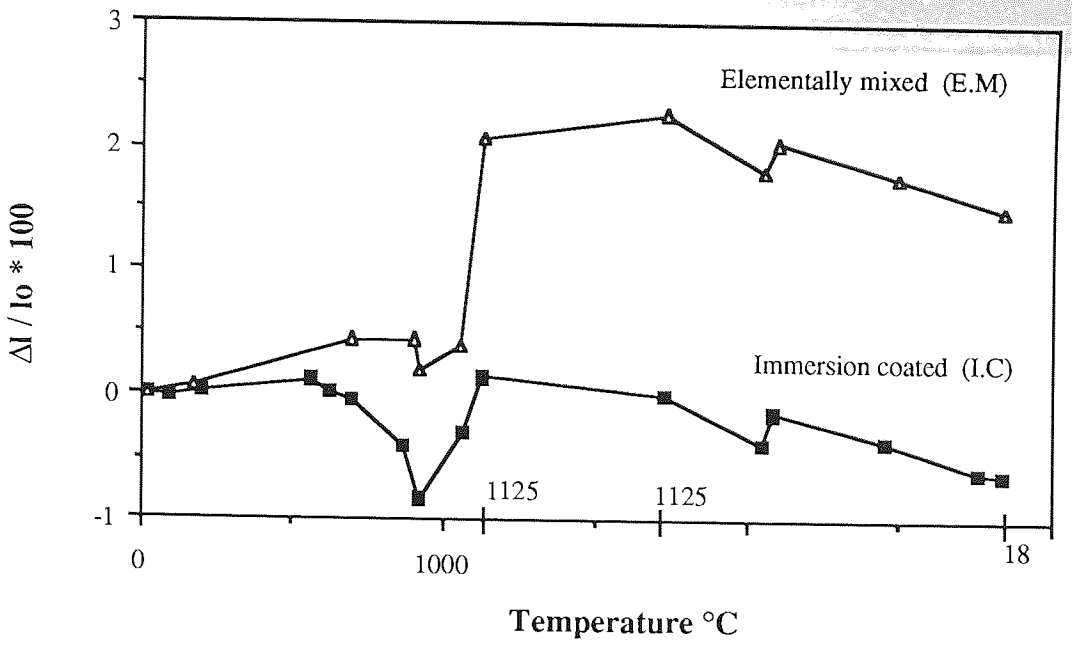

Figure 4.58 - TMA traces of immersion coated and elementally mixed Fe - 4Cu compacts.

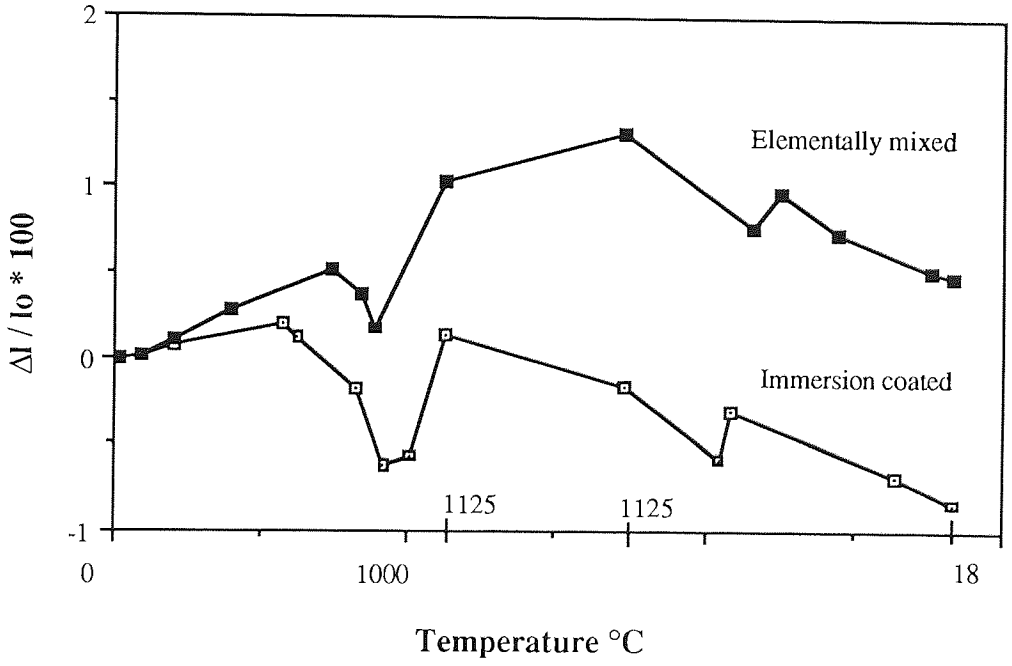

Figure 4.59 - TMA traces of immersion coated and elementally mixed Fe-4Cu- 0.6 C compacts.

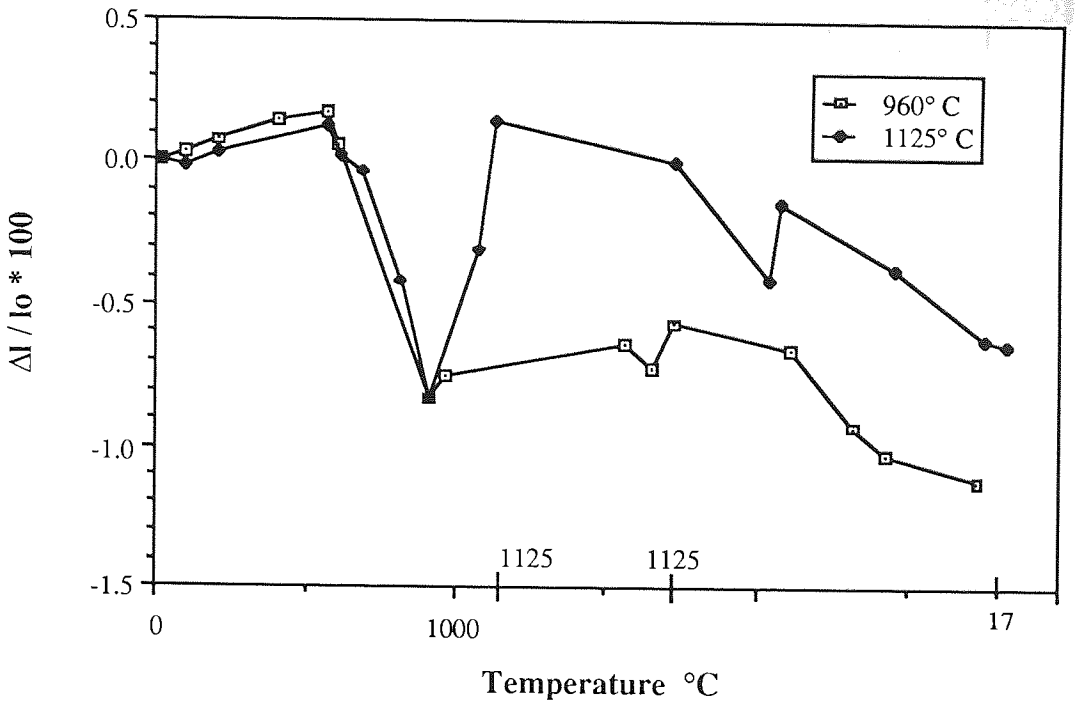

Figure 4.60 - Dilatometric curves of immersion coated compacts, sintered isothermally at 960 and 1125 °C.

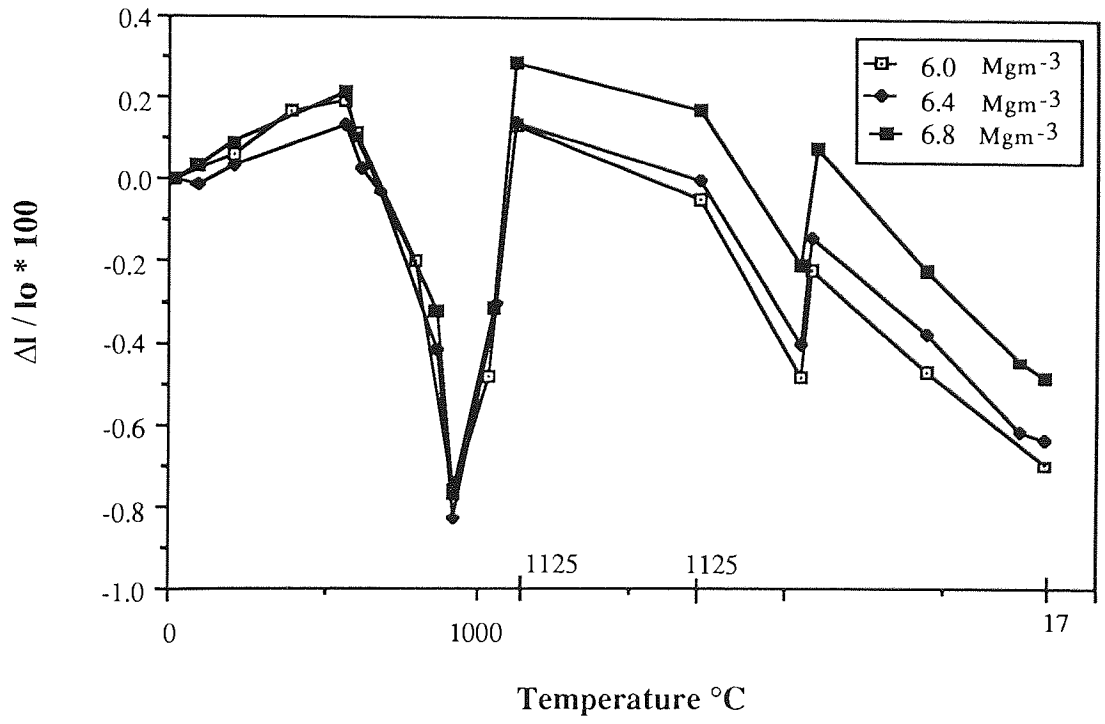

Figure 4.61 - The effect of density upon dimensions of Fe - 4Cu immersion coated compacts at 1125 °C.

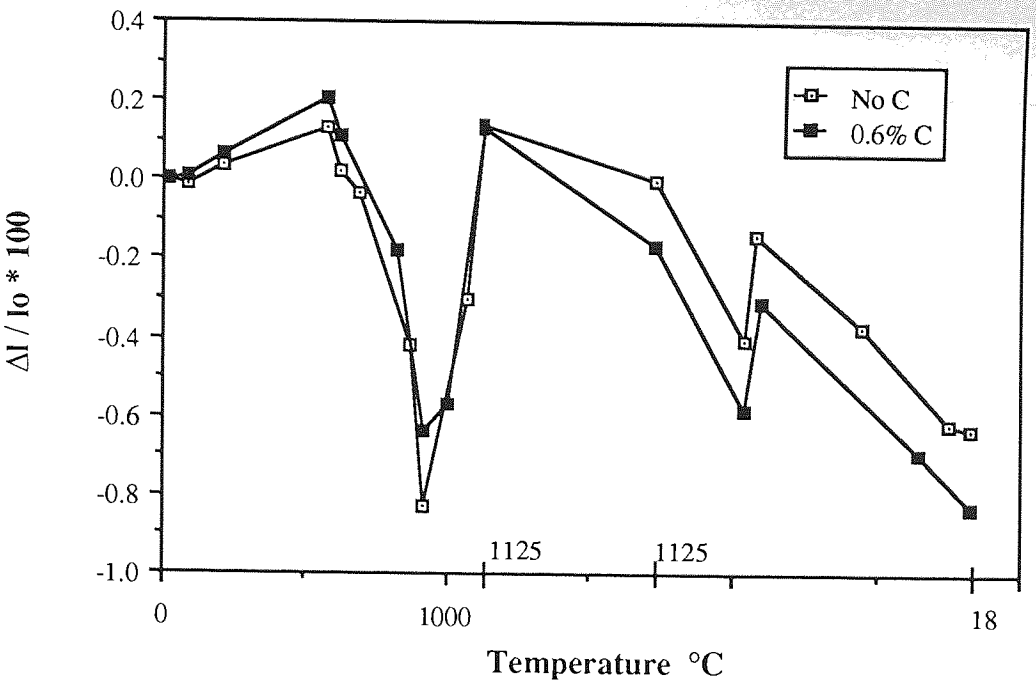

Figure 4.62 - The effect of carbon upon dimensions of Fe - 4Cu immersion coated compacts at 1125 °C.

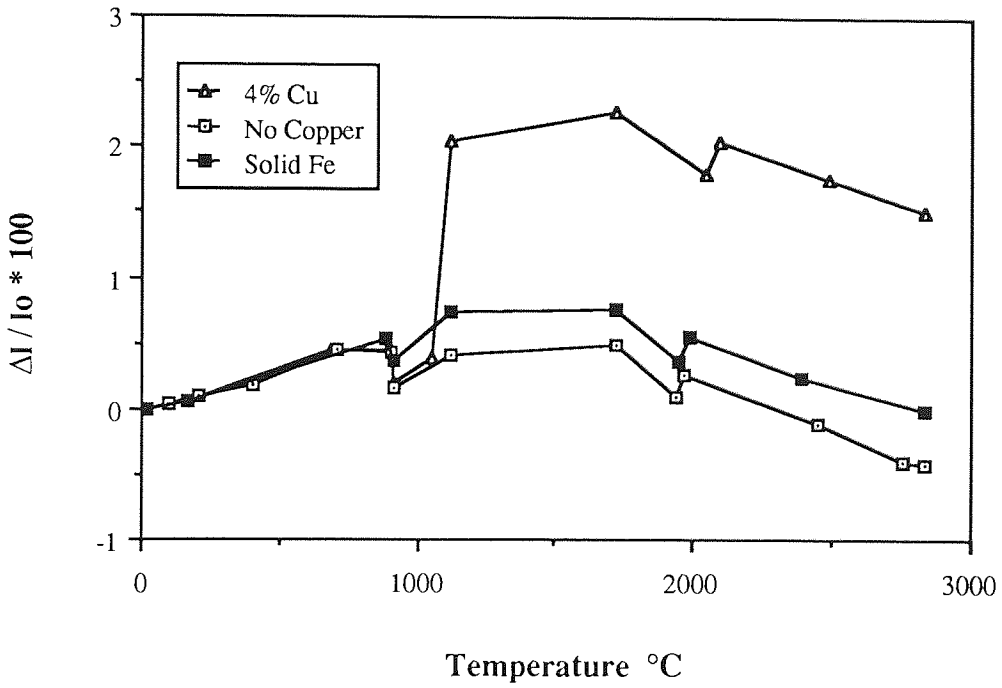

Figure 4.63 - Comparison of dilatometric traces of a plain iron compact , pure solid iron slug and and Fe-4Cu E.M compacts.

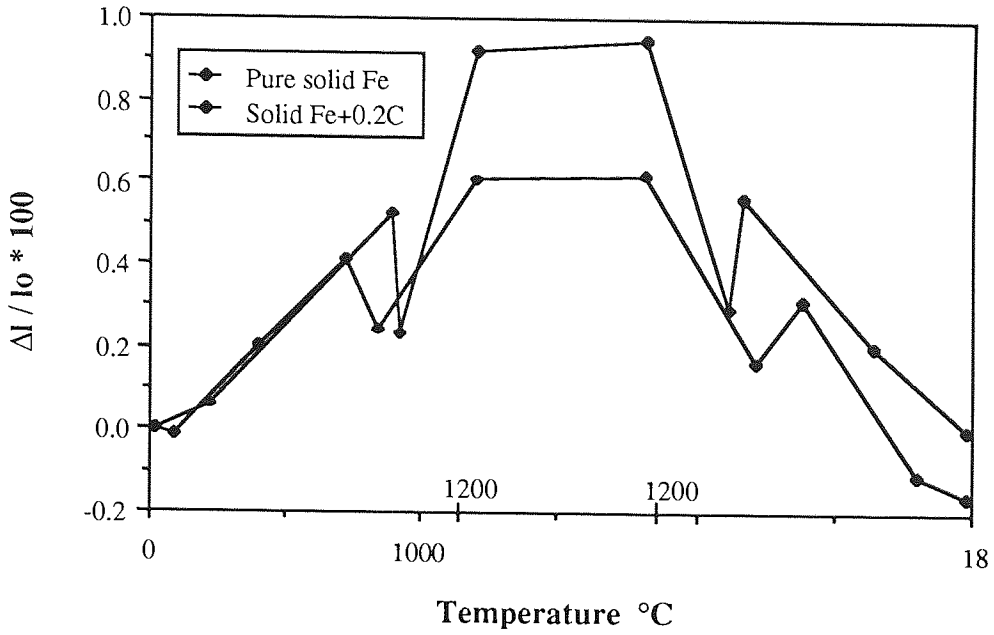

Figure 4.64 - The effect of carbon upon expansion of solid iron slug at 1200°C.

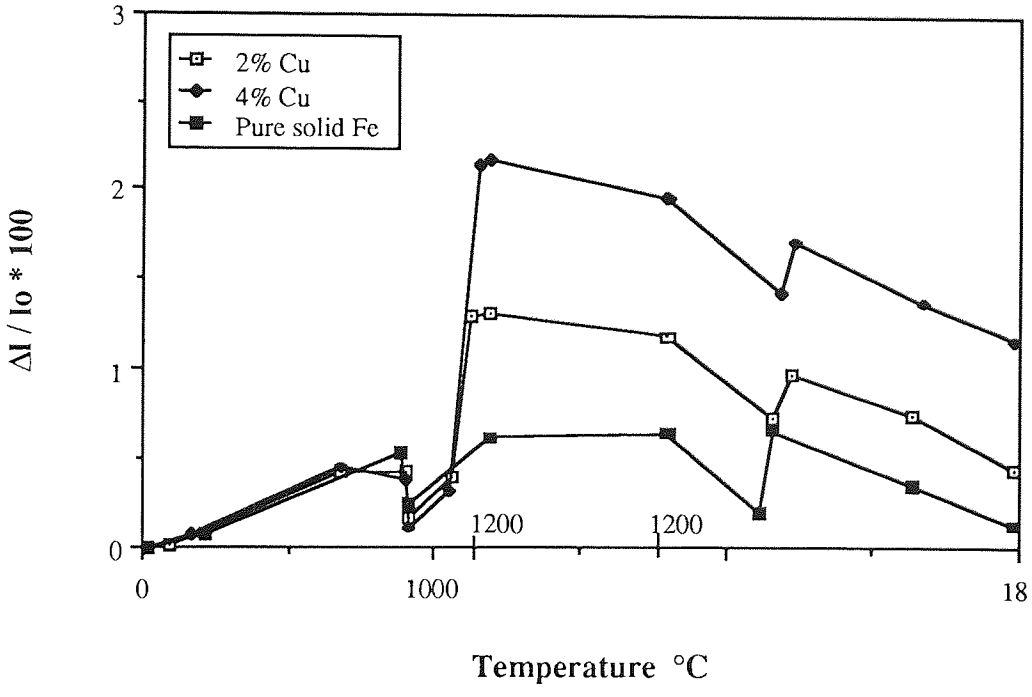

Figure 4.65 - The dilatometric curves of Fe-2Cu and Fe-4Cu compacts and pure iron slug at 1200°C.

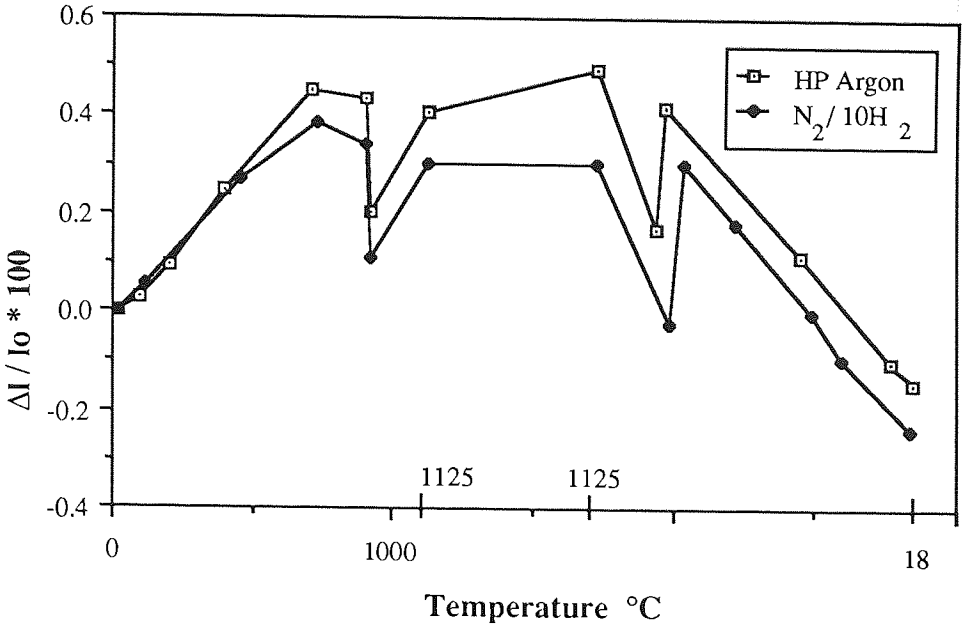

Figure 4.66 - The effect of atmosphere on dilatometric curves of plain iron compacts.

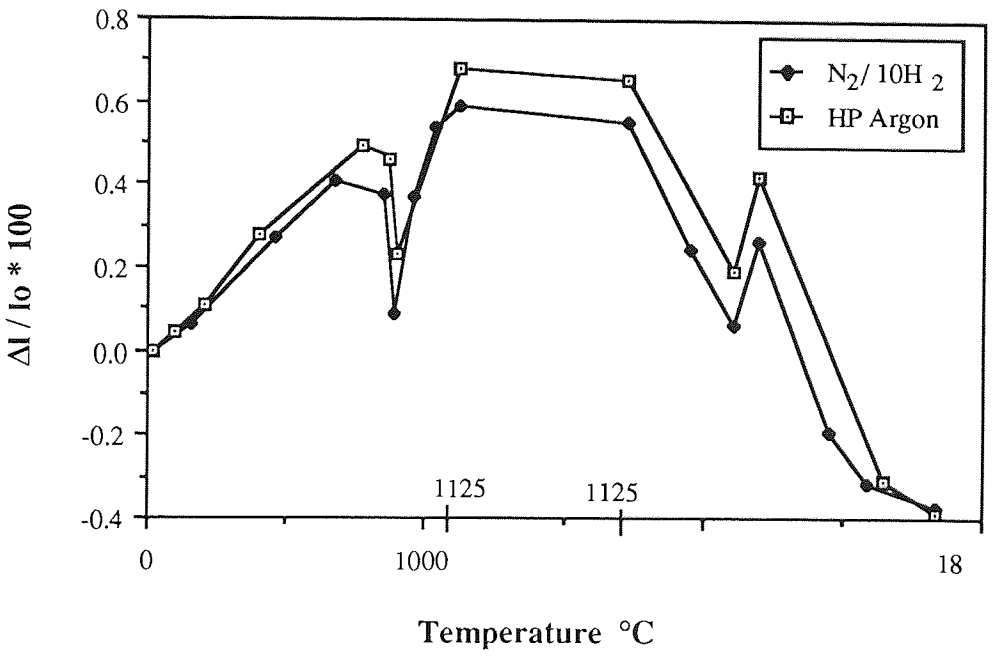

Figure 4.67 - The effect of atmosphere on dilatometric curves of Fe-0.6C compacts.

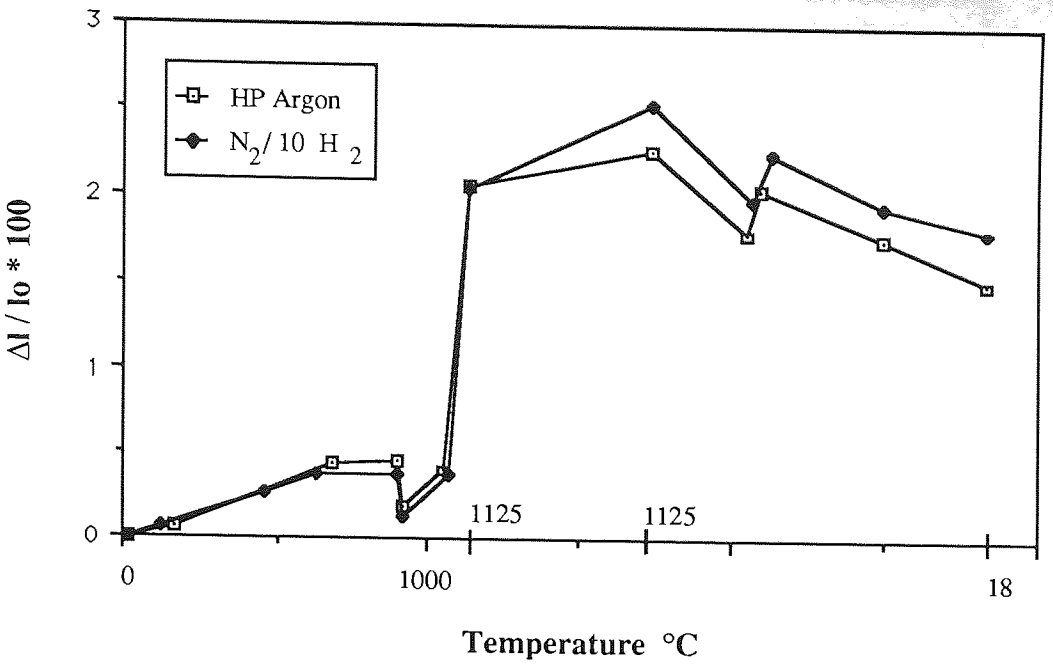

Figure 4.68 - The effect of atmosphere on TMA traces of Fe-4Cu elementally mixed compacts

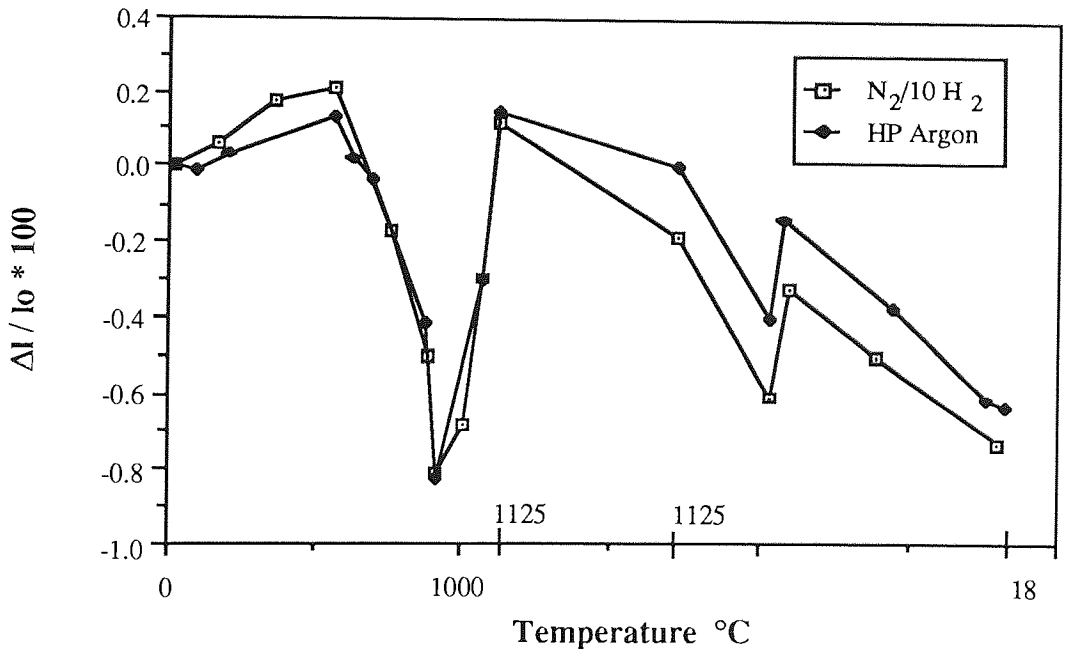

Figure 4.69 - The effect of atmosphere on TMA traces of Fe-4Cu immersion coated compacts.

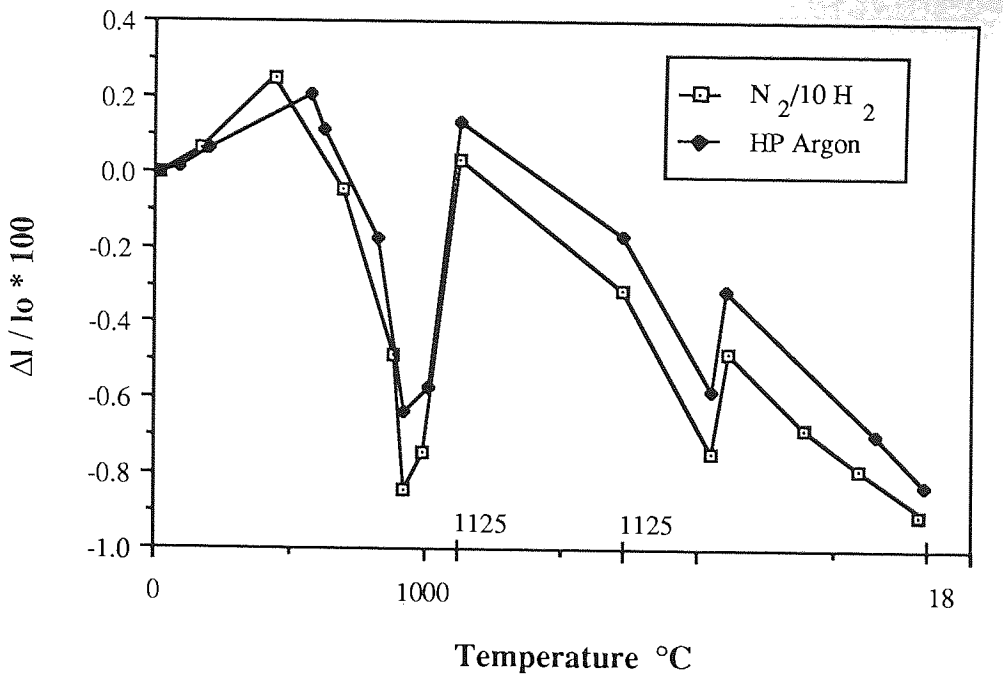

Figure 4.70 - The effect of atmosphere on TMA traces of Fe-4Cu-0.6C immersion coated compacts.

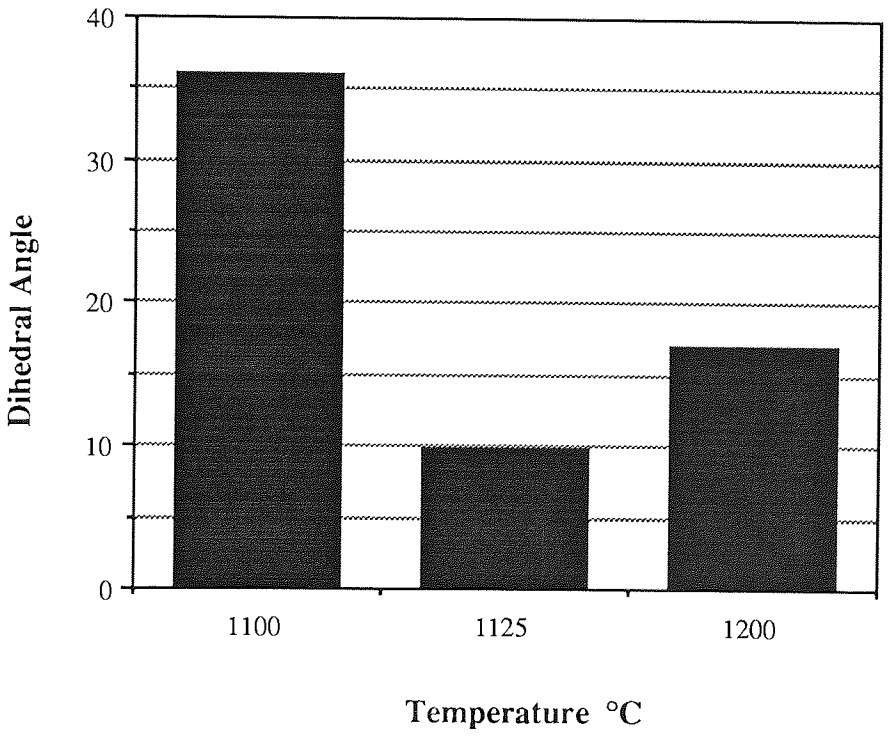

Figure 4.71 - The effect of sintering temperature upon dihedral angle of Fe-4Cu compacts.

5. Discussion

5. Discussion

5.1 Anchorbraze Study

As a starting point in the experimental work, experiments were done with Anchorbraze (AB72). It was considered that examination of the behaviour of a brazing alloy known to be "non penetrating", could provide some useful clues to the significant microstructural changes which prevent copper penetration during brazing.

Anchorbraze contains Cu, Ni, Si and B, and when used as a sinter-braze at 1125°C, the brazing stages were as follows:

a) Braze alloy melted around 1049°C.

b) The liquid metal ran along the iron / Anchorbraze interface by capillary forces.

c) Anchorbraze alloyed with the base metal.

As the brazing metal is melted, it alloys with the base metal. The alloy so formed has a higher flow temperature than the braze metal, preventing further penetration as sinter-brazing proceeds. This alloy is seen as the grey phase (phase 2) in Figure 4.2. The alloying constituents are shown in Table 4.2. It mainly consisted of iron and the copper content was much less than phase 1, the liquid phase.

Knopp (1975), suggests a brazing system employing "SKC2" supplied by Hoganas Corporation. The chemical composition of the brazing alloy was not disclosed in the paper, but the brazing mechanisms were similar to that of AB72. The use of an iron compact made from a reduced iron oxide powder was considered to give a smoother brazed joint than a compact made from atomised powder (Knopp, 1975).

It is therefore clear that "pore blockage", is the prime objective during brazing if pore penetration is to be avoided. In the case of Anchorbraze, the pores were

blocked by an alloy of a higher melting point than the brazing material. In the present study, copper penetration into the pores was reduced by filling the pores with an oxidation product which is discussed in section 5.6.

5.2 Copper Infiltration.

In general, following conditions should be met for effective liquid phase sintering and infiltration.

1- The solid phase should be soluble in the liquid, but the reverse solubility of the liquid in solid should be low. In the iron - copper system, iron is soluble in copper and a high density results with a copper concentration of 4-8%. If there is a high solubility of the liquid phase in the solid, then it is possible that the liquid phase will be transient and will loose its effect as homogenization takes place.

2- Good wetting is essential. In order to achieve complete wetting of the solid particles, it is necessary for the solid / liquid surface energy to be much less than the solid / solid surface energy, otherwise, the wetting angle (or contact angle), is high. If these conditions are met, the shrinkage rate of the compact should increase demonstrating enhanced sintering.

As the samples are heated to the infiltration temperature of 1100°C (Figure 4.3), interdiffusion of iron and copper proceeds. At the interface, the solubility of iron in copper and copper in iron increases with temperature. Copper has a higher solubility in iron especially above the α to γ transformation. Maximum solubility of copper in iron is 8% at 1094°C. However Rivlin (1984), quoted that it can be as high as ~10%. The maximum solubility of iron in copper is 4% at 1094°C. Copper melting point is 1084°C but with iron in solution, it could rise to 1094°C. Copper becomes saturated with iron very quickly. During cooling, the intersolubilities are

reduced, copper precipitates as small copper rich zones which can lead to precipitation hardening. Excess iron precipitates at Fe / Cu interfaces as a thin dark band (Figure 4.3 and 4.4). However, at high sintering temperatures and times, complete diffusion of copper in iron occurs so that no isolated copper regions remain as shown in Figure 4.5. In the early stages, the rate of dissolution of iron is higher at Fe / Cu interface than in the later stage of infiltration, which can be seen in Figure 4.4, 4.5 and 4.31. As the liquid copper runs down further into the capillaries, it becomes saturated with iron (up to 4%) and the rate of iron dissolution is decreased. Hence when cooled, the copper rich phase near the interface would have a different chemical composition and solidus / liquidus temperatures, than the copper rich phase at the end of copper infiltration. In other words, the iron structure is hardly altered by the molten copper in the last stage of the infiltration. There is a strong tendency for the liquid copper to go into the micropores and penetrate into iron interparticle contact points first. This may be due to high stress concentrations due to compaction, in these regions. The liquid phase causes the rearrangement of the solid iron particles, resulting in a better packing and hence shrinkage of the compact. Hence all three mechanisms, namely, rearrangement, solution-reprecipitation and solid state diffusion, contribute to densification and microstructural evolution during liquid phase sintering and infiltration. These mechanisms have been explained in chapter 2.

5.2.1 Dimensional Changes.

Comparing the dimensional changes of the compacts with different densities (Figure 4.6 and 4.7), it can be seen that generally, the lower density compacts expand less (or shrink more) than the ones with a higher density. This could be

due to more rearrangement taking place in the compact having a low density. In the denser compacts the movement of iron particles is much more restricted, therefore less rearrangement is expected which results in less shrinkage.

Considering Figures 4.6 and 4.7, it can be seen that an increase in temperature, promotes more swelling in compacts of both low and high density. Therefore, increasing the sintering (or infiltration) temperatures increase the liquid phase content and the transport rate, thereby furthering copper penetration and diffusion into the matrix and the grain boundaries. Moreover, the mechanical properties may be adversely affected because of resulting coarse grain sizes. Thus, there is an optimum temperature for processing most liquid phase structures. In a similar manner, decreasing the amount of liquid phase hinders the densification process, especially during particle rearrangement. One more point that can emerge from Figure 4.7 is that no significant change in the swelling characteristics was observed up to 1125°C. Above this temperature the transport mechanisms appear to be more active. Increasing the sintering time from 10 to 40 minutes (Figure 4.8), increased swelling. The difference between the two curves (0.2%) may be due to a higher level of copper diffusion into iron, and more grain boundary penetration, when sintering for 40 minutes.

Lower compact densities at the same copper content result in less growth, as shown in Figures 4.9 and 4.10. This is partly because their greater surface area to volume ratio provides greater driving force for shrinkage. The smaller number of particle contacts also reduces the extent of the iron-iron interface, hence the expansion from grain boundary penetration and diffusion of copper. A second reason is due to the rearrangement effects. Low densities facilitate easier sliding of the particles and thus more efficient packing during liquid phase sintering. The non-infiltration specimens all behaved in a similar manner to one another, and the shrinkage of the

non-infiltrated samples overall was greater than the infiltrated samples. This effect is thought to be due to the elimination of the rearrangement and solution reprecipitation mechanisms in the non-infiltrated compacts (Figures 4.15 and 4.16). The effect of temperature on dimensions of a 6.9 Mgm^{-3} infiltrated compact is shown in Figure 4.11, which indicates that the change in sintering time from 10 to 40 minutes tends to have a negligible effect on dimensions as the sintering temperature approaches 1200°C. However, high sintering temperature, was significant when samples of differing densities were infiltrated (Figure 4.7). This confirms the above argument of higher rearrangement and driving force for shrinkage in low density compacts.

Figure 4.11 shows that the specimen infiltrated at 1100°C for 10 minutes had an overall shrinkage of 0.1 % (ie after liquid phase formation). On the other hand, the specimen infiltrated for 40 minutes had an expansion of more than 0.2 %. Thus in the first mentioned sample, the amount of shrinkage was more than the amount of expansion. It is important to realise that, both solid and liquid phase sintering mechanisms are operative in the Fe - Cu compacts. It is quite clear that the shrinkage effects must be associated with the iron, since it forms the base structure of the compacts and, being an elemental metal powder compact, inherently tends to shrink. On the other hand, the growth effect is connected with the interaction of copper with iron. Therefore, the compact undergoes both shrinkage and expansion during the sintering cycle. As a result, the detected dimensional change, is the net effect of the ongoing sintering mechanisms, which are described in more detail in chapter 2.

The effects of solid and liquid phase mechanisms during sintering are compared in

Figure 4.13 and 4.14. The non-infiltrated specimen (Figure 4.13), shrank down to 0.2 % at 1125°C and underwent no further significant change up to 1200°C. This implies that mechanisms of neck growth and densification are complete by this stage. In a powder metallurgy compact, a coherent network of interconnected porosity exists which allows expulsion of entrapped gases to the sintering atmosphere as densification proceeds. High temperatures or long times, results in the closure of capillarities to form isolated pores. The pores shrink until the enclosed gas pressure becomes equivalent to the surface tension of the pore, thereby reducing densification. This is in agreement with Arthur's (1954 / 55) study who showed that the increasing presence of closed porosity prevents the flow of gases, and produces a reduction in the densification rate.

Copper infiltration and copper growth are greatly influenced by the sintering temperature. Figure 4.17(b) shows that the specimen infiltrated at 1200°C for 10 minutes had the highest expansion of about 1.0%. The corresponding copper concentration profiles for the densities of 6.99 and 6.40 Mgm^{-3} are shown in Figure 4.39. Copper penetration was higher in the compact with the higher density, namely, to 6.0 mm below the compact surface at 1200°C. Note that, near the surface, the copper concentration initially remained constant around 2.5 to 3.0%, and then dropped to a minimum. However, compacts infiltrated at 1125°C, did not exhibit a region of uniform copper concentration. Instead, the copper concentration gradually dropped from 4.0% at the surface, to zero (Figure 4.40). It is then clearly evident that copper distribution is homogenised if the compact is treated at 1200°C (Figure 4.39), whereas a large concentration gradient is recorded when infiltrated at 1125°C (Figure 4.42). However, the maximum depth to which copper infiltration proceeded, remained the same, indicating that maximum depth of

infiltration could be achieved at 1125°C.

Surface diffusion would be operative in all the sintering experiments, particularly at the early stages since the low activation energy requirement is achieved at low temperatures. The driving force for the surface diffusion is associated with the vacancy concentration differences in the neck region. Thummler and Thoma (1967), reported that surface diffusion has a negligible effect upon densification, but plays an important role in pore spheroidisation which can improve the mechanical properties.

At high temperatures, volume diffusion becomes the predominant mechanism in the densification (or shrinkage) of ferrous compacts. It involves the transportation of both material and dislocations from the inner neck region to the outer concave surface. Neck growth occurs and particle centres move together, which results in a significant densification effect. In the present study, a maximum shrinkage was exhibited by a 6.34 Mgm^{-3} plain iron compact, sintered at 1200°C for 40 minutes [Figure 4.18(b)] which would comply with the mechanisms described above.

Double infiltration technique, appreciably reduced the swelling rate and the total amount of swelling of iron compacts (Figure 4.19). During double infiltration, the necks between the iron particles become wider and some of the gain boundaries are removed, due to self diffusion of iron. A much more rigid structure is thus formed which resists the copper growth. The effect can be seen in Figure 4.20. The structure of a two step infiltrated compact, shows very large copper rich regions compared to the double infiltrated one which shows a more homogeneous microstructure and smaller copper rich phase. Thus, the double infiltration technique, gives a more homogeneous, high density compact.

5.2.2 Area of Copper Infiltration

Area of copper infiltration is a measure of the volume of infiltration. Figures 4.22 and 4.23 illustrate the change in area of infiltration as a function of density and temperature. Generally, an increase in density, increases the copper infiltration area. For example, considering those samples infiltrated for 40 minutes, an increase in density from 6.35 to 7.4 Mgm^{-3}, increased the measured infiltration area from 3250 to 5000 mm^2. However, the amount of infiltration for compacts with a density of 6.35 Mgm^{-3} was the same when infiltrating for 10 and 40 minutes (Figure 4.22). Therefore, the infiltration volume was hardly affected with an increase in infiltration time for low density compacts.

Densities of 6.35 Mgm^{-3} and 7.40 Mgm^{-3} represent compacts with the degree of porosities of 19 and 6% respectively. Thus, the degree of microporosity is higher in the latter. It is thought that, as the liquid flows and spreads into narrow capillaries it will tend to fill the smallest pores first because of surface tension and the favourable interfacial energy reduction . This would promote the penetration of the liquid copper, but offset the volume growth due to grain boundary penetration, as previously shown in Figure 4.6 and 4.7. The preferential filling of micropores at the expense of large pores can cause the formation of large pores at the original copper sites in liquid phase sintering. Later, the large pores can be filled by the remaining melt. This occurs mainly with densities above 6.35 Mgm^{-3} as can be seen in Figure 4.22. However, at increasingly high densities, the relative proportion of closed porosity is increased. The infiltration of these compacts is likely to be reduced as the compact behaves like dense metal.

5.3 Multiple Regression Analysis

Multiple regression analysis of the data clarified the extent by which the variations in temperature, time and density (ie the independent variables) could influence dimensional changes and penetration area (ie the dependent variables) of the infiltrated specimens.

Tables 4.5 and 4.8 shows the correlation matrices. It can be seen that no correlation exists between the independent variables, therefore more confidence can be held of the correctness of the statistical results.

Examination of the graph of the residual error (Figure 4.26), shows that no pattern exists among the calculated results. This implies that the regression model for dimensional changes (Table 4.7) is valid. However, some pattern was noticed in the graph of residual error in the regression model for the infiltration area. This shows that the independent variables do not quite explain the regression model (Table 4.10).

This is further evidenced by comparing the respective coefficients of determination (R^2), which defines the total variability of dependent variable (Y), as a function of the experimental variable (X). The more closely X and Y are linearly related, the closer R^2 will be to 1. R^2 was 0.89 and 0.43 for dimensional changes and infiltration area respectively, indicating good linearity in the regression model for the former and poor linearity in the regression model for the latter. Tables 4.6 and 4.9 show the correlation coefficient (R). 94 % of the points lay on a straight line in dimensional change model compared to only 65% in the model for the infiltration area, hence, more scatter in the latter. It could therefore be stated that, the area of copper infiltration and the sintering variables are much less linearly related than those of the dimensional changes. The t-statistic was 12.53 for the temperature and

5.52 for the density, in the dimensional change regression system (Table 4.7). This implies that the temperature had the highest, and density the lowest effect upon dimensional changes. This was later confirmed in the TMA curves for Fe-Cu compacts (sections 5.7.1 and 5.7.2). However, the corresponding t-statistics of the infiltration area were 4.0, 1.96 and 1.46 for density, time and temperature respectively, suggesting that density had the most and temperature had the least contributing factor in copper infiltration. This is in accordance with the result previously seen in Figures 4.22 and 4.23.

In summary, the regression model for dimensional changes (Tables 4.6, 4.7) greatly correlates the experimental conditions, whereas the regression model for infiltration area (Tables 4.9, 4.10) correlates to a lesser extent. It is thought that there may be other factors besides time, temperature and density, which should have been taken into account, as the independent variables. These could include pore radius, contact angle between the solid and liquid and the viscosity of copper.

5.4 Dihedral Angle

The effect of carbon upon the mean dihedral angle, ϕ, is illustrated by the use of histograms in Figures 4.28, 4.29 and 4.32. There is a clear shift in the dihedral angle towards higher values, as a function of increasing carbon content. This trend is in good agreement with the work of Berner et al. (1974) as previously seen in Figure 2.22. Comparison in microstructure of Fe-Cu-C an Fe-Cu system are shown in Figure 4.34. Fe-Cu compact exhibited small pores, filled with copper and very low dihedral angles. In contrast, Fe-Cu-C compact exhibited a large copper rich phase, less porosity and large dihedral angles. The corresponding SEM

X-ray photomicrographs (Figure 4.35), revealed more large segregated copper regions with Fe-Cu-C system whilst copper was comparatively uniformly distributed in Fe-Cu system. It has been suggested that (Jamil and Chadwick, 1984) in a microstructure, the most frequently observed angle is taken as the true dihedral angle, ϕ of the system, within ±5°. However, this is only correct if the true ϕ of the system is about 120° (Harker and Parker, 1945). In the present work, the dihedral angle distributions in Fe-Cu-C compacts clearly show that the dihedral angle is far from 120°. Thus, the mean dihedral angle was estimated and used in calculations, as suggested by Riegger et al. (1960). Assuming the solid / liquid interfacial energy is γ_{SL}, grain boundary energy for copper infiltrated compacts could be calculated from the equation:

$$\gamma_{gb} = 2\,\gamma_{SL} \cos\frac{\phi_{mean}}{2}$$

where;

γ_{gb} = grain boundary interfacial energy (Jm^{-2})

γ_{SL} = solid / liquid interfacial energy (Jm^{-2})

ϕ_{mean} = mean dihedral angle

The measured mean and zero dihedral angles are shown in Table 5.1.

Compact Type	ϕ_{mean}	ϕ_{zero}
Fe	9.86	27
Fe-0.15C	20.28	12
Fe-0.6C	41.5	3

Table 5.1 - Effect of graphite upon dihedral angle and grain boundary interfacial energy of the copper infiltrated compacts.

The increase in ϕ as a consequence of carbon addition is probably due to a decrease in γFe grain boundary energy, γ_{gb}. However, this is assuming that γ_{SL} is not affected by carbon.

Solid / liquid interfacial energy is closely dependent upon solubility of the solid within the liquid (Wassink 1967). If the intersolubility is decreased, the interfacial energy will increase. Specific relationships were not given, but Taylor (1957), showed that in the Al-Sn-X system (where X= Bi, Pb or Cd), the change in interfacial energy with solubility conforms to the Gibbs adsorption equation:

$$d\gamma_{SL} \alpha \, d \log c \quad \ldots\ldots\ldots (5.1)$$

where: $d\gamma_{SL}$ = change in solid/liquid interfacial energy.

d log c = change in concentration of the solid component in the liquid component.

This relationship could be applied to the present study of infiltration and dihedral angle measurements. With melt formation and spreading, grain boundary penetration will lead to a chemistry change in the liquid copper. During solid dissolution and up to the solubility limit, the liquid chemistry and interfacial energy will be changing. With time, the solid-liquid surface energy will stabilize at a value lower than that of the initial copper infiltrant. Such a behaviour is predicted by the model of Aksay et al. (1974). The dissolution reaction during liquid spreading, decreases the solid-liquid interfacial energy below the equilibrium value. After spreading and reaction have come to completion, the system approaches an equilibrium interfacial energy and dihedral angle. Figure 4.71, illustrates the variations in the dihedral angle with temperature. Because of the rapid decrease in

dihedral angle at 1125°C, there is expected to be an over penetration of the liquid copper into iron grain boundaries. The trend is similar to that observed in the work of Salter (1966) (Figure 2.23), who reported a rapid reduction in the dihedral angle at 1150°C during liquid phase sintering.

The effect of carbon upon zero dihedral angles and dimensions is shown in Figures 4.36 and 4.37 respectively. The results clearly show that the proportion of zero dihedral angles is closely related to compact growth. The pronounced fall in the proportion of zero dihedral angles must be due to a reduction in γ_{gb} or an increase in γ_{SL} or a combination of the two. The relationship between the compact growth and zero dihedral angles confirms the theory that the grain boundary penetration is the predominant factor for the copper growth phenomenon.

Bredz and Schwartzbart (1959), reported that as soon as copper penetrates the grain boundaries, carbon starts to move towards the copper rich areas. In other words, copper increases the activity of carbon. Note that carbon diffusivity in γ iron is ~40,000 times greater than the diffusivity of copper. This view is supported by Darken (1948), who suggested that, the rate of carbon migration into the grain boundaries depends on copper and silicon variations. Copper attracts, and silicon repels carbon.

Likewise, the activity of copper in liquid iron increases in the presence of carbon (Rivlin, 1984). The net effect will be an increase in γ_{SL}. Finally, since one of the criteria for grain boundary penetration is that $\gamma_{gb} > 2\gamma_{SL}$ (Wassink, 1967), the grain boundary penetration by molten copper is reduced. The excess liquid copper, having not been able to penetrate the grain boundaries will move from pore to pore further down the capillaries. The result will be a higher infiltration area in carbon

containing compacts as shown in Figure 4.38.

5.5 The Effect of Carbon upon the Solubility of Copper in Iron.

The EPMA results of copper solubility in iron, shows that the addition of 0.6% carbon reduced the concentration from 7.0 to 4.2 %. This indicates that carbon tends to reduce the solubility of copper in iron. Line concentration profiles along iron grains also revealed the same trend. This is in agreement to Elliot (1959), who suggested that carbon reduced growth because the solubility of copper in iron was reduced. However, Krantz (1969), contested the solubility hypothesis on the basis that the Fe-Cu-C ternary phase diagram study by Ishiwara et al. (1926), showed that carbon had a negligible effect upon the solubility of copper in γFe. In contrast, Parameswaren (1979), reported that at 1150°C, an increase in carbon from 0 to 1.0wt. % reduces the solubility of copper in iron from 8.1 % to 7.2 % (Figure 2.16). Therefore, it appears that carbon has only a limited effect upon the equilibrium solubility. The reason why the copper solubility is reduced in presence of carbon could be due to a non equilibrium state after sintering and lower diffusivity of copper across iron grains due to a high dihedral angle and lower solid / liquid contact area in carbon containing compacts. It has previously been shown that the value of mean dihedral angle at the grain junction increases with increasing carbon, from 9.8° to 41.5° with an 0.6 % carbon addition. The high carbon content, leads to a high concentration of molten, undissolved copper at the entrance of an iron grain boundary (Figure 4.34). Thus copper penetration and diffusion into the iron grains from the grain boundaries is greatly reduced. Therefore, it is suggested that although carbon reduces the equilibrium solubility of copper in iron only to a limited extent, it greatly affects the dihedral angle and solid / liquid

interfacial energy and indirectly affects diffusion of copper into iron particles.

5.6 Oxidation Treatment.

Oxidation can improve mechanical properties, corrosion resistance and reduce penetration of liquid copper into the pores of powder metallurgy compacts (Franklin and Davies, 1977). Porous compacts have a greater active surface area, which is due to higher surface area of the powders and are therefore, able to absorb more oxygen. Consequently, the rate of oxidation is higher in low density compacts, as shown in Figure 4.44. The Figure shows that with an increase in density from 6.4 to 7.4 Mgm^{-3}, the weight gain as a result of oxidation was reduced from 2.1 % to 0.5 % in the compacts oxidised for 30 minutes. Comparing the two curves for weight gain related to density, it is evident that convergence occurs towards higher densities. In other words, the oxidation time only plays an important role in the low density compacts. This is because the ratio of interconnected porosity to closed porosity is higher in the low density compacts, allowing greater access of the oxidising atmosphere to metal surface. Similar observations were reported by Franklin and Davies (1977), in which the variation in open porosity and in weight with time, showed a sudden decrease in open porosity at the critical times. A change in slope is indicated on the weight gain curves corresponding to the sudden change in area available for oxidation.

As oxidation proceeds, the oxide thickness is increased with time, while the pore radius is decreased. Figure 4.46, illustrates that complete closure of pores by the oxidation product occurred close to the surface where the supply of oxygen is greatest. However, little or no oxide was seen in the core. As soon as the

interconnected pores at the surface are blocked, supply of oxygen to the pores in the core is reduced and consequently further oxidation of the core is dramatically decreased.

X-ray diffraction analysis on a sample surface, oxidised at 500°C for 130 minutes detected magnetite, haematite and α iron (Table 4.16). The main peak belonged to magnetite, suggesting that it was the thickest layer of the oxides. The oxide layers can clearly be seen especially on the surface of the compact in Figure 4.46. This is in agreement with Regel (1963), who suggested that at temperatures up to 570°C, the oxide layer consists mainly of magnetite (Fe_3O_4).

The oxide layer in the closed pore was cracked [Figure 4.46(b)], possibly due to the pressure build up due to a reduction in pore diameter as oxidation proceeds.

Pilling and Bedworth (1923), defined the Pilling - Bedworth ratio for oxidation as follows:

$$P.B = \frac{Wd}{wD} \quad \ldots\ldots\ldots (5.2)$$

where

W = molecular weight of oxide

w = formula weight of metal

D = density of oxide

d = density of metal

Pilling and Bedworth (1923), suggested that:

If P.B < 1, the oxide formed should be cellular and discontinuous.

If P.B > 1, the oxide should be compact and continuous. The P.B ratios for iron and its oxides are shown in Table 5.2.

	Density -Mgm^{-3}	P.B. ratio
Fe	7.85	1.00
FeO	5.62	1.80
Fe_3O_4	5.17	2.10
Fe_2O_3	5.25	2.13

Table 5.2 - The Pilling - Bedworth ratio for iron and its oxides.

It is can be seen from Table 5.2 that, the P.B ratios for iron oxides are all greater than unity, indicating a compact and continuous oxide layer. Since the volume of the oxide formed is greater than the original volume of metal, oxide growth generates a compressive stress in the oxide scale, which results in cracks being formed on the surface oxide layer. This effect was observed in the experiments as shown in Figure 4.46(a). A gap between the oxide layer and iron can be seen which could be due to the higher shrinkage rate of iron compared to that of the oxide layer.

According to Birks and Meier (1983), oxide layers are formed by ionisation of iron at iron / magnetite interface as follows:

$$Fe = Fe^{3+} + 3e^{-} \quad \ldots\ldots\ldots\ldots\ldots\ldots \quad (5.3)$$

The iron ions and electrons migrate outward through the magnetite. At the magnetite / haematite interface, magnetite is formed by the reduction of haematite according to:

$$Fe^{3+} + 3e^{-} + 4Fe_2O_3 = 3Fe_3O_4 \quad \ldots\ldots\ldots \quad (5.4)$$

This reaction results in the advancement of magnetite / haematite interface, which is schematically shown in Figure 3.9. If iron ions and electrons, in excess of

requirements for the reduction of haematite to magnetite, are mobile in the haematite, they will migrate through this phase and new haematite will form at Fe_3O_4 / gas interface according to:

$$2Fe^{3+} + 6e^{-} + \frac{3}{2}O_2 = Fe_2O_3 \ldots\ldots (5.5)$$

At this interface also oxygen ionises and moves inward according to:

$$\frac{1}{2}O_2 + 2e^{-} = O^{2-} \ldots\ldots\ldots\ldots (5.6)$$

In a closed porosity, the partial pressure of oxygen is reduced as oxygen is absorbed onto the oxide surface. Since there is a high concentration of iron ions and low concentration of oxygen ions, the haematite layer is gradually reduced to magnetite. The resultant will be a thinner haematite and a thicker magnetite in the closed porosity. This is clearly shown in Figure 4.46, which compares the Fe_2O_3 layer (ie the white layer) on the surface and in the pore.

Figure 4.45, illustrates the effect of oxidation time on copper infiltration area. The compacts oxidised for 30 minutes, showed a penetration area of 3916 mm^2 compared to 4868 mm^2 for the non-oxidised one. It is not clear whether this is due to the wetting behaviour of copper in contact with the oxide or due to the high closed porosity. It could be due to both factors since oxide layers greatly reduce wetting (Milner, 1958).

Therefore, oxides reduce the porosity of the compacts and thereby permit conventional bonding techniques such as brazing to be used to bond compacts together. This involves interposing the brazing filler metal between the faying surfaces and heating the compacts to a temperature for a time sufficient to form a brazed bond. In practice, the faying surfaces should be masked prior to this

treatment to protect them from oxidation. If not, it will be necessary to remove the oxide from the faying surfaces as by fluxing or mechanical means such as abrading before brazing.

Preferably, oxidation is accomplished by treating the compacts in dry, superheated steam at a temperature within the range 450-570°C for 30 minutes to convert a substantial portion of the iron into Fe_3O_4 (Sanderson, 1975). Thereafter, the faying surfaces are prepared for brazing. Superheated steam is used since the presence of condensed water will result in the formation of Fe_2O_3. This is undesirable since the lower oxide does not adhere to the iron and it also promotes corrosion. Similarly, the oxidation temperature, should be controlled so that it does not rise above about 570°C, since FeO is likely to be formed. This is also undesirable, because FeO is unstable at temperatures below 570°C and dissociates into Fe_3O_4 and metallic iron (Smithells, 1967). Since Fe_3O_4 acts as a protective layer for the FeO, the latter becomes entrapped beneath the Fe_3O_4 layer and is likely to cause corrosion of the compacts (Sanderson, 1975).

5.7 Dimensional Changes

A useful approach to the question of overall dimensional change can be based upon the idea of taking separate account of shrinkage and growth factors. Whichever factor is the greater will determine whether a shrinkage or growth effect prevails. When considering the interaction of copper and iron during sintering, it is necessary to separate the mechanisms into those causing shrinkage and those causing growth. It is quite clear that shrinkage effects must be associated with the iron and the growth effects to the presence of copper. The accepted sintering

mechanisms in the iron compact will cause shrinkage. The effect of copper may be summarised as:-

a) penetration of liquid between the iron particles.

b) penetration of liquid into the grain boundaries.

c) diffusion of copper atoms into iron particles from the particle surface.

d) diffusion of copper atoms into the iron grain from the grain boundaries.

One of the objectives of the present work was to establish the circumstances under which the various mechanisms operate and which had the greatest effect on dimensions.

5.7.1 Dilatometry at 960°C

These experiments correspond to sintering just above α to γ transformation and well below the melting point of copper. The effect of density on the dilatometric curves (D-curves), is shown in Figures 4.48 and 4.49. Figures show that the compacts with the lower density expanded less than the higher density compacts, presumably due to higher surface area / volume ratio. Since the copper powder was in the solid phase at this temperature, the mechanism of expansion is due to diffusion of copper. Solid phase surface diffusion occurs due to low activation energy requirements.

Comparison of the mode of α to γ transformations shows that the transformation is more defined in the compacts containing no copper. This is due to diffusion of copper, promoting growth and masking the transformation shrinkage. Both copper containing and plain iron compacts continued to expand up to 960°C from which, no significant change in the dimension was recorded during the 20 minutes

isothermal sintering. This confirms the temperature dependency of the growth mechanism as mentioned in the regression model. The extent of diffusion during the heating period is increased with an increase in copper additions (Figure 4.50). However, when cooled to room temperature, both copper containing samples recorded the same amount of overall shrinkage. This suggests that copper diffusion alone does not significantly contribute to copper growth phenomenon.

The comparisons between the D-curves of elementally mixed (E.M) and immersion coated (I.C) compacts are made in Figures 4.51 and 4.52. Firstly, the Figures show that carbon did not have a significant effect on the dimensional changes and α to γ transformation of either type of compact. This is because at this low sintering temperature, carbon redistribution is low. It has been shown previously in chapter 2, that the presence of CO is a prerequisite for rapid carbon redistribution within the compact. However, the Ellingham diagram for oxides shows that as the temperature is reduced to ~900°C, the driving force, in terms of the free energy for the formation of CO is reduced and CO_2 becomes the stable oxide of carbon. As a result, carbon redistribution is at a reduced level within the compact. Secondly, on return to room temperature, the I.C specimen showed a shrinkage of 1% compared to 0.2% to that of the E.M compact. This shows that the densification mechanisms due to solid state diffusion and pore elimination were more active in the I.C compact. One more reason for this could be due to the modification in the surface shape and area of the iron particles as a result of immersion coating process. When iron powder is introduced into the $CuSO_4$ solution, copper is deposited at the expense of iron. In other words some iron is dissolved and replaced by copper, producing a rough surface. This leads to an increase in the surface area of the iron powders. On the other hand, the immersion coating process, reduced the compressibility of I.C compacts compared to E.M compacts. It was noticed in the

compaction of these powders that about 13% higher loads were necessary, to compact the I.C powder to the same density as the elementally mixed powder.

In $CuSO_4$ solution, the following reactions take place simultaneously:-

$$Cu^{2+} + H_2O = Cu^{+}\text{-}OH + H^{+} \ldots\ldots (5.8)$$

$$Fe^{2+} + H_2O = Fe^{+}\text{-}OH + H^{+} \ldots\ldots (5.9)$$

$$2H^{+} + Fe = Fe^{2+} + H_2 \ldots\ldots (5.10)$$

Thus, hydrogen is evolved during the reaction which may lead to hydrogen embrittlement of iron powder and therefore, a decrease in the compressibility of the copper coated powder.

Finally, it is well known that oxides reduce the solid state surface diffusion of iron particles. It is considered that surface oxides are removed in the immersion coating process and replaced with copper which then protects the surfaces during sintering, and therefore, improves the densification mechanisms and interparticle bonding. The resultant will be more shrinkage in the I.C compacts, as illustrated in their corresponding D-curves.

5.7.2 Dilatometry at 1125°C

Figure 4.54 compares the dimensional changes of wrought Armco iron slug and a plain iron compact. Both specimens expanded in a similar way up to the temperature T_1. Again, from T_1 to T_2, expansion and shrinkage were equal. It could be stated that T_1 is normally higher with increasing particle size, with decreasing specific surface of the powder and increasing compaction pressures. When cooled from the sintering temperature, similar shrinkage occurs in both

specimens. A much less clearly defined α to γ transformation is seen in the compact compared to the fully dense specimen. This is due to the solid state sintering of the iron particles which superimposes a shrinkage upon the normal linear expansion.

After transformation is completed, shrinkage is reduced due to the following reasons:

a) shrinkage rate due to differences in the self diffusion coefficient. Buffington et al. (1961), have shown that in αFe at 900°C, the self diffusion coefficient D, is $3*10^{-10}$ cm^2s^{-1}, whereas at 1050 the value of D is approximately two orders of magnitude less, at $1.2*10^{-10}$ cm^2 s^{-1}.

b) γFe, exhibits a higher coefficient of thermal expansion than αFe. Values for αFe (0 - 900°C) and γFe (1000 - 1200°C) have been given as $12.89*10^{-6}$ $°C^{-1}$ and $23.25*10^{-6}$ $°C^{-1}$ respectively (BISRA, 1953).

The Fe-Cu compacts exhibit a rapid growth at 1125°C due to interparticle and grain boundary penetration of the copper rich liquid phase (Figure 4.55). The start of the boundary penetration is apparent at 1100°C lasting for 3 minutes (Figure 4.4). A slight expansion occurs during the isothermal sintering period even though an excess of liquid copper is present. Higher copper content resulted in more growth (Figure 4.56), due to the higher content of the liquid phase and hence proportion of the grain boundaries containing the copper rich liquid. The Figure also shows that during isothermal heating, the rate of expansion of the Fe-8Cu compact was higher than that of the 2 and 4% copper content. In other words, copper growth was completed at the end of isothermal sintering in Fe-2Cu, whilst it was still proceeding in the Fe-4Cu and Fe-8Cu.

The concurrent mechanisms which occur during the 20 minutes isothermal sintering and contribute to densification or shrinkage are solution-reprecipitation and rearrangement. Apparently these mechanisms are more active in the Fe-2Cu compact than in the Fe-4Cu and Fe-8Cu compacts (Figure 4.56). For Fe-Cu-C compacts (Figure 4.57), this shrinkage must be linked with solid-state sintering since, as discussed before, liquid copper can not penetrate into their iron grain boundaries. Indeed according to Whalen and Humenik (1967), interparticle penetration of the liquid phase is a necessary condition for liquid phase sintering. However, in the presence of carbon, expansion will occur due to solution effects which cause an increase in the lattice parameter of γFe (Roberts 1953). The presence of copper will produce a similar effect but to a lesser extent due to its lower diffusivity.

Comparison between the isothermal sections in the D-curves of Fe-4Cu-0.6C and Fe-4Cu-0.15C shows less expansion in the lower carbon containing compact. Since both have the same amount of liquid phase, it suggests that expansion due to carbon diffusion was not complete at the end of the isothermal sintering in Fe-4Cu-0.6C compact.

The overall shape of the D-curves of the E.M compacts more closely resemble those reported by Dautzenberg and Dorweiller (1985) (Figures 2.29, 2.30), rather than those of Trudel and Angers (Figures 2.27, 2.28). In the work of the first mentioned workers, a change in the slope of the curves during the isothermal section of the sintering cycle was observed as carbon is increased. No such change was observed in the investigations of the other workers.

According to Mead and Brichenall (1956), the self diffusion coefficient of γFe increases from $2.4*10^{-11}$ cm^2 s^{-1} to $1*10^{-10}$ cm^2 s^{-1} by 1.0% carbon addition. It is therefore suggested that the increased shrinkage observed in carbon containing compacts is a function of both increased self diffusion coefficient of iron, and reduced grain boundary penetration by liquid copper due to an increase in the dihedral angles. Finally, a graphite addition had more effect on the sintering mechanisms of Fe-Cu compacts at 1125°C than at 960°C, presumably because of better activation and redistribution of the graphite at the higher temperature as described in section 5.7.1.

The D-curves of E.M and I.C compacts are shown in Figures 4.58 and 4.59. At the end of transformation and after the point of copper melting, the specimens showed an expansion which was more pronounced with the E.M specimen. It is suggested that since the area of the copper / iron interface is much larger and copper distribution is better in the I.C compacts, the extent of solution / reprecipitation mechanism during liquid phase sintering is thus higher than the E.M compacts. This leads to higher shrinkage in the I.C specimens as shown in Figures 4.58 and 4.59. As a high solution / reprecipitation mechanism proceeds, there will be less free liquid copper available to penetrate in to the grain boundaries of the iron matrix hence, lower expansion in the I.C compacts.

Graphite additions, reduced the expansion of the E.M specimen to a greater extent than the I.C specimen. During the isothermal sintering (20 minutes), the E.M compact expanded, while the I.C compact shrank. This is because, carbon diffusion into the iron particles is greatly reduced by the presence of copper coating in the I.C compacts. More over, since copper is in close contact with the iron

powder, copper diffusion into iron takes place first and this greatly restricts the diffusion of carbon. However, with the E.M compacts, carbon diffuses before copper melts. The D-curves in Figure 4.57 show that, the Fe-Cu-C elementally mixed (E.M) compact expanded more than Fe-Cu E.M compact during the isothermal sintering period, as a result of carbon diffusion. Figure 4.62 confirms previous observations of little effect of carbon on dimensional changes of the I.C compact. γ to α transformation and dimensions were hardly affected by a 0.6 % carbon addition.

Comparing the D-curves of copper containing compacts at 1125°C with those at 1200°C (Figures 4.56 and 4.65), showed a shrinkage during the isothermal sintering at 1200°C, but a compact of similar constitution shows an expansion when sintered at 1125°C. This observation can be related to the reduced dihedral angle at 1125°C. After the point of copper completely melting (1094°C), there is a rapid reduction in the dihedral angle (Figure 4.71), resulting in the growth of the compact. As the temperature is increased to 1200°C, the equilibrium interfacial energy and dihedral angle is reached that lowers the compact growth, as shown in Figure 4.71.

5.8 Effect of Atmosphere

Figures 4.66 and 4.67 illustrate the effect of atmosphere on plain iron and Fe-0.6C compacts sintered at 1125°C. They reveal that $N_2/10H_2$ atmosphere promotes more shrinkage than argon especially during isothermal sintering. This is attributed to the reduction of the surface oxides by the $N_2/10H_2$ atmosphere, promoting surface diffusion which leads to better densification and shrinkage. However, during and

after the isothermal sintering of Fe-Cu compacts, the one sintered in HP argon registered higher shrinkage, which was retained at room temperature (Figure 4.68). The reason for this is thought to be due to reduction of oxides in Fe-Cu compacts by hydrogen, thus making copper penetration into the grain boundaries more efficient. Same heating rate of 20°C min^{-1} was employed on both experiments. However, if a lower heating rate is used, the overall growth of specimens are expected to be greater than when carried out under higher heating rates. This may be explained by the reasoning put forward by Elliot (1959). Slower heating rates provide a longer time period during heating for volume diffusion to occur. The resultant swelling of the individual grains is evident as a net compact growth. At high copper contents where an excess of liquid is present an increase in growth is observed. However, in compacts containing low copper levels (ie, less than the solubility limit in γFe), slow heating rates can reduce growth since no excess copper may remain when the melting point is attained.

The results in the case of I.C compacts are somewhat different. It was previously shown that copper penetration into the grain boundaries of the I.C compacts is lower than the E.M compacts. The rearrangement and solution / reprecipitation mechanisms are considered to be more active in the I.C compacts due to better contact and distribution of copper. Therefore, these compacts are likely to behave in the same way as those shown in Figures 4.66 and 4.67, under a reducing atmosphere.

Finally, the immersion coating technique appears to be an attractive method for depositing copper onto iron. Since, FeO is formed on the iron surface which reduces the adhesion of the porous copper coating to iron, and promotes corrosion. However, the oxides can then be removed by a subsequent reduction process in a reducing atmosphere.

6. Concluding Summary

6. Concluding Summary

1. The comparison between the dilatometric curves of the elementally mixed (E.M), and immersion coated (I.C) Fe-4Cu compacts show that a significant difference in the sintering and densification mechanisms exists between the two type of compact constitution.

2. In I.C compacts, copper is thinly spread over iron particles, therefore greater solid state copper diffusion into iron takes place than in the E.M compacts. The effect is less expansion of the I.C specimen during sintering, as there is relatively less copper to melt and penetrate into the particle contact points and the grain boundaries. For example, after 20 minutes isothermal sintering at 1125°C, the Fe-4Cu E.M compact showed an expansion of about 2%, whereas the corresponding I.C sample recorded zero expansion.

3. For an E.M specimen sintered at 1125°C, the expansion is about four times higher than when sintered at 960°C (ie 2.0% at 1125°C compared to 0.5% at 960°C). The difference in expansion is considered to be due to copper penetration into the grain boundaries in the specimen sintered at 1125°C.

4. For an I.C compact, after 20 minutes isothermal sintering at 960°C, the amount of shrinkage was about 1.0%, compared to zero when sintered at 1125°C. This confirms that the mechanisms of liquid phase sintering (which causes expansion) are less active in the I.C compacts.

5. After a complete sintering cycle at 1125°C, the growth of the E.M compact was greater by about 1.5% than that of the I.C compact.

6. It was possible to derive a reliable parameter for dihedral angle by inspecting micrographs and recording the number of zero dihedral angles observed, and the mean value.

7. The penetration of liquid copper into the grain boundaries of iron particles is dependent upon the dihedral angle. The smaller the dihedral angle, the greater the extent of copper penetration. This mechanism is one of the major causes of the copper growth phenomenon.

8. The dihedral angle is ~10° at 1125°C and is then increased to ~18° at 1200°C, as the system achieves its equilibrium condition.

9. Carbon addition to Fe-Cu compacts reduced the copper growth phenomenon. Addition of 0.6% carbon, reduced the number of zero dihedral angles from 27 to 3, and increased the mean dihedral angle from 9.8 to 41.5 degrees.

10. The extent of copper growth and penetration of liquid copper into the iron grain boundaries, is directly proportional to the number of zero dihedral angles. For example, the extent of expansion in a compact with 3 zero dihedral angles was three orders of magnitude lower than the compact with 27 zero dihedral angles.

11. Prior oxidation of iron compacts at 500°C, reduced the volume of copper infiltration by about 60%, by filling the interconnected porosity, with a duplex oxide layer of magnetite and haematite. The amount of weight gain due to oxidation was directly proportional to the density of the compacts.

12. It was shown that copper infiltration area and dimensional changes may be represented by two regression models, with temperature, density and time as the independent variables. The regression model for dimensional changes greatly correlates the experimental conditions. The correlation coefficient R_1, is 0.94. The multiple regression equation, with the dimensional change Y, as the dependent variable and density ρ, time t, and temperature T, as independent variables can be written as:

$$Y = -10.335342 + 0.29587\ \rho + 0.007288\ t + 0.007585\ T$$

The regression model for infiltration area correlates the experimental conditions to a lesser extent with a correlation coefficient R_2, of 0.65, indicating that other factors such as; pore radius and viscosity of the liquid copper should have also been taken into account. The regression equation, with infiltration area Y', as the dependent variable, can be written as:

$$Y' = -12530.4911 + 1404.4624\ \rho + 14.4586\ t + 5.7740\ T$$

13. The extent of copper infiltration was higher in the high density compacts. The infiltration area of a 6.9 Mgm^{-3} compact, infiltrated for 40 minutes was ~20% higher than the infiltration area of a 6.35 Mgm^{-3} compact. This is considered to be due to the greater number of smaller pores and fine capillaries in the 6.9 Mgm^{-3} compact and hence greater capillary force for infiltration to proceed.

14. Carbon additions increased the extent of copper infiltration in iron compacts. Addition of 0.6% graphite, increased the infiltration area from about 4500 mm^2 to about 5600 mm^2. This effect is thought to be due to the restricted copper diffusion and penetration into the iron particles in the graphite containing compact, leaving a greater proportion of the liquid copper for infiltration.

7. References

7. References

Adam N.K, "The Physics and Chemistry of Surfaces", Dover Publications Inc., 1968.

Allen K.W , "Fundamental Aspects of Adhesion", Adhesion in Engineering Design, (ed.) Lees W.A , The Design Council, London, 1984, ISBN 0850721504.

Aksay I.A, Hodge C.E, Pask J.A, "Phase Distribution in Ceramics" , (eds.) Frechette V.D, Lacourse W.C, Burdick V.L, Plenum Press, New York, 1974, pp.229-321.

Asnis A.E and Zamkov V.N, "Features of the Process of Depositing Copper on Chromium-Nickel Steel.", Welding Production, 1961, 8, 7, pp.38-42.

Asnis E.A, Prokhorenko V.M, "Mechanism of Cracking During the Welding or Depositing of Copper on to Steel.", Welding Production, 1965, 2, 11, pp.15-17.

Arthur G. ,"Porosity and Permeability Changes During Sintering of the Copper Powder", Journal of Institute of Metals, 1954-55, 83, pp.329-336.

Asaka K., Hayasaka T. , Ozawa S. , "Preparation of high density sintered alloys", Metal Powder Report, 1983, pp.621-625.

Bates J.F, and Knapton A.G, "Metals and Alloys in Dentistry", International Metals Reviews, 1977, 22, pp.39-60.

Bailey G.L.J , Watkins H.C, "The Flow of Liquid Metal on Solid Metal Surfaces and its Relation to Soldering, Brazing and Hot Dipping", Journal of Institute of Metals, 1951-52, 80, pp. 57-76.

Berner D. , Exner M.E , Petzow G. , "Swelling of Fe-Cu Mixture During Sintering and Infiltration", Modern Developments in P/M, MPIF, 1974, Vol. 6, pp.237-249.

Bikerman J.J, "Surface Chemistry", Academic Press Inc. , N.York, 1958.

Bikerman J.J, "Contact Angles, Spreading and Wetting", Proceedings of 2nd International Congress On Surface Activity, 1957, London, Vol. 3, pp. 125-130.

Birks N. , Meier G.H ,"Introduction to High Temperature Oxidation of Metals", Edward Arnold, 1983 , ISBN 071313464X.

BISRA, British Iron and Steel Research Association,"Physical Constants of Some Commercial Steels at Elevated Temperatures", Butterworth, 1953.

Bockstiegel G.,"Ershcheinungsbild und Ursachen von Volumenanderungen beim Sinteren von Preblingen aus Eisen-Kupfer und Eisen-Kupfer-Graphit Pulvermischungen", Stahl Und Eisen, 1959, 79, pp.1187-1201. (Brutcher Translations 5375 & 5573).

Bockstiegel G. and Blande C.A, "Segregation Phenomena During Infiltration of

Sintered Iron with Molten Copper - Nickel", Powder Metallurgy International, 1971, 3, (3), pp.137-142.

Bockstiegel G. ,"Dimensional Changes During Sintering of Iron-Copper Powder Mixes and Means to Reduce Them", Metallurgie,1962, III, 4, pp.67-78.

Bozhko A.M, "Mechanism by Which Molten Copper Penetrates into Steel", Automatic Welding, July 1968, Vol. 21, pp.26-29.

Bredz N. , Shwartzbart H.,"Metallurgy of Bonding in Brazed Joints. II- Migration of Filler Metal into the Base Metal", The welding Journal, 1959, 38, (8), pp.305-314.

Buffington F.S , Hirano K. , Cohen M. ,"Self Diffusion in Iron", Acta Metallurgia, 1961, 9, pp.343-349

Burdon, R.S "Surface Tension and Spreading of Liquids", 2nd. ed., Cambridge University Press, Cambridge, United Kingdom, 1949.

Cambel L. , Lund J.A. ,"Supersolidus Sintering of Loose Steel Powders", International Journal of P/M, 1972, 8, (3) , pp.131-140.

Caplan D. , Cohen M., "Scaling of Iron at 500°C" , Corrosion Science,1963, 3, pp.139-143.

Carr, J. , Kearns J., " Metallic Stearates for P/M" , Precision Metal Molding , 1967, 25, (4), pp.61-64.

Cannon H.S , Lenel F.V, "Some Observations on the Mechanism of Liquid Phase Sintering", Proceedings of the First Plansee Seminar, Metallwerk Plansee, Rutte, Austria, 1953, pp.106-121.

Chatfield C., "Statistics for Technology", 3rd. edition, 1983.

Chen P.C, Klar E. ,"New Copper Infiltrating Powders", Modern Developments in Powder Metallurgy, 1980, 13 , pp. 371-384.

Chun G.C , Luo X.Y, "Closure of Isolated Pores During Liquid Phase Sintering of Fe-Cu", Modern Developments in P/M, Vol.15, Principles & Process, MPIF. pp.445-475.

Courtney T.H , Lee J.K, " An Analysis for Estimating the Probability of Particle Coalescence in Liquid Phase Sintered Systems", Metallurgical Transactions -A, 1980, 11A, pp.943-947.

Courtney T.H, "Densification and Structural Developments in Liquid Phase Sintering", Metallurgical Transactions -A, 1984, Vol. 15A, pp.1065-1074.

Coffman A.W , Parr S.W, "Surface Tension of Metals With Reference to Soldering Conditions", Industrial and Engineering Chemistry, 1927, 19, pp. 1308-1311.

Dautzenberg N. , Dorweiller, H.J ,"Dimensional Behaviour of Copper-Carbon Sintered Steel", Powder Metallurgy International, 17, (6), 1985, pp. 279-282.

Dautzenberg N., Hewing J. ,"Reaction Kinetics of Mixed Alloyed Steels of Iron and Graphite Powder", Powder Metallurgy International, 1977, 9, (1), pp.6-9

Darken L.S,"Diffusion, Mobility and their Interrelation through Free Energy in Binary Metallic Systems", Transactions of AIME, 1948, 175, pp.184-201.

Danninger H. , "Pore Formation During Sintering of Fe-Cu and its Effects on Mechanical Properties", Powder Metallurgy International, Vol.19, No.1, 1987, pp.19-23.

Daniels E.J, and Macnaughtan D.J," The Use of Tin in Refrigerating Equipment", Proceedings of the British Association of Refrigeration, 1936-7, 33, (1), pp.78-86

de Laplace P.S, Mechanique Celeste, Supplement to Book 10, 1806.

Ditchburn R.W, "Surface Motion of Sputtered Particles", Proceedings of Cambridge Philosophical Society, 1933, 29, pp. 131-135.

Dowson G. , "The sintering of Bronze", Metal Powder Report, 1984, 39, pp.71-73.

Edwards A.L., "Multiple Regression and the Analysis of Variance and Covariance", W. H. Freeman and Company, U. S. A, 1979.

Elliot J.E, "Growth of Sintered Metal Compacts", Metallurgia, Vol. 59, 1959, pp. 17-27.

Eremenko, V.N & Naidich Y.V, & Lavrinenko I.A, "Liquid Phase Sintering", Consultants Bureau, New York, NY, 1970.

Farooq S. , Bose A. , German R.M, "Theory of Liquid Phase Sintering: Model Experiment on W-Ni-Fe Heavy Alloy System", Progress in P/M, Proceedings of 1987 Int. conf. on P/M, Vol.43, pp.65-77.

German R.M , D'Angelo K.A., "Enhanced Sintering Treatments for Ferrous Powders", International Metals Reviews, 1984, 29, pp. 249-272.

Gessinger G.H , Fischmeister H.F , Lukas H.L, " The Influence of Partially Wetting Second Phase on the Sintering of Solid Particles", Powder Metallurgy, 1973, 16, pp. 119-127.

German R.M , Churn K.S, " Sintering Atmosphere Effects on the Ductility of W-Ni-Fe Heavy Metals", Metallurgical Transactions- A, 1984, 15A, pp. 747-754.

German, R.M, "Liquid Phase sintering", Plenum Press, New York and London, 1985.

German, R.M, " Liquid Phase Sintering", 1985, Plenum Press, N.York & London, pp. 113-119.

Good R.J, "A Thermodynamic Derivation of Wenzel's Modification of Young's Equation for Contact Angles, Together with a Theory of Hysteresis", Journal of American Chemical Society, 1952, 74, pp. 5041-5042.

Green M.L , Wong C.C, "Liquid Phase Sintering of a Cr-Co-Fe Permanent Magnet Alloy", Modern Developments in P/M, 12, H.H.Hausner, H.W.Antes and G.D Smith (eds.), MPIF, Princeton, NJ, 1981, pp. 453-472.

Gummeson, P.U, "Iron Powder Metallurgy", Vol. III, 1968, New York, Plenum Press, p.304.

Gummeson P.U , Stosuy A. , "Iron Carbon Behaviour During Sintering", Technical Bulletin Publication, 1967, Hoganas, U.S.A.

Gummeson, P.U , Forss L., "The Effect of Copper Addition on Iron Powder", Proceeding of 11th Annual Meeting, Metal Powder Association", 1955, pp. 56-65.

Gummeson V. , Stosuy A. , "Artificial Graphite Versus Natural Graphite for P/M Parts", Metal Powder Report, Nov. 1986, 41, (11), pp. 851-852.

Hansen M. , Anderko T. , "Constitution of Binary Alloys", Mc Graw Hill, N.York, 1958.

Harkins W.D , Jordan H.F,"A Method for Determination of Surface and Interfacial Tension from the Maximum Pull of a ring", Journal of American Chemical Society , 1930, 52, pp. 1751-1772.

Harkins W.D and Jordan H.F, "A Method for The Determination of Surface and Interfacial Tension from The Maximum Pull on a Ring", Journal of American Chemical Society, 1930, 52, pp. 1751-1772.

Harkins W.D, "The Physical Chemistry of Surface Films", Reinhold, N.York 1952.

Harker D., Parker E., "Grain Shape and Grain Growth", Transactions of ASM, 1945, Vol.34, pp. 156-195.

Heckel R.W," A New Approach to the Study of Powder Compaction", Progress in P/M. , 1961, 17, pp.66-81.

Heckel, R.S,"Die Wall Lubrication Improves P/M Parts", Precision Metals, December 1967, 25, Dec. 1967, pp. 41-47.

Hill P.A ,"Homogeneity and Strength of Sintered Mixed Elemental Steel Compacts", Undergraduate project report, 1979, Mechanical and Production Engineering Department, Aston University, Birmingham, England.

Hough R.R , Rolls R., "Copper Diffusion in Iron During High Temperature Tensile Creep", Metallurgical Transactions , September 1971, Vol. 2, pp.2471-2475.

Hoganas Iron Powder, Data sheet No. 1, October 1980, Hoganas AB, Box 501, S-26301 Hoganas, Sweden.

Hondros E.D,"The influence of phosphorus in Dilute Solid Solution on the Absolute Surface and Grain Boundary Energies of Iron", Proceedings of Royal Society of London , 1965, 286, pp. 479-498.

Huppmann W.J and Petzow G., "Sintering Processes" , (ed.) G.C. Kuczynski, 1980, N.York, Plenum Press, pp. 189-201.

Ishiwara T. , Yonekura T. , Ishigaki T. , "On The Ternary Diagram of The System Fe - Cu - C", Tokoku Imperial University Science Report, 1926, 15, pp. 81-114.

Jamil S.J , Chadwick G.A ,"Investigation and Analysis of Liquid Phase Sintering of Fe- Cu-C Compacts", Powder Metallurgy, 1985, 28, (2), pp.65-71.

James B.A, "Die Wall Lubrication for Powder Compaction: a Feasible Solution?", Powder Metallurgy, 1987, 30, (4), 273-280.

James M.R, "Coated Cemented Carbide Cutting Tools", The British Foundryman, September 1977, pp. 483-490.

Johnson & Co Inc., "A Brazing System for Joining Ferrous P/M Components", Technical Paper, Jan. 1975, Thomas Read South Hawthorne, N.J, 07506.

Kaysser W.A, Huppmann W.J, Petzow G., "Analysis of Dimensional Changes During Sintering of Fe-Cu", Powder Metallurgy, 1980, 23, (2), pp. 86-91.

Kastkin B.S and Tsaryuk A.K, "Special Features of Plastic Deformation in HAZ", Automatic Welding, 1965, 18, (2), pp. 1-7.

Kaysser W.A, Zivkovic M. , Petzow G., "Shape Accommodation During Grain Growth in The Presence of a Liquid Phase", Journal of Material Science, 1985, 20, pp. 578-584.

Khan F. , Cizeron G., "Rearrangement Phenomenon Developed Inside Powder Compacts: Theoretical Model Expressing the Associated Shrinkage", Journal of Material Science, 1984, 19, (8), pp. 2599-2605.

Kingery W.D, Niki E., Narasimhan M.D, "Sintering of Oxide and Carbide-Metal Compositions in Presence of a Liquid Phase", Journal of American Ceramics Society , 1961, 44, pp. 29-35.

Kingery W.D, "Kinetics of High Temperature Processes", 1959, N. York & London, pp.187-192.

Knopp, W.V,"Brazing Problems in P/M", The International Journal of P/M & Powder Technology , Jan. 1975 , Vol. 11, (1), pp.63-65.

Kothari N.C, "Densification and Grain Growth During Liquid Phase Sintering of W - Cu - Ni Alloys", Journal of Less Common Metals, 1967, Vol. 13, pp. 457-468.

Krantz, T. , "The Effect of Density and Composition on The Dimensional Stability & Strength of Iron-Copper Alloys". International Journal of Powder Metallurgy, 1969, 5, (3), pp. 35-43.

Kwon O.J, Yoon D.N, "Closure of Isolated Pores in Liquid Phase Sintering of W-Ni", American P/M Institute, 1981, Vol. 17, No. 2, pp. 127-133.

Langmuir R. , "The Mechanism of Surface Phenomena of Floation", Transactions Faraday Society, 1920, 15, pp. 62-74.

Latin A. , "The Influence of Fluxes on The Spreading Power of Tin Solder on Copper". Transactions of Faraday Society , 1938, 34, pp.1384-1395.

Lenel F.V, "Sintering with a Liquid Phase", Physics of Powder Metallurgy, Mc Graw Hill, N.York, 1951, pp. 238-253.

Lenel F.V, "Sintering in the Presence of a Liquid Phase", Transactions of AIME, 1948, Vol. 175, pp. 878-896.

Lecomte du Nouy P. , "A New Apparatus for Measuring Surface Tension", Journal of General Physiology, 1919, 1, pp. 521-524.

Lester G.R , "Contact Angle of Liquids at Deformable Solid Surfaces", Journal of Colloid Science, 1961, 16, pp.315-326

Lisovskii, A.F, "Thermodynamics of Penetration of a Liquid Phase into Sintered Compacts", Soviet P/M & Metall. Ceramics, 1974, 13, pp. 832-835.

Lograsso B.K, German R.M, "Liquid Phase Sintered Titanium Carbide - Tool Steel Composites for High Temperature Service", Progress in P/M, Proceeding of 1987 International Conference in P/M, Vol. 43, pp. 415-439.

Lumpkins, E.R, "A Theoretical Review of Copper Infiltration of P/M Compacts". Powder Metallurgy International, 1985, 17, (3), pp.120-123.

Majima K. , Mitani H. ,"Sintering Mechanism in Mixed Powder Compacts of the Fe-Cu-C Ternary System", Transactions of Japan Institute of Metals, 1977, 18, pp.663-672.

Masuda Y. , Watanabe R. , "Ostwald Ripening Process in Sintering of Metal Powders", Sintering Processes, G.C. Kuczynski (ed.), Plenum Press, N.York 1980, pp. 3-21.

Maulik P. , Price W.J.C, "Effect of Carbon Additions on Sintering Characteristics and Microstructure of BT42 High Speed Steel", Powder Metallurgy, 1987, 30, pp. 240-248.

Makarova R.V, Teodorovich O.K, Frantsevich I.N, "The Coalescence Phenomenon in Liquid Phase Sintering of the System W-Ni-Fe and W-Ni-Cu", Soviet P/M and Metall. Ceramics , 1965, 4, pp. 554-559.

Maulik P. , Price W.J.C, "Effect of Carbon additions on sintering characteristics and microstructure of BT 42 high speed steel". P/M, 1987, Vol. 30, (4), pp. 240-248.

Mead H.W , Brichenall C.E ,"Self Diffusion of Iron in Austenite", Trans. AIME, 1956, 206, pp.1136-1339

Milner D.R, "A Survey of Scientific Principles Related to Welding and Spreading", British Welding Journal, March 1958, pp. 90-105.

MPIF Standard 49, "Infiltration" , 1982. MPIF, Princeton, N.J, U.S.A.

Naidich Y.V, Lavrinenko I.A, Petrishchev, "Study of Capillary Adhesive Forces between Solid Particles with a Liquid Layer at the Point of Contact. 1- Spherical Particles", Soviet P/M and Metall. Ceramics , 1965, 4, pp. 129-133.

Nowotarski M.S, "Effect of Atmosphere on Reduction and Annealing of Water Atomised Copper Powders", Modern Developments in P/M, Proceedings of Conference , 17-22 June 1984, Toronto, Canada, pp. 389-403.

Nordgren A. , Melander A. , "Influence of Porosity on Strength of WC-10%Co Cemented Carbide", Powder Metallurgy, 1988, Vol. 31, No. 3, pp. 189-200.

Ohno R. , "Rates of Dissolution of Rotating Iron Cylinders in liquid Copper and Cu-Fe Alloys", Metallurgical Transactions , Vol.4, April 1973, pp. 909-915.

Onoda M. , Kameda R. , Koiso T., "Application of Sinter-Brazing", Metal Powder Report, November 1983, pp. 632-643.

Parameswaren K. , Metz K. , Morris A. , "Phase Equillibria for Iron Rich Fe-Cu-C Alloys: 1500 to 950°C". Metallurgical Transactions- A, Vol. 10A, 1979, pp. 1929-1939.

Pettersson H. ,"An Investigation of the Penetration of Steel into Molding Sand", Trans. American Foundrymen's Society, Vol. 59, 1951. pp.35-55

Phadke V.B , Davies B.L, "Precipitation Hardening in Sintered Fe-Cu alloys". Powder Metallurgy International, Vol. 9, (2), 1977, pp. 64-67.

Pilling N.B, Bedworth R.E ,"The Oxidation of Metals at High Temperatures", Journal of Institute of Metals, 1923, 29, pp.529-591.

Plateau, Statistique Experimental et Theorique des Soumis aux Seules Forces Moleculaires, 1983.

Powders Diffraction File, 1978, "Hanawalt Method", Search Manual, Inorganic Compounds, JCPOS, International Centre for Diffraction Data.

Pozdnyak N. Z. ,"Study of Structure Formation During Sintering of Iron - Graphite Alloys", Soviet Powder Metallurgy, 1963, 5, pp.403-407

Pritchard T. ,"Brazing Sintered Powder Compacts", Metal Industry, Feb. 1964, pp. 184-185

Price G.H.S , Smithells C.J , Williams S.V, "Sintered alloys. Part 1 - Copper - Nickel - Tungsten Alloys Sintered with a Liquid Phase Present", Journal of Institute of Metals, 1938, Vol. 62, pp. 239-264.

Regel F.W,"The Steam Treatment of Sintered Iron Parts", Engineers Digest, 1963, 24, (11), pp. 91-93.

Rennhack E.H, "Strengthening Effect of Copper in Infiltrated Sintering Iron Parts", Progress in P/M, 1961, 17, pp. 12-18.

Rivilin V.G. , "Phase Equilibrium in Iron Ternary Alloys", International Metals Reviews, 1984, 29, (2), pp. 96-121.

Rigger O.K , Van Vlack L.H, "Dihedral Angle Measurement", Transaction of the Metallurgical Society of AIME, 1960, vol. 28, pp. 933-935.

Roth T.A,"The surface and Grain Boundary Energies of Iron, Cobalt and Nickel", Journal of Material Science and Engineering, 1975, 18, pp. 183-192

Roberts C.S,"Effect of Carbon on the volume Fractions and Lattice Parameters of Retained Austenite", Transactions AIME, 1953, 197, pp.203-204

Salter W.J.M, "Effect of Alloying Elements on Solubility and Surface Energy of Copper in Mild Steel", Journal of Iron & Steel Institute , May 1966, Vol. 204, pp. 478-488.

Sanderson T.H ,"Steam Atmosphere Heat Treatment", Heat Treatment of Metals, 1975, (4), pp.109-112.

Schwarzkopf P., "The Mechanism of Infiltration", Symposium on P/M, Iron & Steel Institute , Preprint, Group II, 1954, pp. 55-58.

Schatz J. ,"Die Metallurgischen Vorgange Zwischen Harlot und Grundwerkstoffen und Flogerungen fur die Lotgerechte Konstruktion", Schweissen Undschneiden, 1957, 9, pp.522-530.

Sebastian K.V , Tendolkar G.S,"Experimental Observations on the Densification by rearrangement in Liquid Phase Sintering", Powder Metallurgy International, 1979, 11, (2), pp. 62-64

Shaler J. , "Theoretical Aspects of the Infiltration of Powder Metallurgy Products". International Journal of P/M, 1965, 1, (1), pp. 3-14.

Shewmon P.G, "Diffusion in Solids", New York, Mc Graw Hill, 1963.

Shuttleworth R. , "The Spreading of a Liquid Over a Rough Solid" , Discoveries of Faraday Society, 1948, 3, pp. 16-22.

Sitnik B.A , "Assessment of the Liability of Steels to Penetration of Molten Copper Alloys", Welding Production, June 1975, 22, (6), pp. 40-42.

Smith, C.S, "Grains, Phases and Interfaces: An Interpretation of Microstructure", Transactions of AIME, 1948, 175, pp. 15-51.

Smith C.S, Palmer E.W, "The Precipitation Hardening of Copper Steels", Technical Report, The American Brass Co. , N.York, 1933, pp. 133-165.

Smithells C.J. , "Metals Reference Book", Vol. 2 ,(4^{th} ed.), 1967, London ,Butterworths, p. 489.

Snape E. , "Infiltration of Iron Compacts with Ni- Containing Copper Infiltrant", Powder Metallurgy International, 1974, 6, (1), pp. 20-23.

Speich G.R , Gula J.A, Fisher R.M, "Diffusivity and Solubility Limit of Copper in Alpha and Gamma Iron", The Electron Microprobe, (ed.) Mc Kinley, Heinrich & Wittry, 1966.

Squire A. ," Iron-Graphite Powder Compacts", Transactions of AIME, 1947, 171, pp. 473-484.

Suezawa Y. ,"A Study of Ag - Cu Brazed Joint Strength of Sintered Steel", Proceedings of International Conf. on Fracture Mechanics and Technology, Hong Kong, March 1977, Vol. 1, pp. 439-450.

Swarzkopf P. and Kieffer R. , "Cemented Carbide", Macmillan, N.York, 1960.

Thummler F., Thomma W., "The Sintering Process", Metallurgical Reviews, 1967, 115, pp.69-103.

Trudel Y. , Angers R. , "Comparative Study of Fe - Cu - C Alloys Made from Mixed and Prealloyed Powders". Modern Developments in Powder Metallurgy, MPIF, Vol. 6, 1974, pp. 305-322.

Trudel Y. , Angers R. "Properties of Fe - Cu Alloys Made from Elemental or Prealloyed Powders". International Journal of P/M & Powder Technology, 1975, 11, (1), pp. 5-16.

Ueda Y., Kunimitsu S., Kondo N. ,"Infiltration of Liquid Copper into Sintered Fe and Fe-Al_2O_3 Compacts", Journal of Japanese Institute of Metals, 1981, 45, (11), pp.1208-1214.

U.S Patent 3, 307, 924, "Copper Infiltrating Composition for Porous Material".

U.K Patent 1465213,"Method of Brazing Compacted Powder Metal Parts", Feb. 1977 .

U.K Patent 1444521,"Copper - Manganese - Zinc Brazing Alloy", Aug. 1976.

U.K Patent 1360890, "Brazing Alloy Composition", July 1974.

U.K Patent 1547117, "Nickel Base Brazing Alloy", June 1979.

U.K Patent 2007137-A, "Brazing of Sintered Powder Metal Parts", May 1979.

U.K Patent 1484641, "Method of Binding Sintered Iron Containing Articles", Sep. 1977.

Van Vlack L.H, "Intergranular Energy of Iron and Some Iron Alloys", Transactions of AIME, 1951, pp. 251-259.

Veidis, M.V ,"Selection of Protective Atmosphere for Bottom Infiltrating of Copper", International Journal of P/M, 1974, 10, (2), pp. 101-103.

Veidis, M.V "Mechanical Properties of Copper Infiltrated Low Alloy Steel Powders", The International Journal of P/M & Powder Technology , 1976, 12, pp. 127-130.

Ward, M. ,"The Use of Lubricants in Iron Powder Metallurgy", Ph.D. Thesis, Aston University, April 1977.

Wassink R.J.K, "Wetting of Solid Metal Surfaces by Molten Metals", Journal of Institute of Metals, 1967, Vol. 95, pp. 38-43.

Wenzel R.N, "Resistance of Solid Surfaces to Wetting by Water", Industrial Engineering Chemistry, 1936, 28, pp. 988-994.

Whalen T.J , Humenik M., "Sintering in the Presence of a Liquid Phase", Sintering and Related Phenomena, G.C.Kuczynski, N. Hooton, C. Gibben (eds.), Gordon and Breach, New York, NY, 1967.

Young T. ,"An Essay on the Cohesion of Fluids", Philosophical Transactions of Royal Society of London, 1805, 95, pp.65-87.

Young T., "Works of Dr. Young", (ed.) Peacock, (London), Vol. 1, p. 418.

Appendices

Appendix: A

Specification for ASC100.29

Apparent Density, Mgm^{-3} (1)	2.95 ± 0.10
Flow, sec / 50 g (2)	max 30
Compressibility, Mgm^{-3} (3)a	min 6.80
Sieve analysis, Tyler mesh, %:	
+65	0
+80	max 1
+100	max 10
-325	10 - 30

Below you will find typical physical and chemical data as well as properties after sintering for ASC100.29.

Physical Data	Asc100.29
Apparent Density, Mgm^{-3} (1)	2.90
Flow, sec/50 g (2)	24
Compressibility, Mgm^{-3} (3)a (lubr. die)	6.81
Compressibility, Mgm^{-3} (3)b (lubr. powder)	6.90
Green Strength, psi (6.0 Mgm^{-3}) (4)	1300
	(6.7 Mgm^{-3}) (4)
	3400

Chemical Analysis

H_2-loss	% (5)	0.1
Carbon	"	0.01
Silicon	"	0.02
Manganese	"	0.05
Sulphur	"	0.01
Phosphorus	"	0.01

---

(1) MPIF Standard 4-45

(2) " " 3-45

(3)a ASTM Standard 331-64 (1970), lubr. Steel die

(3)b " " " " lubr. Powder

(4) " " 312-64 (1970)

(5) MPIF Standard 2-64

Properties after compacting at 6 tons/cm2 with 0.65 % Zn-stearate admixed and sintering for 60 minutes at 1120° C in H_2.

Sintered Density, Mgm^{-3} (6)	7.20
Dimensional Change, % (7)	-0.16
Ultimate Tensile Strength, psi (kp/mm2) (8)	32.000 (23)
Elongation, % (8)	20
Hardness, HB	65

(6) MPIF Standard 10-63, on TS test specimens

(7) From green to as sintered on TS test specimens

(8) MPIF Standard 10-63

(9) HB 2, 5/62, 5

Anchorbraze 72

Chemical Composition

Copper	38.0 - 42.0
Nickel	40.0 - 44.0
Manganese	14.0 - 17.0
Silicon	1.6 - 2.0
Boron	1.3 - 1.7
Other	1.0 Max.

Apparent Density	1.85 - 2.20 Mgm^{-3}	Aim 2.0 max.
Flow	Recommended 20 Sec. Max. CARNEY	
Screen Analysis	+40 Mesh	5% Max.
	-200 Mesh	5% Max.

Green Properties

Blend Powder with 5% Armco 444 Flux (-80 Mesh) and 0.5% Emersol 150 Stearic Acid. Blend Time 10 Minutes

Green Density	30 tsi	4.80 - 4.90 Nominal
	40 tsi	5.05 - 5.15 Nominal
Green Strength	30 tsi	300 psi Minimum
	40 tsi	400 psi Minimum

Appendix: B

Sample Impregnation with Araldite

The specimens tested in this project were quite porous. This can create problems when polishing the micros, especially on diamond polishing pads, by pulling the particles out of the surface.

To overcome this problem and maintain the actual pore morphology, the samples were impregnated with Araldite resin in the following manner:

Araldite epoxy resin (MY 778) was mixed with araldite harder (HY 951) in the ratio of 8:1 by volume. The mix was placed in a dessicator for about 5 minutes for bubbles to come over the surface. A small amount of that was then dropped on each sample so that it could cover the surface of the compacts. They were then placed in the desicator for about 15 minutes to force the entrapped air out of the porosity of the samples. After this period, the air forces the araldite into the porosity. The samples were then placed in a safe place for 24 hrs for the araldite to set. After the Araldite is set, the samples were polished on 1200 silicon carbide grit to remove the excess araldite and reveal the surface of the samples.

The set Araldite in the porosity acts as a reinforcement which holds the particles together and prevents disintegration during subsequent diamond polishing, and thus, maintains the true pore morphology.

Appendix: C

Computer Programmes

During heating, the alumina tube surrounding the specimen expands at a higher rate than the specimen. Therefore, the net expansion detected by the probe is only a certain fraction of the actual specimen expansion. Moreover, since a high heating rate is employed (20°C min^{-1}), the alumina probe and specimen holder tube will expand at different rates. (Figure 3.13). It was necessary to correct all the TMA traces for their corresponding baseline drift. Three baseline runs were obtained with no samples and with the probe touching the floor of alumina tube, from room temperature to 960, 1125 and 1200°C at a heating rate of 20°C min^{-1}. The following programme collects the TMA data and corrects them for their respective baseline drift. The programme is capable of first selecting the sintering temperature and then choosing its corresponding data for correction from the resident data bank. A separate programme is written to read the corrected data and use it to draw the TMA graphs, (Appendix C).

Programme Notes:-

tb = baseline temperature

db = baseline drift

d1 = change in length of the sample

d = calculated change in length by interpolation.

ihc = heating or cooling conditions. Temperature rising (ihc = 1)
, temperature falling (ihc = 2).

dl = actual change in length = d1 - d

ib, depends on which set of data has been input. The programme then chooses the right set of data for that particular temperature.

Therefore: ib = 1 for 962°C , 2 for 1125°C , 3 for 1200°C

in, is used in an array and decides which set of data has to be read for the baseline drift .

Since there may not always be a baseline correction at a certain sintering temperature, the programme calculates a value for the baseline drift by interpolation.

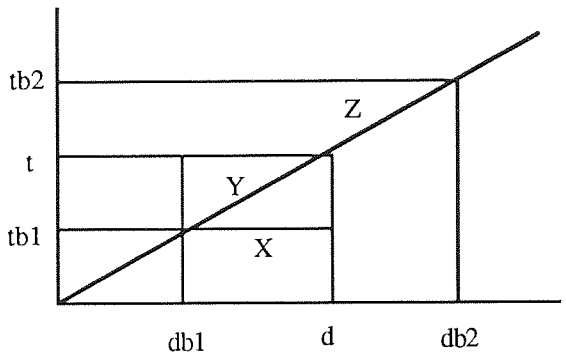

$$d = db1 + X$$

t, lies between tb2 and tb1. The baseline drift at that temperature is calculated from similar triangles:-

$$\frac{Y}{t - tb1} = \frac{Z}{tb2 - t} \qquad \frac{Y}{Z} = \frac{t - tb1}{tb2 - t} \quad \ldots\ldots\ldots\ldots\ldots(1)$$

and $$\frac{Y}{X} = \frac{Z}{db2 - db1} \qquad \frac{Y}{Z} = \frac{X}{db2 - db1} \quad \ldots\ldots\ldots(2)$$

From (1) and (2):

$$\frac{t - tb1}{tb2 - t} = \frac{X}{db2 - db1}$$

Thus

$$X = \frac{(t - tb1)\,(db2 - db1)}{tb2 - t}$$

Finally, d = db1 - X = baseline drift correction at the sintering temperature, t.

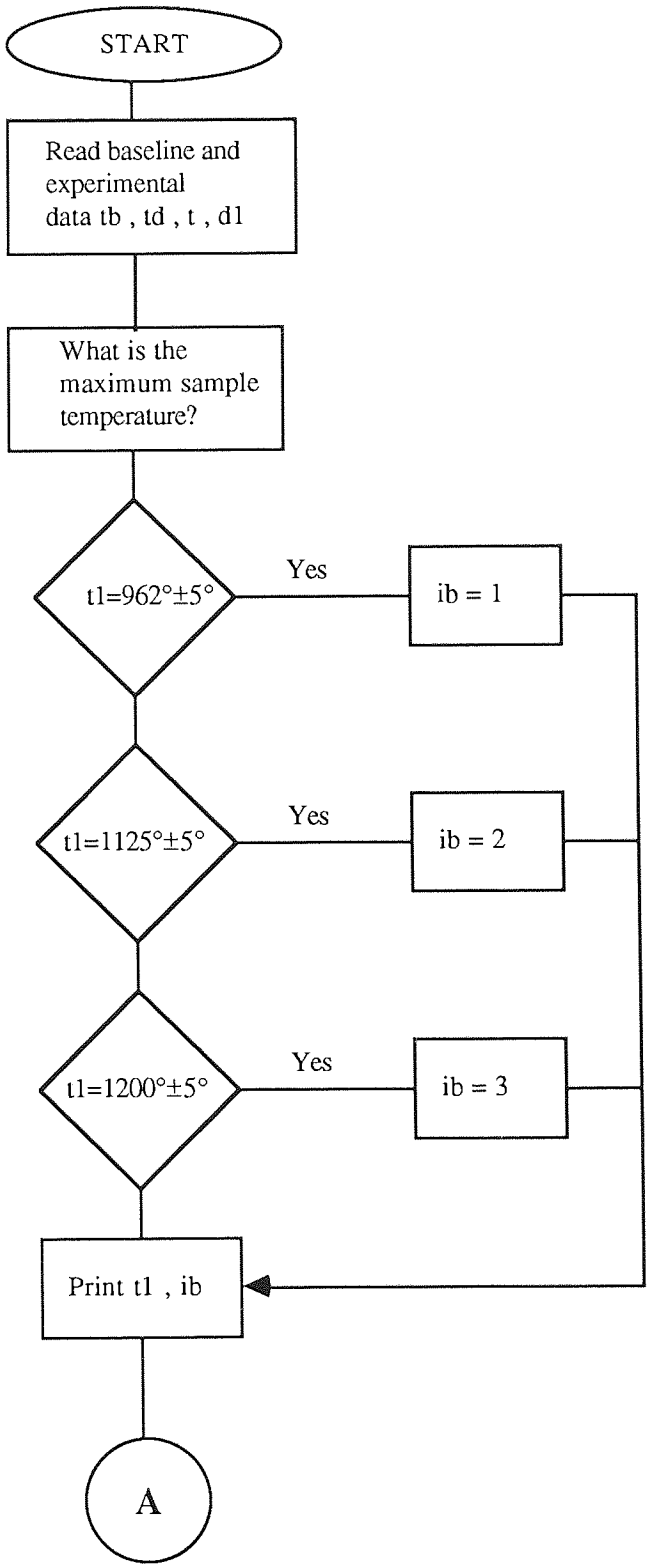
START
Read baseline and experimental data tb , td , t , d1
What is the maximum sample temperature?
t1=962°±5°
Yes
ib = 1
t1=1125°±5°
Yes
ib = 2
t1=1200°±5°
Yes
ib = 3
Print t1 , ib
A

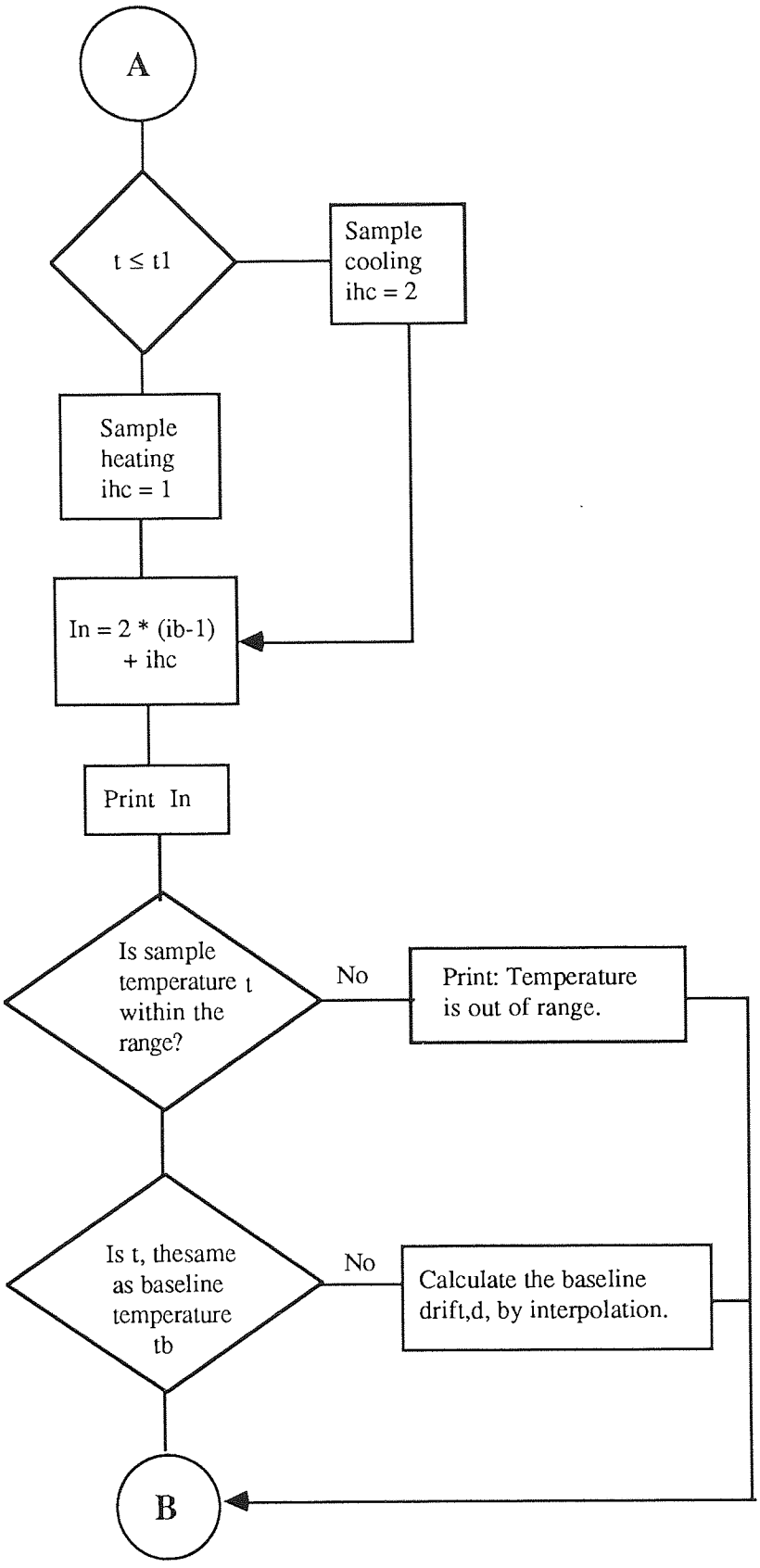
A
t ≤ t1
Sample cooling ihc = 2
Sample heating ihc = 1
In = 2 * (ib-1) + ihc
Print In
Is sample temperature t within the range?
No
Print: Temperature is out of range.
Is t, thesame as baseline temperature tb
No
Calculate the baseline drift,d, by interpolation.
B

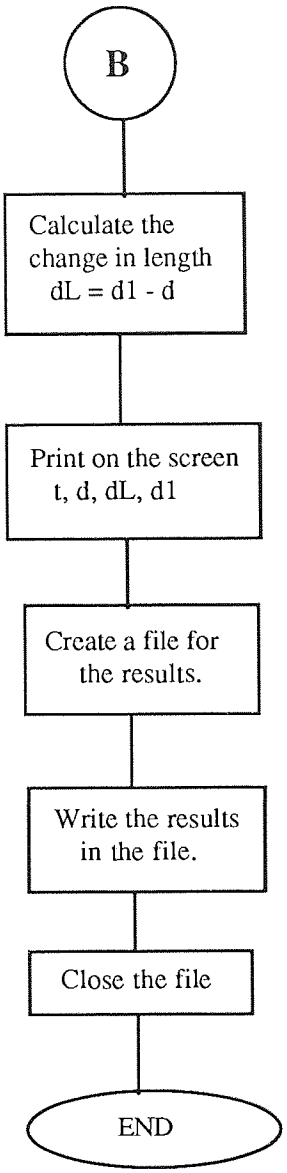
B
Calculate the change in length dL = d1 - d
Print on the screen t, d, dL, d1
Create a file for the results.
Write the results in the file.
Close the file
END

This programme is to collect the experimental results and to correct them for their corresponding baseline drift.

```
10 DIM tb(20,6), db(20,6)
REM *****BASELINE TEMPERATURES FOR EXPERIMENTS RUN AT
962°C.*****
11 DATA  18,94,169,215,258,360,409,456,602,688
12 DATA  730,788,844,939,954,962,962,962,962,962
13 DATA  18,80,133,169,215,310,380,503,610,755
14 DATA  860,923,946,962,962,962,962,962,962,962

REM *****BASELINE TEMPERATURES FOR EXPERIMENTS RUN AT
1125°C*****
17 DATA 18,94,169,215,258,360,409,456,602,688
18 DATA 730,788,844,939,962,1037,1111,1125,1125,1125
19 DATA 18,80,133,169,215,310,380,494,637,820
20 DATA 946,1052,1125,1125,1125,1125,1125,1125,1125,1125

REM *****BASELINE TEMPERATURES FOR EXPERIMENTS RUN AT
1200°C*****
23 DATA 18,94,169,215,258,360,409,456,602,688
24 DATA 730,788,844,939,962,1037,1119,1180,1200,1200
25 DATA 18,133,169,215,310,380,438,566,722,915
26 DATA 1169, 1200,1200,1200,1200,1200,1200,1200,1200,1200

REM *****BASELINE DRIFT FOR EXPERIMENTS RUN AT 962°C*****
15 DATA  0,-5,-6,-6,-5,-2,0,5,9,13,15,17,19,23,25,29,29,29,29,29
16 DATA  0,5,10,14,18,25,29,35,38,38,37,35,33,31,31,31,31,31,31,31
```

```
REM*****BASELINE DRIFT FOR EXPERIMENTS RUN AT 1125°C*****
21 DATA 0,-5,-6,-6,-5,-2,0,5,9,13,15,17,19,23,24,27,29,35,35,35
22 DATA 0,5,10,14,18,25,29,35,39,41,41,40,35,35,35,35,35,35,35,35

REM *****BASELINE DRIFT FOR EXPERIMENTS RUN AT 1200°C*****
28 DATA 0,-5,-6,-6,-5,-2,0,5,9,13,15,17,19,23,24,27,29,31,36,36
29 DATA 0,10,14,18,25,29,32,37,40,42,41,37,37,37,37,37,37,37,37,37

REM *****READING ALUMINA BASELINE DATA*****
200 FOR j=1 TO 6
210 FOR i=1 TO 20
220 READ tb(i,j)
230 NEXT i
240 NEXT j
250 FOR j=1 TO 6
260 FOR i=1 TO 20
270 READ db(i,j)
280 NEXT i
290 NEXT j

 REM *****READING EXPERIMENTAL DATA FROM THE
 CLIPBOARD*****
 320 OPEN "Clip:" FOR INPUT AS#1
 330 LET t1=0
 340 FOR i=1 TO 40
 350 IF EOF(1) THEN CLOSE#1: GOTO 400
 360 INPUT #1,t,d1
```

```
PRINT i,t,d1
370 IF (t>t1) THEN LET t1=t
380 NEXT i

REM *****DECIDING WHICH BASELINE DATA RANGE TO CHOOSE*****
400 LET t2=ABS(t1-962)
410 LET t3= ABS(t1-1125)
420 LET t4=ABS(t1-1200)
430 IF(t2<5) THEN ib=1
440 IF (t3<5) THEN ib=2
450 IF (t4<5) THEN ib=3
460 PRINT t1,"ib=";ib
310 LET t=0

REM***** READING EXP. DATA & CREATING AN OUT PUT FILE*****
20 OPEN "Clip:" FOR INPUT AS#1
25 OPEN "out1"FOR OUTPUT AS#2
30 FOR i=1 TO 40
33 LET t1=t
35 IF EOF (1) THEN CLOSE#1: CLOSE#2:GOTO 100
40 INPUT#1, t,d1

REM *****LOOKING WHETHER SAMPLE TEMP. IS ASCENDING OR
DESCENDING*****.
50 IF (t=<t1) THEN ihc=2 ELSE ihc=1
60 GOSUB 500

REM*****dl=True change in length. d1=Observed length. d=Calculated baseline
drift.*****
```

```
70 LET dl=d1-d
75 PRINT i,t,d1,d,dl
80 PRINT#2, i,t,d1,d,dl
90 NEXT i
95 CLOSE#1

REM*****WRITING THE RESULT BACK INTO THE CLIPBOARD*****
100 OPEN "I",#1,"out1"
OPEN "clip:" FOR OUTPUT AS #2
WHILE NOT EOF(1)
INPUT#1 , i,t,d1,d,dl
WRITE#2 , i,t,d1,d,dl
WEND
CLOSE#2:CLOSE#1
END


REM*****CHECKING IF SAMPLE TEMP. IS OUT OF RANGE*****
500 LET in=2*(ib-1)+ihc
PRINT"in=";in,"tb(1,in)=";tb(1,in),"tb(20,in)=";tb(20,in)
510 IF(t < tb(1,in))THEN GOTO 600
520 IF(t > tb(20,in)) THEN GOTO 600

REM*****LOOKING IF THE SAMPLE TEMP. IS THE SAME AS BASELINE
TEMP.*****
530 FOR j=2 TO 20
540 IF(t =< tb(j,in))THEN GOTO 620
550 NEXT j
```

```
600 PRINT " temperature out of range"
610 RETURN

REM *****INTERPOLATING TO CALCULATE BASELINE DRIFT AT THE
SINTERING TEMP.*****
620 LET d=db(j-1,in)
630 IF(tb(j,in)=tb(j-1,in)) THEN GOTO 610
640 LET t2=(t-tb(j-1,in))*(db(j,in)-db(j-1,in))
650 LET d=t2/(tb(j,in)-tb(j-1,in))+db(j-1,in)
660 RETURN
```

This programme is to enable the "Cricket Graph", read and print the corrected data.

```
DIM t(40)
OPEN "Clip:"FOR INPUT AS#1
OPEN "out 2" FOR OUTPUT AS#2
LET t1=0
FOR i=1 TO 40
IF EOF(1) THEN CLOSE#1: LET j=i-1: GOTO 400
INPUT#1 ,t(i)
IF t(i)>t1 THEN LET t1=t(i):LET A=i :PRINT i,"t(i)=";t(i):PRINT#2,t(i)
NEXT i
```

```
400 LET t(A+1)=t1+600: LET i=A+1
PRINT "i=";i,"t(i)=";t(i):PRINT#2 , t(i)
FOR i=A+2 TO j
LET dt= t(i)-t1
LET t1= t(i)
LET t(i)= t(i-1)-dt
PRINT "i=";i,"t(i)=";t(i):PRINT#2,t(i)
NEXT i
CLOSE#2
OPEN"I",#1,"out 2"
OPEN "Clip:"FOR OUTPUT AS#2
WHILE NOT EOF(1)
INPUT#1,t3
WRITE #2 ,t3
WEND
CLOSE#2:CLOSE#1
500 END
```